OPTICAL FIBRE SENSORS FOR NOVEL MEDICAL DEVICES DURING ANAESTHESIA

Francisco Ulises Hernandez Ledezma, MSc

Thesis submitted to the University of Nottingham for the degree of Doctor of Philosophy (PhD)

SEPTEMBER 2017



Dedication

to my loving parents, sisters, nieces and nephew

Abstract

This research focuses on the development of optical fibre sensors that can be applied during critical care. The sensors developed are: (i) an optical fibre humidity sensor based on the deposition of a hygroscopic film onto the distal tip of the fibre and forming a Fabry-Pêrot cavity; (ii) chemical functionalization of U-shaped fibres and Long Period Gratings (LPGs). Fibre Bragg Gratings (FBGs) are only used for temperature monitoring in this work.

The current trends in a new generation of humidity sensors suggest that electronic-based technologies could be soon replaced by photonic sensors due to better response times. Optical fibre technology has been considered as a promising platform for providing engineering solutions to unmet clinical needs. For example, anaesthetized patients are transferred from the induction room to the MRI room and taken back, with the need for continuous monitoring of vital signs such as respiration, but some technologies lack compatibility with MRI fields. In the operating room, patients are under anaesthesia, intubated and mechanically ventilated, but some under-humidification or over-humidification of the ventilation air causes secondary effects. Anaesthesiologists rely on total intravenous anaesthesia (TIVA) and monitoring of vital signs as indicators of unconsciousness; current investigations have shown that there is a need to measure the concentration of propofol in real time directly from the blood or breath of patients. Similarly, patients in the intensive care unit (ICU) after surgery require continuous monitoring of diverse biochemical parameters. In this research, the application of optical fibre sensors is demonstrated as an engineering solution for some of these clinical challenges. The simultaneous measurement of humidity and temperature with an optical fibre sensor, a biosensor for propofol detection and another for protein detection were fabricated and demonstrated in this work.

The sensitivity, response time and hysteresis of a novel optical fibre humidity sensor has been investigated over a humidity range of 5% Relative Humidity (RH) to 95% RH using a controlled bench-top set-up. The optical fibre

humidity sensor proposed has a very simple and low cost porous structured sensing element obtained with poly(allylamine hydrochloride) (PAH) and silica (SiO_2) using the layer-by-layer (LbL) fabrication method. The fast response of the sensor (1.13 ± 0.3 s) enabled changes in humidity in individual breaths to be resolved. After calibration, the performance of the sensor was evaluated in the breathing circuit of a mechanical ventilator and respiratory equipment where its faster response allowed monitoring of breath to breath humidity levels during different modes of ventilation. It also has the capability to provide absolute humidity (AH) measurements when an FBG is included for simultaneous temperature measurements.

An LPG sensor anchored with SiO_2 core and gold (Au) shell nanoparticles has been investigated as a biosensing platform for protein detection. The well-known protein interaction between biotin and streptavidin (SV) was used as a proof of concept. The proposed sensor presented Langmuir adsorption to SV concentrations with a limit of detection (LoD) down to 15.13 nM and a lowest detected concentration of 2.5 nM. In addition, U-shaped fibres and LPGs functionalized with host-guest imprinted TiO_2 thin films were used to test propofol detection in aqueous solutions. These sensors also presented Langmuir adsorption in the mili-molar range in aqueous solutions and a lowest detected concentration of 0.65 μM. Detection limits of propofol were improved with the addition of mesoporous silica nanoparticles (MSNs) and inorganic molecular imprinting to allow detection down to 99 nM in aqueous solution and 30 ppb in gaseous phase.

In conclusion, this research has successfully demonstrated the use of novel optical fibre sensors in laboratory and real conditions through embedding the developed sensors in critical care equipment usually used during anaesthesia.

Author's published research papers

Journal articles:

1. Sergiy Korposh, Suguru Kodaira, Roman Selyanchyn, **Francisco H. Ledezma**, Stephen W. James, Seung-Woo Lee, "Porphyrin-nanoassembled fiber-optic gas sensor fabrication: Optimization of parameters for sensitive ammonia gas detection", *Optics and Laser Technology*, 101, 1 – 10 (2018).
2. **Francisco U. Hernandez**, Stephen Morgan, Barrie Hayes-Gill, Daniel Harvey, William Kinnear, Andrew Norris, David Evans, Jonathan Hardman, and Serhiy Korposh., "Characterisation and Use of a Fibre Optic Sensor based on PAH/SiO_2 Film for Humidity Sensing in Ventilator Care Equipment," *IEEE Transactions on Biomedical Engineering*, 63(9), 1985-1992 (2016).
3. L. Marques, **F.U. Hernandez**, S.W. James, S.P. Morgan, M.Clark, R.P. Tatam and S. Korposh., "Highly sensitive optical fibre long period grating biosensor anchored with silica core gold shell nanoparticles," *Biosensors & Bioelectronics*, 75, 222-231 (2015)

Conference papers:

4. R Correia, R. Sinha, A. Norris, S. Korposh, S. Talbot, **F.U. Hernandez**, B.R. Hayes-Gill, S.P. Morgan., "Optical fibre sensing at the interface between tissue and medical device," *Proc. SPIE*, 5th International Conference on Biophotonics, (May 2017).
5. **F. U. Hernandez**, T. Wang, S. Korposh. R. Correia, B.R. Hayes-Gill, J. Hromadka, N.N. Mohd Hazlan, A. Norris, D. Evans, S.-W. Lee, and S.P. Morgan., "Optical fibre sensors during critical care," *Proc. SPIE*, 5th International Conference on Biophotonics, (May 2017).
6. R. Correia, O.R. Blackman, **F.U. Hernandez**, S. Korposh, S.P. Morgan, B. R. Hayes-Gill, S.W. James, D. Evans, and A. Norris., "Highly sensitive contact pressure measurements using FBG patch in endotracheal tube cuff," *Proc. SPIE 9916*, Sixth European Workshop on Optical Fibre Sensors, 99161F (May 2016).

7. **F.U. Hernandez**, R. Correia, S. P. Morgan, B. Hayes-Gill, D. Evans, R. Sinha, A. Norris, D. Harvey, J. G. Hardman, and S. Korposh., “Simultaneous temperature and humidity measurements in a mechanical ventilator using an optical fibre sensor,” *Proc. SPIE 9916*, Sixth European Workshop on Optical Fibre Sensors, 99160C (May 2016).
8. **F. U. Hernandez**, R. Correia, S. Korposh, S.P. Morgan, B. R. Hayes-Gill, S.W. James, D. Evans, and A. Norris., “Measurements of endotracheal tube cuff contact pressure using fibre Bragg gratings,” *Proc. SPIE 9634*, 24th International Conference on Optical Fibre Sensors, 963435 (September 2015).
9. L. Marques, **F.U. Hernandez**, S. Korposh, M. Clark, S. Morgan, S.W.James, R.P. Tatam., “Sensitive protein detection using an optical fibre long period grating sensor anchored with silica core gold shell nanoparticles,” *Proc. SPIE 9157*, 23rd International Conference on Optical Fibre Sensors, 91574S (June 2014).

Acknowledgements

First of all, I would like to express my gratitude and admiration to my supervisors Prof. Stephen P. Morgan, Dr. Sergiy Korposh and Prof. Barrie Hayes-Gill. Admiration for your mentoring skills and my gratitude is not only for your professionalism through the PhD experience but also for your empathy, friendship and all the memories that we have together.

I would like to express a massive THANK YOU to Dr. Siavash Mirahmadi for his support and unconditional friendship. My very great appreciation to Dr. Ricardo Correia for helping with his expertise and for his friendship. Thank you to my dear friends in the laboratory of optical fibre sensors and colleagues for your support and make an encouraging environment at our working place: David Gomez, Qimei Zhang, Jiri Hromadka, Baptiste Jayet, Liang Liang Liu, Chong Liu, Shiemaa Sidahmed, Wan Zaki Wan, Shony Erdody, Chalani Abeywardena, Hattan Ballaji and Chenyang He.

Thank you to Prof. Seung-Woo Lee, Dr. Tao Wang and Dr. Hack-keun Lee for collaborating with my research, the discussions and meetings, and helping me during my stay in the University of Kitakyushu. I also appreciate your friendship.

Thank you to the collaborators from QMC Nottingham University Hospital: Dr. Andrew Norris, Prof. Jonathan G. Hardman, Dr. Dave Evans and Dr. Rishie Sinha for providing access to the materials needed and for the useful discussions and meetings about this research.

Thank you to the University of Nottingham, the ministry of Education of Mexico (SEP) and the National Council of Science and Technology of Mexico (CONACYT) for providing the scholarship and funding support that allowed me to complete the experimental work of my PhD studies.

Table of Contents

Abstract iii
Author's published research papers v
Acknowledgements vii
Table of Contents viii
List of Figures xii
List of Tables xviii
List of acronyms xix
Chapter 1. Introduction to optical fibre technology for healthcare applications and background information. 1
1.1 Optical fibre essentials 1
1.1.1 Geometrical optics approach of guided rays within the fibre 3
1.1.2 Guided modes propagation of electromagnetic waves in optical fibres 5
1.2 Major categories and types of optical fibres used in this research 10
1.3 Working principle and general classification of optical fibre sensors: extrinsic and intrinsic 11
1.4 Types of optical fibre sensors used in this research project 14
1.4.1 Fibre Bragg Grating (FBG) for temperature and strain measurements 14
1.4.2 Long Period Grating (LPG) for temperature and chemical sensing 16
1.4.3 Fabry-Pêrot interferometric sensor for humidity and temperature 20
1.4.4 U-shaped fibre as refractometer and optical fibre chemical sensor 23
1.5 Optical fibre sensors based on nano-thin films 25
1.6 Optical fibre sensors in healthcare: current status and future trends 33
1.7 Summary 38
1.8 Structure of the thesis 38
Chapter 2: Clinical challenges for the research project and literature review .41
2.1 Automatic closed-loop systems during critical care 41
2.1.1 Control of the contact pressure during intubation 45
2.1.2 Monitoring respiratory rate and humidification during mechanical ventilation 47
2.1.3 Monitoring bacteria biofilm growth during intubation 49
2.1.4 Monitoring anaesthetic and protein delivery in the ICU 50
2.2 Review of sensors and optical fibre sensors in the ICU and anaesthesia 53

2.2.1 Humidity, temperature or respiratory rate (RR) sensors: The breathing monitoring in the ICU or in clinical studies during critical care using different technologies 53
2.2.2 Breathing monitoring with optical fibre sensors 60
2.2.3 Depth of General Anaesthesia and anaesthetic delivery monitoring 66
2.3 Aims and objectives of the research project 73
2.4 Summary 75
Chapter 3: Fabrication and characterization of optical fibre sensors 76
3.1 Spectroscopic and imaging methods for nano-film characterization 76
3.1.1 Scanning Electron Microscopy (SEM) and Transmission Electron Microscopy (TEM) 77
3.1.2 Fourier Transform Infrared (FTIR) spectroscopy 78
3.1.3 Ultraviolet-Visible (UV-Vis) spectroscopy 80
3.1.4 Nuclear Magnetic Resonance (NMR) spectroscopy 81
3.2 Fabrication of optical fibre sensors 83
3.2.1 Fabrication of LPGs 83
3.2.2 Fabrication of FBGs 90
3.2.3 Preparation of fibre tip for Fabry-Pêrot sensor 93
3.2.4 Preparation of U-shaped fibres 93
3.3 Chemical functionalization using the Layer-by-Layer (LbL) technique 95
3.3.1 LPG functionalization for protein detection 97
3.3.2 Fabry-Pêrot functionalized sensor for humidity sensing 102
3.4 Chemical functionalization with imprinted metal oxide films for detection of propofol 106
3.4.1 TiO_2 film based on Liquid Phase Deposition (LPD) imprinted for host-guest interaction and detection of propofol 113
3.4.2 Sol-gel preparation of mesoporous silica nanoparticles (MSNs) and TiO_2 imprinted for propofol detection 122
3.5 Summary comments 127
Chapter 4: Optical fibre humidity sensor 128
4.1 Introduction 129
4.2 Adsorption of water vapour molecules in the Fabry-Perot sensing film 131
4.3 Results of PAH/SiO_2 film deposition onto the optical fibre tip 134
4.4 Humidity sensor tip calibration 136
4.5 Humidity sensor response time constant 141

4.6 Temperature and absolute humidity simultaneous calibration 143
4.7 Sensor testing in a breathing circuit connected to a positive pressure ventilator 145
4.8 Sensor testing in an animal study.....153
4.9 Preliminary tests and protocol design for a clinical study in volunteers: Application to facemask and nasal cannulas 160
4.10 Chapter conclusions.....166
Chapter 5: Optical fibre sensors for detection of biochemical parameters....168
5.1 Optical fibre sensor for protein detection 169
5.1.1 LPG biosensor parameters.....171
5.1.2 Results of PAH/SiO_2 :Au film deposition onto the LPG surface.....172
5.1.3 Protein binding detection 174
5.1.4 Biosensor parameters in aqueous solutions and the effect of SiO_2 NPs diameter 177
5.1.5 Sensor specificity, dynamic measurements and analytical estimation of the limit of detection (LoD) 179
5.2 Optical fibre sensor for propofol detection in aqueous solutions and gas phase 184
5.2.1 Results of imprinted TiO_2 deposition (based on LPD) onto U-shaped fibres 187
5.2.2 Results of imprinted TiO_2 deposition (based on LPD) onto LPG fibres 192
5.2.3 Propofol binding in aqueous solutions using U-shaped and LPG fibres 195
5.2.4 Results of imprinted MSN-TiO_2 deposition onto U-shaped fibres.....201
5.2.5 Improvement of sensitivity in aqueous solutions.....203
5.2.6 Propofol detection in gas phase 205
5.3 Chapter conclusions.....207
Chapter 6: Discussion, conclusions and future work.....209
6.1 General discussion for the optical fibre humidity sensor 209
6.2 Conclusions for the optical fibre humidity sensor.....212
6.3 General discussion for sensing biochemical parameters of interest in the ICU 213
6.4 Conclusions about sensing biochemical parameters of interest in the ICU .216
6.5 Future work 218
Appendix: Control of contact pressure and bacteria monitoring during intubation .220

References 225

List of Figures

Figure 1.1: An optical fibre is a cylindrical dielectric waveguide with an inner core and an outer cladding.	2
Figure 1.2: Comparison of conventional step-index SMF and MMF (schematic modified from [4]).	2
Figure 1.3: (a) Schematic of the mechanism of the light rays guided inside an optical fibre (modified from [3]); (b) The meridional rays intersect the fibre axis and reflect in the same plane without changing their angle of incidence (always $\theta < (\pi/2) - \emptyset_c$), similar to if they were in a planar waveguide (adapted from [4]).	4
Figure 1.4: (a) Electric radial field distribution (at only one plane) of the zeroth order mode and of the LP_{34} order mode. (b) Intensity distributions of these modes in the transverse plane and measured (or seen) at the end face of the optical fibre (adapted from [3] and [4]).	5
Figure 1.5: Examples of the radial distribution $u(r)$ for the modes LP_{01} (left) and LP_{34} (right). The coloured and uncoloured regions represent half of fibre core and cladding, respectively (cf. Fig. 1.4).	8
Figure 1.6: Graphical construction of the characteristic equation for $l = 0$ and $V = 10$, and either the – or + signs in Eq. (1-9) can be used. The LHS has multiple branches intersecting the abscissa at the roots of $J_{l+1}(X)$. The RHS intersects each branch once and meets the abscissa at $X = V$ (taken from [4]).	9
Figure 1.7: (a) Exemplar of a three-fibre displacement sensor (modified from [8]). (b) Examples of optical fibre bundles manufactured by MTI Instruments Inc. as standard fotonic sensor probes (transversal views to the fibre axis, adapted from [9]).	12
Figure 1.8: Extrinsic and intrinsic optical fibre sensors (modified from [10]).	13
Figure 1.9: (a) Scheme of the operation of an FBG sensor created in a single mode fibre. (b) Graphical depiction of the wavelength shift expected from the Bragg reflection when cooled and heated. (c) Schematic of the FBG sensor embedded in a UV curable epoxy based patch for improving sensitivity for contact pressure measurements [15].	15
Figure 1.10: Schematics for: (a) typical transmission spectrum from an LPG sensor, (b) LPG sensor coated with a functional thin film as a platform for chemical sensing, and (c) input spectrum from a broadband light source (the baseline of the input spectrum preserves at the output).	17
Figure 1.11: Phase matching curves for modes LP_{014} to LP_{020} (copied from [25]).	18
Figure 1.12: Illustration of the properties of an LPG near the PMTP; arrow shows direction of the shift of the phase matching curve for the increases of the effective refractive index of the cladding mode caused by increasing optical thickness (taken from [26]).	19
Figure 1.13: Schematics for: (a) operation of the SMF coupler containing a FBG and a 90^0 well cleaved tip at port 1; (b) the optical fibre sensor works as reflection optode when a multilayer film of PAH/SiO_2 is deposited onto the tip of port 1 (the optical thickness of the film changes when exposed to a humidified environment).	21
Figure 1.14: Photograph of a fabricated U-shaped fibre (radius R=1.4 mm) having a schematic illustration of the cladding, a nano-thin film coating and the light rays propagation inside the core (radius a=100 μm).	24
Figure 1.15: Optical fibre sensors based on nano-thin films and coatings (modified from [35]). The branches containing apples represent the sensors used in this PhD project. SPR=Surface Plasmon Resonance, fs-laser= femto-second laser and PCF=Photonic Crystal Fibre.	26
Figure 1.16: Current status and future trends of optical fibre sensors (adapted from [68]). The optical fibre sensors developed in this research project contribute to the fields enclosed with red circles.	33
Figure 2.1: Scheme for a generic closed-loop control [96].	42
Figure 2.2: Intubation with an ETT (modified from [101]).	44
Figure 2.3: Adhering the OFS to ICU equipment (Respir8® facemask in this case) used for non-invasive ventilation. This photograph elucidates how the OFS could be adhered inside the mask to monitor temperature, AH and RR. The Respir8® only contains an electronic RR monitor inside the mask (on the other side, not visible in the photograph).	44
Figure 2.4: Monitoring propofol concentration.	45
Figure 2.5: This photograph shows a commercial ETT only for illustrating its main components. This case shows a Soft seal ® Cuff North Polar Preformed ETT (Portex® Smiths medical, Kent, UK).	46

Figure 2.6: (a) Portable Non-invasive Positive Pressure Ventilator (NIPPY3+, B&D Electromedical Ltd, Warwickshire, UK). (b) Mechanical Ventilator Dräger Evita (Draeger Medical UK Ltd, Hemel Hempstead, UK) used for invasive ventilation in the ICU at Nottingham University Hospitals NHS Trust.	48
Figure 2.7: Relative proportions of common bacterial microorganisms that cause VAP [115].	49
Figure 3.1: Basic schematics and ray diagrams of (a) SEM and (b) TEM (adapted from [169]).	78
Figure 3.2: Basic schematics for (a) beam propagation inside the spectrometer (Spectrum 100 Perkin Elmer) and (b) the universal ATR accessory based on diamond and a focusing element. The silicon wafer substrates used were coated with gold.	79
Figure 3.3: Basic schematic of the working principle of a dual beam spectrophotometer.	81
Figure 3.4: Schematic of a continuous wave NMR spectrometer (modified from [175]). The RF receiver is usually connected to an amplification stage and processed in a PC.	82
Figure 3.5: Schematics for the fabrication set-ups of LPGs. (a) Fabrication via amplitude mask. (b) Fabrication via point-by-point (adapted from [25]).	84
Figure 3.6: Optical microscope image of a 50:50 duty cycle LPG with period of 110.8 μm.	85
Figure 3.7: (a) Photograph of the fabrication set-up implementing the amplitude mask method. (b) Steel alloy amplitude mask (all dimensions are in mm and the thickness of the mask is 0.2 mm).	87
Figure 3.8: (a) Exemplar of the evolution of bands during fabrication process of LPG3 (also shown in fig 3.8 b); the attenuation bands start to increase linearly after 5 min. (b) Comparison of three LPGs fabricated with the same period and same parameters: total length 3 cm and speed of 0.025 mm/s in the translation stage.	88
Figure 3.9: Comparison of three LPGs with same period and fabricated in a point-by-point fashion (Fig. 3.5b).	89
Figure 3.10: Schematic illustration of the fabrication set-up for FBGs readily available in the optical fibre sensors research group at the University of Nottingham. The phase masks grating size is 10 mm x 10 mm.	91
Figure 3.11: (a) FBG with Bragg wavelength at 1551.36 nm used in this project for temperature sensing. (b) Multiplexing of two FBGs written in the same fibre and centered at 1539.67 nm and 1545.12 nm.	92
Figure 3.12: In this research SEM was used for characterisation of films deposited on fibres; this case shows a single-mode bare fibre tip with (a) SEM 187x magnification and scale 200 μm; and (b) 1498x magnification and scale 50 μm.	93
Figure 3.13: Fabrication method of U-shaped fibres when exposed to a blue propane flame. After fabrication all the bending radii were measured with optical microscope (refer to Fig. 1.14 in chapter 1). (a) Fibre is held using an horizontal crocodile-clamp. (b) Fibre is exposed to the flame until it bends. (c) Fibre is held using a vertical crocodile-clamp and exposed again to the propane flame until it bends forming a U-shape as shown in (d).	94
Figure 3.14: Schematic illustration of the LbL technique (modified from [184]). (a) A hydroxylated substrate is immersed in a polycation solution and it will produce a positively charged material after dipping deposition; (b) electrostatic self-assembly of the first anionic layer using negatively charged nanoparticles; (c) First bilayer and iteration of the LbL deposition to produce a multilayer thin-film structure.	97
Figure 3.15. (a) Schematic illustration of the layer-by-layer deposition of $(PAH/SiO_2:Au)_3$ film onto an optical fibre LPG (this figure only depicts deposition of two consecutive layers); (b) Teflon deposition cell system	100
Figure 3.16: (a) TEM images of 300 nm (scale bars: left hand, 100 nm and right hand, 20 nm) SiO_2:Au NPs	101
Figure 3.16: (b) TEM images of 80 nm (scale bars: left hand, 50 nm and right hand, 20 nm) SiO_2:Au NPs.	101
Figure 3.17: SEM images of $(PAH/SiO_{2(300nm)}:Au)_3$ film deposited onto an optical fibre LPG. (a) scale bar: 10 μm and (b) scale bar: 5 μm.	101
Figure 3.18: (a) Schematic illustration of the construction of a (PAH/SiO_2) thin film using the LbL method onto the tip of a SMF coupler. (b) Photograph of the set-up for deposition of PAH and SiO_2 NPs onto the fibre-tip.	104
Figure 3.19. SEM images of the optical fibre humidity sensor probe coated with the PAH/SiO_2 film. (a) Fibre covered by 3 alternate bilayers of PAH and SiO_2 NPs. (b) Fibre covered by 5 alternate bilayers of same film. The scale bar on the left side is 200 μm; and 50 μm on the right hand side in both bullet points a) and b).	105

Figure 3.20: (a) Cyclodextrins (host) and (b) propofol molecules (guest) can form inclusion complexes through host-guest interactions (adapted from [195] and [196]). The protons of the cyclodextrins are shown in purple in (a) and the protons of propofol are shown in red in (b).	107
Figure 3.21: (a) ^{1}H NMR spectrum of propofol measured when dissolved individually in deuterated DMSO (y-axis is the real part of the Fourier transform). (b) Chemical shifts detected when propofol is exposed to NMR spectroscopy can be confirmed elsewhere [199],[200].	108
Figure 3.22: (a) ^{1}H NMR spectrum of β −CD measured when dissolved individually in deuterated DMSO (y-axis is the real part of the Fourier transform). (b) Chemical shifts detected when β −CD is exposed to NMR spectroscopy (spectrum taken from [201]) can also be confirmed in reference [174].	109
Figure 3.23: (a) Chemical shifts for H1 proton of β −CD (cf. Fig. 3.20) without complexation (blue) and afte preparing in solutions with propofol at different concentration ratios (inset shows the tube samples introduced in the NMR spectrometer). (b) Chemical shifts for the other protons of β −CD (*cf*. Fig. 3.20) without complexation (blue) and after preparing in a complexation solution with propofol at different concentration ratios.	110
Figure 3.24: (a) Chemical shifts for proton A and B of propofol (cf. Fig. 3.20) without complexation (blue) and after preparing in a complexation solution with β −CD at different concentration ratios. (b) Chemical shifts for the other protons of propofol without complexation (blue) and after preparing at different concentration ratios.	111
Figure 3.25: Summary of the changes in chemical shifts calculated from Fig 3.23 and Fig. 3.24 with respect to the blue spectra for both guest and host molecules. (a) Variations for the protons of propofol and (b) variations for the protons of β −CD.	112
Figure 3.26: (a) Host-guest inclusion demonstrated through results presented in Fig. 3.25. (b) Representation of cyclodextrin and another type of guest molecule inclusion, both anchored on a cargo platform made of TiO_2 (schematic adapted from [205]).	113
Figure 3.27: Set-up for the deposition of imprinted and non-imprinted TiO_2 films onto U-shaped fibres. The light source used was an HL2000 and the spectrometer was a HR2000 both from Ocean Optics.	117
Figure 3.28: (a) Comparison of the absorbance from imprinted and non-imprinted TiO_2 film deposited by LPD onto glass substrates. (b) Second derivative method from results shown in plot (a).	118
Figure 3.29: (a) Plain gold coated silicon wafer substrates used for deposition of imprinted and non-imprinted TiO_2 films. (b) Plasma surface treatment chamber used at 0.24 torr of vacuum to functionalize the gold-coated substrates (allowing then deposition of titanium films afterwards).	120
Figure 3.30: Comparison of ATR-FTIR spectra between pure TiO_2 and TiO_2 / (β −CD:Propofol).	122
Figure 3.31: Schematic illustration of sol-gel approach; R=alkyl radical and M is a network-forming of metal alkoxides such as Ti or Si (adapted from [134]).	123
Figure 3.32: Schematic of the deposition process of the surface sol-gel method containing molecular imprints of an organic template molecule (propofol) (adapted from [226]).	125
Figure 4.1: The OFS works as a Fabry-Pêrot cavity when a multilayer film of PAH/SiO_2 is deposited onto the tip (the optical thickness of the film changes when exposed to a humidified environment).	131
Figure 4.2: H_2O vapour adsorption on the metal oxide surface (modified from [32]).	132
Figure 4.3: (a) Total reflection spectra measured using the set-up shown in Fig. 3.18 after deposition of bilayers of PAH/SiO_2 onto the tip of the fibre; (b) Tracking of the optical reflection intensity at the second local maxima (λ =1564.8 nm) after depositing each of 23 bilayers of PAH/SiO_2 on the tip of the fibre and simulation result using Eqs. (1.15), λ =1564.8 nm and n_{eff} = 1.28.	135
Figure 4.4: Humidification system to calibrate the optical fibre humidity sensor against a capacitive sensor; temperature inside the measuring cell was constant at 25.4 ℃ $\pm$ 0.4 ℃.	136
Figure 4.5: Dynamic change of the optical fibre humidity sensor (response at λ = 618.13 nm, applying 5-point average filter every 20 s in time domain) modified with 4 bilayers thin film (blue line, (PAH/SiO_2)$_4$) upon exposure to the different levels of humidity (red trace). The values correspond to flowmeter settings of (a) L_2=1 L/min, L_1=0 L/min; (b) L_2=0.8 L/min, L_1=0.2 L/min; (c) L_2=0.6 L/min, L_1=0.4 L/min; (d) L_2=0.4 L/min, L_1=0.6 L/min; (e) L_2=0.2 L/min, L_1=0.8 L/min; (f) L_2=0 L/min, L_1=1 L/min.	138
Figure 4.6: Calibration curves for three, four and nine alternate bilayers of PAH/SiO_2 film showing the sensitivity for each case. For the purpose of clarity, the calibration curves are placed in the same plot showing differences in reflection intensity with respect to the first experimental value in each calibration curve.	139

Figure 4.7: Hysteresis of the optical fibre humidity sensor with 9 bilayers. The red trace is obtained by increasing the RH from 5% RH to 76% RH, and plotting reflection intensity measured in the fibre against RH measured in the capacitive sensor. The blue trace shows the decrease in RH from 76% RH to 5% RH.	140
Figure 4.8: Set-up to measure the humidity response time constant.	141
Figure 4.9: Comparison of the response of the optical fibre humidity sensor with $(PAH/SiO_2)_3$ and the internal capacitive sensor depicted in Fig. 4.8.	142
Figure 4.10: Set-up to test the optical fibre temperature-humidity sensor in a drying and heating chamber.	143
Figure 4.11: (a) Bragg wavelength from the spectra measured when port 1 of the fibre coupler was placed with two thermocouples inside a drying and heating chamber (Fig. 4.10); (b) AH measured with the OFS when the temperature increased from 22 ^{0}C to 60 ^{0}C.	144
Figure 4.12: (a) Experimental set-up to measure the humidity level inside a breathing circuit connected to the ventilator. (b) Photograph of the experiment to measure humidity inside the breathing circuit without HME connected and the humidifier is based on heating the water container. (c) HME connected to the T-piece and exhalation valve of the breathing circuit.	146
Figure 4.13: Comparison of readings for 20 cm H_2O of pressure support mode and 101 L/min in the ventilator settings; the red trace corresponds to the response of the capacitive sensor and the blue trace outputs the reflection intensity change of the optical fibre humidity sensor with nine bilayers. (a) Using HME in the breathing circuit and (b) without using HME in the breathing circuit.	148
Figure 4.14: Calculation of AH from the result obtained in Fig. 4.13a using the response of the fibre (blue trace). The use of the HME in the breathing circuit keeps a stable variation of temperature (23.1 ^{0}C $\pm$ 0.5 ^{0}C).	148
Figure 4.15: Comparisons of nine bilayer fibre response (blue trace) and capacitive sensor response (red trace) at 15 cm H_2O in IPPV mode and 12 breaths/min; the black traces correspond to the output of a moving average filter for each device response. The inset shows a zoomed time axis where the breath to breath variations in humidity can be observed using the optical fibre sensor.	150
Figure 4.16: (a) Comparison of different breaths/min for same pressure of IPPV. (b) Comparison of different pressures of IPPV for the same frequency of breaths/min. The behavior shown in both figures is consistent for the whole experiment (600 s duration).	151
Figure 4.17: Comparisons of the bare fibre response (blue trace) and capacitive sensor response (red trace) at 20 cm H_2O in IPPV mode and 12 breaths/min; the inset corresponds to the change in temperature during full measurement.	152
Figure 4.18: (a) Fibre optic pressure and perfusion sensors bonded to the ETT cuff and then enclosed within an external cuff; the optical fibre humidity-temperature sensors were attached to the interior lumen of the ETT. (b) Photograph of the OFS attached to the interior lumen of one ETT used during the study.	154
Figure 4.19: (a) Photograph of the intubated pig with the setup within the operating theatre. (b) (Up) Veterinary anaesthesia ventilator (Matrix® Model 3000, Midmark Animal Health Inc) and (down) Kontron Instruments monitors for end-tidal carbon dioxide ($ETCO_2$), nitrous oxide (N_2O), fraction of inspired oxygen (FiO_2), Electrocardiogram (ECG), temperature from rectal probe and the co-oximetry value (SaO_2) from arterial blood monitor.	155
Figure 4.20: (a) Optical reflection intensity measured with the optical fibre humidity sensor placed inside the lumen of the ETT (the inset shows a close up of the breaths per min measured between 1000 and 1060 s). (b) Wavelength shift from the FBG-based fibre placed inside the lumen of the ETT for the first 1400 s (the inset shows a close up of the breaths per min measured between 1000 and 1060 s).	157
Figure 4.21: Optical reflection intensity measured at 618.13 nm with the optical fibre humidity sensor during the rotation maneuvers of the ETT; the insets show 1 min of the recording at different times during the animal study.	158
Figure 4.22: (a) Comparison of the wavelength shift and optical reflection intensity measured at 618.13 nm during the last 2385 s of the animal study; (b) shows a close up of the green area shown in (a) and (c) shows a close up of the last part of the measurement shown in orange in (a).	159
Figure 4.23: OFS bound to a facemask and protected with hypodermic needle containing the wool/foam material used in the HME; the capacitive data logger can also be placed inside the facemask for comparison and the volunteer will be expected to follow up the breaths indicated from a mobile application.	161

Figure 4.24: (a) Optical fibre humidity sensor bound outside the nasal cannula and protected with the hypodermic needle. (b) Study with volunteers will be planned to use a mobile app metronome for delivering different breath frequencies.	161
Figure 4.25 (a): Comparison of the response of the optical fibre humidity sensor (in blue and containing 9 bilayers of PAH/SiO_2) and the electronic humidity sensor (in red) when both are tested inside a Venturi mask (Fig. 4.23) and using two different percentages of FiO_2 (in each case the breath was changed from 10 to 40 bpm).	162
Figure 4.25 (b): Close up from 1st section shown in Fig. 4.25a (corresponding to delivering 24% FiO_2 into the Venturi mask). The electronic sensor can measure a baseline for the change in relative humidity, but the optical fibre humidity sensor is the only one capable of measuring both frequencies 10 and 40 bpm.	163
Figure 4.25 (c): Close up from 2nd section shown in Fig. 4.25a (corresponding to delivering 50% FiO_2 into the Venturi mask). The electronic sensor can measure a baseline for the change in relative humidity, but the optical fibre humidity sensor is the only one capable of measuring both frequencies 10 and 40 bpm.	163
Figure 4.26: The optical fibre humidity sensor bound outside the nasal cannula (Fig. 4.24) is able to measure breath frequencies from 10 bpm to 40 bpm and apnea lapses between them	164
Figure 4.27: (a) Comparison between the change in intensity (measured from total reflection spectrum) and relative humidity (measured with a commercial electronic logger). (b) Comparison between the Bragg wavelength shift and temperature (measured with electronic logger). (c) Future application of the OFS as respiratory rate and humidity-temperature monitor in facemasks (photograph shows a commercial respiratory counter with facemask - respiR8®- together with the OFS proposed adhered to the facemask).	165
Figure 5.1: (a) The transmission spectrum of an LPG of period 110.7 μm measured with the LPG in water before and after film deposition. (b) In air: black line before and red line after (PAH/$SiO_{2(80\ nm)}$:Au)$_3$ film deposition; blue line presents the transmission spectrum after binding of biotin.	173
Figure 5.2: Transmission spectrum of the (PAH/$SiO_{2(80\ nm)}$:Au)$_3$ coated LPG modified on exposure to SV of different concentrations in: (a) air and (b) aqueous solution. Similarly, the transmission spectrum of the (PAH/$SiO_{2(300\ nm)}$:Au)$_3$ coated LPG modified on exposure to same SV concentrations in: (c) air and (d) aqueous solution.	175
Figure 5.3: Wavelength shifts of LP_{018} and LP_{019} calculated from the transmission spectra plotted in Fig. 5.2 after the adsorption of same 5 concentrations of SV (standard deviations are calculated from five blank measurements of the LPG used). (a) and (b) Response of (PAH/$SiO_{2(80\ nm)}$:Au)$_3$ coated LPG in air and solution, respectively. (c) and (d) Response of (PAH/$SiO_{2(300\ nm)}$:Au)$_3$ coated LPG in air and solution, respectively.	176
Figure 5.4: SV adsorption isotherms and their linearization for the coated LPGs. (a) & (c) Langmuir isotherm fits of (R-LP_{019} – L- LP_{019}) data from Fig. 5.3b and 5.3d respectively and (b) & (d) linearizations of Langmuir isotherm (Figs. 5.4a and 5.4c) using Eq. (5.3). The error bars represent the standard deviation of 5 blank measurements and the green lines provide the 95% confidence level [266],[267].	177
Figure 5.5: Transmission spectrum of the (PAH/$SiO_{2(80\ nm)}$)$_3$ + biotin coated LPG without Au NPs on exposure to SV of eight different concentrations in: (a) air and (b) solution.	180
Figure 5.6: (a) Transmission spectrum of the (PAH/$SiO_{2(80\ nm)}$:Au)$_3$ coated LPG on exposure to SV of eight different concentrations in air. (b) Comparison of the response to SV adsorption between the (PAH/$SiO_{2(80\ nm)}$:Au)$_3$ and (PAH/SiO_2)$_3$ coated LPGs in solution. (c) The change in transmission of the (PAH/$SiO_{2(80\ nm)}$:Au)$_3$ coated LPG measured at fixed wavelength of 834 nm on immersion into solutions of different SV concentration. (d) The change in transmission of the non-gold coated LPG (PAH/SiO_2)$_3$ measured at 833 nm on immersion into the same set of SV solutions.	181
Figure 5.7: (a) Langmuir adsorption isotherm for the (PAH/$SiO_{2(80\ nm)}$:Au)$_3$ coated LPG on exposure to SV concentrations in solution (Fig. 5.6b). (b) Statistical estimation of the LoD based on references [266] and [267].	183
Figure 5.8: (a) Transmission spectra of a U-shaped fibre (diameter 1.70 mm) on exposure to different wt.% of EtOH. (b) Maximum intensity peak tracking (at 611 nm) of the transmission spectra measured in (a) of this figure; the standard deviations are based on the measurement of five transmission spectra in every solution.	187
Figure 5.9: (a) Equivalence between EtOH % and RI as published in reference [270]. (b) Sensitivity to RIU (same U-shaped fibre) obtained from the peak response measured in Fig. 5.8b but calculated only from 0 wt. % to 70 wt. %.	188

Figure 5.10: (a) U-shape fibre immersed in solution for imprinted TiO_2 deposition (kept inside for 21 h.) (b) Development of the imprinted TiO_2 film on the inner walls of the vial after 2 days. (c) Formation of a thicker imprinted TiO_2 film after 3 days	189
Figure 5.11: (a) Photograph of the U-shape probe coated with the imprinted TiO_2 film after immersion in the precursor solution (Fig. 5.10a) for more than 33 h. (b) Transmission spectra recorded in air before and after deposition of the film for 41 hr. and using the set-up of Fig. 3.27. (c) Tracking of the single wavelength 611 nm before, during and after the film deposition for 41 hr.	190
Figure 5.12: All film precursor depositions used 0.8 mM final concentration of β −CD/Propofol complex. Imprinted TiO_2 film deposition tracked from the maxima of transmission spectra for different concentrations (see table 5.2).	192
Figure 5.13: (a) Relative wavelength shifts from the attenuation bands of two LPGs tested in 50 wt.% of EtOH ($\mathrm{Diff} = |\mathrm{R} - \mathrm{LP}_{019} - \mathrm{L} - \mathrm{LP}_{019}|$). (b) Evolution of the transmission spectra of LPG2 (Λ =109 μm) during deposition of the imprinted TiO_2 film (Environmental humidity and temperature were constant during all deposition, 41 % RH $\pm$ 3% and 25 ^{0}C $\pm$ 2 ^{0}C).	193
Figure 5.14: (a) Evolution of the transmission spectra of an LPG2 with period Λ =110.5 μm during deposition of the imprinted TiO_2 film. (b) Photograph of the LPG gauge when coated for more than 21 hr and using the experimental set-up of Fig. 3.15b (Environmental humidity and temperature were constant during all deposition, 66 % RH $\pm$ 2% and 24.8 ^{0}C $\pm$ 2 ^{0}C); the coated section length is ca. 4 cm in this case.	194
Figure 5.15: (a) Change of the peak intensity (cf. Fig. 5.11b) after template removal in EtOH and after immersion of the U-shaped fibres in four stock aqueous solutions of propofol (in the milimolar range). (b) Normalized comparison of the response of the fibre during immersion of the four propofol aqueous solutions shown in (a).	196
Figure 5.16: (a) Experimental set-up for a continuous test of the binding of propofol onto U-shaped fibres. (b) Simultaneous binding test in two U-shaped fibres. LS=Light source and Spec=Spectrometers (as in Fig. 3.27).	196
Figure 5.17: (a) Change of transmission spectra after pipetting the first eight concentrations of propofol (stock 0.5 mM). (b) Real time response at fixed wavelength while pipetting same stock solution with an inset to show the response to the first four concentrations. (c) Inset showing response to the middle of the range of concentrations tried and (d) shows a comparison between the response of a bare fibre and a U-coated fibre functionalized with the set 2 of concentrations from Table 3.3.	197
Figure 5.18: (a) Effect of functionalizing deposition time on sensitivity for the binding of propofol. (b) Re-usability of the same U-coated fibre and response after self-cleaning using UV light (all standard deviations are based on three measurements at the same concentration and using the same stock solution of propofol).	199
Figure 5.19: Comparison of sensitivities for the low concentration range between U-shaped fibres coated with two different sets of concentrations (Table 3.3) and a non-imprinted TiO_2 coated fibre.	200
Figure 5.20: (a) Experimental set-up for a continuous test of the binding of propofol onto LPG coated fibres. (b) Results for the binding of propofol using the two coated LPGs of Figs. 5.14a and 5.13b and implementing the set-up shown in (a).	201
Figure 5.21: Intensity change at 625 nm for the deposition results onto a U-shaped fibre using dip coating method and the prepared film as described in section 3.4.2	202
Figure 5.22: Transmission spectra changes over the deposition onto a U-shaped fibre using the dip coating method and deposition film explained in section 3.4.2.	203
Figure 5.23: Transmission spectra changes over the binding of propofol in the nano-molar range.	204
Figure 5.24: Absorbance spectra calculated from data of Fig. 5.23.	204
Figure 5.25: Experimental set-up for propofol detection in gas phase.	205
Figure 5.26: (a) Comparison of the transmission spectra when the U-shape fibre was exposed to 6 ppm and 30 ppb. (b) Mean and standard deviations of the maxima (655 nm) when exposed to same concentrations three times and using the set-up of Fig. 5.25.	206

List of Tables

Table 1.1: Major categories of optical fibres used in Biophotonics applications (modified from [3]); only the types of fibres highlighted in green were used in this research project.	10
Table 2.1: Current clinical challenges during critical care which are candidates for implementing an automatic closed-loop individual system using OFS technology.	44
Table 2.2: Medical devices or techniques (non-optical) used in critical care and their limitations.	59
Table 2.3: Optical fibre sensors used for breathing monitoring.	65
Table 2.4: Medical devices or techniques implemented to measure propofol in blood.	70
Table 2.5: Medical devices or techniques implemented to measure propofol in gas phase.	72
Table 3.1: Materials for the LPG functionalization for protein detection. All reagents were of analytical grade and were used without further purification. Distilled water (with conductivity of 18.3 MΩcm) was obtained by reverse osmosis followed by ion exchange and filtration in a Millipore-Q (Millipore, Direct-QTM).	98
Table 3.2: Materials for the functionalization of fibre tips. All reagents were of analytical grade and were used without further purification. Distilled water (with conductivity of 15 MΩcm) was obtained by reverse osmosis followed by ion exchange and filtration in a Millipore-Q (Millipore, Direct-QTM).	102
Table 3.3: Materials and typical final mixed concentrations used for the imprinting β −CD:Propofol complex on TiO2 films. This deposition process is used onto optical fibres for detection of propofol (chapter 5).	115
Table 3.4: FTIR spectral data for TiO_2 reported in reference [206].	121
Table 3.5: FTIR modes for TiO_2/ β −CD reported in references [205],[215],[220],[221],[222],[223].	121
Table 4.1: Optical fibre-based humidity sensors with high sensitivities reviewed in [38].	129
Table 5.1: Current technologies found in the literature for measuring propofol concentration either in blood or from breath.	185
Table 5.2: Summary of the U-shaped probes used in this part of the research.	191

List of acronyms

Absolute humidity (AH)

Airway climate explorer (ACE)

Attenuated total reflectance (ATR)

Beta-cyclodextrin (β −CD)

Depth of general anaesthesia (DGA)

Electrocardiogram (ECG)

Electronic noses (e-noses)

Endotracheal tube (ETT)

Ethanol (EtOH)

Evanescent wave (EW)

Fraction of inspired oxygen (FiO_2)

Fourier transform infrared (FTIR) spectroscopy

Gas chromatography mass spectrometry (GC-MS)

Heat and moisture exchanger (HME)

High-performance liquid chromatography (HPLC)

Infrared (IR)

Intensive care unit (ICU)

Intermittent positive pressure ventilation (IPPV)

Ion molecule reaction-mass spectrometry (IMR-MS)

Layer-by-layer (LbL)

Limit of detection (LoD)

Linearly polarised (LP) mode

Liquid phase deposition (LPD)

Magnetic resonance imagining (MRI)

Mesoporous silica nanoparticles (MSNs)

Methanol (MetOH)

Multimode fibre (MMF)

Nanoparticles (NPs)

Nuclear magnetic resonance (NMR)

Optical fibre sensor (OFS)

Phase matching turning point (PMTP)

Photonic crystal fibre (PCF)

Poly(allylamine hydrochloride) (PAH)

Proton transfer reaction mass spectrometry (PTR-MS)

Quartz crystal microbalance (QCM)

Refractive index (RI)

Refractive index unit (RIU)

Relative humidity (RH)

Research and development (R&D)

Respiratory rate (RR)

Scanning electron microscopy (SEM).

Silica nanoparticles (SiO_2 NPs)

Single mode fibre (SMF)

Solid-phase extraction (SPE)

Streptavidin (SV)

Super luminescent diode (SLD)

Surface plasmon resonance (SPR)

Target-controlled infusion (TCI)

Thoracic impedance pneumography (TIP)

Titanium dioxide (TiO_2)

Total intravenous anaesthesia (TIVA)

Transmission electron microscopy (TEM)

Ultraviolet (UV)

Ultraviolet-visible (UV-Vis)

Ventilator associated pneumonia (VAP)

Volatile organic compounds (VOCs)

Chapter 1. Introduction to optical fibre technology for healthcare applications and background information

This chapter explains the essential concepts of the transmission of light through an optical fibre, provides the background necessary to understand how fibres function, describes various commercial major categories of fibres for use in biophotonics applications and presents a classification of optical fibre sensor (OFS) technologies and its applications in healthcare.

1.1 Optical fibre essentials

In this section the principles of light transmission through optical fibres relevant to this thesis are briefly explained with two main methods: (i) a geometrical optics approach with guided light rays and (ii) the guided modes propagation of electromagnetic waves (scalar wave optics). These theoretical methods are found elsewhere in the optics literature [1], [2] and here they will be only described in a general way without exhaustive mathematical formalism (sections 1.1.1 and 1.1.2).

Conventional optical fibres are those mostly used in telecommunication networks worldwide (Fig. 1.1) and they consist of a central *core* (silica-based glass) waveguide of refractive index n_1 which is embedded in an outer *cladding* (silica-based glass) of slightly lower refractive index $n_2 \cong n_1(1-\Delta)$; the parameter Δ is called the core-cladding index difference [3], [4]. An elastic polymer buffer coating (Fig. 1.1) protects the fibre from mechanical abrasions and environmental abrasive effects that can affect the glass.

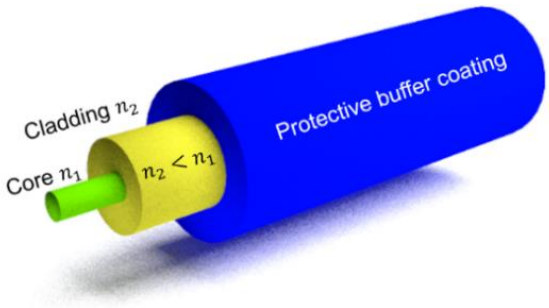


Figure 1.1: An optical fibre is a cylindrical dielectric waveguide with an inner core and an outer cladding.

Two types of conventional optical fibres can be distinguished from variations in the size of the core (Fig. 1.2): A single-mode fibre (SMF) can support only one mode of propagation (small core diameters can only support a single mode), whereas many hundreds of modes can propagate in a multimode fibre (MMF).

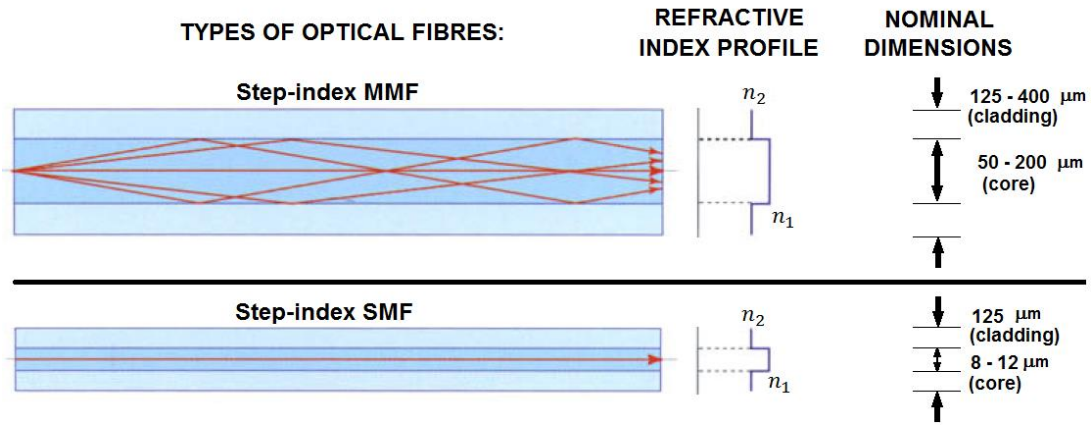


Figure 1.2: Comparison of conventional step-index SMF and MMF (schematic modified from [4]).

In a step-index fibre, n_1 is uniform throughout the core and experiences an abrupt change at the cladding boundary (Fig. 1.2). Typical values of the core-cladding index difference are between $1\% \leq \Delta \leq 3\%$ for MMFs and $0.2\% \leq \Delta \leq 1.0\%$ for SMFs [3].

1.1.1 Geometrical optics approach of guided rays within the fibre

For simplicity, this approach considers only meridional rays (Fig. 1.3b) that are confined to the meridian planes (planes of incidence that pass through the core axis). Then, an optical ray in a fibre is guided by total internal reflections within the fibre core if its angle of incidence at the core-cladding boundary (Fig. 1.3) is greater than the critical angle $\emptyset_c$ (Eq. 1-1) and remains so as the ray propagates through the fibre [2], [4].

$$\emptyset_c = \sin^{-1}\left(\frac{n_2}{n_1}\right) \tag{1-1}$$

Equation (1-1) is derived from applying the Snell's law at the core-cladding interface $n_1 \sin\emptyset_c = n_2 \sin(\pi/2)$ in Fig. 1.3a and determines the minimum or critical angle that supports total internal reflection at the interface [2]. Rays striking this interface at angles less than $\emptyset_c$ will refract out of the core and be lost in the cladding (dashed line in Fig. 1.3a). In addition, incident rays from air become also guided rays if, upon refraction at the air-fibre face boundary, they make an angle θ (Fig. 1.3a) with the fibre axis that is smaller than the complement of the critical angle$\left(\overline{\emptyset_c}\right)$, i.e., when $\theta < \overline{\emptyset_c}$ and $\overline{\emptyset_c} = (\pi/2) - \emptyset_c$ [3], [4].

As shown in Fig. 1.3a, after applying Snell's law at the air-core boundary, the acceptance angle (θ_0) of the fibre establishes an acceptance cone of external rays that are guided within the fibre (Eqs. 1-2 and 1-4).

$$\begin{aligned}\sin\theta_0 &= n_1 \sin\left(\overline{\emptyset_c}\right) = n_1 \sin\left(\frac{\pi}{2} - \emptyset_c\right) = n_1 \cos\emptyset_c \\ &= n_1\sqrt{1-(n_2/n_1)^2} = \sqrt{{n_1}^2 - {n_2}^2}\end{aligned} \tag{1-2}$$

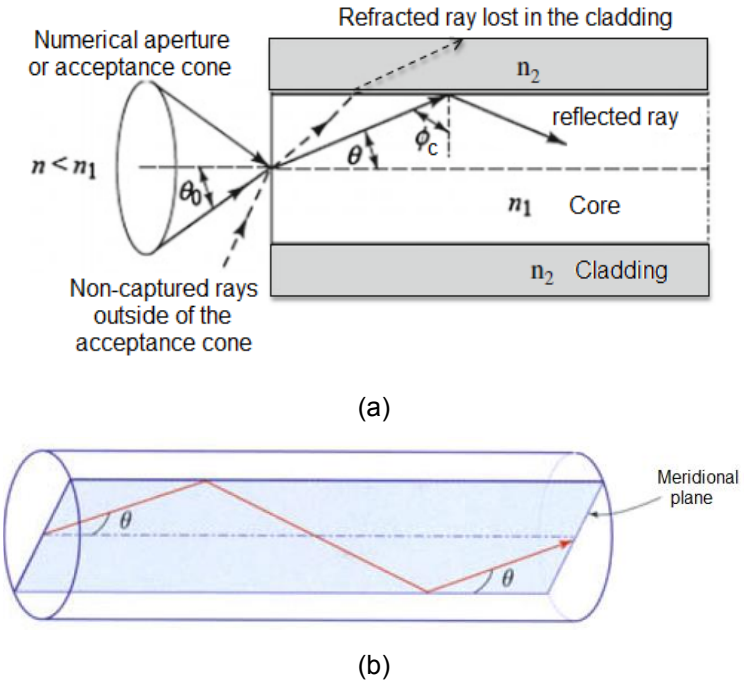


Figure 1.3: (a) Schematic of the mechanism of the light rays guided inside an optical fibre (modified from [3]); (b) The meridional rays intersect the fibre axis and reflect in the same plane without changing their angle of incidence (always $\theta < (\pi/2) - \emptyset_c$), similar to if they were in a planar waveguide (adapted from [4]).

By definition, the numerical aperture (NA) of an optical fibre (Fig. 1.3a) is a measure of the light acceptance or gathering capability for incoming light (Eq. 1-3) and NA is generally listed on optical fibre datasheets.

$$NA = \sqrt{{n_1}^2 - {n_2}^2} \approx n_1\sqrt{2\Delta} \quad \text{since } n_2 \cong n_1(1-\Delta) \tag{1-3}$$

The acceptance angle (θ_0) of the fibre is therefore,

$$\theta_0 = \sin^{-1} NA \tag{1-4}$$

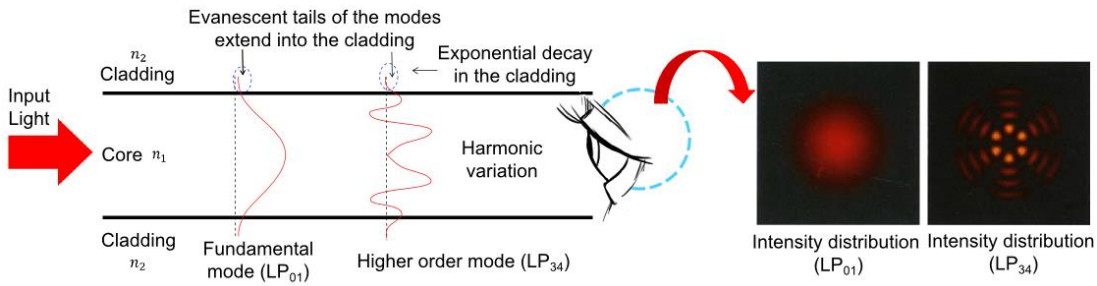
and rays incident from air at angles greater than θ_0 are refracted into the fibre but are guided only for a short distance since they do not bounce through total internal reflection [4]. Ray theory can explain and simulate some measurable parameters of interest in telecommunications such as dispersion, attenuation

and bend-loss sensitivity. However, this approach explains only approximately other phenomena such as the interaction of leaked light through the cladding (evanescent wave) and the surrounding media that usually occurs when using optical fibre sensors, i.e., in some cases the protective buffer jacket (Fig. 1.1) is stripped and removed in order to have a gauge section exposed to the environment for sensing applications. This leads to the second approach which considers the propagation of light as electromagnetic waves inside the optical fibre.

1.1.2 Guided mode propagation of electromagnetic waves in optical fibres

Electromagnetic waves (modes in the form of light) are confined within the fibre and are guided in a direction parallel to the fibre axis. Each guided mode consists of a pattern of electromagnetic field distributions that is repeated periodically and transmitted along the fibre (Fig. 1.4).

Mode theory describes how the oscillating electromagnetic fields travel along the fibre, propagating energy in the waveguide and shows that the guided modes are not exclusively confined to the core but expand partially into the cladding (Fig. 1.4a).



(a) (b)

Figure 1.4: (a) Electric radial field distribution (at only one plane) of the zeroth order mode and of the LP_{34} order mode. (b) Intensity distributions of these modes in the transverse plane and measured (or seen) at the end face of the optical fibre (adapted from [3] and [4]).

There are special solutions of the Maxwell equations (for the electromagnetic fields) called modes and their propagation is simplified by treating them as being linearly polarised (LP_{lm}); each guided LP_{lm} mode has a distinct propagation constant (β_{lm}) and a characteristic field distribution in the transverse plane (Fig. 1.4 shows two examples, LP_{01} and LP_{34}). The assumptions and conditions for the modes to be guided in a cylindrical waveguide (fibre) are fully detailed in many optics textbooks [1], [4], [5].

In summary, monochromatic electromagnetic fields (U) obey the Helmholtz equation (1-5) in cylindrical coordinates (r, ϕ, z)

$$\frac{\partial^2 U}{\partial r^2} + \frac{1}{r}\frac{\partial U}{\partial r} + \frac{1}{r^2}\frac{\partial^2 U}{\partial \phi^2} + \frac{\partial^2 U}{\partial z^2} + n^2 k_0^2 U = 0 \qquad (1\text{-}5)$$

where $U = U(r, \phi, z)$, $k_0 = 2\pi/\lambda_0$ (wavenumber and wavelength λ_0) and $n = n(r)$ is the refractive index of the core or cladding.

The general mathematical form of the guided modes travelling in the z direction with propagation constant (β_{lm}) and periodically harmonic in the angle (ϕ) with period 2π is written as:

$$U(r, \phi, z) = u(r)e^{-il\phi}e^{-i\beta z}, \quad l = 0, \pm 1, \pm 2, \ldots \qquad (1\text{-}6)$$

where $u(r)$ is the characteristic field distribution or radial profile of each mode (as shown in Fig. 1.4a) in cylindrical coordinates.

Substituting Eq. (1-6) into Eq. (1-5) leads to an ordinary differential equation for the radial profile $u(r)$ [4],

$$\frac{d^2 u}{dr^2} + \frac{1}{r}\frac{du}{dr} + \left(n^2(r){k_0}^2 - {\beta_{lm}}^2 - \frac{l^2}{r^2}\right)u = 0 \qquad (1\text{-}7)$$

The mode is guided (or bound) in step-index fibres only if the propagation constant is smaller than the wavenumber in the core ($\beta_{lm} < n_1 k_0$) and greater than the wavenumber in the cladding ($\beta_{lm} > n_2 k_0$). This condition can be established mathematically as:

$$k_{T_{lm}}{}^2 = n_1{}^2 k_0{}^2 - \beta_{lm}{}^2 \tag{1-8a}$$

$$\gamma_{lm}{}^2 = \beta_{lm}{}^2 - n_2{}^2 k_0{}^2 \tag{1-8b}$$

so that $k_{T_{lm}}{}^2, \gamma_{lm}{}^2 > 0$, $k_{T_{lm}}, \gamma_{lm}$ are real and always satisfy $k_{T_{lm}}{}^2 + \gamma_{lm}{}^2 = (NA)^2 \cdot k_0{}^2$ from Eqs. (1-8) [4].

The *characteristic equation* (1-9) for step-index fibres is the solution of Eq. (1-7) and results from applying the boundary conditions which turns out to be approximately equivalent to the conditions that scalar function $u(r)$ is continuous and has a continuous derivative at the core-cladding boundary when $r = a$ (radius of the core, Fig. 1.5),

$$X\frac{J_{l+1}(X)}{J_l(X)} = \pm Y\frac{K_{l+1}(Y)}{K_l(Y)} \tag{1-9}$$

where $X = k_{T_{lm}} \cdot a$ and $Y = \gamma_{lm} \cdot a$ are normalized parameters for $k_{T_{lm}}$ and γ_{lm} [4]. The characteristic equation contains the family of Bessel functions as solutions, i.e., $J_l(X)$ is the Bessel function of the first kind and order l, and $K_l(X)$ is the modified Bessel function of the second kind and order l [4].

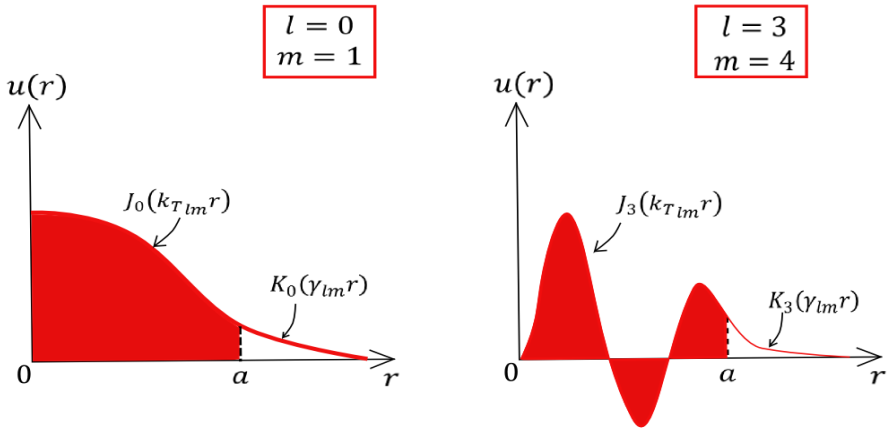


Figure 1.5: Examples of the radial distribution $u(r)$ for the modes LP_{01} (left) and LP_{34} (right). The coloured and uncoloured regions represent half of the fibre core and cladding, respectively (cf. Fig. 1.4).

Another important parameter that governs, approximately, the number of modes (M) of the fibre and their propagation constants is the *V parameter* which is calculated in terms of known quantities such as the radius of the core (a), the numerical aperture of the fibre (NA) and the wavelength used (λ_0):

$$V = 2\pi \frac{a}{\lambda_0} NA \quad \text{and} \quad M \cong \frac{4V^2}{\pi^2} + 2 \tag{1-10}$$

Eq. (1-10) always satisfies $V^2 = X^2 + Y^2$ and the approximation only applies when the V parameter is large [4].

The parameters $k_{T_{lm}}$ and γ_{lm} determine the rate of change of $u(r)$ in the core and cladding respectively (Fig. 1.5). A larger value of $k_{T_{lm}}$ will produce more oscillations of $u(r)$ in the core, and a larger value of γ_{lm} will generate a more rapid decay of $u(r)$ and smaller penetration of the wave into the cladding [4]. In general, the field distributions of low order modes are concentrated near the fibre axis and do not penetrate deep into the cladding region. On the other hand, the fields of higher order modes are located nearer the core edges and penetrate deeper into the cladding [3], [6].

Finally, there is a graphical method (Fig. 1.6) for solving the characteristic equation (1-9) and it is convenient to highlight that for each azimuthal index l,

the characteristic equation has multiple m solutions with specific propagation constants β_{lm} $(m = 1,2,3, \ldots M_l)$ and $u(r)$ also depends on both l and m. One exemplar is shown in Fig. 1.6. The graph of the characteristic equation is obtained by plotting both its right-hand side (RHS) and left-hand side (LHS) versus X and finding the intersections.

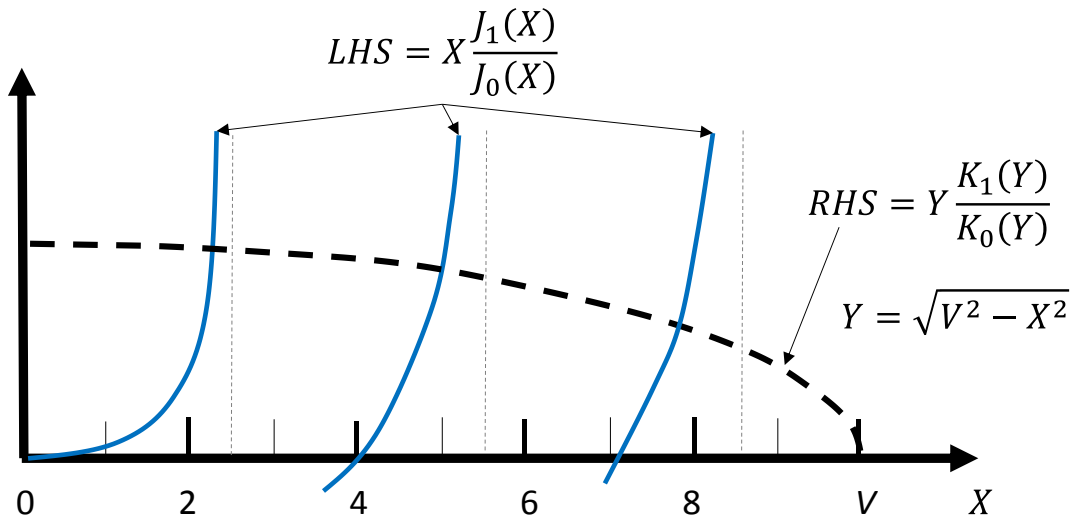


Figure 1.6: Graphical construction of the characteristic equation for $l = 0$ and $V = 10$, and either the – or + signs in Eq. (1-9) can be used. The LHS has multiple branches intersecting the abscissa at the roots of $J_{l+1}(X)$. The RHS intersects each branch once and meets the abscissa at $X = V$ (reproduced from [4]).

In Fig. 1.6, the number of modes equals the number of roots of $J_{l+1}(X)$ that are smaller than V. Each intersection value is a solution and is denoted as X_{lm} $(m = 1,2, \ldots, M_l)$; once the X_{lm} values are found, it is possible to determine $k_{T_{lm}}$, γ_{lm}, β_{lm} and the radial distributions $u_{lm}(r)$. It should be noted that the values of these last propagation constants depends on the effective refractive index of the core (n_1) and cladding (n_2) and this creates the potential for a variety of optical fibres to be designed. For instance, changing the physical variation properties of the refractive indices or depositing chemical coatings onto the cladding of a fibre to change its effective refractive index, open up new possibilities for optical fibres to be used as sensors.

1.2 Major categories and types of optical fibres used in this research

Table 1.1 presents a classification for the types of optical fibres frequently used in biophotonics applications and the fibres specifically used in this project are highlighted in green. As shown in Table 1.1, the performance characteristics of each type of optical fibre are important when considering what fibre to use for a particular application, i.e., it is necessary to know optical signal attenuation as a function of wavelength, optical power-handling capability, the degree of signal loss as the fibre is bent, and the mechanical properties of the fibre.

In this project, only the types of optical fibres highlighted in green (Table 1.1) were used for the development and chemical functionalization of optical fibre sensors. The use of conventional solid-core silica-based fibres is not a restriction for its implementation in this research project (as plastic optical fibres can also be used). Silica fibres, however, provided a widely used platform for implementing the sensors in this thesis. The optical signal attenuation is, however, not critical for the applications in this thesis due to the short propagation distances involved.

Optical fibre types		***Characteristics***
Conventional solid-core silica fibres	Multimode	Multimode propagation
	Single-mode	Single-mode propagation
Special solid-core fibres	Photosensitive	High photosensitivity to UV radiation. Ideal for Bragg Gratings fabrication.
	UV-resistant	Low UV sensitivity and reduced attenuation below 300 nm.
	Bend-loss insensitive	High NA and low bend-loss sensitivity.
	Polarization-maintaining	High birefringence. Preserve the state of polarization.
Double-clad fibres		Single-mode core and multimode inner cladding.

Table 1.1: Major categories of optical fibres used in biophotonics applications (modified from [3]); only the types of fibres highlighted in green were used in this research project.

Optical fibre types	*Characteristics*
Hard-clad silica fibres	Silica core with plastic cladding. Increases fibre strength and power transmission.
Coated hollow-core fibres	Low absorption for mid-IR and high optical damage threshold.
Photonic crystal fibres	Low loss; transmit high optical power without nonlinear effects.
Plastic optical fibres	Low cost, fracture resistance and biocompatibility.
Side-emitting fibres and side-firing fibres	Emit light along and perpendicularly to the fibre axis.
Mid-infrared fibres	Efficient IR delivery; large refractive index and thermal expansion.
Optical fibre bundles	Increase sensitivity and some of the fibres in the bundle can be used for self-referencing applications.

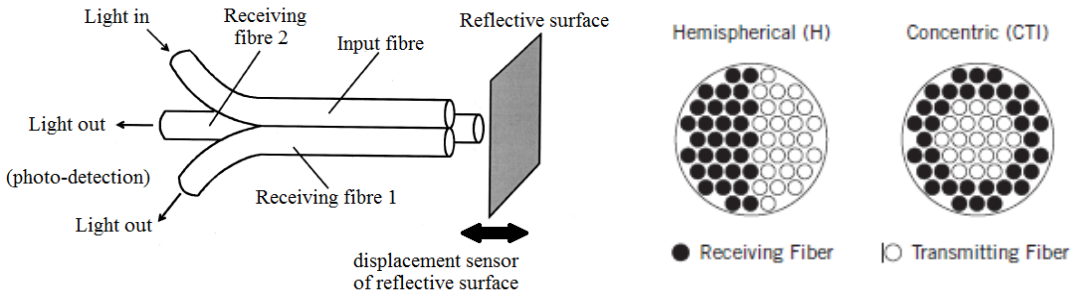
Table 1.1: (Continuation) Major categories of optical fibres used in biophotonics applications (modified from [3]); only the types of fibres highlighted in green were used in this research project.

The wide variety of optical fibres available on the market makes it possible to have a range of optical fibre sensors that are designed depending not only on the characteristics explained in Table 1.1, but also to be fabricated with the modifications to the optical fibre structure as explained in the next sections.

1.3 Working principle and general classification of optical fibre sensors: extrinsic and intrinsic

Usually, an optical fibre used as sensor requires a connection to a light source on one end of the fibre and a photodetector on the other. However, for some applications the source and photo-detection system might be connected to different fibres working in parallel (Fig. 1.7a) or to an optical fibre coupler (centre of Fig. 1.8). The basic working principle of an optical fibre sensor (OFS) consists of physically modifying (stressing or bending for instance) or interacting (physically or chemically) with the transmission of light through the fibres while connected to the photodetector and having the light source ON. The first OFS was called the *Fotonic sensor* (a fibre displacement sensor, Fig. 1.7a) patented in 1967 [7] and it serves as an exemplar to show how an OFS

works, i.e., the fibre simply guides the light to a target region where the optical signal can be reflected, backscattered or partially transmitted; the light is then collected by a different fibre (or bundle, Fig. 1.7b) and returned to a photodetector to be processed.



(a) (b)

Figure 1.7: (a) Exemplar of a three-fibre displacement sensor (modified from [8]). (b) Examples of optical fibre bundles manufactured by MTI Instruments Inc. as standard fotonic sensor probes (transversal views to the fibre axis, adapted from [9]).

There are numerous types of architectures of optical fibre sensors but, in principle, all sit within two broad categories: *extrinsic* and *intrinsic sensors* (Fig. 1.8) [10].

Extrinsic sensors guide light to a reactive medium where the optical signal interacts and the light is modulated; the reflected light (top of Fig. 1.8) or scattered (not shown) is then collected by the same or a different fibre and returned to a remote location for acquisition and processing [7], [11]. Some examples of extrinsic sensors are shown in Fig. 1.8, using either two separate fibres (transmitter-receiver) or optical fibre couplers (2X2 or 2X1 splitting fibres). Extrinsic sensors using light reflections from the reactive medium are called reflection optrodes and nowadays they are widely used for direct measurements of absorbance, reflectance or fluorescence from the sample or analyte under study [7].

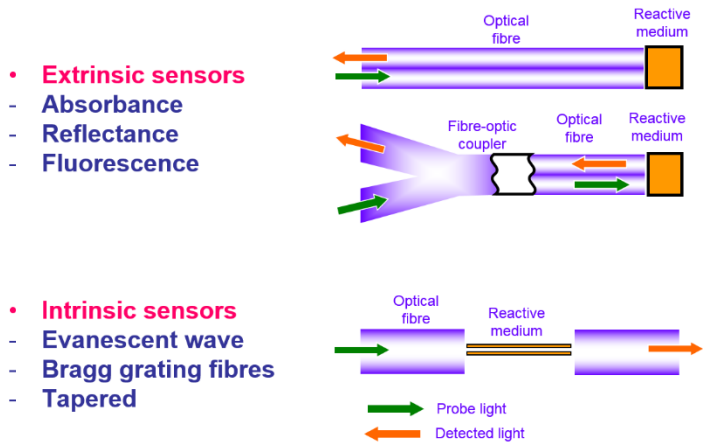


Figure 1.8: Extrinsic and intrinsic optical fibre sensors (modified from [10]).

On the other hand, ***intrinsic sensors*** keep the light within the fibre at all times such that external chemical or physical parameters of interest modulate the light as it propagates along the fibre [7], [11]. Examples of intrinsic sensors (Fig. 1.8) are optical fibres containing Fibre Bragg Gratings (FBGs) or Long Period Gratings (LPGs) and fibres where the cladding has been partially removed such as in tapered or evanescent wave-based optical fibres [7], [12]. In particular, four types of optical fibre sensors will be explained in detail in the next section (1.4): FBG, LPG, Fabry-Pêrot interferometric sensor and U-shaped sensor.

In many applications, extrinsic and intrinsic fibre sensors act as sensing elements themselves as refractometers, i.e., they are sensitive to the refractive index of the surrounding medium. However, integration of novel functional coatings or nano-films onto optical fibres (at the tip or onto the gauge section, Fig. 1.8) is one of the new trends in the field of novel sensing technologies currently increasing the spectrum of applications, especially for the detection of biochemical parameters [13]. This raises a different type of classification of OFS technology (section 1.5) which depends on the type of chemical coating, the deposition method used and the particular type of optical fibre structure implemented.

1.4 Types of optical fibre sensors used in this research project

In this subsection a description of each optical fibre sensor used as a monitoring platform in this research is given: FBG, LPG, Fabry-Pêrot sensor and U-shaped fibre. A brief description of their sensing principles are explained and, for some sensors, the functional materials deposited either at the tip of the fibre, on a U-shaped fibre or on Long Period Grating (LPG) are explained in chapter 3.

1.4.1 Fibre Bragg Grating (FBG) for temperature and strain measurements

The sensing principle of this type of sensor is depicted in Fig. 1.9a; the reflected Bragg wavelength for uniform gratings [14], [15] is calculated through Eq. (1.11) and it depends on the effective refractive index of the core (η_{eff}) and the period of the grating (Λ).

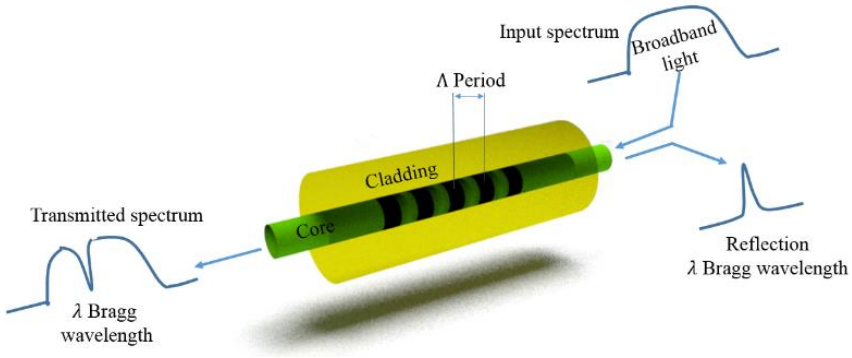
$$\lambda_{\text{Bragg}} = 2\eta_{\text{eff}}\Lambda \tag{1.11}$$

In addition, changes in strain and temperature affect both the effective refractive index and grating period of the FBG, resulting in a wavelength shift of the Bragg wavelength. For instance, heating the grating will shift the Bragg wavelength to higher values and cooling will shift it to lower wavelengths (Fig. 1.9b). The total wavelength shift ($\Delta\lambda$) due to isotropic strain (ε) and temperature change (ΔT) can be approximated by Eq. (1.12) [16].

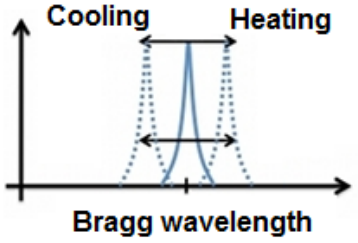
$$\Delta\lambda = \lambda_{\text{Bragg}}\left[(1 - P_e)\varepsilon + \left((1 - P_e)\cdot\alpha + \xi\right)\Delta T\right] \tag{1.12}$$

where P_e is the photoelastic constant, ξ is the thermo-optic coefficient of the optical fibre and α is the thermal expansion coefficient [14], [16].

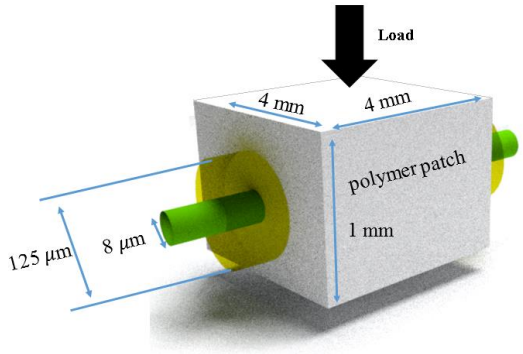
Fig. 1.9c presents a method to convert strain to contact pressure through transverse load measurements on a polymer patch surrounding the FBG section. It has been demonstrated [15] that FBGs embedded within a cube of epoxy polymer patch convert transversal load to a strain along the axis of the optical fibre which produces a linear wavelength shift dependent on the applied load and increases sensitivity by a factor of 15 when compared to direct transverse loading of the bare fibre [17].



(a)



(b)



(c)

Figure 1.9: (a) Scheme of operation of an FBG sensor created in a single mode fibre. (b) Graphical depiction of the wavelength shift expected from the Bragg reflection when cooled and heated. (c) Schematic of the FBG sensor embedded in a UV curable epoxy based patch for improving sensitivity for contact pressure measurements [15].

In this PhD project, exploratory work (see Appendix) for developing a method to measure the contact pressure between an ETT cuff and a trachea

model was implemented with bare FBGs [18]. As part of a multidisciplinary collaboration [15], the FBG was encased in an epoxy UV-cured polymer which improved the sensitivity and the tensile strength of the gauge section for the same application. The characteristics of the OFS containing patched FBGs allows continuous measurements of contact pressure within the desirable clinical range. However, the FBGs fabricated and used in this research were predominantly used for temperature measurements.

1.4.2 Long Period Grating (LPG) for temperature and chemical sensing

LPGs differ from FBGs in the way light (LP modes) is coupled in the core-cladding. An FBG couples light from the forward-propagating mode to a backward counter-propagating mode, while an LPG couples light between the guided core mode and various co-propagating cladding modes [19], [20]. LPGs also have specific empirical differences from FBGs: (1) FBGs normally have a grating period in the range of units of micrometers while LPGs have a grating period in the range of hundreds of micrometers; (2) the gauge length of LPGs (in the range of cm) is larger than the length of FBGs (of the order of mm); (3) transmission spectra of LPGs have broader attenuation bands than the narrow bands regularly obtained in FBGs; (4) the optical set-up for the fabrication of LPGs differs from that required for FBGs (chapter 3), and the principle of using LPGs as sensors differs from that of using FBGs where the central wavelength (λ_i) of the LPG attenuation bands (Fig. 1.10) in the transmission spectrum is calculated by the phase matching condition, Eq. (1.13) [21], [22],

$$\lambda_i = \left(n_c - n_{\text{clad}}^i\right)\Lambda \tag{1.13}$$

where Λ is the period of the grating, n_c is the refractive index of the mode propagating in the core, and n_{clad}^i is the effective index of the i-th axially symmetric and linearly polarized cladding mode [21].

Similarly, the temperature sensitivity of the central wavelength (λ_i) of the LPG can be calculated using Eq. (1.14a) [23] and the sensitivity to the variation of the surrounding refractive index (n_3) can be calculated using Eq. (1.14b) [22],

$$\frac{d\lambda_i}{dT} = \frac{d\lambda_i}{d(\delta n_{eff})}\left(\frac{dn_c}{dT} - \frac{dn_{\text{clad}}^i}{dT}\right) + \Lambda\frac{d\lambda_i}{d\Lambda}\cdot\frac{1}{L}\frac{dL}{dT} \tag{1.14a}$$

$$\frac{d\lambda_i}{dn_3} = \frac{d\lambda_i}{dn_{\text{clad}}^i}\cdot\frac{dn_{\text{clad}}^i}{dn_3} \tag{1.14b}$$

where L is the length of the LPG, Λ its period, $\delta n_{eff} = n_c - n_{\text{clad}}^i$ (differential effective index) and the cross-sensitivity to strain is not considered in this treatment [22], [23].

The use of LPGs as refractometers or chemical sensors arises from the fact that the effective indices of the cladding modes (η_{clad}^i) are dependent upon the difference between the effective refractive index of the cladding and that of the medium surrounding the cladding n_3 (Fig. 1.10b).

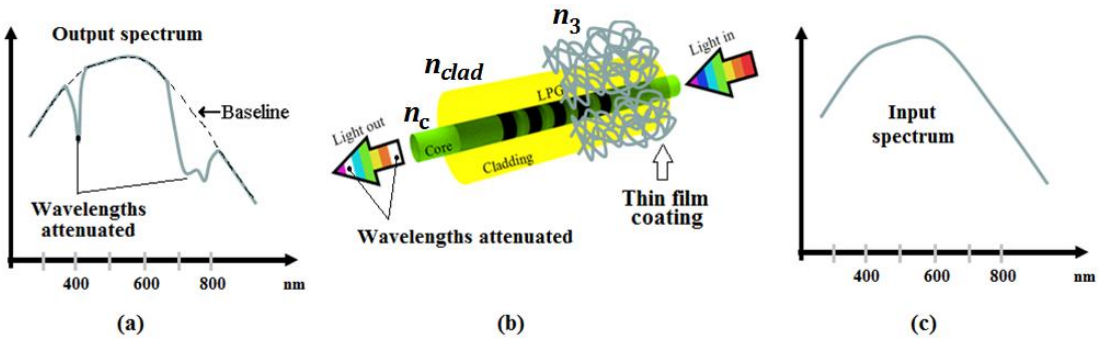


Figure 1.10: Schematics for: (a) typical transmission spectrum from an LPG sensor, (b) LPG sensor coated with a functional thin film as a platform for chemical sensing, and (c) input spectrum from a broadband light source (the baseline of the input spectrum is preserved at the output).

The operation of the LPG as a chemical sensor (Fig. 1.10b) is based on the measurement of changes in the optical properties (for instance, refractive index) induced by the interaction of the film deposited onto the cladding with

the analyte under study. In particular, there is a wavelength shift (a change in λ_i in Eq. 1.13) after changing the concentration of the studied analyte (taken as a change in the refractive index of the surrounding medium). The phase matching condition described by Eq. (1.13) contains a turning point at which it has been demonstrated [24], [25], [26] that the sensitivity of the attenuation band ($d\lambda_i/dn_3$ in Eq. 1.14b) to perturbation of the surrounding environment is at its maximum, i.e., there is an optimum sensitivity when the LPG is fabricated with a period near or at the Phase Matching Turning Point (PMTP) [25]. Fig. 1.11 shows a family of phase matching curves (Eq. 1.13) from the 14th linearly polarized mode (LP_{014}) to the mode LP_{20}. Thus, for the case of an LPG fabricated with a period $\Lambda = 110$ μm (dashed line in Fig. 1.11), there is a prediction of an attenuation band at ca. 670 nm which corresponds to the coupling of the mode LP_{018} and a turning point would be located between 800 nm and 950 nm related to the coupling of the mode LP_{019}.

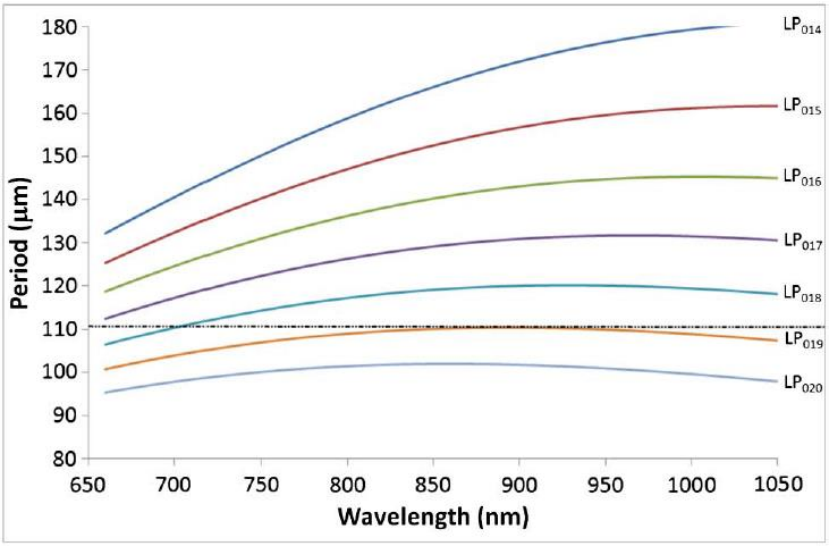


Figure 1.11: Phase matching curves for modes LP_{014} to LP_{020} (copied from [25]).

The evolution of the transmission spectrum of an LPG working near or at the PMTP phenomenon can be explained with reference to Fig. 1.12. In Fig. 1.12a, the grating period is such that phase matching to the mode LP_{018} is satisfied, but it is not possible to couple to the mode LP_{019}, with a resulting LPG

transmission spectrum of the form shown in Fig. 1.12b. Changes in the optical thickness (product of the geometrical thickness and refractive index) of the coating causes an increase in the effective refractive index of the cladding modes. This causes the phase matching curves to change accordingly, "moving upwards" as illustrated with the arrow in Fig. 1.12c, resulting in the development of a resonance band corresponding to coupling to the LP_{019} cladding mode, and a small blue-shift in the central wavelength of the LP_{018} attenuation band (Fig. 1.12d). When the horizontal line corresponding to the LPG period is tangential to the phase matching curve (Fig. 1.12e) at the PMTP, a broad attenuation band corresponding to the mode LP_{019} (Fig. 1.12f) starts to form. Further increase of the optical thickness of the coating results in conditions at which the coupling to the same cladding mode occurs at two different wavelengths (Fig. 1.12g) leading to the further development of the LP_{019} attenuation band, which subsequently splits into two bands (Fig. 1.12h), the so called dual resonance caused by the increase of the effective refractive index of the corresponding cladding mode.

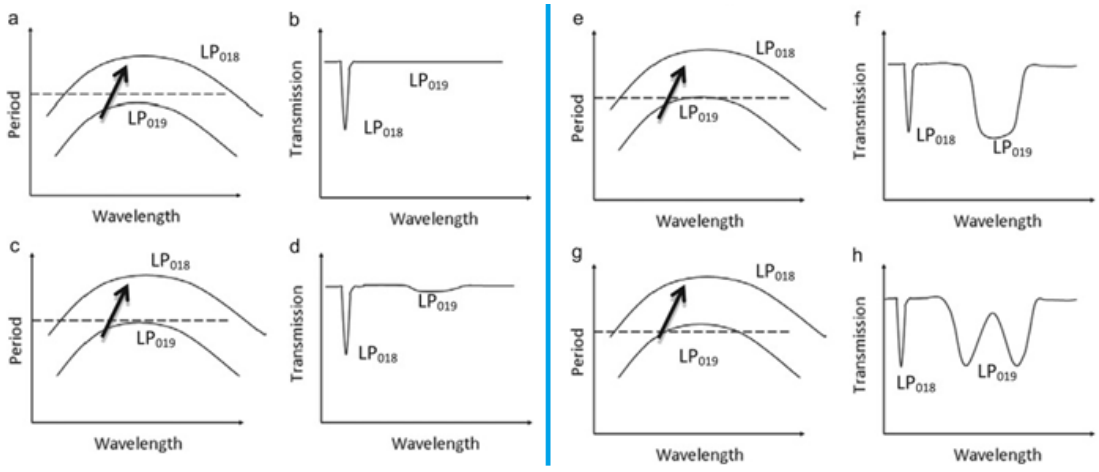


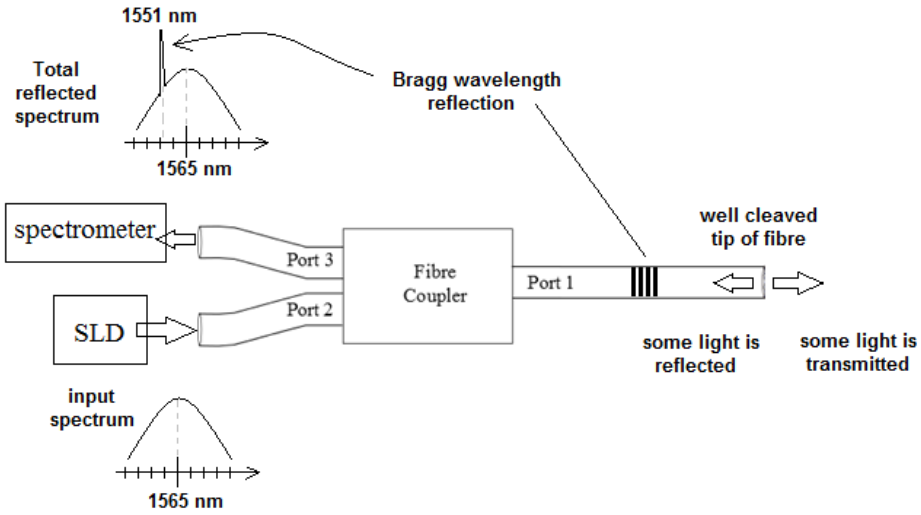
Figure 1.12: Illustration of the properties of an LPG near the PMTP; arrow shows direction of the shift of the phase matching curve for increases of the effective refractive index of the cladding mode caused by increasing optical thickness (taken from [26]).

In this research project, LPG sensors were fabricated with grating periods between 110 μm and 111 μm to obtain operation at or near the PMTP, and

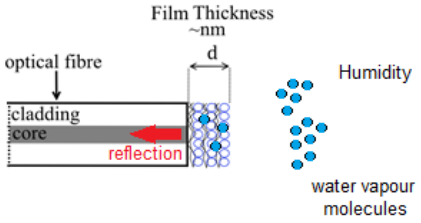
they were coated to provide the LPGs selective response to various biochemical parameters, as explained in chapter 5. The LPG sensors fabricated and used in this research disregard cross-sensitivity to temperature, strain and bending as they were tested under constant temperature in bench set-ups where the fibres were immobilized while measuring changes to the refractive index of the surrounding medium. Nevertheless, further trials of LPGs as bio-chemical sensors should consider these types of cross-sensitivities in practical applications, for instance, by encasing the LPG gauge to protect against bending movements or by including in the system a non-coated fibre sensitive to strain/bending as a reference optical fibre to eliminate motion artefacts. Similarly, a reference optical fibre based on LPG or FBG could be used as temperature sensor for simultaneous compensation of temperature effects on the measurement system.

1.4.3 Fabry-Pêrot interferometric sensor for humidity and temperature

This type of sensor uses a MMF coupler [27] or SMF coupler containing an FBG and a hygroscopic film in port 1 (Figs. 1.13a and 1.13b). This OFS works as a Fabry-Pêrot cavity when a multilayer hydrophilic coating of Poly(allylamine hydrochloride) (PAH) and silica (SiO_2) nanoparticles (NPs) (using the layer-by-layer technique, section 3.3) is deposited onto the cleaved tip of port 1 (Fig. 1.13b). This hydrophilic film has been studied extensively in this research project [27], and it has demonstrated suitable hygroscopic properties for humidity sensing [28]. The chapter 4 of this work will further explain the advantages of using this sensing material compared to others, for example, its deposition onto the tip of the fibre is simple and cost-effective, the humidity response time constant is fast enough, with low hysteresis and its durability and robustness is demonstrated through differential trials in situ applications.



(a)



(b)

Figure 1.13: Schematics for: (a) operation of the SMF coupler containing a FBG and a 90^0 well cleaved tip at port 1; (b) the optical fibre sensor works as a reflection optode when a multilayer film of PAH/SiO_2 is deposited onto the tip of port 1 (the optical thickness of the film changes when exposed to a humidified environment).

Fig. 1.13 depicts the working principle of the Fabry-Pêrot OFS for temperature and humidity sensing. In this case, the input spectrum from a superluminescent diode (SLD optically isolated, Fig. 1.13a) is reflected from the fibre tip of port 1 and the Bragg wavelength reflected (λ~1551 nm) adds to the total reflection spectrum detected in the spectrometer through port 3. The FBG provides the sensor capability for measuring temperature and the deposition of different bilayers of PAH/SiO_2 onto the tip of port 1 affects the total reflection spectrum (due to additive superposition and film transmission loss factors [29]), giving the Fabry-Pêrot OFS hygroscopic properties such that

changes in humidity will modify the optical thickness of the film and the total reflectance (R_{FP}) as described by equations (1.15) [30], [31],

$$R_{FP} = |r_{FP}|^2 = \frac{P_R}{P_T}; \tag{1.15a}$$

$$P_R = \text{total reflected power}; \quad P_T = \text{incident power}$$

$$P_R = R_1 + (1-A)^2(1-\alpha)^2(1-R_1)^2 \cdot R_2 \cdot e^{-4\alpha L} + 2(1-A)(1-\alpha)(1-R_1)\sqrt{R_1 R_2} \cdot e^{-2\alpha L} \cos\left(\frac{4\pi\eta_f L}{\lambda}\right) \tag{1.15b}$$

$$P_T = 1 + R_1 \cdot R_2 \cdot e^{-4\alpha L} + 2\sqrt{R_1 R_2} \cdot e^{-2\alpha L} \cos\left(\frac{4\pi\eta_f L}{\lambda}\right) \tag{1.15c}$$

$R_1 = \left[\eta_{fibre} - \eta_f / \eta_{fibre} + \eta_f\right]^2$ is the Fresnel coefficient at the interface fibre-film and $R_2 = \left[\eta_f - \eta_{air} / \eta_f + \eta_{air}\right]^2$ is the Fresnel coefficient at the interface film-air; α is the transmission loss factor inside the film (absorbance) and A is the loss coefficient at the first interface fibre-film [29]; η_{fibre} is the refractive index of the fibre, η_{air} is the refractive index of the air, L is the physical thickness of the nano-coating and η_f is the effective refractive index of the film which depends on the water vapour molecules absorbed inside the film [27] and also satisfying the Bruggeman effective medium model criteria [32].

In this project, the implementation of the OFS depicted in Fig. 1.13 was applied to estimate AH as this parameter depends on measuring temperature and relative humidity simultaneously. Equations (1.15) were simulated and compared with experimental data to demonstrate the performance and total reflectance of this humidity sensor over the increase of film dimension, i.e., film thickness increased through the sequential deposition of layers of PAH and SiO_2 NPs (using the LbL method, section 3.3).

1.4.4 U-shaped fibre as refractometer and optical fibre chemical sensor

To design a U-shaped probe in a multimode fibre, the plastic buffer is removed with a stripping tool and the cladding of the fibre is reduced while simultaneously exposing to propane flame and deforming into a U shape until the desired bending radius is reached (Fig. 1.14). In this project, the desired bending radius was decided empirically as being between 1 mm and 2 mm based on primary references using U-shaped sensors and reporting diameters in this range as giving the best performance in terms of sensitivity [33], [34]. The probe shown in the photograph of Fig. 1.14 also includes an overlay schematic of the propagation of light rays, the cladding and a functional coating deposited on the outer surface of the bend (not drawn to scale). In this research, deposition of nano-thin films on the outer surface of the U-shape probe has been tested with the aim of performing biochemical recognition through host-guest interactions (section 3.4.1) and using molecular imprinting techniques (sections 3.4.1 and 3.4.2).

The sensing principle of a U-shape fibre probe is based on the fraction of power from the evanescent wave tail leaking from the cladding modes, and the bending transferring more power to them to interact with the analytes present in the surrounding medium [33]. Ray theory approximations can be used in Eq. (1.16) to calculate penetration depth (d_p) of the evanescent wave generated in the sensing region when light (free space wavelength λ_0) is launched into the fibre (Fig. 1.14) [33],

$$d_p = \frac{\lambda_0}{2\pi n_c(\cos^2\theta_{cr} - \cos^2\theta)^{1/2}} \tag{1.16}$$

where n_c is the refractive index of the core, θ is the angle of incidence with respect to the normal of the core-cladding interface in the straight region (Fig. 1.14) and $\theta_{cr} = \sin^{-1}(n_{cl}/n_c)$ is the critical angle of the fibre in the sensing region (n_{cl} is the effective refractive index of the cladding).

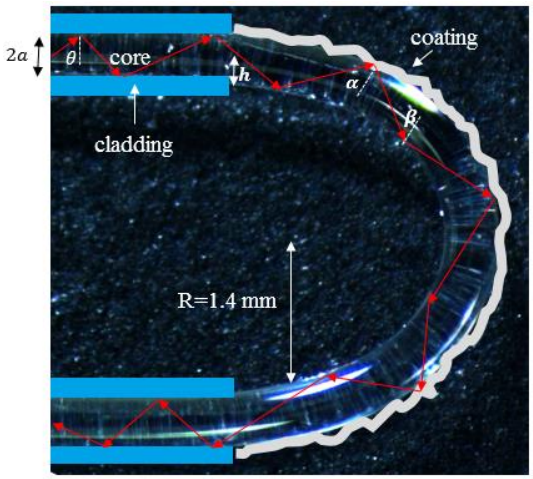


Figure 1.14: Photograph of a fabricated U-shaped fibre (radius R=1.4 mm) having a schematic illustration of the cladding, a nano-thin film coating and the light rays propagating inside the core (radius *a*=100 μm).

In a recent publication [34], the appearance of *lossy resonance modes* have been simulated and experimentally demonstrated when the outer surface of U-shaped probes have been coated with a thin film material having higher refractive index than the reduced cladding (sensing region). In this study of 2016, Paliwal *et al*. [34] have validated the ray theory confined through the calculation of the parameters $\theta, h, \alpha(h), \beta(h)$ shown in Fig. 1.14 and calculated transmittance through the fibre using Eq. (1.17),

$$P_{trans} = \frac{\int_0^{2a}\int_{\alpha_1(h)}^{\alpha_2(h)} R^{N_{ref}} k_0^2\, n_1^2 \sin\theta\cos\theta\, d\theta dh}{\int_0^{2a}\int_{\alpha_1(h)}^{\alpha_2(h)} k_0^2\, n_1^2 \sin\theta\cos\theta\, d\theta dh} \qquad (1.17)$$

where $k_0 = 2\pi/\lambda_0$, n_1 is the dispersion relation of the optical fibre core calculated from Sellmeier's equation [34] and $R^{N_{ref}}$ is the reflected power at the interface fibre-film which depends on the number of reflections at the outer bent region given by $N_{ref} = L\cot\alpha/2a$ (L is the gauge length of the sensing region).

In Fig. 1.14, the parameter *h* is the ray's entrance height, *β* is the angle of the ray in the inner bent region (Eq. 1.18) and *α* is the angle of the ray in the outer bent region with the normal to fibre-film interface (Eq. 1.19) [34],

$$\beta(h) = \sin^{-1}\left[\frac{R+h}{R}\sin\theta\right] \tag{1.18}$$

$$\alpha(h) = \sin^{-1}\left[\frac{R+h}{R+2a}\sin\theta\right] \tag{1.19}$$

Here, R is the bending radius, a is the radius of core and the variation limits for the integral in Eq. (1.17) are from the lower limit given by $\alpha_1(h) = \sin^{-1}[(R+h)\sin\theta_{cr}/R + 2a]$ to the upper limit given by $\alpha_2(h) = \sin^{-1}[(R+h)\sin(\pi/2)/(R+2a)]$.

In this PhD project, U-shaped fibre probes were prepared and coated with molecularly imprinted techniques to demonstrate the detection of biochemical parameters. The performance of U-shaped sensors was supported with LPG sensors for the same biosensing applications.

1.5 Optical fibre sensors based on nano-thin films

Fig. 1.15 shows a schematic concept as an apple tree for a classification of optical fibre sensors based on nano-thin films [35]; the branches containing the apples represent the type of optical fibre sensors developed and used in this PhD research project.

The fibre optic sensors using thin films as sensing elements differ from the type of fibre structure used (main branches in Fig. 1.15) and the type of coating and deposition method implemented (secondary branches in Fig. 1.15). The breakthrough of all the optical fibre sensors presented in Fig. 1.15 is their ability towards new applications and detection of new biochemical parameters. As said before, they also differ from the type of coating deposited through different

methods (see references [12], [35] and [36] for more details): e-beam evaporation, direct current (DC) sputtering, radio frequency (RF) sputtering, dip-coating, spin-coating, electro-chemical plating, thermal evaporation, sol-gel coatings or layer-by-layer (LbL), to name a few. In this project, only inorganic molecular imprinting (sol-gel preparations), layer-by-layer (LbL) and Liquid Phase Deposition (LPD) were used for the integration of nano-thin films onto the optical fibre sensors proposed in this thesis.

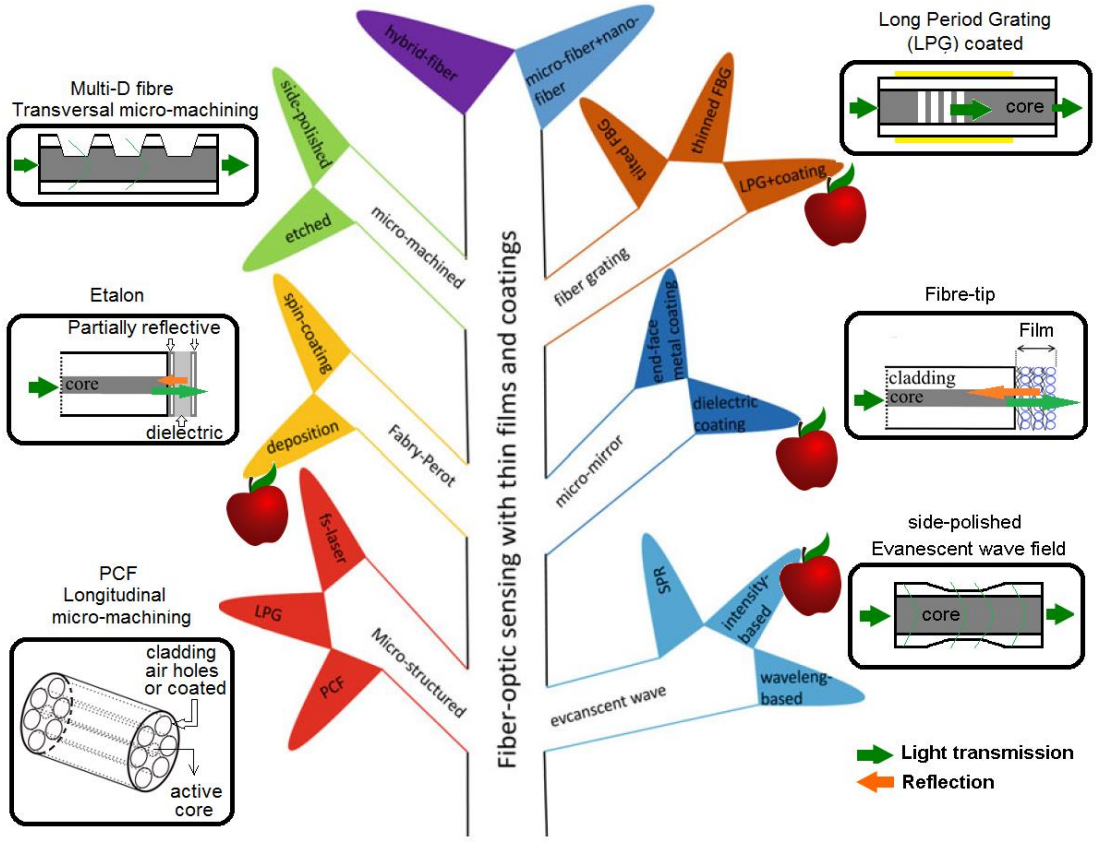


Figure 1.15: Optical fibre sensors based on nano-thin films and coatings (modified from [35]). The branches containing apples represent the sensors used in this PhD project. SPR=Surface Plasmon Resonance, fs-laser= femto-second laser and PCF=Photonic Crystal Fibre.

The gamut of published examples for each type of OFS presented in the branches of Fig. 1.15 is immense and some inputs can be found in recent book or journal reviews [12], [37], [38], [39] but this section will explain briefly only the characteristics of those apple branches (Fig. 1.15) related to this research

project: ***evanescent wave based sensors***, ***micro-mirror / Fabry-Pêrot*** and ***sensors based on Gratings*** (FBGs and LPGs) all aimed to the detection of biochemical parameters based on deposition of nano-coatings.

Evanescent wave (EW) sensors.- A standing electromagnetic field (evanescent wave) leaks from the electromagnetic modes propagating inside the optical fibre (Figs. 1.4 and 1.15) and the optical fibre can be used as refractometer itself in this way or be used after depositing a thin film coating to assure specificity and sensitivity for the desired chemical analyte to be sensed. The evanescent wave is strengthened when the cladding is etched, side-polished, tapered or bent [35]. Thus, another way of using these type of sensors is when they are bent to form a U-shaped optical fibre and, in this research, only these U-bent sensors were implemented for biochemical detection.

The field of evanescent wave-based sensors published in the literature is extensive and here I present only a brief list of examples. The purpose of this list is not to disclose the limits or issues of each exemplar explained, but to show the different applications of EW sensors[1]:

(1) Buerck *et al*. [40] demonstrated a distributed on-line sensing system using EW sensors (with hydrophobic polysiloxane cladding) for chemical analysis and pollution monitoring in groundwater.

(2) Selyanchin *et al*. [41] proposed an EW sensor coated with polymer poly(allylamine hydrochloride) (PAH) and tetrakis-(4-sulfophenyl) porphine (TSPP) for monitoring volatile gaseous compounds excreted from the human skin as a mean of reflecting metabolic conditions of the organism.

(3) Zubiate *et al*. [42] fabricated an EW D-shaped optical fibre coated with tin doped indium oxide (ITO) for obtaining a sensitivity of 8742 nm/Refractive Index Unit (RIU). This sensor surpassed the sensitivity regularly obtained from surface plasmon resonance (SPR) based optical fibre devices.

(4) Nguyen *et al*. [43] proved an SPR and EW based sensor depositing gold

[1] The literature review and works directly related to this PhD are presented in chapter 2.

and silver layers onto the end facet side and tip of an optical fibre for cocaine detection using simple instrumentation.

(5) Verma and Gupta [44] have shown that an U-shaped gold coated fibre increased 25 times the SPR sensitivity compared to an straight EW gold coated optical fibre.

(6) Paliwal *et al*. [34] demonstrated an improved method to obtain lossy mode resonances (LMR) when a material of higher refractive index than the cladding was deposited onto a U-shaped optical fibre to be used as refractometer.

(7) Khijwania *et al*. [33] produced a U-shaped optical fibre coated with Poly vinyl alcohol (PVA) and anhydrous $CoCl_2$ for measuring humidity in a linear dynamic range from c.a. 20 % Relative Humidity (%RH) to c.a. 92.39 %RH. Similarly, part of this PhD research work [45] demonstrated a U-shaped optical fibre coated with PAH and silica nanoparticles (SiO_2 NPs) for measuring humidity in the clinical range of interest (60%RH to 95%RH) during humidification in critical care.

Micro-mirror / Fabry-Pêrot sensors. - These two types of sensors can be considered equivalents as both work under the same condition; a nano-film is deposited onto the tip of the optical fibre (middle left and right, Fig. 1.15). The nano-coating can be a metal, polymer or dielectric material sensitive to environmental parameters and the main difference between micro-mirror and Fabry-Pêrot (or etalon) arises from the non-generation (intensity based) or generation (wavelength based) of interference from the reflections at the coated tip of the fibre [35]. The working principle of these sensors is based on the Fresnel reflection coefficients [5] and the way the refractive index of the nano-film deposited interacts with the surrounding medium changing the reflections (and absorbance) from the coating at the tip [2], [35].

Fabry-Pêrot optical fibre sensors have been manufactured by micro-machining or etching the tip of the fibre and covering the cavity with a silicon membrane [46] or polymer diaphragm [47] for implementing miniature pressure sensors. However, here I present only a brief list of Fabry-Pêrot

examples when a nano-thin film has been deposited onto the cleaved tip of the optical fibre[2]:

(1) There is a broad field of publications for sensing temperature using Fabry-Pêrot sensors. As first example, Lee *et al*. [48] deposited dielectric films based on alumina (Al_2O_3) and zirconium dioxide (ZrO_2) onto the tip of a sapphire fibre for sensing high temperatures from 250 ^{0}C to 750 ^{0}C. As a second example, Jedrzejewska-Szczerska *et al*. [49] proposed a deposition of zinc oxide (ZnO) onto the tip of an standard SMF for measuring temperatures between 50 ^{0}C and 300 ^{0}C.

(2) Chen *et al*. [50] published a label-free Fabry-Pêrot interferometric immunosensor when chitosan and polystyrene sulfonate were deposited onto the tip of the optical fibre for demonstrating an antibody and antigen (immunoglobulin G) detection biosensor.

(3) Arregui *et al*. [51] demonstrated an optical fibre humidity sensor using a nano Fabry-Pêrot cavitiy formed using a cationic polymer made of gold and poly(diallyldimethyl ammonium chloride) (PDDA) and an anionic polymer made of poly(sodium 4-styrene-sulfonate) (PSS) in order to monitor relative humidity in a range between 11 %RH and 100 %RH.

(4) Arregui *et al*. [30] extended the previous application to a sensor capable of simultaneously measuring temperature (with an FBG) and humidity by depositing a nano-film based on PDDA and PolyR-478 onto the tip of the fibre (over the same relative humidity range).

(5) Similarly to the work in point (4), part of this PhD research published an OFS capable of measuring simultaneously temperature (with an FBG) and humidity using a nano-thin film based on PAH and SiO_2 NPs. Absolute humidity calibration was obtained and demonstrated in a benchtop model using a mechanical ventilator [27], [28] and its feasibility to apply as a point-of-care testing device in critical care was demonstrated [45].

[2] The literature review and works directly related to this PhD are presented in chapter 2.

Bragg grating sensors. – Both type of sensors FBGs and LPGs are distributed Bragg reflectors constructed in a short segment of the fibre core that reflect (in the FBG) or transmit (in the LPG) attenuated particular wavelengths [35]. These properties are achieved by creating a periodic variation in the refractive index of the core which filters or blocks certain wavelengths [4]. Two main processes are used for writing Bragg gratings in the core of photosensitive optical fibres using ultraviolet (UV) light: interference and masking [35]. These two methods will be explained later in chapter 3 of this PhD thesis. In practical terms, FBGs are not sensitive to the surrounding refractive index and they are normally used for temperature and strain (or controlled pressure) measurements [19]. However, there are some examples of FBGs using hygroscopic thin films which tend to swell in contact with water moisture and apply strain when deposited onto the FBG section. For example, some works have been published using polymide [52], [53], di-ureasil [54], Pyralin [55], or poly(methyl methacrylate) (PMMA) [56], among others. In this PhD project, FBGs were only used experimentally for temperature measurements and LPGs were functionalized with nano-thin films for propofol and protein detection. Currently, there is a well-established state-of-the-art in the fabrication and functionalization of LPGs between teams at the University of Nottingham, Cranfield and Kitakyushu University [13], [57] as LPGs offer a powerful platform for chemical or biochemical sensing and there is a ready ability to multiplexing LPG arrays and apply them in a wide range of potential applications [45], [58]. Additionally, LPGs have been employed extensively in part because they offer a wavelength-encoded approach and they facilitate the controled coupling of light between modes of the optical fibre structure at specific resonant wavelengths, showing higher sensitivity to perturbation of the surrounding refractive index [13].

Here, I present a brief list of published examples using LPGs with nano-thin films[3]:

[3] The literature review and works directly related to this PhD are presented in chapter 2.

(1) Schuster *et al*. [59] demonstrated an LPG sensor assisted with an in-line gold coated tip to achieve an SPR biosensor with miniaturized sensing area.

(2) Wang *et al*. [60] have shown an LPG coated with poly(diallyldimethyl ammonium chloride) (PDDA) and tetrakis(4-sulfophenyl)porphine (TSPP) to detect ammonia from breath and demonstrated the potential use of this sensor as a non-invasive tool.

(3) The known ability to tune the sensitivity of the LPGs with appropriate choice of grating periods and their main characteristics when they are functionalized with nanostructured coatings to be used as chemical sensors have been widely discussed by James and Tatam [20], [61].

(4) Examples of practical applications of LPG chemical sensors reported by the teams from the Universities of Nottingham, Cranfield and Kitakyushu include indoor air quality assessment using LPG arrays for the simultaneous measurement of temperature (bare LPG), humidity and volatile organic compounds (VOCs) when the LPG gauges were coated with PAH/SiO_2 NPs and PAH/SiO_2 NPs infused with calixarene respectively [62] or using metal organic frameworks to detect VOCs [63]; beverage quality assessment has also been studied when the LPGs were coated with PAH/SiO_2 NPs to identify drinks made from grapes and other materials [64].

(5) Regarding biomedical applications, Korposh *et al*. [65] demonstrated an LPG coated with molecular imprinted polymers for vancomycin detection and demonstrated high selectivity of the sensor when exposed to different drugs. Additionally, another LPG coated with SiO_2 NPs and PAH infused with poly(acrylic acid) (PAA) was employed for the sensitive detection of a cancer biomarker spermine (SPM) [21]. Similarly, part of this PhD project investigated the application of coated LPGs to be used as biosensors [26] and also to detect propofol in aqueous solutions.

All the optical fibre sensors of Fig. 1.15 share, to some extent, a gamut of advantages towards the specific niche of applications, but all share a series of challenges, especially for industrial applications [66]:

(1) The mechanical stability on small diameter optical fibres is usually the

main frequent problem.

(2) Some nano-films deposited onto optical fibres cannot be reset or re-used.

(3) Some sensors require temperature control or compensation.

(4) Specificity needs to be investigated but this is not often an issue since the range of gas or analyte species has common properties and either the detection of any chemical of the family may be of importance or the detection for a specific compound is higher than the others from the same family, as for example demonstrated for detection of methanol in reference [67].

(5) All the biosensors have a natural lifetime or long term stability which is greatly dependent upon how the environment affects the nano-film and the immobilization chemistry technique used for its deposition onto the optical fibre [66]. Much of the efforts in OFS research and development (R&D) is devoted to overcome these drawbacks and, in this research project, I demonstrate the potential feasibility of the optical fibre sensors proposed to be applied in ventilation care equipment or as new approach technology for protein or propofol detection, both of which are important biochemical parameters during medical care in the Intensive Care Unit (ICU) or during anaesthesia.

A brief state of the art of optical fibre sensors applied to care health is explained in the next section. *A literature review of the field of optical fibre sensors and some other important sensors (e.g. electronic, chemiresistive sensors) applied during anaesthesia, in the intensive care unit (ICU) or during critical care in clinical studies is disclosed in the chapter 2 in conjunction with the engineering challenges to be solved in the targeted application of this PhD project*, i.e., optical fibre sensors for medical devices during anaesthesia or critical care.

1.6 Optical fibre sensors in healthcare: current status and future trends

The current status of the day-by-day use of optical fibre sensors, mostly reviewed in [68], gives an idea of the future trends regarding personal healthcare (Fig. 1.16). As *fibres on the body*, fibre sensors have been proposed as wearables when combining natural or synthetic fibres and embedding optical fibres. For instance, FBGs, LPGs and Optical Time-Domain Reflectometers (OTDR) have been embedded into elastic bandages or attached to clothing for measuring heartbeats and movements due to respiratory rate during magnetic resonance procedures or critical care [69], [70], [71]. Polymer Optical Fibres (POFs) have received special attention for the development of wearables as they provide higher robustness, compatibility to the processes in the textile industry, more flexibility, are lightweight, have higher elasticity and higher break-down strain. All suitable characteristics for their integration into textiles [68], [72].

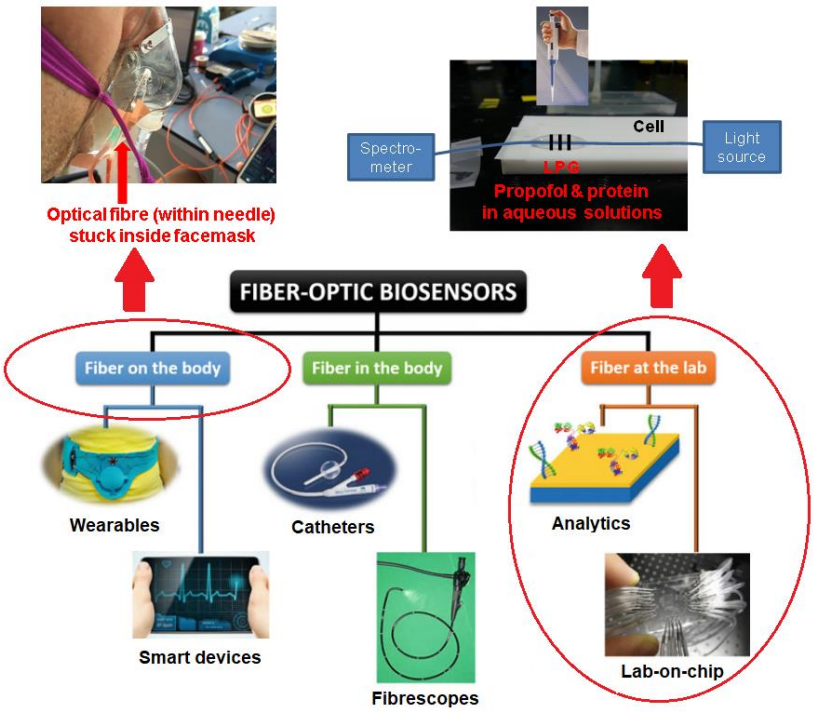


Figure 1.16: Current status and future trends of optical fibre sensors (adapted from [68]). The optical fibre sensors developed in this research project contribute to the fields enclosed with red circles.

Optical fibre sensors have also been combined with the LED of smartphone and its own CCD camera (left, Fig. 1.16). For instance, fibre optic SPR sensors with FBGs developed at the Leibniz University Hannover [73], a hand-held reader which couples optical fibres and smartphones for testing Enzyme-Linked Immunosorbent Assays (ELISA) [74], and another fibre optic SPR sensor using gold nano-coating for immunoglobulin G biodetection was adapted to a smartphone platform [75].

Regarding the *fibres in the body* (centre, Fig. 1.16), apart from the well-known utilization of fibrescopes as an imaging system through the veins, arteries or the digestive tube, it is worthwhile noting a series of recently published works. For example, the reconstruction of an aorta phantom model shape has been possible by using FBG-based sensors combined with ultrasound [76], exploration of the lower gastrointestinal tract of the human body using a fibre optic manometer catheter and multiplexing of FBGs is now in clinical use across Australia and New Zealand [77] and intramuscular pressure by using Fabry-Pêrot optical fibre interferometers have been tested clinically and commercialized by Samba Sensors Inc. [78]. Similarly, dual bladder and abdominal pressure monitoring during in-vivo urodynamic analysis has been possible with the use of Fabry-Pêrot optical fibre configurations [79]. Finally, the Swan-Ganz catheter has been in clinical use since 1970 [80] but it is currently commercialized by Ewards Lifesciences Corporation allowing the continuous measurement of venous oxygen saturation through optical fibre technology.

Fibres at the lab (right, Fig. 1.16) is the most classical use of optical fibres as biosensors, i.e., the chemical functionalization of optical fibre surfaces for anchoring molecular bioreceptors capable of detecting the analytes of interest [68]. There are two ways to apply the fibres at the lab: *Analytics* and *lab-on-chip* / *lab-on-fibre*. The former involves actuating and sensing on the functionalized surface of the fibre or the surface of the structure itself [36]; the latter involves using light from transmitter and receiver optical fibres in conjunction with micro-optics components or micro-electromechanical

systems (MEMS), usually implemented in microfluidic channels to measure biochemical properties of the analyte under study. Nowadays, lab-on-fibre is possible using micro-structured optical fibres (Fig. 1.15), containing nano-coatings [81], new combinations of D-shaped coated fibres containing LPGs [82] or patterning and functionalizing the optical fibre tip [36], [83]. The types of optical fibre sensors through functionalization of the fibre surfaces were already presented in previous section. It is important to clarify that biosensors implemented as lab-on-chip or lab-on-fibre can be also classified according to the type of target biomolecule, i.e., enzyme/protein-based sensors, immunosensors, cell/tissue sensors, aptasensors, sensors based on DNA chains or based on microorganisms [68]. Part of this research will present the development of two analytical approaches for the detection of protein and propofol using OFS-functionalized technology.

The trend of OFS technology is increasing nowadays and it has provided a range of solutions in a wide and diverse spectrum of disciplines in biomedical engineering and clinical practice including spectroscopy, endoscopy, tissue pathology, blood flow monitoring, light therapy, biosensing, laser surgery, dentistry, dermatology and health status monitoring [6], [13], [69], [70]. The application of optical fibre sensors in healthcare involves its use during medical practice in any type of service providing medical care, then allowing new areas of exploitation of this technology but also requiring new education for healthcare providers, professionals and patients.

Most of the content of this subsection is based on a recently published review book about the current status and future possibilities of optical fibre sensors [68]. There are three main postulations in this review book [68]:

(1) Current R&D requires an update to the concept of biosensors.

(2) OFS technology should be used in medicine due to a series of unique advantages (explained in next paragraphs).

(3) Current status sets the challenges to be fulfilled and the vision for the future in OFS technology in healthcare.

Technically, a biosensor could be defined as “a device capable of detecting biological or biochemical substances, called analytes, with high sensitivity and using a rapid, direct and specific biomolecular recognition” [68]. On a side, Socorro and Diaz [68] propose this concept needs to be updated because R&D groups are developing sensors based on attaching bioreceptors to different substrates, depending on the transducing phenomenon used and technology applied, for example, Quartz Crystal Microbalance (QCM) [84], [85], lab-on-chips using Micro-Electro-Mechanical Systems (MEMS) [86] or OFS technology, to name a few. In another example, Socorro and Diaz [68] suggest the biosensor concept requires to be broadened and cover the day-by-day demands of current society. For instance, recent technologies permit patients self-caring such that the medical devices can be used as a wearable or they are integrated in smartphones for personal health statistics or vital signs; these are also biosensing applications since they are monitoring biological variables. Therefore, the proposed updated and more general definition for biosensor that Socorro and Diaz [68] recommend is as follows: “device capable of monitoring a specific biomedical variable (including biochemical or physical) and provide information that can give a rapid and accurate diagnosis of a patient’s health condition”.

Nowadays, OFS technology deserves to be applied in medicine due to the following reasons [68]:

(1) *Biocompatibility*. - The optical fibre is mainly based on silica which does not present any side effects to biological substances.

(2) *Reduced size*. - Even when frequently used fibrescopes have a diameter core of 1 mm, they can be introduced in the body for visual diagnosis.

(3) *Low Cost*. - Commercial prices for telecommunications fibres are accessible worldwide and the interrogation electronic devices can be reduced to a single LED and photodetector.

(4) *Flexibility and Low Weight.* - Without these characteristics it would not be possible to reach places inside the human body where it is impossible to operate without an open surgery.

(5) *Capability to work in hazardous or complex media*. - OFS technology has demonstrated to work well in environments such as magnetic resonance imaging (MRI) [87] or ionizing radiation (γ −rays or x −rays) [88], [89]. It has also been applied in complex matrices of blood serum where the presence of other biological components complicates optimal detection conditions [87], [90].

(6) *Diversity of optical fibre structures*. – As shown in section 1.5, there are several optical fibre architectures to be applied with many possible nano-film deposition methods for creating bioreceptors.

(7) *Optical fibre itself is a sensing platform*. - The optical fibre sensors can be used for measuring traditional parameters such as temperature, strain, pressure or refractive index of the surrounding medium. However, sensitivity and specificity to biochemical parameters can be tailored and optimized when depositing coatings onto the OFS used.

Fig. 1.16 presented a schematic of the future trends reviewed in [68], classified in three main areas: fibres on the body using wearables, smart devices or mobile phones; fibres in the body using catheters or fibrescopes, and fibres at the lab which is the most traditional use of optical fibres as classical biosensors. In this PhD thesis the development of an OFS for humidity, temperature and respiratory rate monitoring during mechanical ventilation contributes to the first field presented in left part of Fig. 1.16. Additionally, the proof of concept of an OFS for protein and propofol detection contributes as an analytical approach (right side, Fig. 1.16) as both biochemical parameters need to be monitored during procedures in the ICU or anaesthesia.

The next chapter will disclose, to the best of the author's knowledge, a specific review of general medical devices vs OFS devices used in the targeted area of application proposed in this PhD research.

1.7 Summary

This chapter has presented the background information about optical fibre sensors and the topics are summarised here:

- Transmission of light within the fibre can be explained with two theories: *ray optics* and *electromagnetic propagation of the linearly polarised guided modes*.
- The major categories of optical fibres are briefly explained, from standard telecommunications fibres and plastic optical fibres to photonic crystal fibres.
- How an optical fibre sensor (OFS) works and the four types of optical fibre sensors used in this project are described with their principle of operation.
- Finally, a classification of optical fibre sensors based on the nano-thin films deposited is presented and a general overview is given of the current and future trends of optical fibre sensors in healthcare.

1.8 Structure of the thesis

Chapter 1 has provided a general introduction and essential concepts to understand how light propagates in an optical fibre and what an OFS is. It included the classifications of optical fibre sensors and a brief discussion of the optical fibre sensors used in healthcare, the current status and the future trends.

Chapter 2 presents a review of the clinical challenges in the ICU and the literature review of general sensors vs optical fibre sensors applied in the ICU or during anaesthesia. The final subsection will present the aim and objectives of the PhD project including the proposed engineering solutions to tackle the clinical challenges.

Chapter 3 reports on the fabrication process used for FBGs, LPGs and U-shaped fibres. It also reports on three main methods for the functionalization of optical fibre sensors: Layer-by-layer method, Liquid Phase Deposition of imprinted TiO_2 and a sol-gel technique based on Mesoporous silica nanoparticles used with molecularly imprinted TiO_2 for propofol detection. All these techniques were useful and implemented for measuring analytes in gas or liquid media.

Chapter 4. The content of this chapter proposes an OFS for measuring temperature and humidity simultaneously. This sensor adds value to solve important clinical problems involved during the care of patients hospitalized in the ICU. The application of this sensor is also supported by an animal study. Ethical approval was obtained and the process was carried out under the provisions of a Home Office license allowing for research work with animals. All procedures were performed in accordance with the UK Animals (Scientific Procedures) Act. 1986 under a project license held by Prof. D. Gardner (PPL 40-3410) and the study was performed in the primary licensed establishment located at Sutton Bonington campus in the University of Nottingham. Additionally, this chapter presents preliminary work from a protocol recently approved as "*Validation of a novel fibreoptic sensor integrated in oxygen delivery devices as a respiratory rate monitor*" in a study with volunteers. This study has been designed in collaboration with anaesthetists at Nottingham University Hospitals NHS Trust.

Chapter 5 shows two optical fibre biosensors, one for protein detection and another for propofol detection. This chapter demonstrates the feasibility of the proposed sensors to target clinically relevant compounds. This research work was mainly performed at the University of Kitakyushu (Japan) as part of a collaboration with the University of Nottingham.

Chapter 6 presents a general discussion, the conclusions obtained with the work developed during the PhD and future work for embedding OFS technology in critical care equipment (facemasks, ETTs) for detection of propofol, humidification conditioning and respiratory rate monitors.

Appendix presents preliminary work developed during this PhD to control the intubation with an FBG-based OFS for measuring the contact pressure exerted from a cuffed ETT in a tracheal model. This appendix also discloses an LPG-based OFS for monitoring bacteria formation during intubation (monitoring bacteria biofilm grow normally found during intubation with ETT).

Chapter 2: Clinical challenges for the research project and literature review

This chapter firstly presents a review of some of the clinical challenges in the intensive care unit (ICU) which resulted from discussions with clinical collaborators from the Nottingham University Hospitals NHS Trust. Four main clinical challenges were identified and they are explained through subsection 2.1; each clinical challenge is substantiated with evidenced publications. The intention of this chapter is also to present (section 2.2) the literature review of general sensors and optical fibre sensors applied in the ICU or during anaesthesia to demonstrate the gaps in this field of application. Therefore, the aim and objectives of this research, explained at the end of this chapter, will introduce the potential applications of optical fibre sensors during critical care via their incorporation into medical devices used in the ICU such as endotracheal tubes (ETTs), facemasks and nasal cannulas.

2.1 Automatic closed-loop systems during critical care

Medical care in the ICU requires multiple procedures, treatments and monitoring for patients who are anaesthetized and/or in critical health conditions. Typically, there is a need to maintain drug concentrations and physiological parameters within specific boundaries in order to optimize treatment effects, support physiology and minimize harm. Intensive care is expensive and is associated with high morbidity and mortality [91]. Complications of treatment and medical errors are well-recognized problems [92]. Goals for improvements in the ICU include reduced length of stay, reduced drug costs, and reduced frequency of complications and errors [93], [94]. Recent reviews have discussed the implementation of "*automated closed-loop control*" during anaesthesia to facilitate patient outcome through monitoring depth of anaesthesia on the one hand [95], [96], and monitoring

anesthetic-drug delivery on the other [97], [98]. A generic closed-loop control system has a controller that monitors one or more variables and adjusts one or more interventions to control that system in response (Fig. 2.1).

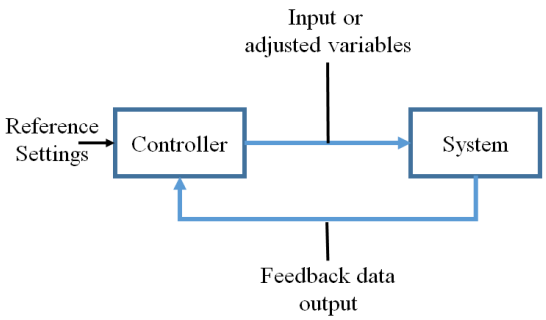


Figure 2.1: Scheme for a generic closed-loop control [96].

Anaesthesiologists themselves represent closed-loop controllers by firstly setting a target point (reference setting, Fig. 2.1) for anaesthetic delivery, monitoring patient output in the form of vital signs (heart rate, blood pressure, breathing or other physiological parameters as indicators of unconsciousness); finally a calculation of an error between feedback data and reference generates a new system input and tailors a new intervention [96]. Anaesthesiologists are regularly compared to airline pilots: induction, maintenance and awakening from anaesthetics have analogy with the take-off, cruising flight and landing of aircraft [99]. Similarly to the airplane industry, automatic closed-loop control during anaesthesia reduces workload during busy times and this advantage is more pronounced in ICU settings where physician and nursing attention is often spread over the critical care unit. An automatic system capable of reducing human error and continuously maintaining an optimal control could have a profound impact on patient outcome [96]. In addition, adopting an automatic closed-loop system in the clinical setting provides a means to achieve safety (fail safe and tolerant to artefacts without jeopardizing patient care), efficacy and reliability in the long term through extensive testing in simulation and supervised clinical trials [100]. In a review of closed-loop systems in anaesthesia, Rinehart *et al*. (2012) have

postulated that “the future of anesthesia will rely on two separate but interdependent technologies: the sensors and monitors on one side, and the controllers on the other”. This research contributes to the former type of technologies through the incorporation of optical fibre sensors in primary care or point-of-care equipment used during critical care, including:

(i) Chapter 4 of this work presents the implementation of a temperature-humidity OFS tested and incorporated in ETTs, facemasks and nasal cannulas.

(ii) Chapter 5 explains the implementation of optical fibre sensors for biochemical detection, explaining firstly a sensor for protein detection and later an anaesthetic OFS monitor tested under in vitro conditions.

(iii) The Appendix presents preliminary work developed to incorporate a pressure OFS to control the contact pressure exerted from the cuffed ETT to a trachea model; this appendix also shows preliminary work developed in this research to monitor bacteria biofilm growth normally found during intubation.

The critical care of patients intubated (Fig. 2.2) and treatment of patients in the ICU involve multiple tasks and challenges that could be controlled as closed-loop individual systems, and also they could be combined into comprehensive controllers for fully integrated care management (Table 2.1) which includes the use of medical equipment such as ETTs, mechanical ventilators and facemasks. Table 2.1 describes and summarizes some clinical challenges during critical care that potentially can be tackled using appropriate engineering solutions with optical fibre technology, the parameters that need to be monitored or controlled, and a schematic of the application. This table of clinical challenges is a result of discussions with clinicians from the Queen’s Medical Centre Nottingham University Hospital (NHS Trust) [45]. An extended explanation of each clinical challenge is considered here. The problems that affect morbidity/mortality during critical care and the proposed engineering solutions are described in detailed subsections afterwards.

<table>
<tr><th>Clinical challenges and parameters that need to be controlled</th><th>Schematic / Portrayal</th></tr>
<tr><td>1. Intubation. Contact pressure between cuff of ETT and trachea wall (red spots in Fig. 2.2).

2. Respiratory Rate (RR) and humidification during invasive ventilation. Humidity and temperature at the T-valve for gas conditioning (Fig. 2.2).

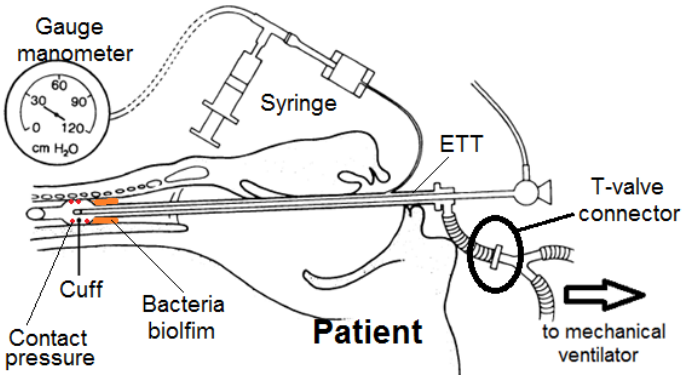
3. Avoid Ventilator-Associated Pneumonia (VAP). Bacteria growth (Fig. 2.2) on surfaces of ETT during intubation.</td><td>

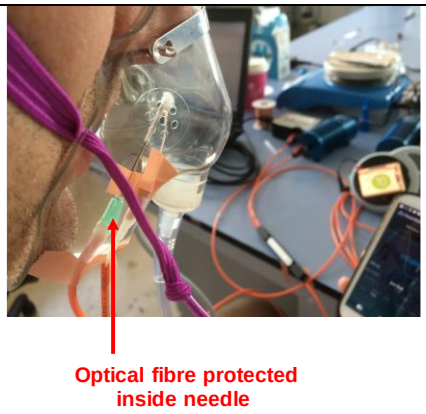
Figure 2.2: Intubation with an ETT (modified from [101]).</td></tr>
<tr><td>4. Respiratory rate and humidification during non-invasive ventilation (Fig. 2.3). Relative Humidity (RH), Temperature, Absolute Humidity (AH), Respiratory Rate (RR).</td><td>

Figure 2.3: Adhering the OFS to ICU equipment (Respir8® facemask in this case) used for non-invasive ventilation. This photograph elucidates how the OFS could be adhered inside the mask to monitor temperature, AH and RR. The Respir8® only contains an electronic RR monitor inside the mask (on the other side, not visible in the photograph).</td></tr>
</table>

Table 2.1: Current clinical challenges during critical care which are candidates for implementing an automatic closed-loop individual system using OFS technology.

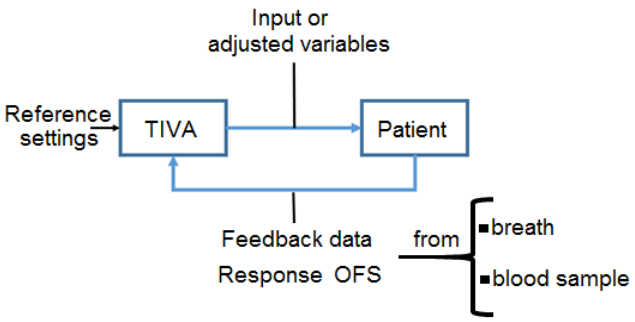
Clincial challenges and parameters that need to be controlled	Schematic / Portrayal
5. Monitoring anaesthetic delivery (Fig. 2.4). Propofol concentration in breath or measured from blood samples. **6. Monitoring protein intake (enteral or parenteral feeding).** Enteral refers to the intake through the nose or mouth and parenteral through the veins. These parameters may be monitored using a closed-loop control like in Fig. 2.4.	 Figure 2.4: Monitoring propofol concentration

Table 2.1: (continuation) Current clinical challenges during critical care which are candidates for implementing an automatic closed-loop individual system using OFS technology. TIVA=Total Intravenous anaesthesia.

2.1.1 Control of the contact pressure during intubation

ETTs (Fig. 2.5) have an inflatable cuff which has two functions [101]:

(1) *A*cts as a barrier for mucosal secretions which can pass from the mouth into the lungs (resulting in infections or Ventilator Associated Pneumonia [91]).

(2) Provides a gas seal and the humidified gas and oxygen delivered by a mechanical ventilator (Fig. 2.2) goes into the lungs without escaping back.

Although an essential part of critical care, there are problems associated with using ETTs. Firstly, it has been demonstrated [101] that if cuff pressures are too high they damage the mucosal lining of the trachea/larynx mainly through applied contact pressure reducing microcirculatory flow and therefore oxygen supply to the epithelial cells [102]. This deterioration of tracheal mucosal blood flow is an important factor in tracheal morbidity associated with

intubation and the most frequently used technique takes into consideration the control of the intra-cuff pressure (measured with a gauge manometer, Fig. 2.2) instead of contact pressure between the cuff and the trachea wall [101], [103], [104], [105]. Therefore, the challenge to overcome in this issue is to monitor the contact pressure made by the cuff directly using a contact pressure OFS rather than controlling the intra-cuff pressure using conventional gauge manometers (Fig. 2.2). In this respect, it is recommended [106] that intra-cuff inflation pressure should be within an optimal safe range between 2.5 KPa and 4.0 KPa (measured with a manometer). Preliminary tests developed to solve this challenge are presented in the Appendix of this PhD thesis and will not be discussed in detail. Most of the results presented in the Appendix were obtained during the first year of my PhD research as exploratory work to test the contact pressure between the cuff of the ETT and a trachea model using bare FBGs. These preliminary results were published as a conference paper [18] in collaboration of researchers from Cranfield University and the QMC university hospital of Nottingham. This work was a preparatory research stage for using optical fibre sensors in ETTs to measure contact pressure. Nonetheless, the research was continued and improved by the collaborators through using patched FBGs and measure contact pressure with higher sensitivity [15].

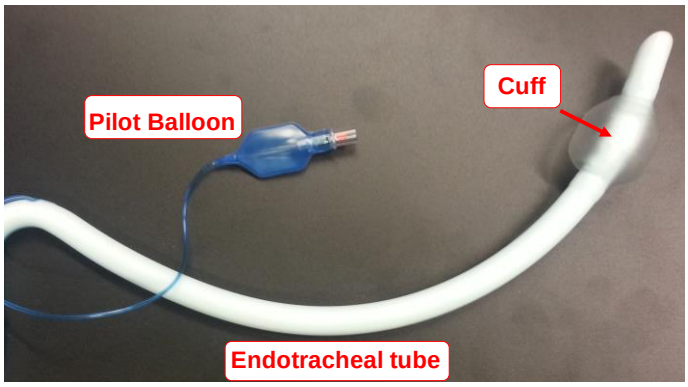


Figure 2.5: This photograph shows a commercial ETT only for illustrating its main components. This case shows a Soft seal ® Cuff North Polar Preformed ETT (Portex® Smiths medical, Kent, UK).

2.1.2 Monitoring respiratory rate and humidification during mechanical ventilation

Humidification of inspired gases is an essential part of the clinical treatment in critical respiratory care, and inhalation of inadequately humidified gas during invasive (through an ETT placed in the patient's trachea) or non-invasive (via a mask placed on the patient's face) ventilation causes drying of the delicate respiratory mucosa and consequent cooling, mucosal injury, drying of (and difficulty clearing) secretions and respiratory deterioration [107]. The human airway has the role of heating and humidifying inspired gas, and recovering heat and moisture from expired gas, but this function is impaired in patients who are intubated (Fig. 2.2) or patients hospitalized in the ICU [107], [108].

Therefore, control of humidity/temperature in mechanical ventilator care equipment (Fig. 2.6) is essential for conditioning delivery of inspired gases. AH levels between 33 mg H_2O/L and 44 mg H_2O /L, and a gas temperature between 34 ℃ and 41 ℃ near the upper airways of the patient (100 % RH at the Y-piece of the breathing circuit, Fig. 2.2) are suggested during invasive ventilation [109], [110]. Levels of AH lower than 5 mg/L represent a significant risk of respiratory complications related to inadequate humidification of inspired air [111]. Optimal humidification levels and respiratory rate during non-invasive ventilation still needs investigation through clinical testing [109], [112].

Humidification is currently an important part of modern intensive care practice. For instance, some studies have demonstrated that patients ventilated with dry gas caused time-dependent injury to respiratory epithelial cells [107]; recommendations have specified that the AH of inspired gas should be between 25 and 30 mg H_2O/L to preserve normal mucociliary function (natural mechanism to preserve the self-clearance function of tracheal mucus) [107], [109]. After admission to the ICU, maintenance of the respiratory function of patients requires adequate control of humidity to prevent airway dryness in non-invasive ventilation in which inadequate humidification and heating of the inspired air has been associated with functional deterioration of

nasal mucosa [108]. In addition, there is a correlation between humidification and the risk of ventilator associated pneumonia (VAP) during invasive mechanical ventilation (Fig. 2.2 and 2.6b) where operation at higher levels of humidity to the airway (near 44 mg H_2O/L) can facilitate maximal mucociliary clearance [103].



(a) (b)

Figure 2.6: (a) Portable Non-invasive Positive Pressure Ventilator (NIPPY3+, B&D Electromedical Ltd, Warwickshire, UK). (b) Mechanical Ventilator Dräger Evita (Draeger Medical UK Ltd, Hemel Hempstead, UK) used for invasive ventilation in the ICU at Nottingham University Hospitals NHS Trust.

Currently, during prolonged invasive mechanical ventilation, respiratory gases are actively humidified by means of a heated water bath in order to achieve levels of humidity approaching 100% RH. In active humidification, gases are kept warm (with heating wires) in the inspiratory limb of the respiratory tubing (Fig. 2.2) in order to reduce condensation. However, due to the limitations of current humidity sensors, humidity and respiratory rate are not actually measured at the patient end of the circuit or inside the patient's airway. There have been a few works [113] [114] aimed at investigating this humidity related clinical challenge with other types of sensors. This project has been the first in investigating an OFS to overcome this clinical challenge.

2.1.3 Monitoring bacteria biofilm growth during intubation

Ventilator Associated Pneumonia (VAP) is one of the most frequent hospital-acquired infections occurring in intubated patients [91]. The principal source of VAP development is the presence of the ETT because it impairs the mucociliary function of the trachea and contaminated oropharyngeal secretions can leak down to the lungs through the cuffed ETT (when not properly sealed). Lastly, after several hours of intubation (typically >48 hr. without prevention techniques) a biofilm develops on both the inner and the outer surface of the ETT, acting as a reservoir for bacterial colonization and for microorganism inoculum to the lungs, resulting in a hospital-acquired infection [92]. In VAP, the most abundant pathogenic bacteria presented in this sepsis are those presented in Fig. 2.7, i.e., the biofilm developed on the walls of ETTs during intubation is mainly formed with bacterium of Pseudomona aeruginosa and Staphylococcus aureus [115].

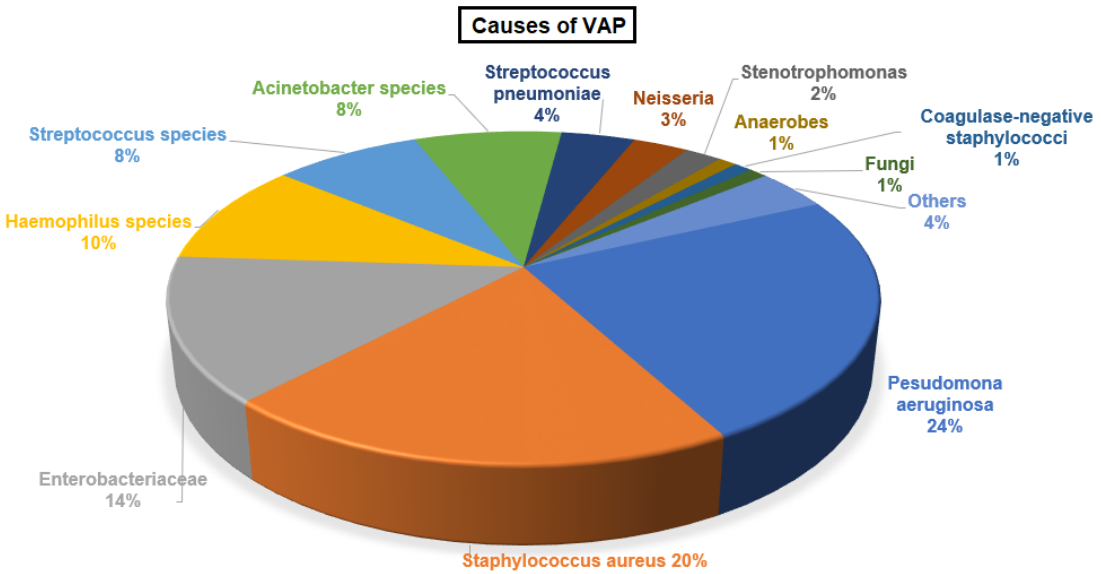


Figure 2.7: Relative proportions of common bacterial microorganisms that cause VAP [115].

These type of bacterium have a distinctive metabolism producing specific Volatile Organic Compounds (VOCs) which opens the possibility to diagnose VAP through breathing detection where those volatile metabolites have been

reviewed carefully for each type of bacteria related to VAP infection (biomarkers for VAP diagnosis) [116]. Bos *et al*. [116] showed that all the VOCs produced by at least one of the bacteria were detectable through Gas Chromatography Mass Spectrometry (GC/MS). Thus, the challenge to overcome in this issue is to develop a chemical OFS for VAP prevention through detecting either bacteria concentration directly or detecting the VOCs released by the breath of patients with VAP. In this PhD project, only preliminary work developed in this direction is presented in the Appendix when testing bacteria biofilm growth on the surface of an LPG fibre. Similarly to section 2.1.1, the respective results for this challenge were also obtained during the first year of my PhD as exploratory work to verify whether optical fibre sensors can be used to monitor biofilm formation onto LPGs. Preliminary results were positive towards the implementation of these types of sensors, however, this application was further undertaken by another PhD student from the research group to which I belong to.

2.1.4 Monitoring anaesthetic and protein delivery in the ICU

The use of anaesthetic during surgery is important to avoid pain and more than 3.5 million patients receive care under anaesthesia every year in the UK [117]. Protein/amino acid supplementation has the potential to improve the recovery of critically ill patients, especially those with low muscle protein mass that might benefit the most from adequate protein nutrition in the ICU [118].

Monitoring and controlling anaesthetic levels in the bloodstream (through all the organs) differs from measuring Depth of General Anaesthesia (DGA) which occurs when there is a transition from wakefulness to loss of consciousness in the brain [95]. Most of the methods use electroencephalography and post-processing algorithms as surrogates for monitoring DGA. This is a current and hotly debated topic of research, with still no gold standard able to measure the depth of anaesthesia, being accepted world-wide [100]. Recent reviews [95], [96] show that the most clinically tried closed-loop automatic method is the

bispectral index algorithm used with electroencephalography as surrogate of DGA.

Monitoring both DGA and the anaesthetic delivery are current open research areas which need more clinical validation to demonstrate safety, efficacy and reliability on the one hand, and to demonstrate improvement in patient outcome and cost-benefit effectiveness on the other [96]. Measurement of actual concentration of anaesthetic in the blood (biophase) or exhaled breath is feasible (Fig. 2.4). A closed-loop control system for automatic administration of anaesthetic has been attainable in Total Intravenous Anaesthesia (TIVA) through Target-Controlled Infusion (TCI) pumps [97], [98], but some practical issues still need to be addressed. These are:

(1) There are pitfalls when operating TCI pumps for delivering anaesthetics because they use computer-controlled models (algorithms for predicting levels of anaesthetic in the blood) based on a relatively small number of healthy volunteers, and extrapolation might fail between patient variability, especially for patients in extreme clinical conditions (pharmacodynamics is different in patients with anaemia, hypoalbuminemia, children or patients with extreme obesity) [98]. Therefore, a rapid on-line and real time analytical method for measuring blood (or breath) concentration of the intravenous drug propofol in patients under anaesthesia is needed.

(2) Due to issues of using TCI pumps, there is a need of measuring anaesthetic concentration in plasma itself in a more cost-effective manner. Currently, plasma concentrations are measured by bulky, expensive and time-consuming (for sample preparation) devices such as High-Performance Liquid Chromatography (HPLC) [119], [120]. In addition, the concentration of propofol in gas phase or from exhaled breath of patients has been measured by either continuous and expensive methods such as proton transfer reaction mass spectrometry (PTR-MS) [120] and ion-molecule reaction-mass spectrometry (IMR-MS) [121] or discontinuous methods (i.e. not rapid tests) such as solid

phase micro extraction or TENAX tubes using Gas Chromatography-Mass spectrometry (GC-MS) [119]. Most of these publications have demonstrated the correlation between the plasma concentration and exhaled breath anaesthetic concentration [119], [120], [121].

The literature review in section 2.3 of this chapter will describe in more detail the current approaches implemented to measure anaesthetic propofol (breath and blood) in vitro or in vivo studies. Last but not least, some pragmatic and experimental studies have focused on protein requirements of ICU patients [122]. These studies give an approximation of an enteral provision of more than 1.2 g protein/Kg (body weight) or suggest that an intake level between 2.0 and 2.5 g/Kg per day appears to be safe, as supported by some outcome-based observational studies [122]. Nonetheless, there is still no consensus about these protein delivery levels and adequate supply of the energy intake through nose/mouth (enteral) and/or through veins (parenteral) for different diagnostic groups of critical illness, but some evidence shows that protein/amino acid supplementation has the potential to improve recovery of patients in critical care, especially patients with low muscle mass [122]. Recently published survey data [118] showed that protein is poorly delivered and the administration comes mostly from enteral nutrition regardless the availability of products to enhance delivery in the ICU setting. Heyland *et al*. [118] have mentioned that “further research should also develop better tools to enable bedside practitioners to monitor optimal or adequate protein intake for individual patients” and improve optimal outcomes of survivors of critical illness. In addition, Heyland *et al*. [118] ask “how do we know when enough administration is enough for an individual patient?” and suggest that perhaps protein/amino acid-sensitive markers in blood such as the protein mammalian target of rapamycin (mTOR) or general control non-derepressible-2 (GCN2), both can regulate protein and cell behavior responses and can reflect how a patient responds to protein therapy. Similarly, α −actin might be a useful marker to assess muscle protein degradation in humans or the nitrogen

balance (urinary) might be another tool to guide protein administration [118].

In this PhD project, the feasibility of two optical fibre sensors for protein and propofol is demonstrated through in vitro studies, giving insight for the potential use for biomarker detection in the ICU. For the case of protein detection the biotin-streptavidin interaction is used as model system to characterise the performance of a biosensor based on LPGs, since the properties of the biotin-streptavidin interaction are well known. Additionally, the biosensing experiments can be repeated for clinically relevant proteins by simply changing the immobilized ligand (instead of biotin) to target the analyte of interest.

2.2 Review of sensors and optical fibre sensors in the ICU and anaesthesia

There are a vast number of specialized devices which have been used in the ICU and during anaesthesia, including, pulse oximeters, ECG, arterial or venous blood flow monitors with catheters and mechanical ventilators, to name a few. This section discusses the sensors and optical fibre sensors implemented to measure parameters such as humidification during mechanical ventilation, respiratory rate (RR) during hospital care, protein or anaesthetic delivery during anaesthesia procedures and especially studies involving medical devices such as mechanical ventilators, ETTs, nasal cannulas and/or facemasks. Technological improvements are proposed for solving some of the challenges explained in section 2.1.

2.2.1 Humidity, temperature or respiratory rate (RR) sensors: The breathing monitoring in the ICU or in clinical studies during critical care using different technologies

This subsection presents a literature review of medical devices or sensors used for humidity-temperature, respiratory rate (RR) or breathing monitoring.

The intention of this subsection is to present sensors based on different technologies (Table 2.2 at the end of this subsection) rather than optical fibre technology. Some of the sensors presented here are commercially available and some others have been used in clinical trials in the ICU (or during anaesthesia).

(1) At present, a variety of monitors for the vital parameters of heart rate based on Electrocardiogram (ECG), arterial blood pressure and oxygen saturation (SpO_2 monitors) are available commercially and their use in the ICU is widespread. Respiratory monitoring in common use includes the clinical measurement (manual counting of chest movements) or thoracic impedance pneumography (TIP) using ECG electrodes [123], [124]. RR monitoring is also performed through measurement of carbon dioxide (CO_2) in exhaled air (capnography) in the ICU [125], [126]. Soto *et al*. [126] demonstrated the efficacy of capnography and TIP to detect apnea events (stop of breathing) during a study of anaesthesia care. However, both techniques and RR monitoring from pulse oximeters are prone to artefacts in their everyday use in the ICU. For instance, ECG electrode displacement, motion artefacts, coughing and sneezing all lead to inaccuracies and false alarms in the devices. Wiklund *et al*. [127] revised the frequency of apnea false alarms with TIP, capnography and pulse oximeters and they found 77% of occurrence with oximeters, 28% with TIP and 27% with capnography, most of them due to sensor displacement, motion artefacts, poor perfusion or a combination of these factors.

(2) Another example of a commercially available RR monitor is the facemask respiR8® (Anaxsys Technology Ltd) which provides continuous RR count performance from breath in critically ill patients. This device consists of a plastic facemask containing an electrochemical sensor for RR counts. Electrochemical sensors react with the gas of interest and produce an electrical signal proportional to the stimulation. In particular, Smith *et al*. [128]

produced a clinical study where they demonstrated the RR counting respiR8® results outside the pre-defined protocol limits of agreement of 95% of reading being within ±2 breaths/min when compared to a manual counting method (220 patients). In addition, respiR8® does not provide humidity and temperature measurements which are important parameters during critical care.

(3) Electronic noses (e-noses) is a developing technology increasingly investigated for breath analysis. An e-nose is a more generic term for a device that identifies specific volatile components and analyzes its chemicals to classify them [129]. Therefore, an e-nose can be an array of electronic sensors but includes a mechanism for pattern recognition, such as neural networks [129]. E-noses allow the recognition of VOCs from breath, but few of them have the potential to be employed in clinical practice such as monitors for isoprene [130], acetone [131], and ammonia [132]. The e-nose devices represent an attempt of simplification of GC/MS in identifying VOC profiles, but the cost of fabrication of the devices, their operation and data analysis still require improvement to satisfy demands of the simple use as healthcare systems. Leopold *et al*. [133] implemented a clinical study with patients mechanically ventilated to investigate the factors that influence the continuous measurements of an array of e-noses (Tin dioxide) and they tested the effects of humidity in the breathing circuit (at the T-piece, Fig. 2.2), patient-ventilator disconnections, nebulization of medication and changes in the ventilator settings. The major drawbacks of this e-nose array [133] were: (i) a time delay of 15 min was needed to reach steady state from the response of the e-noses to allow the sensors to adapt to a new event, thus breath-by-breath responsiveness was not obtained; (ii) all the e-noses showed cross-sensitivity to humidity; (iii) they were highly affected by ventilator disconnections (signal processing was required) and changes in individual VOC concentrations could not be identified.

(4) Quartz Crystal Microbalance (QCM) is another technique which is gaining popularity in recent years and it has been intended to be applied for human breath and respiratory pattern recognition [85]. QCM is a mass-sensitive transducer which uses a piezoelectric quartz crystal covered with two electrodes on both sides of the piezoelectric. A variant oscillatory potential is applied between the electrodes and any mass loaded onto one of the electrodes will change the frequency of oscillation related to the change in mass [134]. Selyanchin *et al*. [85] fabricated a new QCM prototype machine (NDK Ltd, Japan) proposed as a system with eight functionalized QCM electrodes for selective response to different breath chemicals (including humidity). They used a similar coating to this PhD research based on PAH and SiO_2 NPs with infusion of porphyrins in order to recognize inspiratory and expiratory patterns with high sensitivity and adequate response time. However, their system showed non-linearity for RH > 90 %, it needed a constant flow of air (0.4 – 0.7 L/min) inside the testing QCM chamber and its size is still not feasible for in situ monitoring during anaesthesia.

(5) Yagi *et al*. [135] combined a custom-made piezoelectric sensor affixed to the surface of the thyroid cartilage and a nasal cannula flow sensor (Pro-Tech ProFlow cannula, Sleep Lab Products, U.S.) to assess the coordination between the swallowing function and breathing with a group 11 volunteers and 10 patients with dysphagia. They developed the first bedside swallowing-breathing monitor designed to prevent aspiration during critical care, but the system was reported with a series of technical limitations: (i) only ca. 84% of full-automatic swallowing detection was achieved; (ii) the sensor is prone to artefacts from talking, snoring and (iii) electrical interference from the hospital theatre may further deteriorate the swallowing detection method.

(6) Bodini *et al*. [113] manufactured a low-power (using Li-Ion battery) wireless electronic system implemented to measure temperature and humidity during artificial ventilation. The module of sensors consisted of two

temperature thermistors (Pt1000) and a humidity capacitive sensor (P14 FemtoCap, response time of 3s). Wireless communication was performed through Bluetooth Low Energy connections and the control was implemented with a Labview interface platform. In a benchtop test using a mechanical ventilator, a Heat and Moisture Exchanger (HME) and a plastic balloon lung simulator, Bodini *et al*. [113] could measure AH (≈1.95 to 3.5 mg H_2O/L) and temperature before (ventilator side) and after (patient side) the HME. They demonstrated that the faster RR and higher minute volume in the ventilator produced higher levels of AH. Nonetheless, their study was not able to detect breath to breath change in humidity due to the slow response of the electronic sensor used.

(7) De Oliveira *et al*. [136] performed an in-vivo trial to characterize the AH levels and temperature in four clinical groups:

I. A control patient group ventilated without the usual heat wired tubes and without a HME.

II. A group with a heat wired Humidifier.

III. A group of patients with only a HME.

IV. A group with both a heat wired humidifier and a HME simultaneously.

They found that the latter group facilitated higher temperature and AH values (mean: 30.1 ^{0}C and 29.4 mg H_2O/L), closer to natural physiological values (avoiding damage to the tracheobronchial epithelia during anaesthesia). Similarly to this PhD project, De Oliveira *et al*. [136] measured RH and temperature at the Y-piece of the breathing circuit (Fig. 2.2) and between the HME and ETT for the fourth group; all the measurements were performed intermittently with a thermo-hygrometer (HM70, Vaisala Humicap®, Helsinki Finland). This hygrometer device used is a hand-held humidity and temperature probe meter with a low response time (between 17 s and 50 s) and diameter of 12 mm. Thus, in this study De Oliveira *et al*. [136] only could measure AH levels every 17 s without breath to breath characterization.

(8) Similar to the previous case, Tanaka *et al*. [114] monitored the optimal temperature and AH values at the Y-piece (Fig. 2.2) of the breathing circuit during a pediatric and adult ICU study. They found that the default humidifier settings are insufficient for adequate respiratory humidification with hypothermic patients at the ICU and demonstrated better and more stable values (mean: 37.5 ^{0}C and 36.9 mg H_2O/L) when the delivery of the humidified gas was controlled with a thermo-hygrometer (Moiscope, Tokyo Japan) as a closed loop system located at the Y-piece. However, the capacitive sensor used for humidity sensing had a response time of 3 s and it had to be taken out from the breathing circuit to dry when studies persisted longer than 10 minutes or when there was high condensation in the circuit.

(9) Zuur *et al*. [112] developed a novel device called an Airway Climate Explorer (ACE) which is proposed as an intra-tracheal temperature and humidity assessment tool to be used in laryngectomized patients [137]. This device consists of an air sampling catheter (5 mm diameter) with a heated sensor housing (40 ^{0}C) to avoid condensation in the embedded and custom-made temperature-humidity sensor (electric sensor RS92K -1.5 mm x 4 mm-, Vaisala Oyj, Helsinki Finland). The ACE sensor had a linear response in the clinical range of AH and response time (based on 1-1/e) < 0.5 s. Among other studies [138], [139], [140], this work represents a valuable tool for simultaneous measurement of temperature, humidity and RR from breath-by-breath traces directly in the human airway. Zuur and collaborators tested the influence of a HME on the tracheal climate of patients [137] and they found that the HME helps to increase AH from 21.4 mg H_2O/L to 24.6 mg H_2O/L, temperature decreased 1.6 ^{0}C and the ACE tool monitoring was fast enough for the assessment of end tidal intra-airway climate variations during normal breathing in patients. The limitations of this approach were: (i) the ACE central canal of the air sampling catheter is susceptible to obstruction by tracheal secretions and needs continuous inspections to prevent condensation of moisture within the device, air leakage around the catheter or movements of

the catheter tip during measurements; (ii) contact of the catheter tip with the trachea wall may produce irresistible coughing; (iii) the signal processing of the ACE signal underestimates the true peak-to-peak breathing values at higher RR frequencies; (iv) the response of the sensor when decreasing humidity is slower than the response to increasing AH, thus the true absolute in vivo humidity minima were considered overestimated by the ACE device; and (v) reproducibility in the serial fabrication process of the electrical sensor used is challenging and this would require a 2-point calibration for daily quality control.

Medical device or technique	***Limitations***
(1) TIP [123], [124] and Capnography [125], [126].	There is 28% of false alarms with TIP and 27% with capnography.
(2) respiR8 ® [128].	It does not measure humidity or temperature.
(3) E-nose [133]	Long time delay (15 min) of responsiveness.
(4) QCM system [85]	Non-linear when RH>90% and its size is still not practical in situ.
(5) Piezoelectric and air flow sensor [135]	The sensor function may be deteriorated by electromagnetic interference.
(6) Electronic wireless prototype [113]	AH was characterized in benchtop set-up but breath to breath was not detected.
(7) Thermo-hygrometers [136]	AH and temperature measured in-vivo intermittently but the response time of the device is 17 s.
(8) Thermo-hygrometer [114].	Low response time of the sensor (3 s) and highly affected by condensation (it had to be taken out for drying).
(9) ACE assessment tool [112], [137]	Air sampling catheter (5 mm) requires constant inspection to avoid obstruction from secretions, prevent condensation from moisture, air leakage around the catheter and motion artefacts (contact with trachea wall). Response time is slower when AH is smaller producing overestimation.

Table 2.2: Medical devices or techniques (non-optical) used in critical care and their limitations.

In summary, there have been developments to control humidity and temperature delivered from mechanical ventilators used in the ICU. However, all the electronic technologies are prone to electromagnetic interference in the theatre room, they cannot be used during MRI and they have a long response time. The ACE assessment tool has been the fastest option (response time < 0.5 s) but the custom-made electronic sensor still requires improvements in repeatability of fabrication and reduction in the faults that produce artefacts.

2.2.2 Breathing monitoring with optical fibre sensors

This subsection presents humidity or breathing monitors using optical fibre sensing technology (Table 2.3 at the end of this section) including some examples with optical fibre sensors which have measured RR and humidity directly from breaths and some others which have measured respiration through the torso or abdomen movements.

(10) Kang *et al*. [141] developed a Fabry-Pêrot approach by coating the tip of an optical fibre with poly(diallyldimethyl ammonium chloride)(PDDA) and polymer PS-119; this sensor showed a fast response to detect breath-by-breath humidity for normal breathing rates of 36 breaths/min (intended to be applied with infants) and also for tachypnea conditions (66 breaths/min). Kang *et al*. [141] demonstrated the performance from a single experiment by placing the sensor next to the nose of a human subject and suggested its potential use for infant monitoring.

(11) Favero *et al*. [142] implemented a PCF spliced at the end of a SMF without the use of any coating for breathing monitoring. Sealing the voids of the PCF probe produced better reproducibility and the overall sensor probe was packaged and protected inside a glass tube which in turn was shielded within another metallic tube (inner/outer diameters 1.7/3.0 mm). In a single

experiment with a human subject, this sensor was tested in a facemask and detected respirations at 110 breaths/min or 135 breaths/min. However, the absence of a nano-thin film does not allow the measurement of humidity levels.

(12) Morisawa *et al*. [143] developed a novel microphone system based on multiple plastic optical fibres (POFs). Although this sensor was designed for the recognition of the pronunciation of vowels, the cladding of the POFs were functionalized with polyvinyl pyrrolidone (PVP) and polyvinylidene difluoride (PVDF) to create fast sensors (rise time 0.8s) with the ability to detect different breathing patterns corresponding to the different pronounced vowels (above 93% of recognition rate). The limitations to overcome from this preliminary study with five subjects were: (i) a complex algorithm for voice recognition is needed; (ii) the performance of the recognition algorithm is affected by slight variations between the sensitivities of five POFs compounding the system, thus reproducibility during the fabrication of the humidity POF sensors with high sensitivity is desirable.

(13) Akita *et al*. [144] fabricated a hetero-core optical fibre sensor to monitor RH in a facemask. The sensor consisted of splicing MMF- SMF (2 cm) -MMF consecutively and the SMF section was coated with a hygroscopic polymer using the Layer-by-Layer method. In this study, Akita *et al*. [144] demonstrated a breath analysis software application developed in Labview where it was possible to measure breathing depth (amplitude of the cycle) and RR in real time. Additionally, their sensor could measure the “breathing status” classified as heavily breathing, normal breathing or stop of breathing (apnea), all tested during sleeping conditions. However, the sensor calibration with ancillary devices was not performed to measure AH or RH and the authors did not specify the number of volunteers measured and the type of coating used for specificity to measure humidity.

(14) Massaroni *et al*. [16] proposed a coated FBG sensor for providing closed loop control to the heated wire humidifiers frequently used during mechanical ventilation. The FBG with highest sensitivity (0.14 nm/%RH) was coated with agar and presented low hysteresis (<10%); the temperature measurement was performed with another FBG insensitive to RH (acrylate coating). Likewise the issue mentioned in previous cited references (bullet points ***7*** and ***8***), Massaroni *et al*. [16] have pointed out that the simple control strategy implemented in commercially available heated wire humidifiers, which is based on maintaining a constant gas temperature at the outlet of the humidification chamber, is not always able to provide optimal gas conditioning during mechanical ventilation. In analogy to this PhD research, Massaroni *et al*. [16] suggested their coated FBG sensor as a suitable application in situ as they calibrated the sensor from 20 %RH to ca. 100%RH, covering steps changes in the high RH range expected during critical care. Nonetheless, their work did not show breath to breath measurements of humidity and temperature in the experimental set-up implemented.

(15) Similar to the previous work, D'amato *et al*. [145] proposed the direct monitoring of the humidified air from a mechanical ventilator using an agarose-coated FBG sensor to obtain a better control of the gas conditioning during artificial ventilation. The sensor, also calibrated from 20 %RH to ca. 100%RH, showed less sensitivity (6.9 pm/%RH) than Massaroni *et al*. [16], demonstrated detection of big step changes of humidity but not breath to breath tracking response.

(16) Pressure sensors based on Fabry-Pêrot configurations at the tip of optical fibres are commercially available, for instance, FISO Technologies has developed the FOP-MIV for medical applications [146]. Intracranial pressure has been attempted to be monitored with optical fibre sensing technology: Innerspace Inc. produced a Fabry-Pêrot-based pressure sensor and Camino Laboratories realized an intensity-modulated based approach [147]. Arterial or

aortic invasive measurements have been possible with Fabry-Pêrot type optical fibre sensors developed by Enterprises, LLC. or Arrow International, Inc. [147]. Nonetheless, only Sondergaard *et al*. [148] have tested the application of a Fabry-Pêrot type optical fibre air pressure sensor (manufactured by Samba Ltd.) to monitor intra-tracheal pressure and RR by placing the sensor in the inner lumen of a pediatric ETT. The size of this type of approach was advisable for monitoring in the pediatric ICU without flow resistance under different modes of ventilation and it was capable of giving correct tracheal air pressure readings unhampered by motion artefacts or secretions in the tube.

(17) Ivanovic and Petrovic [149] measured respiratory volumes through the use of LPGs in 25 healthy volunteers; the study consisted in successfully using a single LPG curvature sensor attached to the subject's thorax for respiration monitoring and it was proposed as a triggering decision system (vs pneumatic sensors integrated in ventilators) to detect a patient's own respiratory effort, assist spontaneous breathing and avoid patient-ventilator dys-synchrony. They found a response breath triggering time between the gold standard (NAVA, Neurally Adjusted Ventilatory Assist) and 200 ms before airflow sensors. However, they obtained large standard deviations around the mean delay values and errors induced by the heart beat registered in the LPG signal. This field of research has been appointed as a main topic for support of mechanical ventilation, especially with patients suffering acute respiratory distress syndrome (ARDS) [150]. Martin-Loeches *et al*. [150] predict that "in 2035, closed loop MV [mechanical ventilation] will probably be very advanced and asynchronies could be reduced by machine learning systems and computerized close loop systems" and the control of respiratory effort will be needed to prevent lung injury during mechanical ventilation.

(18) Allsop *et al*. [71] implemented a series of in-line curvature LPG sensors on a garment used to monitor RR from thoracic or abdominal movements. Nine

LPG sensors were encapsulated in silicone rubber with low temperature cross-sensitivity, multiplexed and interrogated with five DFB lasers. A 5X5 fibre coupler and five photodetectors were needed to operate the overall system. The garment with sensors was tested in six volunteers and demonstrated to be qualitatively in accordance with a commercial spirometer to measure torso volume change due to respiration.

(19) Massaroni *et al*. [69], Zawawi *et al*. [151] and Krebber [70] have published sensor reviews containing three types of optical fibre structures: FBGs, fibres with microbending/macrobending configurations and intensity modulated fibres; all aimed to be applied as wearable systems to measure RR. Apart from being non-invasive, the main metrological advantage of all these approaches is that they are MRI compatible. The main future challenge that optical fibre wearables should address is the robustness of the textiles against stress and washing cycles and their sterilizability [69]. In general, series of FBGs are able to measure small strains due to their high sensitivity but interrogation systems are expensive and need to have a good multiplexing detection performance [69], [70]. Bending configurations and intensity modulated fibres are straightforward to interrogate and involve lower cost and more compact components, but they are less sensitive than FBG sensors and they are more frequently used to monitor large movements (e.g. abdominal movements) [151], [70].

Bullet points ***17*** to ***19*** presented several optical fibre sensors implemented as wearable systems in garments, sensing harnesses or elastic bandages aimed to measure respiration from thoracic or abdominal movements. All these sensors have found a niche of application in industry [69], [147] and most of them have been developments for the European projects i-Protect (intelligent PPE system for personnel in high-risk and complex environments) and OFSETH (optical fibre sensors embedded into technical textile for healthcare) [70].

In addition, all the approaches described previously from ***(17)*** to ***(19)*** differ from the sensor proposed in this PhD research for breathing monitoring as they were implemented to directly measure respiration movements; the method followed in this project is more similar to the references cited in ***(10)*** to ***(16)***, i.e., the measurement of either RR or humidity from the breath directly, but only Massaroni *et al*. [16] and D'Amato *et al*. [145] identified (as in this research) the real application of optical fibre sensors for a better closed loop control in conditioning the humidified gas delivered by mechanical ventilators during critical care or anaesthesia. Similarly, previous references cited in subsection 2.2.1 in bullet points ***(6)*** to ***(8)***, the authors of these investigations identified the same clinical challenge but their proposed devices were not able to measure breath-by-breath response using different technologies. Finally, Massaroni *et al*. [16] have mentioned that "Although several groups of research proposed fibre optic-based systems for simultaneous measurements of temperature and humidity using different principles of work, only Hernandez and coauthors [this PhD research] focused their attention on the measurements of these parameters in mechanical ventilation".

Medical device or technique (breathing)	***General comments***
(10) Fabry-Pêrot coated with PDDA/PS-119 [141]	Respiration test in a single experiment placing the sensor near the nose of a human subject. It was not calibrated to measure RH or AH.
(11) PCF spliced to a SMF [142]	Measures RR in facemask but not humidity and temperature.
(12) POF system [143]	Reproducibility during fabrication with high sensitivity is desirable for the application.
(13) Hetero-core OFS [144]	Calibration was not performed to measure RH or AH. The authors did not specify which coating was used to measure humidity.

Table 2.3: Optical fibre sensors used for breathing monitoring.

Medical device or technique (respiration volumes as wearables)	***General comments***
(14) FBG coated with agar [16]	Not applied to measure breath-by-breath changes in humidity.
(15) FBG coated with agarose [145]	Not applied to measure breath-by-breath changes in humidity.
(16) Fabry-Pêrot interferometric [148]	RR can be measured through pressure monitoring with the OFS. Intra-tracheal pressure was well characterized inside the lumen of a pediatric ETT. Humidity was not measured.
(17) curved LPG [149]	Single LPG sensor attached to subject's thorax for respiration monitoring. Heart beats and motion artefacts interfered with the LPG signal.
(18) LPGs multiplexed [71]	Novel system but still needs to be made smaller and portable for enabling unobtrusive ambulatory monitoring of RR.
(19) FBGs [152], [153] Macrobending fibres [154] Microbending fibres [155] Intensity-modulated [156]	Optical fibres used as wearables is at forefront of current research; one application is to measure RR. Bending configurations and intensity modulated fibres are straightforward to interrogate and involve lower cost and more compact components. However, they are less sensitive to strain than FBG sensors.

Table 2.3: (Continuation) Optical fibre sensors used for breathing monitoring.

2.2.3 Depth of General Anaesthesia and anaesthetic delivery monitoring

There are sensors aimed to monitor the Depth of General Anaesthesia (DGA monitors) which are mainly based on Electroencephalography (EEG) in conjunction with processing closed-loop algorithms and its feedback outputs such as the Bispectral Index as a surrogate for evaluating patient unconsciousness [95], [157]. The different types of DGA monitors have been clinically tested and are partially acceptable as closed-loop control systems during anaesthesia [95], [100]. However, the future improvements need to

combine an instrument capable of giving adaptive control feedback about the real anaesthetic delivery and actual concentration of the anaesthetic in the bloodstream or from the breath of anaesthetized patients, i.e., closed-loop control of anaesthesia should not be only dependent on pharmacokinetic/pharmacodynamic algorithms [98] or with single values of the bispectral index [100], [120]; several clinical studies have demonstrated the correlation between the anaesthetic concentration taken from breath samples and the concentration from the plasma [120], [121], [119].

In this subsection, Table 2.4 summarizes recently published sensors or medical devices used or proposed for measuring actual concentration of propofol in blood. Table 2.5 presents those devices or sensors aimed to measure propofol concentration from the breath of anaesthetized patients. The desired clinical concentration of propofol in plasma ranges from 1 to 10 μg/ml [158] and the expected range of propofol in breath is from 2 to 32 ppb [119], [159]. This subsection briefly explains the advantages and disadvantages of each of the approaches or studies found in the literature aiming to track propofol in vitro or in vivo from induction to the end of anaesthesia.

(20) *Lab-on-chip spectrophotometric device using optical fibres* [160].- This work performed a sequential injection analysis of propofol in plasma samples through a flow cell. There is azo-coupling derivatization of propofol with diazonium salt reagent before passing the samples through the cell for absorbance analysis with standard broadband light and spectrophotometer device. The azo-coupling derivatization was simple, fast, and easy to perform with inexpensive reagents. The derivatization produced a convenient shift in the absorbance of propofol from the UV (271 nm) to visible (483 nm) which avoids absorbance interference from endogenous substances in plasma. The sequential injection system still needs improvements in sensitivity and rapid detection of azo-coupled samples.

(21) *Optical system using optical fibres and disposable imprinted solid-phase extraction (SPE) column* [90].- On-line detection of propofol in simulated whole blood samples and using fluorescence measurements after reaction of propofol with Gibb's reagent. The disposable imprinted SPE column was prepared (long process) with a traditional imprinting method of propofol and, before fluorescence measurements with a xenon lamp and photomultiplier tube, the whole blood samples were eluted with MetOH through the imprinted-SPE column. This system showed rapid propofol detection in vitro (5 min) with good specificity, but the system needs to use several optical components such as filters and collimators to perform the fluorescence measurements.

(22) *Lab-on-chip using micro-optical components and disposable microfluidic biochip* [158]. - The microfluidic biochip with molecularly imprinted polymer for optical detection of anesthetic propofol is disposable and it is encapsulated in a plastic case (448 cm^3) containing microelectronics, laser diodes on top of the biochip and photodetectors at the bottom part of the biochip. First, propofol (98% dissolved in MetOH) is injected through the microfluidic imprinted biochip (1 min), then the Gibbs reagent is injected through the microfluidic system and, after 1 minute, the absorbance measurement (655 nm) through the biochip is performed. This system is more compact in size, it uses smaller propofol and reagent volumes and its response is faster than the works explained before in ***(20)*** and ***(21)***. However, the interference from endogenous substances in real plasma still needs to be investigated and the limit of detection (LOD) with this device was 0.25 ppm which is outside the clinical range.

(23) *Prototype system for measuring blood plasma levels of propofol using SPE methodology, coupled with colorimetric (Gibbs reagent) and spectrometric techniques* [161].- The total time required for the analysis of the sample was 4.5 min including preparation and absorbance measurements performed at 595 nm using a conventional tungsten-halogen lamp and

spectrometer. The prototype was tested with patient blood samples (lysed with water and filtered) and the authors pointed out the non-specificity of this device for propofol, i.e., the SPE cartridge used did not discriminate between phenolic substances present in clinical specimens (it is not molecularly imprinted).

(24) Pelorus 1000 from Sphere Medical (Cambridge, UK) [162] is a commercial device for analyzing propofol concentrations in whole blood and it combines some characteristics of the previous study reported in ***(23)***. The concentration analysis takes 5 min without requirement for sample preparation and the device requires 0.7 ml of sample blood volume which is diluted and lysed internally. Propofol is extracted from the lysed blood using SPE (non-imprinted) and the presence of the anaesthetic in the extract is detected through absorbance spectroscopy after reaction with Gibbs reagent. Similarly to McGaughran *et al*. [161], Liu *et al*. [162] identified the non-specificity of the SPE cartridge in the system and they tested the presence of 18 exogenous and endogenous cross-interference compounds; in their study, only conjugated bilirubin was found to interfere with propofol detection.

(25) All the previous works cited from ***(20)*** to ***(24)*** showed slightly different methodologies for detecting propofol concentration from blood samples; the common characteristic was that all were tested in vitro conditions and all suggested to use the approach as an on-line monitoring tool for propofol analysis during anaesthesia, i.e., a type of closed-loop control technique (5 min of processing time) that can be combined with TCI pumps or TIVA. Kivlehan *et al*. [163] proposed a more portable device for the same purpose, consisting of a membrane-coated electrochemical sensor embedded onto the surface of an intravenous catheter to test concentrations of propofol from human blood samples. Propofol can be oxidized electrochemically and sensitivity was increased when the working electrode (carbon, Au, Ag or Pt) was coated with a polyvinyl chloride (PVC) membrane. The electrochemical sensor showed good stability, responded in less than 10 s and the LOD was

80 nM when calibrated with HPLC in propofol aqueous samples. However, the minimum detected concentration was 1.25 μM when propofol was spiked in human whole blood and injected through the sensor.

All the works explained from bullet point ***(20)*** to point ***(25)*** were evaluated in vitro conditions. However, all of them have the potential for in vivo monitoring. In comparison, the latter approach seems the most feasible in terms of design for a closed-loop monitoring and quantification of propofol levels in blood using the electrochemical sensor embedded on the outer surface of an indwelling catheter and working in combination with TCI pump or TIVA protocols. Nonetheless, the use of an electrochemical sensor in situ would prevent its use during MRI and would be prone to other types of electromagnetic interferences in the operating room.

Determination of propofol in vivo is still most commonly performed using HPLC analysis from blood samples. HPLC is a very precise technique, but requires expensive and bulky device (requiring intensive training for the operator) and is time-consuming for sample preparation and analysis (> 1 hr). Nevertheless, the methods and commercial device Pelorus 1000 presented before in this subsection could easily replace HPLC for this niche of application in a more cost-effective manner.

Medical device or technique Propofol in blood or aqueous solutions	***General Comments***
(20) Lab-on-chip spectrophotometric device using optical fibres [160]. *Validated with UV-Vis spectroscopy.	Absorbance measurements at the visible range (483 nm) after reaction of propofol with diazonium salt via sequential injection in the lab-on-chip cell. System still needs improvement in sensitivity and rapid detection.

Table 2.4: Medical devices or techniques implemented to measure propofol in blood.

Medical device or technique Propofol in blood or aqueous solutions	***General Comments***
(21) Optical system using optical fibres and disposable solid-phase extraction (SPE) column [90]. *Validated with HPLC.	Fluorescence measurements after reaction of propofol with Gibb's reagent. Use optical filters-collimators and long preparation of traditional molecular imprinting of propofol on a solid phase extraction sorbent.
(22) Lab-on-chip using micro-optic components and disposable microfluidic biochip [158]. *Validated with UV-Vis spectroscopy.	Small and disposable microfluidic biochip with molecularly imprinted polymer for optical detection of anesthetic propofol. Still needs investigation in real plasma samples and the LOD obtained was outside the clinical range.
(23) Prototype system using SPE, coupled with colorimetric and spectrometric techniques [161]. *Validated with HPLC	Absorbance measurements were performed at 595 nm using conventional tungsten-halogen lamp and spectrometer. The prototype was tested with patient blood samples, but the device does not have specificity for propofol.
(24) Pelorus 1000 [162] *Validated with HPLC	Commercial device using colorimetric techniques, SPE and coupled with absorbance spectroscopy. Non-specificity still needs investigation.
(25) PVC-coated electrochemical sensor [163] *Validated with HPLC	Sensor embedded onto the surface of a catheter to test concentrations of propofol from human blood samples. It still needs clinical verification in vivo.

Table 2.4: (Continuation) Medical devices or techniques implemented to measure propofol in blood.

In analogy to HPLC for analysis of propofol in blood, GC-MS has been the most frequently used technique for highly accurate analysis of propofol in gas phase [164] and this method has endured as an off-line monitoring tool which is also expensive, bulky and time-consuming for analysis. Therefore, a faster, easier, less expensive and more compact method for measuring propofol from breath samples is needed. This is a current topic of research due to the fact that some investigations [119], [120], [121] have demonstrated the correlation

between the concentration of propofol in blood and the measured concentration from the breath of anaesthetized patients. Table 2.5 summarizes all the clinical studies using bulky devices (except the last one) for the measurement of propofol from breath. Most of them have verified the plasma concentration with HPLC and while some of them are considered for on-line monitoring, some others are exclusively off-line monitoring tools. In analogy, a more compact device capable of detecting propofol in gas phase would be also suitable for closed-loop control during anaesthesia for calculating levels in blood as they have been shown to be correlated.

Medical device or technique Propofol from breath	***General Comments***
Proton transfer reaction mass spectrometry (PTR-MS) [120]. *Validated with HPLC.	New device that measures Volatile Organic Compounds (VOCs) at low concentrations and real time. On-line continuous monitoring in-vivo.
GC-MS and HPLC [119], [164]	Gas sampling made with Tenax tubes and tested in GC-MS after thermodesorption. Off-line monitoring discontinuous in-vivo.
Ion-molecule reaction mass spectrometry (IMR-MS) [121]. *Validated with HPLC.	Measures organic and inorganic compounds from head space gas sampling and plasma. On-line and off-line monitoring in-vivo during mechanical ventilation.
Membrane inlet-ion mobility spectrometry (MI-IMS) [165]. *Validated with HPLC.	Gas samples analysis using bispectral index (EEG) during anaesthesia. On-line and off-line monitoring in-vivo.
GC-MS with Headspace Solid-Phase Microextraction.	Gas samples. On-line and off-line monitoring in-vivo.
Photoacoustic spectroscopy in the UV region [166].	On-line monitoring in-vitro. This is the approach most compact in size.

Table 2.5: Medical devices or techniques implemented to measure propofol in gas phase.

2.3 Aims and objectives of the research project

The overall aim of this PhD is to develop and apply OFS technology in critical care equipment or during anaesthesia with a view to ultimately applying optical fibre sensors as a key component of future automatic closed-loop individual systems needed to improve patient care in the ICU. This includes the discussion and evaluation of individual optical fibre sensors chemically functionalized, characterized and implemented to improve the control of the humidification and temperature of air delivered to patients during mechanical ventilation in the ICU, respiratory rate control, and measurement of the concentration of biochemical parameters such as anaesthetic propofol and proteins.

Attention is given to the fact that this PhD research is a pioneering implementation of an OFS for a closed-loop control of gas conditioning (humidity and temperature) and respiration monitoring during invasive or non-invasive ventilation. In addition, this work aims to contribute to fulfill the gaps explained for controlling and monitoring delivery of anaesthetic propofol and protein at the ICU, i.e., a more portable, faster and cost-effective device for the detection of these biochemical parameters during critical care, as the literature review has evidenced.

Overall, the care of patients in the ICU and treatment of anaesthetized patients involves the challenges explained in Section 2.1. Amongst other tasks, the individual fibre-optic engineering solutions to those clinical challenges could be combined into comprehensive controllers for a fully integrated and novel care management when all the sensors are embedded in ICU equipment for multi-sensing such that the fabrication of sensorised facemasks, ETTs, nasal cannulas or breathing circuits for mechanical ventilators will be feasible.

There are several specific objectives to reach the general aim of the PhD. These are:

(1) To understand how an optical fibre sensor works, obtain an idea of the current status and future trends with optical fibre sensors for healthcare applications, and grasp some of the current clinical challenges discussed over a period of three years with anesthesiologists and collaborators of this research from the Nottingham University Hospitals NHS Trust: the possibility to develop closed-loop controls with OFS technology for monitoring humidity, temperature and RR during invasive or non-invasive ventilation; the need of protein control delivery in the ICU and control delivery of anaesthetic propofol during anaesthesia preferably with non-invasive methods. All these challenges are supported through the literature review process.

(2) To explain the working principle and fabrication of the four types of optical fibre structures used in this research project: Fabry-Pêrot tip, FBG, LPG and U-shaped fibre.

(3) To characterize the nano-thin films used for functionalization of optical fibre sensors specifically implemented to monitor humidity, protein and propofol. The characterization is performed with ancillary methods such as SEM, TEM, UV-Vis spectroscopy and FTIR. Optimization parameters of nano-thin film deposition is given for each coating proposed, for instance, the number of consecutive layers applied to create the film or deposition times to obtain different sensitivities.

(4) To calibrate a humidity OFS and FBG against a commercially available capacitive sensor and thermocouples. Investigation of the impact in sensitivity of the number of layers deposited for functionalization is disclosed. Test of sensor in a benchtop set-up with a Lung Ventilator Analyzer is presented. Additionally, testing of the sensor in an animal study corroborates its efficacy and preliminary results in a study with volunteers will support its application for a clinical protocol.

(5) To investigate whether an OFS can be developed for monitoring biochemical parameters such as propofol and protein at the sensitivity required to meet the real need application during anaesthesia. A widely

studied and well known protein interaction between biotin and streptavidin will be explored as a proof of concept of the optical fibre biosensor for protein detection, the selectivity to other proteins can be tailored by changing the nature of the ligand, making the approach used a generic platform for biosensor development.

(6) To perform preliminary investigations into some of the other clinical challenges explained in section 2.1 such as detection of bacteria and monitoring of the pressure exerted by the cuff of an endotracheal tube using a contact pressure OFS. These results will be only explained in the Appendix of this work.

2.4 Summary

This chapter has presented the unmet clinical challenges to overcome in this research. It has introduced the general concept of closed-loop systems needed to improve and automatize as much as possible the critical care of patients. The last part of this chapter has disclosed the specific literature review of sensors and optical fibre sensors in the ICU. This review supports the aim and objectives to follow in this research.

Chapter 3: Fabrication and characterization of optical fibre sensors

This chapter serves as a methodology section for the fabrication of the optical fibre sensors developed in this research. It firstly introduces a general description of the characterization methods used to study the properties of the nano-films fabricated for the functionalization of optical fibres. It continues with a description of fabrication methods of the LPGs and FBGs used in this project (via UV laser beam). Surface chemistry techniques or processes for functionalizing optical fibres and their application as biosensors are presented afterwards. Here, three main methods were used to functionalize optical fibre surfaces: (i) the Layer-by-Layer (LbL) deposition method; (ii) Liquid Phase Deposition (LPD) of titanium dioxide (TiO_2) with molecular imprinting of host-guest molecules, and (iii) sol-gel deposition of mesoporous silica nanoparticles (MSNs) and TiO_2 with molecular imprinting of guest molecules. The second purpose of this chapter is to present the results from the spectroscopic and imaging techniques for the characterization of the materials developed as bio-sensing films.

3.1 Spectroscopic and imaging methods for nano-film characterization

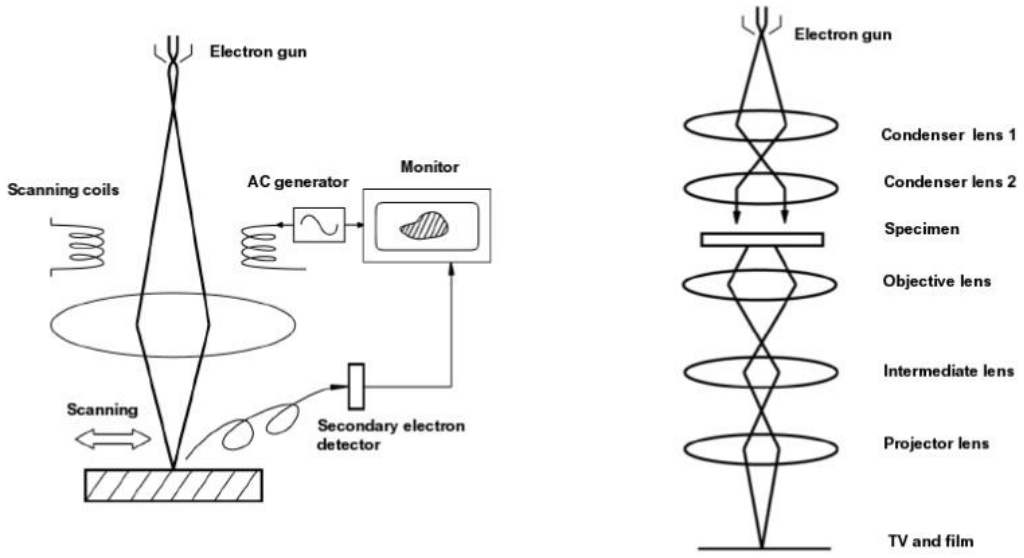
Regarding the imaging techniques, the Nanoscale and Microscale Research Centre at the University of Nottingham provides Scanning Electron Microscope (SEM), Transmission Electron Microscope (TEM) and spectroscopy research facilities. However, the other spectroscopic techniques such as Fourier Transform Infrared (FTIR), Ultraviolet-Visible (UV-VIS) spectroscopy and Nuclear Magnetic Resonance (NMR) spectroscopy were measured and used in the human odour bio-sensing laboratory at the University of Kitakyushu (Faculty of Environmental Engineering) as part of an academic collaboration which I performed from February 2016 until October 2016 during my 3rd year

of PhD. All these analysing methods will be briefly explained in the next four subsections.

3.1.1 Scanning Electron Microscopy (SEM) and Transmission Electron Microscopy (TEM)

In this research, SEM and TEM microscopy techniques were mainly used to obtain images of the deposition onto optical fibres of thin-films constructed of Poly(allylamine hydrochloride) (PAH) and SiO_2 nanoparticles (NPs). These techniques were also employed for visualizing Au shell NPs onto SiO_2 NPs as the improvement for protein biosensing using optical fibre sensors.

SEM and TEM are spectroscopic and imaging techniques that employ a focused and high-energy beam of electrons directed to the sample of interest to scan and investigate its structure (Fig. 3.1). Briefly, as the electrons interact with the sample atoms will emit other electrons (secondary electrons or inelastically scattered electrons in SEM), elastically scattered electrons in TEM and also X-rays [167]. The detection of these secondary electrons and elastically scattered electrons allows visualizing the topography while the X-rays analysis gives information about the chemical composition of the sample [167], [168], [169]. These imaging techniques are capable of visualizing sample structures with micro- and nano-scale resolution [168], and in this project a Philips FEI XL30 SEM and a JOEL 2000FX TEM have been used both for the purpose of visualizing some of the nano-films deposited on the surface of optical fibres to be used as biosensors (sections 3.3.1 and 3.3.2). TEM can achieve higher spatial resolution down to the scale of several Angstroms (~0.19 nm) as compared to SEM [168].



(a) (b)

Figure 3.1: Basic schematics and ray diagrams of (a) SEM and (b) TEM (adapted from [169]).

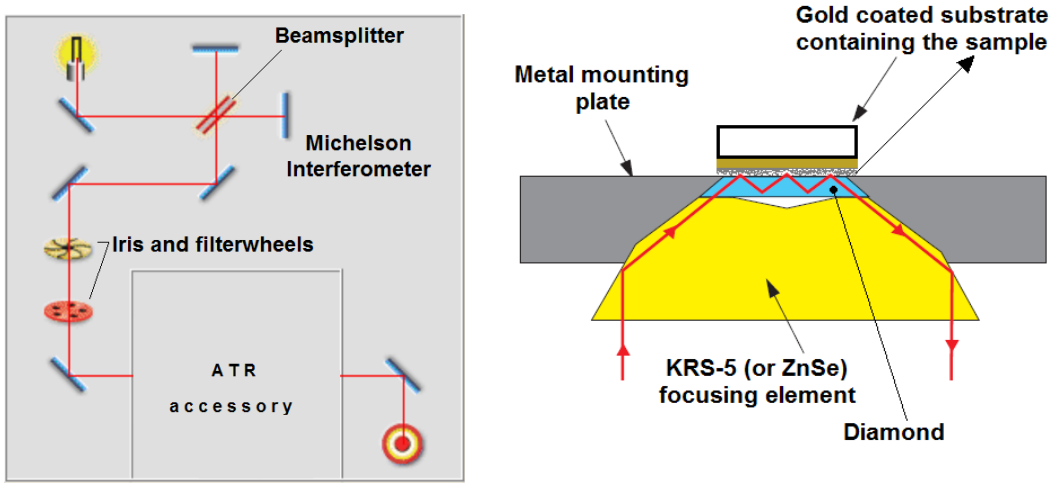
Both TEM and SEM require sample pre-treatment before5 it can be characterised. TEM requires specialized grids and thinner samples (from ~0.19 nm to ~100 nm) than those normally visualized in SEM. In TEM, the sample placed on the grid is dispersed in ethanol and dried before introducing into the specimen port for characterisation. SEM needs the sample to be coated with a thin (5 nm for the samples reported in this research) platinum film using a sputter coater to allow electrical discharge of the sample surface during the interaction with the electron beam.

3.1.2 Fourier Transform Infrared (FTIR) spectroscopy

In this research, an FTIR spectrometer (Spectrum 100, Perkin Elmer) was used in an Attenuated Total Reflectance (ATR) mode for characterizing the differences between two thin-films based on TiO_2: one made of pure TiO_2 and other imprinted with organic molecules. This type of spectroscopy is frequently used as the workhorse of chemical analysis for molecular detection. Fig. 3.2a shows the basic beam propagation inside the spectrometer until the

photodetection system and the smaller square margin presents the stage containing the ATR accessory (Fig. 3.2b details the type of ATR used). In Fig. 3.2a, the laser beam (633 nm) is directed to a Michelson interferometer and the interferogram obtained is passed through an iris and a filterwheel to control the convergence and resolution, and the filter can define the regions of the spectrum of interest. Finally, the interferogram is passed through the ATR accessory and detected in the photodetection system to be processed in the Fourier domain.

The ATR spectroscopy uses the phenomenon of total internal reflection which occurs in the diamond crystal and enables the measurement of the vibrational modes from the atoms of the sample placed between the crystal and the gold coated substrate (Fig. 3.2b), i.e., the laser radiation undergoes total internal reflection through the crystal where an evanescent wave protrudes 1.66 μm beyond the diamond [170] and penetrates the sample that is placed on its surface. Part of this radiation is absorbed by the sample which is produced from the vibrational modes of the atoms due to the optical field of a surface plasmon originated from the gold surface [171], [172].



(a) (b)

Figure 3.2: Basic schematics for (a) beam propagation inside the spectrometer (Spectrum 100 Perkin Elmer) and (b) the universal ATR accessory based on diamond and a focusing element. The silicon wafer substrates used were coated with gold.

The universal ATR accessory employs a Dicomp™ crystal containing a focusing element made of zinc selenide (ZnSe) or Thallium-bromoiodide (KRS-5). The focusing element provides interfacing optics for the laser radiation through the flat surface and it has a cavity at the centre of its surface in contact with the diamond to allow reflection within the blue diamond depicted in Fig. 3.2b. The radiation undergoes total internal reflection in the diamond and exits the crystal at a point opposite to the point of entry. The universal ATR accessory was used in this project because it is ideal for the analysis of solids, liquids, pastes or gels, and works over the spectral range of interest for the majority of applications [170].

3.1.3 Ultraviolet-Visible (UV-Vis) spectroscopy

This technique was applied as a complementary method to FTIR for characterizing the differences between two films based on TiO_2: one pure TiO_2 film and another with imprinted organic molecules. In this research, this spectroscopy technique was applied using a UV-Vis spectrophotometer (V-570 JASCO) to confirm the specific absorbance wavelengths of the organic materials hosted onto the TiO_2-based films. The spectrophotometer uses a dual beam system with single monochromator and halogen lamp as a light source (Fig. 3.3). It alternates the light between the sample optical path and a reference optical path (containing blank measurements) using an optical chopper at a speed that minimizes medium or light source drifts [173].

In this research, the nano-sensing films developed were deposited onto transparent silica glass substrates (well washed in ethanol and ultrapure water) and tested in the sample optical path. Transparent glass substrates, washed in ethanol and water, were also used as a reference for blank measurements.

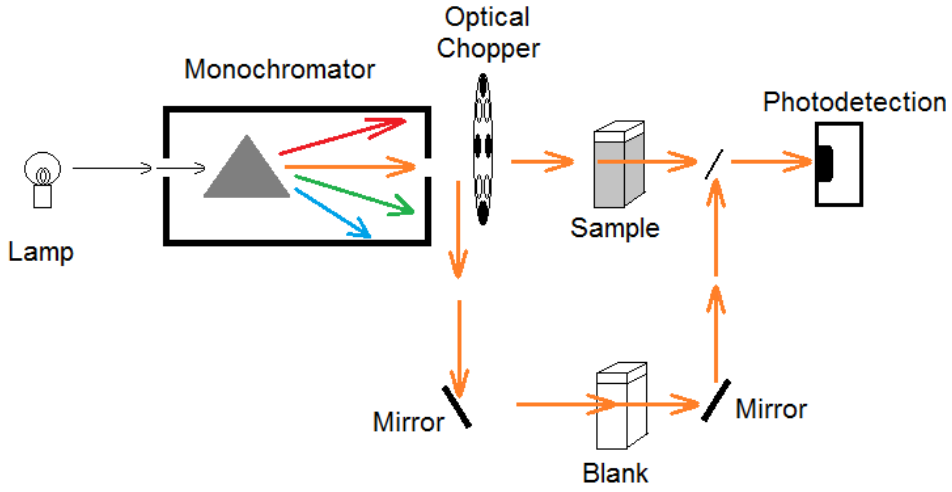


Figure 3.3: Basic schematic of the working principle of a dual beam spectrophotometer.

3.1.4 Nuclear Magnetic Resonance (NMR) spectroscopy

NMR spectroscopy is a powerful method for the elucidation of molecular structure and to study inclusion complexation phenomena between host and guest molecules at the atomic level [174]. In this research, NMR spectroscopy was used to demonstrate the host-guest inclusion between beta-cyclodextrin (β −CD, host) and propofol (guest molecule). The NMR spectrometer used was a 500 MHz FT-NMR (JEOL USA Inc.). Fig. 3.4 shows a basic schematic of the instrumentation to measure NMR signals from liquid samples dissolved in commonly used solvents (deuterium oxide D_2O, deuterochloroform $CDCl_3$ or deuterated dimethyl sulfoxide DMSO-d_6). Preparation of the sample is important to allow magnetic field homogeneity during stimulation (Fig. 3.4) through the sample placed in the NMR tube, so any factor disturbing field homogeneity will have a detrimental effect on spectrum lines shape [175]. The solvent used to dissolve the host-guest molecules used in this research was 10% (v/v) DMSO in D_2O.

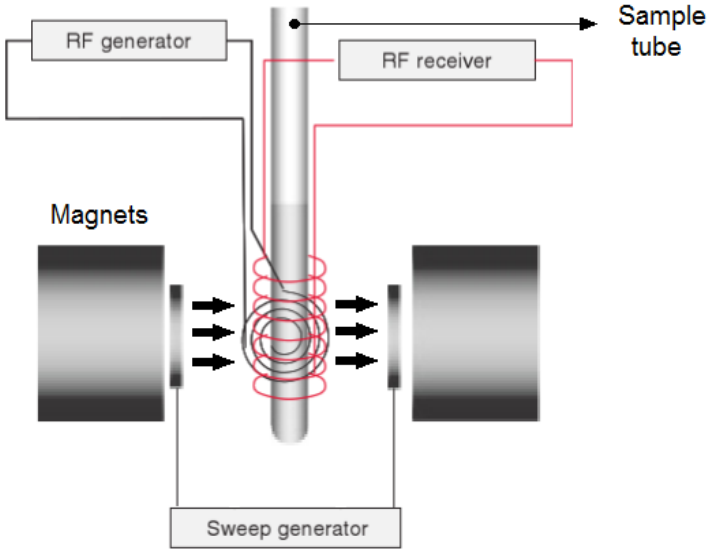


Figure 3.4: Schematic of a continuous wave NMR spectrometer (modified from [175]). The RF receiver is usually connected to an amplification stage and processed in a PC.

Briefly, the liquid sample is placed between the pole pieces of a magnet (permanent or electromagnet) surrounded by a cross coil arrangement of a transmitter and receiver coils (Fig. 3.4). When the combination of magnetic field and frequency matches the resonant frequency of each nucleus, energy[4] is emitted and captured by the receiver coil and plotted against frequency in order to obtain the NMR spectrum [175]. Continuous wave technology (Fig. 3.4) is nowadays an older system and it has been replaced by modern pulsed Fourier Transform NMR spectrometers using higher magnetic fields (with superconducting magnets) and faster acquisition and processing for the full spectrum (all the signals or frequencies of interest are excited simultaneously) [175], [176].

The resonance frequency originated from NMR spectra is $f = \gamma B_0(1-\sigma)/2\pi$ where γ is the magnetogyric ratio, B_0 is the magnetic field and σ is the shielding constant which depends on the distribution of the electronic charge in the vicinity of the nucleus [174]. Therefore, changes in this electronic

[4] This energy is called nuclear Zeeman splitting [176] and it directly depends on the magnetogyric ratio (characteristic constant of every isotope), the magnetic field applied and the shielding constant (electronic distribution charge in the vicinity of the nucleus) [174].

distribution due to interactions of nuclei with B_0, and interactions transmitted through chemical bonds will produce chemical shifts (δ) in the NMR spectra [174], [176]. By definition, the chemical shift is a dimensionless parameter given by $\delta = 10^6(f - f_{ref})/f_{ref}$ where the factor 10^6 is introduced for convenience so that δ is expressed in ppm units, and f_{ref} is the resonance frequency of a nucleus of reference [174].

Finally, NMR spectroscopy can be applied for analysing liquid and solid samples and nowadays is successfully used to study reaction mechanisms in all branches of chemistry. In NMR spectroscopy, magnetic isotopes of hydrogen, carbon or nitrogen (^{1}H, ^{13}C, ^{15}N) are mainly used for labelling the experiments that are devised to follow the outcome of a particular atom during the reactions of interest [176]. In this research, only proton (^{1}H) NMR spectroscopy was used to study the inclusion complexation between host-guest (β −CD/Propofol) molecules.

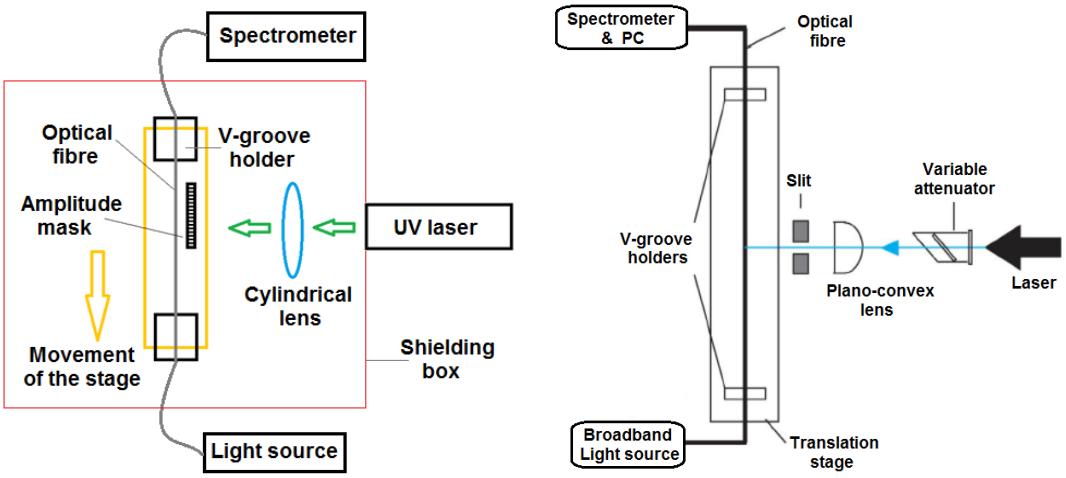
3.2 Fabrication of optical fibre sensors

This subsection will explain the process and some of the facilities available at the Optics and Photonics research group at the University of Nottingham to fabricate optical fibre sensors. For the particular case of the fabrication of LPGs and FBGs, the Optics and Photonics research group owns a designated laser interlocked area and all the procedures with lasers explained here complied with the University Code of Practice for laser safety [177], [178].

3.2.1 Fabrication of LPGs

The manufacture of LPGs operating at the phase matching turning point was performed using an UV laser via two methods: **(1) the amplitude mask technique** (Fig. 3.5a) at the University of Nottingham and **(2) the point-by-**

point approach (Fig. 3.5b) from Cranfield University (as part of a research collaboration [26]).



(a) (b)

Figure 3.5: Schematics for the fabrication set-ups of LPGs. (a) Fabrication via amplitude mask. (b) Fabrication via point-by-point (adapted from [25]).

On the other hand, LPG fibres with periods of 110.0, 110.7 and 110.8 μm were obtained from Cranfield University[5] (***fabricated using point-by-point technique***) and the main components of the fabrication system (Fig. 3.5b) were:

(1) Photosensitive boron-germanium co-doped optical fibre (PS750, Fibercore).

(2) Frequency-quadrupled Nd:YAG UV laser emitting at 266 nm (Spectra Physics Quanta-Ray, repetition rate 10 Hz, output energy 110 mJ at 266 nm, pulse width 4-5 ns).

(3) Circular plano-convex lens of focal length 70 mm.

[5] Although those LPG fibres were created at Cranfield University, the research group at the University of Nottingham has already replicated the experimental set-up for the fabrication using the point-by-point approach.

(4) Mechanical slit (resolution 7nm) automatically controlled [25], [179] and positioned 9.5 mm beyond the focus of the beam (the beam diameter at the slit was 3.4 mm and the fibre was positioned 1 mm behind the slit).
(5) Linear translation stage (PI, M-110.1DG, resolution 7 nm and maximum travel 5mm) for adjusting the slit width.
(6) Linear stage (PI, M-150.11, resolution 8 nm and maximum travel 50 mm) for translating the fibre (held with V-grooves and magnets) in a transverse direction to the laser beam.
(7) Broadband tungsten-halogen light source (HL-2000, Ocean Optics).
(8) Fibre coupled CCD spectrometer (HR4000, resolution 0.02 nm, Ocean Optics).
(9) Variable attenuator to facilitate the control over the laser power incident on the optical fibre [179].

The use of a mechanical slit in the ***point-by-point approach***, allowed selection of the period of the LPG. The slit width could be fixed to half the section width of the desired period, establishing a 50:50 (irradiated section: non irradiated section) duty cycle (Fig. 3.6) or any other desired duty cycle. Before each LPG was fabricated, the period could be verified by exposing the optical fibre, still having the polyacrylate buffer jacket, to the 266 nm laser for 5 s and running it to the programmed exposure profile in Fig. 3.5b.



Figure 3.6: Optical microscope image of a 50:50 duty cycle LPG with period of 110.8 μm.

Prior to point-by-point fabrication, the buffer jacket was removed using an active solvent [25] that softens the polyacrylate coating around the desired section of the optical fibre which was later wiped off with isopropyl alcohol. In this research LPGs were fabricated with a 50:50 duty cycle by exposing bare section of the optical fibre to the laser beam (when the final laser output was approximately 3.8 mW) for a set time and then translating the fibre by a distance equal to the period, repeating the process until the desired LPG length was obtained (typically 3.5 or 4 cm). The broadband light source and spectrometer HR4000 with resolution of 0.02 nm (Fig. 3.5b) are connected to record the generation of the attenuation bands generated from the transmitted light during the fabrication process. The time for writing a full LPG was dependent on the chosen grating pitch, the required length of the LPG and dwell time for each period written. For instance, for an LPG with $\Lambda = 110.0\ \mu\mathrm{m}$ the total time for fabrication was ~3.5 hr when using a slit width of 55 $\mu\mathrm{m}$, dwell time of 35 s for each pitch and total length of 4 cm.

On the other hand, LPG fibres with periods of 109.0, 109.5, 110.0, 110.5 $\mu\mathrm{m}$ were fabricated via an ***amplitude mask*** using a system readily available in our laboratory at the University of Nottingham. The main components used in the fabrication set-up (Figs. 3.5a and 3.7) were:

(1) Photosensitive boron-germanium co-doped optical fibre (PS750, Fibercore).

(2) Frequency quadrupled Nd:YAG UV laser emitting at 266 nm (Photonic Solutions Ltd, Continuum minilite I, adjustable repetition rate 1 -15 Hz, output energy 2 mJ at 266 nm, pulse width 3 - 5 ns) used for side-illuminating the optical fibre.

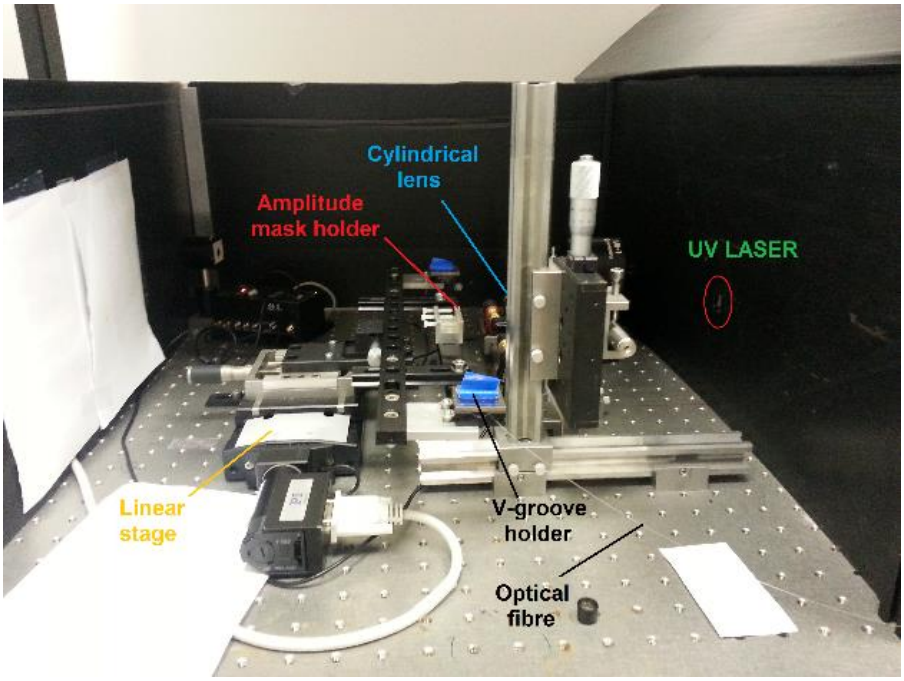
(3) Cylindrical lens with a focal length of 100 mm.

(4) Four customized amplitude masks (109.0, 109.5, 110.0 and 110.5 $\mu\mathrm{m}$, Fig. 3.7b) made of steel alloy (1Cr18Ni9Ti, Suzhou Sunshine Laser Technology Co., Ltd).

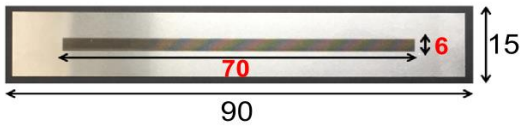
(5) Linear stage (PI, M-405.DG, resolution 8.5 nm and maximum travel 50 mm) for translating the fibre (held with V-grooves and magnets) in a transverse direction to the laser beam (Fig. 3.5a).

(6) Broadband tungsten-halogen lamp (HL-2000, Ocean Optics).

(7) Fibre coupled CCD spectrometer (HR4000, resolution 0.13 nm, Ocean Optics).



(a)



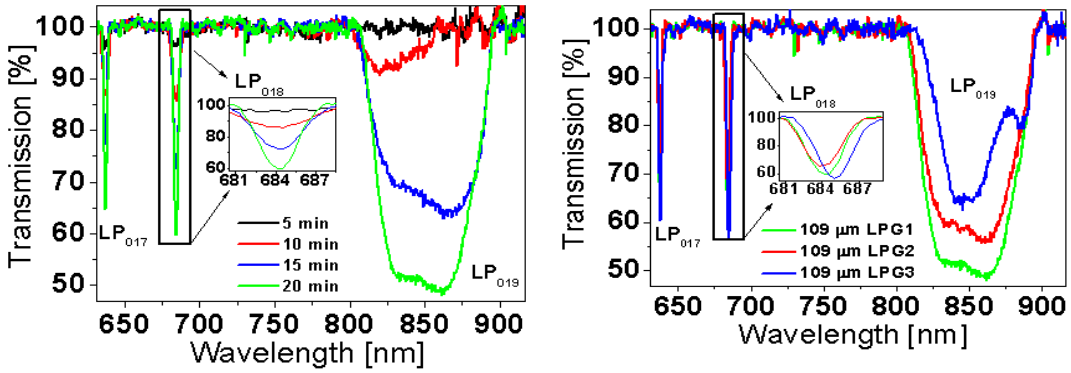
(b)

Figure 3.7: (a) Photograph of the fabrication set-up implementing the amplitude mask method. (b) Steel alloy amplitude mask (all dimensions are in mm and the thickness of the mask is 0.2 mm).

Prior to fabrication using the amplitude mask technique, the buffer jacket of the fibre was mechanically removed (using stripping tool) over the calculated LPG section (3 cm in this case), and that section of optical fibre was wiped

using 2-propanol. The laser used for the side-illumination had a final power of 5 mW and 3 mm diameter. An amplitude mask introduces a spatial modulation to the intensity of the laser beam incident on the fibre [179], [57]. The lens in conjunction with the amplitude mask produced a 3 mm long line focus aligned with the axis of the fibre and the beam waist along that axis was calculated to be 1 mm. The fibre was in the proximity of the amplitude mask and both were moved across the laser beam as shown schematically in Fig. 3.5a.

During the amplitude mask technique fabrication, the transmission loss from the LPG attenuation bands was monitored and recorded every 10 s using the HR4000 spectrometer depicted in Fig. 3.5a. Transmission losses are frequently reported around 40% [25], [57] for LPGs with grating periods between 110.0 and 111.0 μm operating at the PMTP and cladding mode LP_{019}. Due to this reason, the speed of the linear stage (using the system in Fig. 3.5a) was optimized to 0.025 mm/s in order to obtain approximately 40% of loss using total translation lengths of 3 cm and exposure times of 20 min. Fig. 3.8a shows the evolution of the attenuation bands of LPG3 (from Fig. 3.8b) during the fabrication process via amplitude mask. Fig. 3.8b presents three LPGs fabricated with the same period (109.0 μm) via amplitude mask and Fig. 3.9 three LPGs with period 110.7 μm via point-by-point approach.



(a) (b)

Figure 3.8: (a) Exemplar of the evolution of bands during fabrication process of LPG3 (also shown in fig 3.8 b); the attenuation bands start to increase linearly after 5 min. (b) Comparison of three LPGs fabricated with the same period and same parameters: total length 3 cm and speed of 0.025 mm/s in the translation stage.

In general terms, the point-by-point approach is flexible through allowing any arbitrary choice of the grating period (adjusting the slit width), yet it takes more fabrication time compared to the amplitude mask technique (3.5 hrs. vs 20 min).

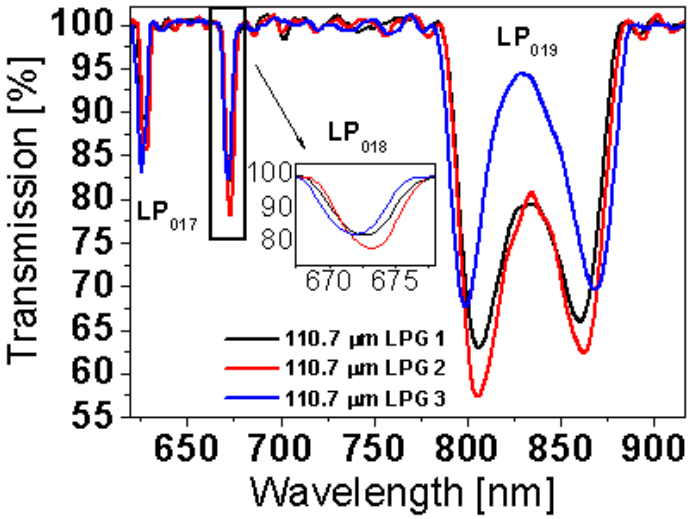


Figure 3.9: Comparison of three LPGs with same period and fabricated in a point-by-point fashion (Fig. 3.5b).

As a conclusion of this subsection, results shown in Figs. 3.8b and 3.9 confirm that variations in the location of the peaks and extinction (%) of the attenuation bands with the same LPG gratings were due to changes in environmental conditions (temperature fluctuated in a total range of 4^0C in all the experiments). Similarly, the tension used to place the fibre in the V-groove holders or laser power variations (as previously stated in reference [179]) affected both techniques of fabrication. Repeatability of the fabrication procedure is desirable in the mass production of LPGs operating at the PMTP for future commercial exploitation of this sensing platform. Recently, Hromadka *et al*. [57] demonstrated a better controlled set-up for a more reproducible fabrication of LPGs via amplitude mask and Wong *et al*. [25] reported the importance of maintaining the temperature (maximum variation of ± 0.5 ℃) in the point-by-point fabrication system by placing it in an insulated

enclosure and obtaining more repeatable fabrication results. In the case of this research, before using any LPG fabricated using either the amplitude mask system or the point-by-point system, the sensitivity to refractive index change (immersing in water or ethanol) of every fibre was checked before functionalization and its use as a biosensor.

3.2.2 Fabrication of FBGs

The system used for the fabrication of FBGs uses most of the components already described in the amplitude mask technique of the previous section with the only exception of replacing the amplitude mask with a phase mask (grating periods: 1067.50 nm, 1072.00 nm and 1075.55 nm, Ibsen Photonics A/S) and introducing two highly reflective mirrors (NB1-K04 with Nd:YAG coating, high reflection range 262 – 266 nm, diameter 1", Thorlabs, Inc.) in the optical set-up as shown in Fig. 3.10. The type of optical fibre suitable for the available phase masks was a boron doped photosensitive fibre (PS1250, Fibercore).

In Fig. 3.10, the UV laser output is diffracted by the phase mask that acts as a beam splitter in the interferometer set-up [180] where the first order beams (± 1) are firstly focused by a cylindrical lens and then reflected by two mirrors at angle θ_m to the phase mask normal. The recombination of the beams on the fibre maximizes mutual coherence of the interfering beams, and the main advantage of this set-up (Fig. 3.10) arises from the fact that maintaining equal handedness of the writing beams compensates any poor spatial profile of the laser source [180]. In Fig. 3.10, θ_p is the half angle between the diffracted first order beams and θ_c is the half angle between the intersecting beams at the fibre.

In contrast to the inexpensive custom made amplitude masks used in this research (Fig. 3.7b), the quality of the grating phase masks is a stringent requirement for a high quality fabrication due to the shorter periods in FBGs. In the optical set-up of Fig. 3.10, the phase mask generates a diffraction

pattern with the desired manufactured periodicity and the optical arrangement is built as a Talbot interferometer [180]. All the phase masks used are designed to mainly operate at ± 1 diffraction orders and the zero order is diminished from fabrication to less than 1.3%. Nonetheless, a beam dump aligned with the laser transmission axis was used to reduce the zero order completely.

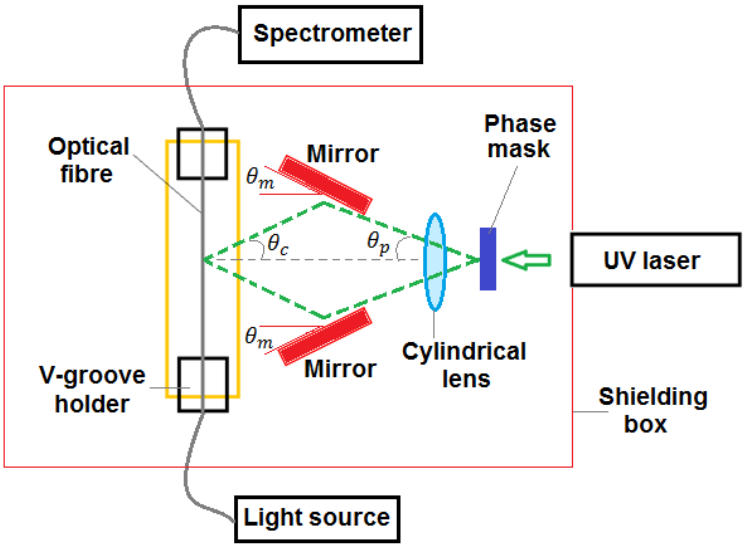


Figure 3.10: Schematic illustration of the fabrication set-up for FBGs readily available in the optical fibre sensors research group at the University of Nottingham. The phase masks grating size is 10 mm x 10 mm.

The phase mask technique implemented with the Talbot interferometer has the advantage of allowing writing of a range of Bragg wavelengths (multiplexing in the same fibre) by tilting the mirrors such that changing the inclination will slightly modify the period of the grating diffraction pattern and Bragg wavelength (Equation 3.1) [180].

$$\lambda_{\text{Bragg}} = \frac{n_{eff}\lambda_w}{\sin(\theta_p + 2\theta_m)} \tag{3.1}$$

where θ_m is the angle tilted from the mirrors in Fig. 3.10, n_{eff} is the fibre effective mode index and λ_w is the writing wavelength of the laser. In addition,

half of the angle between the diffracted first orders satisfies $\theta_p = \sin^{-1}(\lambda_w/\Lambda_p)$, where Λ_p is the manufactured phase mask period and also, considering the geometry of the interferometer, $\theta_c = \theta_p + 2\theta_m$ [180].

Writing the Bragg wavelength with high accuracy requires high-resolution rotary control of the interferometer mirrors which was performed through the use of piezoelectric inertia actuators (PIAK10, typical step size of 20nm, Thorlabs Inc.) automatically controlled (T-cube piezoelectric controller, Thorlabs Inc.).

In this research, FBGs with lengths between 2 and 3 mm and Bragg wavelengths within the range of 1520 to 1560 nm could be fabricated with the phase masks available (Λ_p =1067.50 nm, 1072.00 nm or 1075.55 nm) and using the experimental set-up schematized in Fig. 3.10. Two examples are shown in Fig. 3.11 demonstrating the production of gratings with repeatable characteristics and obtaining Bragg reflections around 60% with a laser power during fabrication between 10 and 15 mW for 20 min approximately.

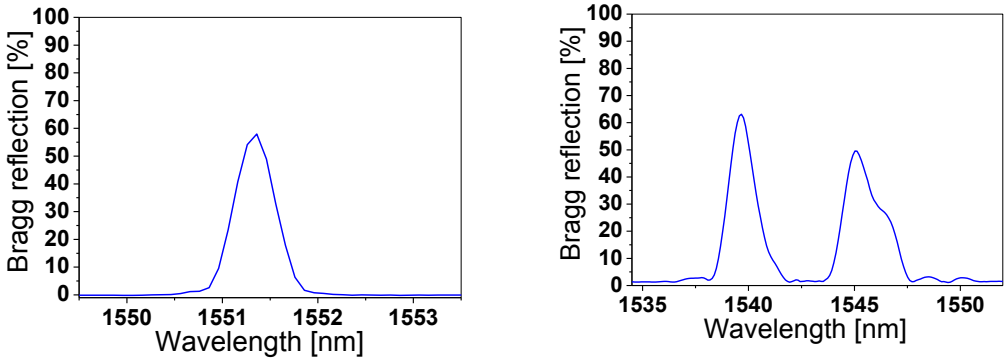
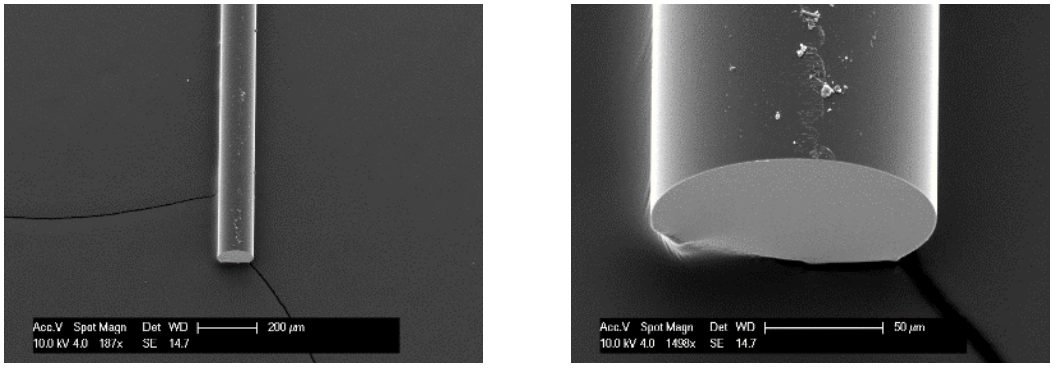


Figure 3.11: (a) FBG with Bragg wavelength at 1551.36 nm used in this project for temperature sensing. (b) Multiplexing of two FBGs written in the same fibre and centered at 1539.67 nm and 1545.12 nm.

3.2.3 Preparation of fibre tip for Fabry-Pêrot sensor

As mentioned in section 2.2.3, the tip of an optical fibre works as an optical interface which reflects light back to the fibre due to Fresnel reflections which are calculated from the differences between the refractive index of the optical fibre and the surrounding environment [181], [2]; these reflections are higher only if the fibre tip is cut predominantly perpendicular to the fibre axis. Fig. 3.12 shows an exemplar of a fibre tip cut using a precision fibre cleaver (VF-15H, INNO^{TM} Instruments) and the images were taken using SEM. In section 3.3.2, the deposition of a thin-film based on PAH and SiO_2 NPs onto the same tip of Fig. 3.12 is presented as an OFS for humidity sensing.



(a) (b)

Figure 3.12: In this research SEM was used for characterisation of films deposited on fibres; this case shows a single-mode bare fibre tip with (a) SEM 187x magnification and scale 200 μm; and (b) 1498x magnification and scale 50 μm.

3.2.4 Preparation of U-shaped fibres

Similarly with tips of optical fibres, films can be deposited onto the U-shaped section of an optical fibre. To prepare a U-shaped probe in a MMF (TECS hard polymer cladding FT200 EMT, Thorlabs Inc.), first the plastic buffer was removed with a specialized stripping tool (Micro-strip .012, Micro Electronics Inc.) and then the cladding of the fibre is reduced while simultaneously exposing to a propane flame and deforming into a U shape until the desired

bending radius is reached. The technique is explained from (a) to (d) in Fig. 3.13 which allowed production of U-shaped sections within the range [1.25, 1.85] in millimeters, an average diameter of 1.54 mm (N=31) and sample standard deviation of 0.17 mm. Additionally, the sensitivity to refractive index change (in ethanol) of every U-shaped fibre fabricated was measured before functionalization for bio-sensing purposes.

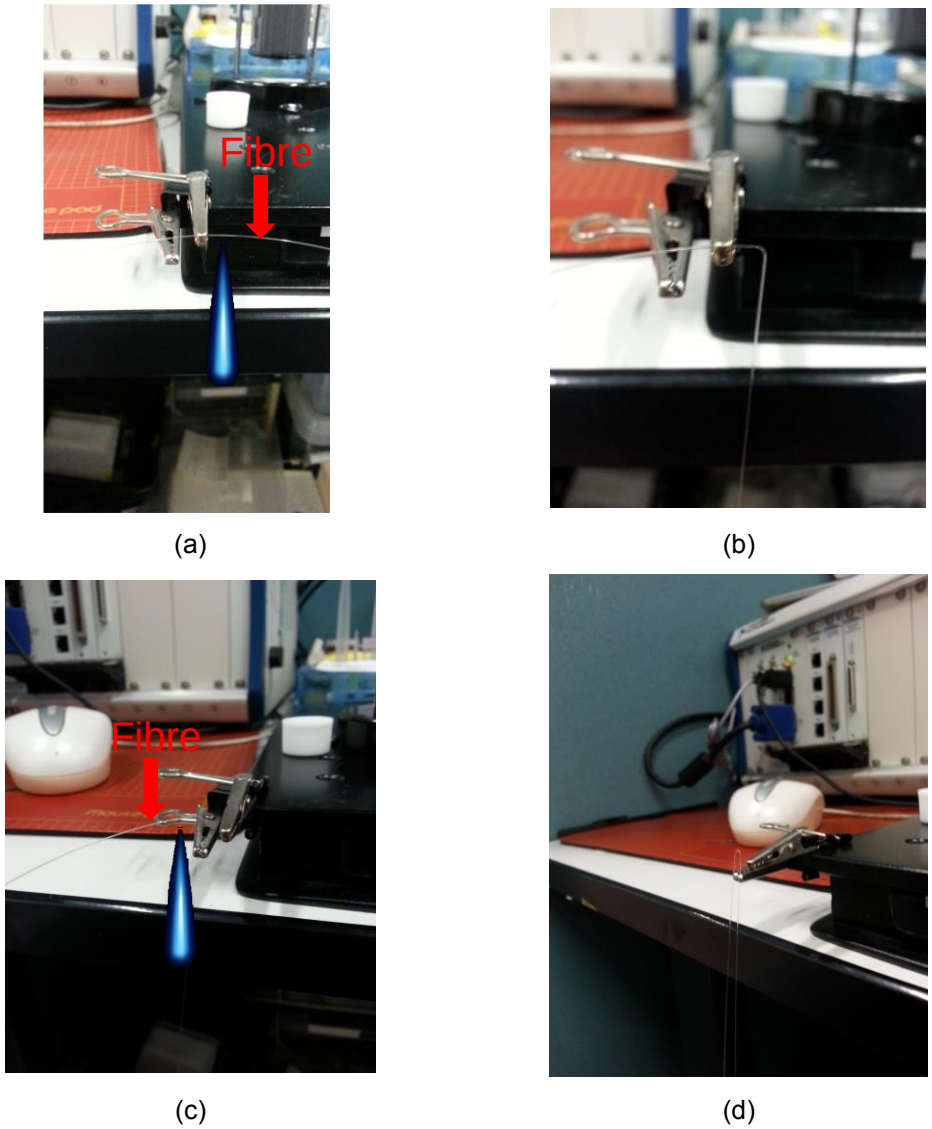


Figure 3.13: Fabrication method of U-shaped fibres when exposed to a blue propane flame. After fabrication all the bending radii were measured with optical microscope (refer to Fig. 1.14 in chapter 1). (a) Fibre is held using an horizontal crocodile-clamp. (b) Fibre is exposed to the flame until it bends. (c) Fibre is held using a vertical crocodile-clamp and exposed again to the propane flame until it bends forming a U-shape as shown in (d).

It should be clarified that, although Fig. 3.13 shows the propane flame from below upwards, in fact the direction of the flame is perpendicular to the plane of the photographs of this page. Firstly, the fibre is held with an horizontally positioned crocodile-clamp (Fig. 3.13a) and exposed to the flame until the fibre bends (~ 5 s) as shown in Fig. 3.13b. Then this bent fibre is positioned in the vertical crocodile-clamp and exposed again to the propane flame (~ 5 s) until it completely bends as shown in photograph of Fig 3.13d.

3.3 Chemical functionalization using the Layer-by-Layer (LbL) technique

The LbL deposition method described in this section is based on the electrostatic self-assembly process between molecules and nanophase entities to materialize into organized aggregates or film structures [182]. Fabrication of multilayer nanostructured thin films involving molecular self-assembly offers three main approaches [182], [183]:

(1) Langmuir-Blodgett (L-B) self-assembly.

(2) Chemical self-assembled monolayer (SAM).

(3) Electrostatic self-assembly based on the LbL technique.

Only the former was not used in this research for the fabrication of nanofilms for biosensing development; L-B films are restricted to amphiphilic molecules, the film structures created with this technique are easily disrupted (thermally or chemically), the deposition substrates are limited to planar surfaces of only a few square centimeters and it is more difficult to form good optical quality films [184].

The LbL technique has been reviewed as a most remarkable method due to its extraordinary simplicity and versatility [185], and its classical method has recently been combined with other types of interactions, including hydrogen bonds, chemical bonds (click chemistry), host-guest interactions, bio-molecularly assisted self-assembly, or acid-base reactions [182], [185].

Nowadays, its advantages as compared to other techniques are widely known [182], [183], [184], [186] and are summarised here:

(1) Easy to fabricate with water-based process at room temperature and pressure.

(2) Flexible to apply on nearly any substrate (any size or topology) and flexibility in molecular selection.

(3) Structure and thickness of the films can be controlled.

(4) Feasibility to deposit hundreds to thousands of layers.

(5) Self-assembly with high quality films (good uniformity) can be obtained.

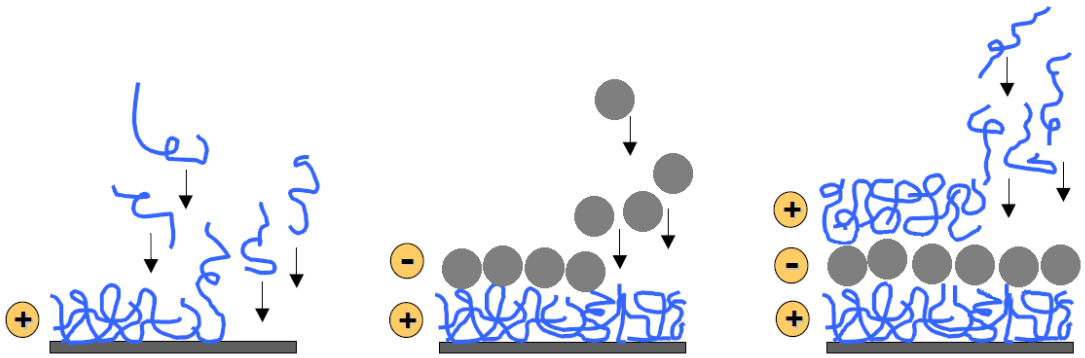
(6) Long term stability and environmental robustness can be achieved.

(7) Broad range of applications can be found in different fields, including optics, electronics, biosensing and surface modification.

(8) Low-cost manufacturing, LbL deposition process may be up scaled in size and volume, and can be easily automated.

The LbL technique applied in this research is schematized in Fig. 3.14. The functionalization of a substrate requires it to firstly be cleaned and negatively charged through chemical processing (silica surfaces can be negatively charged through a hydroxylation process [26], [187]). The charged substrate is dipped into an aqueous solution containing polycations which are electrostatically attracted to the pre-charged substrate and assemble themselves into a molecular monolayer (Fig. 3.14a). After rinsing away with deionised water the loose particles (particles not ionically bonded or adsorbed) and drying with nitrogen, a polyanionic monolayer (in this case using SiO_2 NPs) is deposited in the same manner (Fig. 3.14b) and subsequent layers are added forming bilayer pairs (Fig. 3.14c) through alternating deposition between the polyanion and polycation solutions. The use of nanoparticles enables wider design opportunities for thin films as described in the next experimental section. In the particular case of this research, the LbL with SiO_2 nanoparticles and a negatively charged PAH polymer will be used for the development of biosensors for protein detection with the aid of Au NPs and chemical co-

assembly (section 3.3.1 and chapter 5) and for humidity sensing (section 3.3.2 and chapter 4).



(a) (b) (c)

Figure 3.14: Schematic illustration of the LbL technique (modified from [184]). (a) A hydroxylated substrate is immersed in a polycation solution and it will produce a positively charged material after dipping deposition; (b) electrostatic self-assembly of the first anionic layer using negatively charged nanoparticles; (c) First bilayer and iteration of the LbL deposition to produce a multilayer thin-film structure.

3.3.1 LPG functionalization for protein detection

The main materials synthesized and implemented for this LPG functionalization are detailed in Table 3.1. The synthesis of SiO_2:Au core/shell nanoparticles were made by first synthesising SiO_2 NPs using the Stöber method and then covalently attaching the Au NPs to the SiO_2 NPs surface to ensure stability. Step by step, the functionalization of the solution of SiO_2 NPs was carried out by adding 25 μl of 3-APTES to the reaction and leaving it to sonicate for an extra 15 min. The solution of APTES-functionalized SiO_2 NPs was added dropwise to the solution of Au NPs in a volumetric ratio of 1:3 (SiO_2-NH_2:Au NPs) and stirred overnight (8 h) to provide stable covalent attachment of the Au NPs to the SiO_2 NPs [26].

<table>
<tr><th>Materials:</th><th>Comments:</th></tr>
<tr><td>Ethanol (EtOH) (99%)</td><td rowspan="10">Chemicals from Sigma-Aldrich UK

Materials highlighted in blue used for:
Synthesis of SiO_2 NPs

Materials highlighted in red used for:
Synthesis of gold (Au) NPs</td></tr>
<tr><td>Tetraethylorthosilicate (TEOS)</td></tr>
<tr><td>Ammonium hydroxide (NH_4OH 28%)</td></tr>
<tr><td>Sodium borohydride ($NaBH_4$)</td></tr>
<tr><td>potassium carbonate (K_2CO_3)</td></tr>
<tr><td>tetrachloroauric acid ($HAuCl_4$)</td></tr>
<tr><td>Streptavidin (SV) (M_w ca. 52.8 kDa) from Bacterium Streptomyces avidinii</td></tr>
<tr><td>Biotin (Molecular weight, ca. 244.31 g·mol^{-1}) ((+)-Biotin N-hydroxysuccinimide ester)</td></tr>
<tr><td>Poly(allylamine hydrochloride) (M_w ~58,000) (PAH)</td></tr>
<tr><td>3-aminopropyltrimethoxysilane (APTES)</td></tr>
<tr><td>Synthesis of SiO_2 NPs (2 sizes of diameters)</td><td>using Stöber's methodology [188]
<table><tr><td>80 nm diameter</td><td>22.5 ml of EtOH + 2 ml of TEOS mixed with 3.5 ml of NH_4OH for 15 min in a sonicator bath.</td></tr><tr><td>300 nm diameter</td><td>7 ml of EtOH + 80 µl of TEOS was mixed with 3 ml of NH_4OH for 15 min in a sonicator bath.</td></tr></table></td></tr>
<tr><td>Synthesis of aqueous Au NPs (diameter 3 to 5 nm)</td><td>using Bonnard's methodology [189], [190]</td></tr>
</table>

Table 3.1: Materials for the LPG functionalization for protein detection. All reagents were of analytical grade and were used without further purification. Distilled water (with conductivity of 18.3 MΩcm) was obtained by reverse osmosis followed by ion exchange and filtration in a Millipore-Q (Millipore, Direct-QTM).

The LbL technique was used to deposit alternate layers of PAH and SiO_2:Au core/shell NPs onto two LPGs (Fig. 3.15) with lengths of 4 cm, period of 110.7 µm and fabricated in a point-by-point fashion. The overall process was carried out using precision pipettes and a Teflon PTFE deposition cell (Fig. 3.15b) as

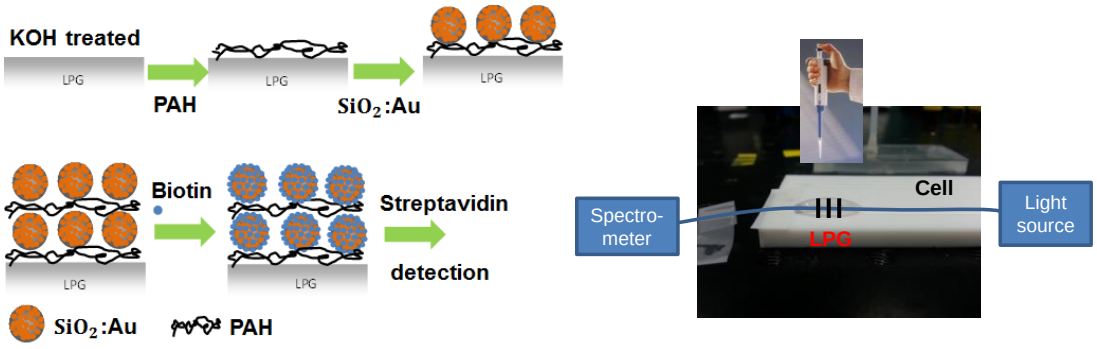
follows:

(1) LPG section was hydroxylated with a 1 wt% ethanolic KOH (ethanol/water = 3:2, v/v) solution to terminate the surface with OH groups (20 min).

(2) Fibre was immersed alternately into a 0.17 wt % solution containing a positively charged polymer PAH, and, after washing and drying, into a 1mg/mL solution containing the negatively charged SiO_2:Au NPs (80 or 300 nm in diameter), each for 15 min. This process was repeated until the required coating thickness was achieved, in this case after 3 deposition cycles (rinsing and drying in between of every layer).

(3) The coated fibre was then immersed in a 6.8 μM aqueous solution of biotin for 30 min to functionalize the SiO_2:Au NPs coating and to provide the sensor with its specificity to streptavidin (SV). The fibre was then rinsed in distilled water and dried by flushing with N_2 gas. The biotin was bound to the surface of each NP which increased the surface area available for the binding of SV compared with a bare fibre.

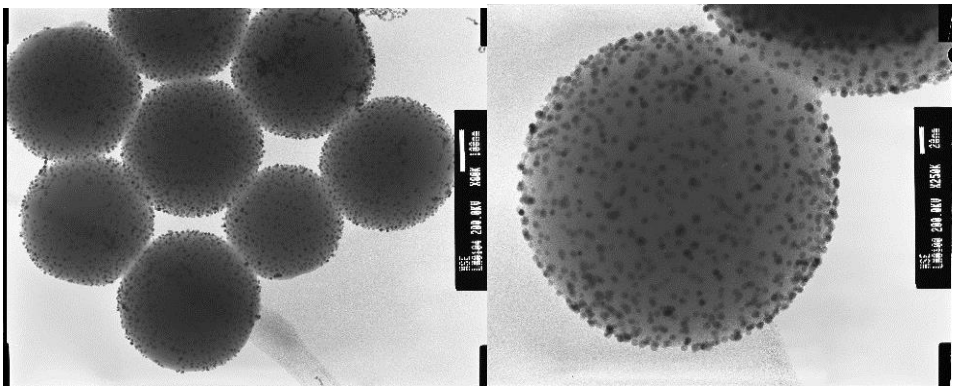
During all the deposition process and test for SV adsorption, the set-up of Fig. 3.15b was implemented, using a broadband light source (HL-2000, Ocean Optics) and a spectrometer (HR4000, Ocean Optics) with wavelength resolution of 0.13 nm; the spectrometer operating software (SpectraSuite®, Ocean Optics) allowed dynamic measurements over the full spectrum range of 200 to 1100 nm and acquiring-saving data with high scanning rate frequencies (in the order of Hz or KHz).



(a) (b)

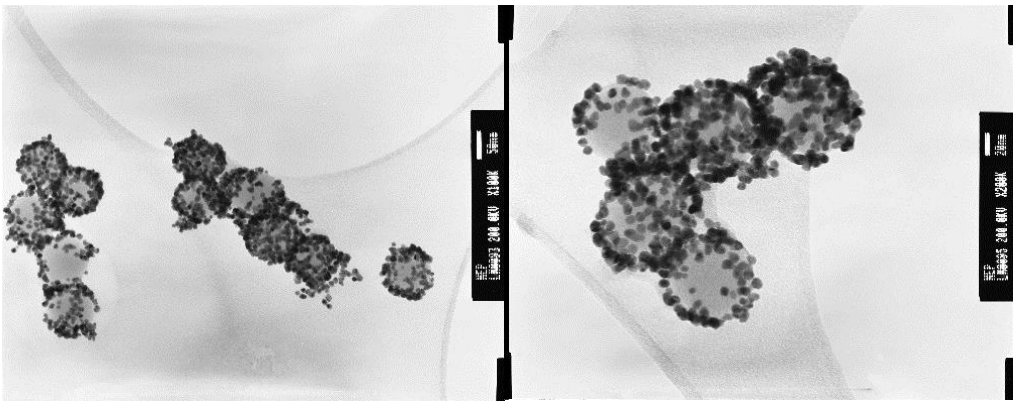
Figure 3.15. (a) Schematic illustration of the layer-by-layer deposition of $(PAH/SiO_2:Au)_3$ film onto an optical fibre LPG (this figure only depicts deposition of two consecutive layers); (b) Teflon deposition cell system

Finally, the SiO_2:Au NPs were imaged using TEM and the morphology of the PAH/SiO_2:Au films were visualized using SEM. Fig. 3.16a and 3.16b show TEM images that demonstrate successful modification of the SiO_2 NPs of 300 and 80 nm diameter respectively with the Au NPs. The Au NPs provide the surface for the deposition of biotin which in turn enables the immobilization of SV molecules. Fig. 3.17 shows the SEM image of the LPG optical fibre successfully coated with three consecutive-assembled bilayers of PAH and SiO_2:Au (300 nm SiO_2 NPs diameter), denoted as $(PAH/SiO_{2(300nm)}:Au)_3$. Complete surface coverage was not achieved most likely owing to the presence of NH_2 functional groups on the SiO_2 NPs that promoted some repulsive charge effects with the PAH and an incomplete aggregation reaction between the polyelectrolyte and the fibre surface. Some improvements consist of providing higher number of ligands that will intensify the negative charge of the SiO_2 NPs and enhancement of the coverage of the SiO_2 NPs with Au NPs through modifying the initial procedure used to synthesize the SiO_2:Au NPs. As will be shown in chapter 5, the surface coverage showed in Fig. 3.17 was sufficient to conduct measurements of the binding between biotin and streptavidin with the LPG-based OFS proposed here.



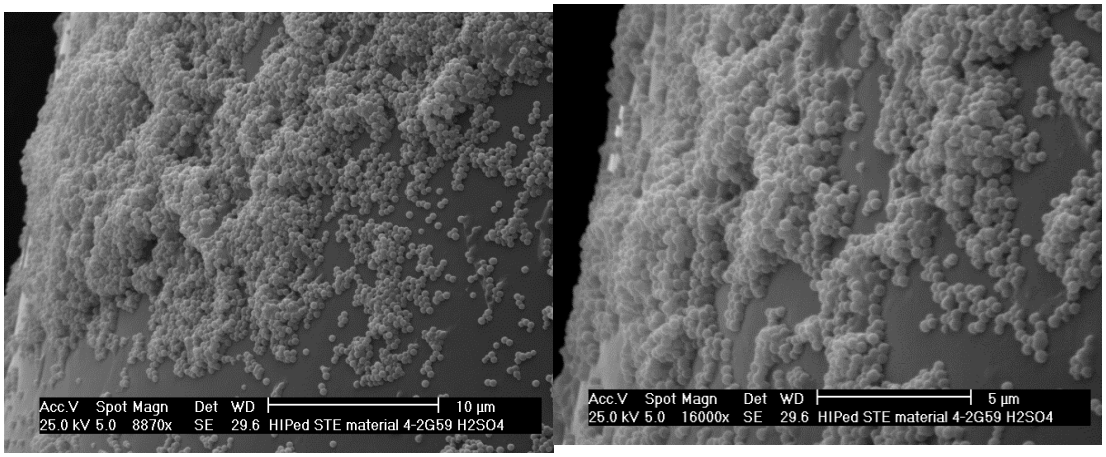
(a)

Figure 3.16: (a) TEM images of 300 nm (scale bars: left hand, 100 nm and right hand, 20 nm) SiO_2:Au NPs



(b)

Figure 3.16: (b) TEM images of 80 nm (scale bars: left hand, 50 nm and right hand, 20 nm) SiO_2:Au NPs.



(a) (b)

Figure 3.17: SEM images of $(PAH/SiO_{2(300nm)}:Au)_3$ film deposited onto an optical fibre LPG. (a) scale bar: 10 μm and (b) scale bar: 5 μm.

3.3.2 Fabry-Pêrot functionalized sensor for humidity sensing

This type of sensor is also called a micro-mirror OFS [191] when a nano-film is deposited onto the fibre-tip (perpendicularly cut and polished as in Fig. 3.12) which generates back reflections and/or interference in the reflected light.

Any type of optical fibre (tip) can be coated using also the LbL deposition method and Table 3.2 summarizes the materials used for the functionalization of fibre tips for creating humidity sensing probes.

Materials:	***Comments:***
SiO_2 NPs used as polyanionic layer.	Purchased from Nissan Chemical (SNOWTEX 20L, diameters in the range 40 – 50 nm, Japan).
PAH (M_W: ~58,000) as polycationic layer.	Purchased from Sigma-Aldrich, UK.
Potassium Hydroxide (KOH) used for hydroxylation.	
Ethanol (EtOH) used for hydroxylation.	
Sodium Hydroxide (NaOH) used for changing pH of polycationic layer.	

Table 3.2: Materials for the functionalization of fibre tips. All reagents were of analytical grade and were used without further purification. Distilled water (with conductivity of 15 MΩcm) was obtained by reverse osmosis followed by ion exchange and filtration in a Millipore-Q (Millipore, Direct-QTM).

The method of deposition of the nano-thin film used for humidity sensing and deposited onto the tip of a fibre followed the steps depicted in Fig. 3.18a:

(i) Treatment of the surface-tip of the fibre with 1 wt% ethanolic KOH for 20 min.

(ii) Wash with distilled water and dry with N_2, followed by immersion of the fibre tip in a 0.17 wt% of positively charged polymer PAH (pH=11) for 15 min.

(iii) Washing and drying, immerse the fibre tip into a solution containing negatively charged SiO_2 NPs for 15 min.

(iv) After deposition of the SiO_2 NPs, wash and dry and repeat steps (ii) and

(iii) until the desirable "X" number of bilayers, denoted as (PAH/ SiO_2)$_X$, is created.

The recommended number of bilayers deposited onto the tip for humidity sensing is strongly related to the sensor sensitivity and this will be explained in more detail in chapter 4.

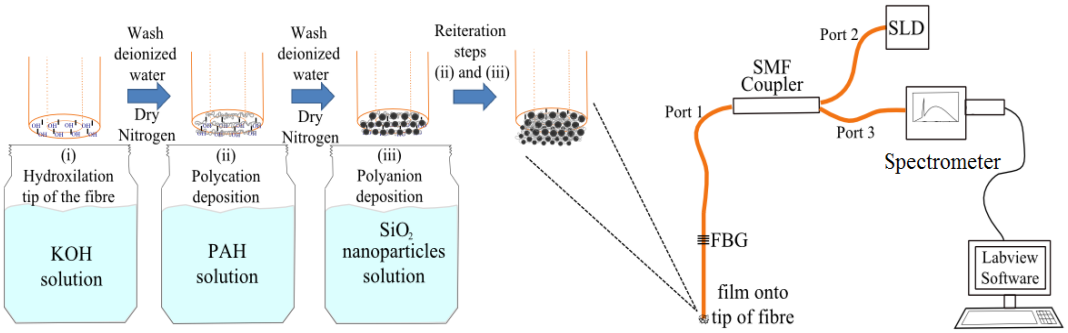
In this research, deposition of bilayers of (PAH/SiO_2) were deposited onto the tips of two types of optical fibre couplers:

(1) SMF coupler (1X2 Coupler 50/50, operating wavelength 1310/1550 nm, C-WD-AL-50-S-1210-35 NC/NC, Newport) spliced to another fibre containing an FBG ($\lambda_B = 1548.85$ nm).

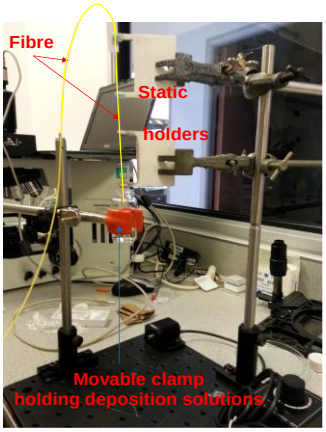
(2) MMF coupler (1X2 Coupler 50/50, operating wavelength 850 nm, FCPL-M12855, Newport).

Fig. 3.18a shows only the case of deposition onto the tip of the SMF coupler while monitoring the source light launched to port 2 from a super-luminescent diode (SLD-761-HP1, central wavelength 1557.6 nm, spectral width 43.8 nm, SUPERLUM, externally isolated) and detecting the light reflections (due to reflections from the film) from port 1 using a spectrometer connected in port 3 (I-MON 512 USB, sub-picometer resolution, Ibsen Photonics A/S).

The set-up for the deposition of bilayers of (PAH/ SiO_2) onto the MMF coupler is exactly the same shown in Fig. 3.18. The only differences being that port 2 is connected to a broadband light source (HL-2000, Ocean optics) and port 3 is connected to a spectrometer (HR4000, Ocean Optics). The I-MON512 spectrometer of Fig. 3.18a uses an interrogation software based on Labview provided by Ibsen Photonics A/S, and the Ocean Optics spectrometer uses the SpectraSuite® software already mentioned before; both cases allow dynamic measurements with high scanning rate frequencies (Hz or KHz) for the full spectral range (200 to 1000 nm with HR4000 and 1510 to 1595 nm with I-MON512) both during deposition and humidity tests.



(a)



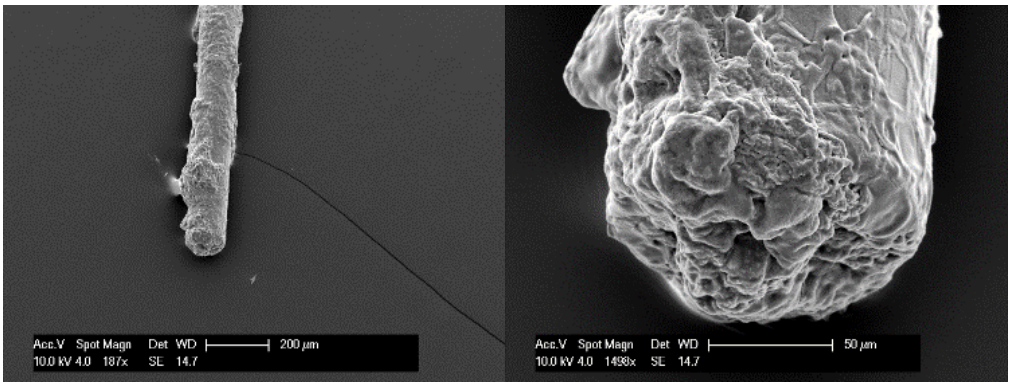
(b)

Figure 3.18: (a) Schematic illustration of the construction of a (PAH/SiO_2) thin film using the LbL method onto the tip of a SMF coupler. (b) Photograph of the set-up for deposition of PAH and SiO_2 NPs onto the fibre-tip.

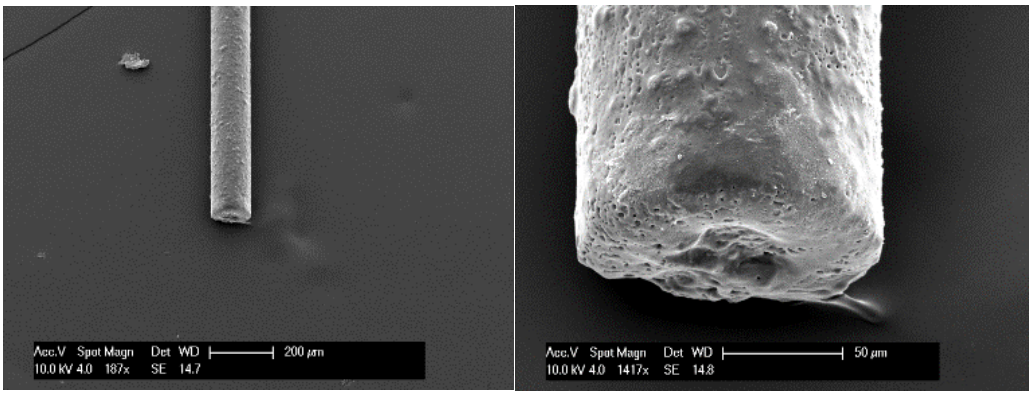
During the deposition of bilayers of PAH/SiO_2 the fibre is fixed using static holders (Fig. 3.18b) and the fibre tip is dipped into the vials containing the solutions using a movable clamp. The results of deposition of bilayers of PAH/SiO_2 onto the tip of both the SMF and MMF couplers and results from humidity tests will be presented in chapter 4.

Finally, Figs. 3.19a and 3.19b show the hydrophilic film created during the LbL assembly process of bilayers of PAH/SiO_2. Comparison of Figs. 3.19a and 3.19b confirms that a highly uniform film is deposited onto the optical fibre only after 4 bilayers [192]. In chapter 4 it will be demonstrated that 3 bilayers of PAH/SiO_2 was sufficient to detect changes in humidity, yet sensor sensitivity is dependent on the number of bilayers deposited (also showed in chapter 4).

The growth of the initial layers is not uniform due to a lack of surface coverage and some parts will not be fully charged after deposition of the first layers of PAH. Coverage can be boosted by controlling parameters such as solution concentration of the polyelectrolytes used and pH [193]. More uniform multilayer growth has been reported with the use of an initial assembly adhesion stage of PAH and Poly(sodium 4-styrenesulfonate)(PSS) in the initial layers [194]. It should be noted that, in Fig. 3.19, only the tip of the optical fibre coated with the PAH/SiO_2 film is interrogated and the surface side of the fibre itself does not contribute to the sensor response for this type of sensor probe.



(a)



(b)

Figure 3.19. SEM images of the optical fibre humidity sensor probe coated with the PAH/SiO_2 film. (a) Fibre covered by 3 alternate bilayers of PAH and SiO_2 NPs. (b) Fibre covered by 5 alternate bilayers of same film. The scale bar on the left side is 200 μm; and 50 μm on the right hand side in both bullet points a) and b).

3.4 Chemical functionalization with imprinted metal oxide films for detection of propofol

Two functionalization methods are explained in this section and further used with the optical fibres (chapter 5) for the detection of propofol; these two functionalizing methods are based on molecular imprinting [134]:

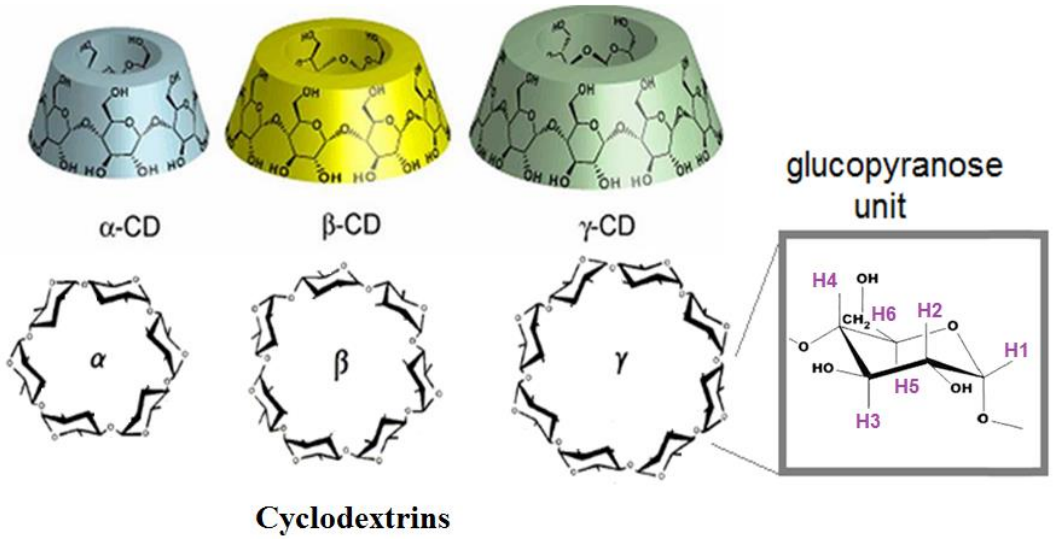
(1) Liquid Phase Deposition (LPD) of titanium dioxide (TiO_2) imprinted with host-guest (β −CD/propofol) molecules for the purpose of detecting propofol.

(2) Sol-gel deposition of mesoporous silica nanoparticles (MSNs) and TiO_2 with direct imprinting of propofol molecules.

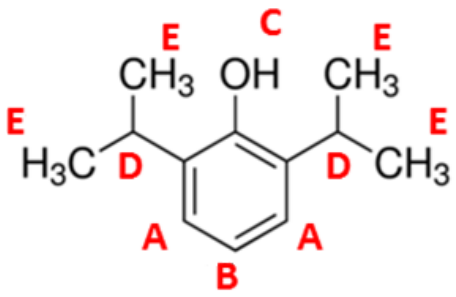
In this section, the first method is characterized with spectroscopy techniques (section 3.4.1) and the second imprinting method served for incrementing sensitivity for propofol detection and limit of detection when compared to the LPD imprinting method.

There are three types of native cyclodextrins: α, β, γ −CDs which can be used as a host compound for guest molecules of propofol (Fig. 3.20). Cyclodextrins are molecules with holes used as a carrier host to facilitate the dissolution of low solubility compounds such as vitamins or hormones in tissue and cell culture or other biotechnology applications involving also anaesthetic drug or protein delivery [195], [196], [197], [198]. In Fig. 3.20, α −CD, β −CD and γ −CD consist of 6, 7 and 8 cyclic glucopyranose units respectively and propofol (2,6-Diisopropylphenol) is considered a small phenolic and hydrophobic molecule used as intravenous anaesthetic agent for induction and maintenance of general anaesthesia [199].

In this research, the complexation (guest inclusion to the host compound) between propofol (2,6-Diisopropylphenol, $M_w = 178.275\ \mathrm{g/mol}$, Sigma Aldrich, without further purification) and β −CD ($M_w = 1134.98\ \mathrm{g/mol}$, Tokyo Chemical Industry Co. Ltd.) was investigated through NMR spectroscopy (Proton ^{1}H 500 MHz JEOL FT-NMR, JEOL USA Inc.).



(a)

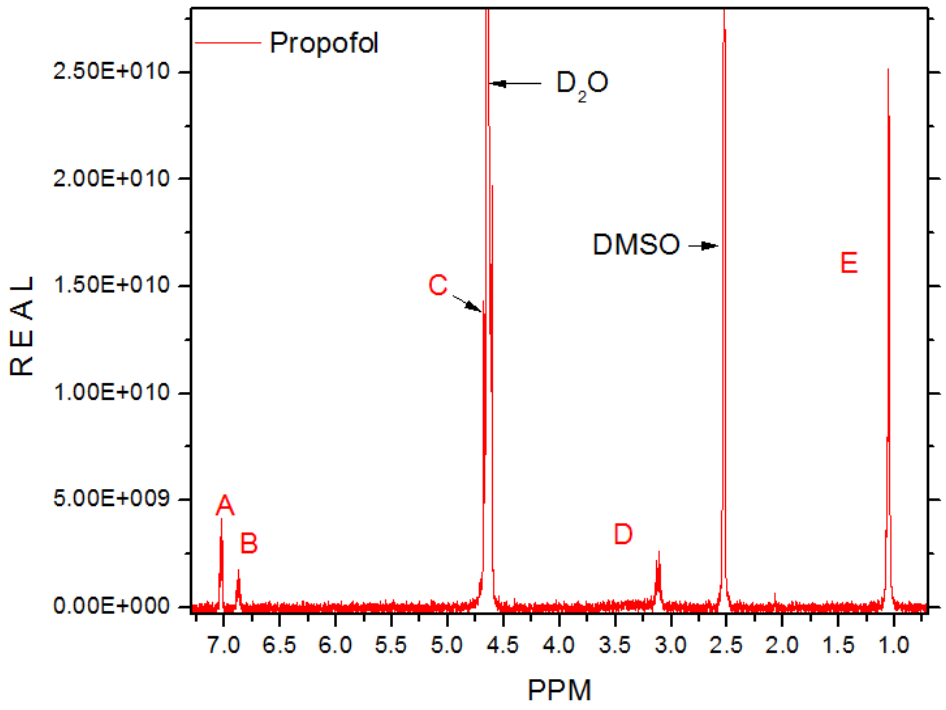


Propofol

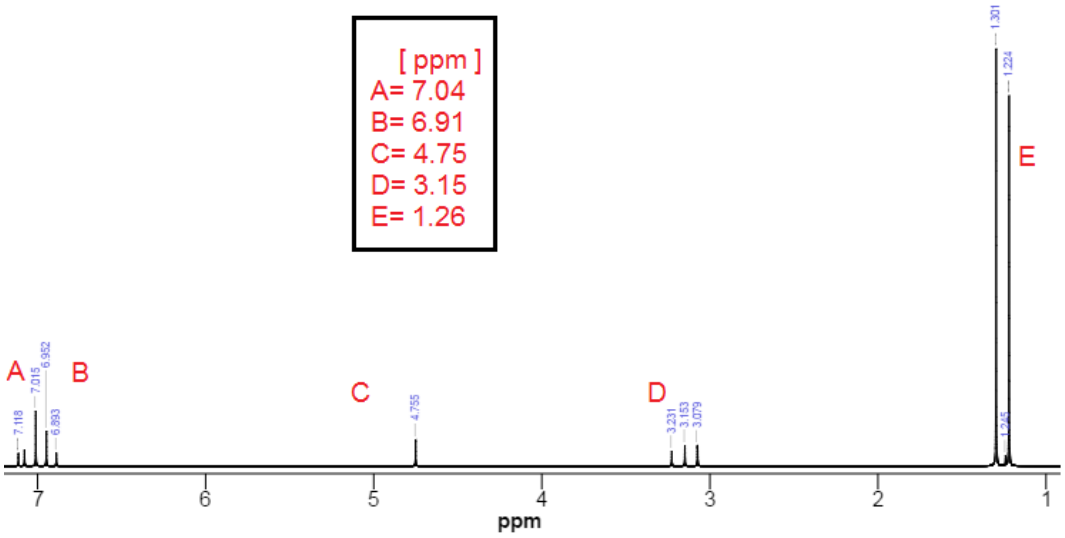
(b)

Figure 3.20: (a) Cyclodextrins (host) and (b) propofol molecules (guest) can form inclusion complexes through host-guest interactions (adapted from [195] and [196]). The protons of the cyclodextrins are shown in purple in (a) and the protons of propofol are shown in red in (b).

The ^{1}H NMR spectrum of 10 mM propofol (Fig. 3.21) and of 10 mM β −CD (Fig. 3.22) were measured individually when dissolved in solvent containing 10 % DMSO and 90% D_2O.

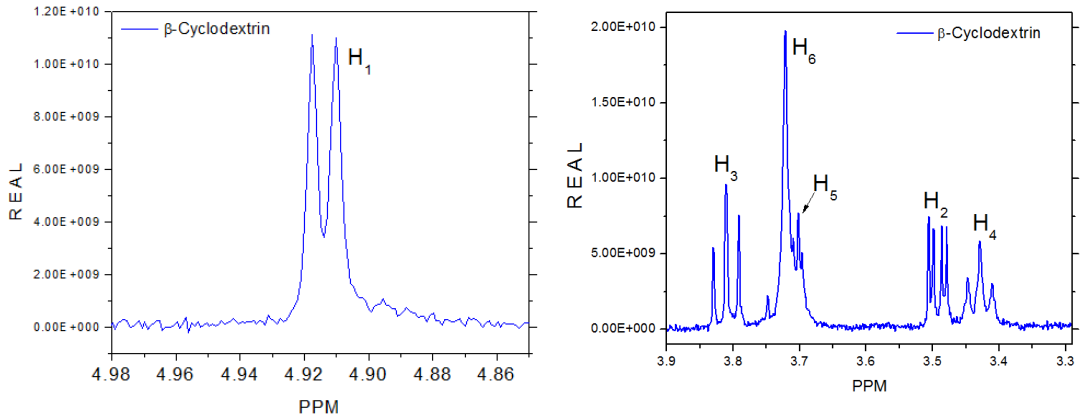


(a)

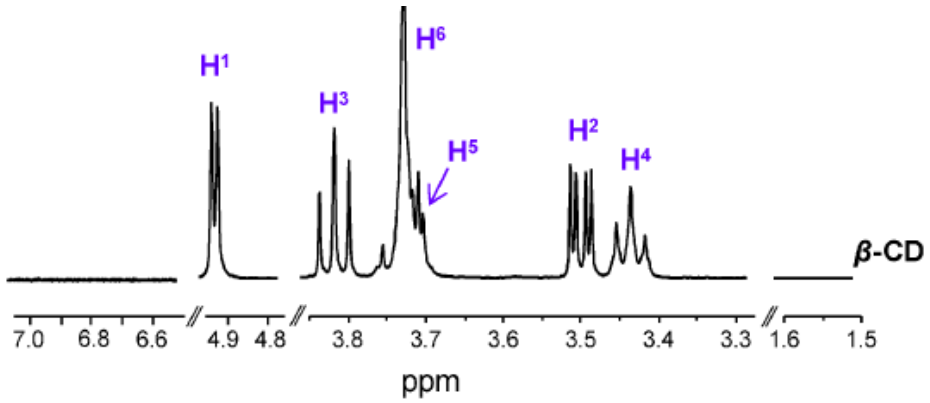


(b)

Figure 3.21: (a) ^{1}H NMR spectrum of propofol measured when dissolved individually in deuterated DMSO (y-axis is the real part of the Fourier transform). (b) Chemical shifts detected when propofol is exposed to NMR spectroscopy can be confirmed elsewhere [199], [200].



(a)



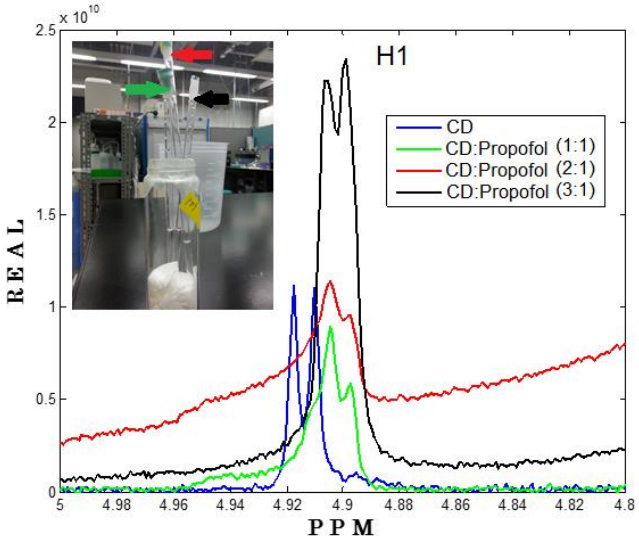
(b)

Figure 3.22: (a) ^{1}H NMR spectrum of β −CD measured when dissolved individually in deuterated DMSO (y-axis is the real part of the Fourier transform). (b) Chemical shifts detected when β −CD is exposed to NMR spectroscopy (spectrum taken from [201]) can also be confirmed in reference [174].

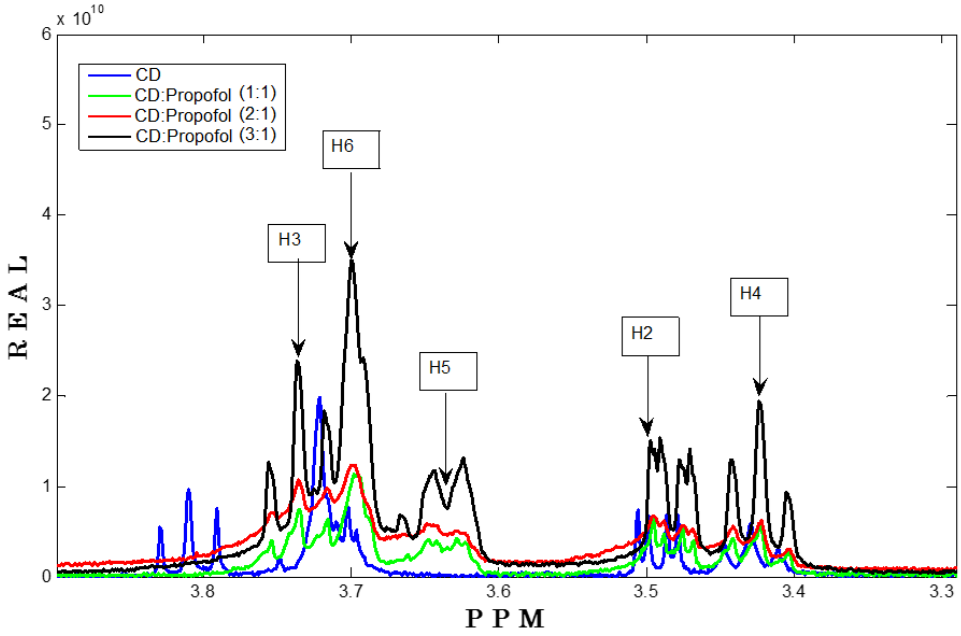
One approach to study the host-guest inclusion between β −CD and propofol is through the analysis of the deviation in the chemical shifts observed in Figs. 3.21 and 3.22 when they are mixed and dissolved in the same solvent (deuterated DMSO). Changes in the chemical shifts of hydrogens indicate variations in the chemical environment of the nuclei from both host and guest molecules and variations greater than 0.05 ppm are considered the most significant in ^{1}H NMR spectroscopy [202], [203].

Therefore, solutions with β −CD **:** Propofol complexes of ratios (1:1), (2:1) and (3:1) were prepared in same solvent (10% DMSO and 90% D_2O) and analyzed through ^{1}H NMR spectroscopy. Fig. 3.23 and Fig. 3.24 show the changes in chemical shift for these complexation solutions prepared (inset of

Fig. 3.23a), tested in NMR and compared with the pure solutions previously plotted in Fig. 3.21 and Fig. 3.22.

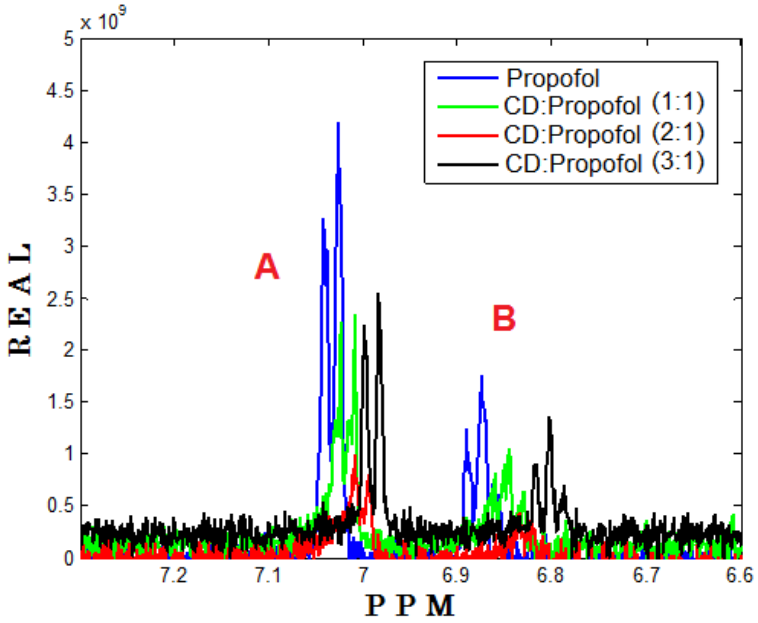


(a)

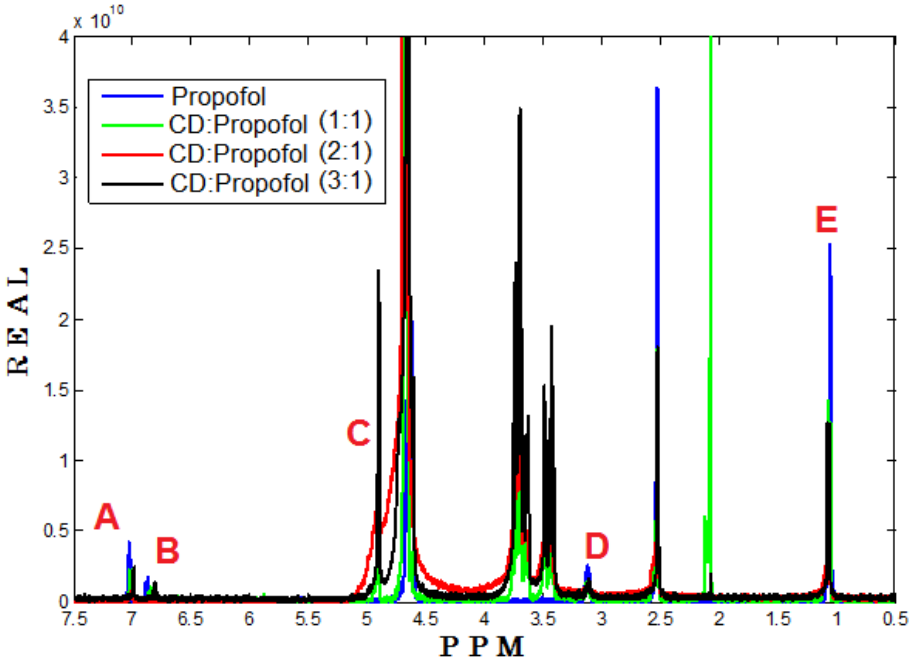


(b)

Figure 3.23: (a) Chemical shifts for H1 proton of β −CD (*cf*. Fig. 3.20) without complexation (blue) and after preparing in solutions with propofol at different concentration ratios (inset shows the tube samples introduced in the NMR spectrometer). (b) Chemical shifts for the other protons of β −CD (*cf*. Fig. 3.20) without complexation (blue) and after preparing in a complexation solution with propofol at different concentration ratios.



(a)



(b)

Figure 3.24: (a) Chemical shifts for proton A and B of propofol (*cf*. Fig. 3.20) without complexation (blue) and after preparing in a complexation solution with β −CD at different concentration ratios. (b) Chemical shifts for the other protons of propofol without complexation (blue) and after preparing at different concentration ratios.

As a summary of the characterization for the complexation β −CD **:** propofol, only the aromatic protons (A and B, Fig. 3.24) of the propofol molecule presented significant variations in chemical shift after complexation with β −CD at three different concentrations (Fig. 3.25a). Similarly, the protons H3 and H5 which are located inside the conical cavity (Fig. 3.25b) of the host molecule β −CD, resulted with the most significant changes in chemical shift after complexation at the three different concentrations (Fig. 3.25b).

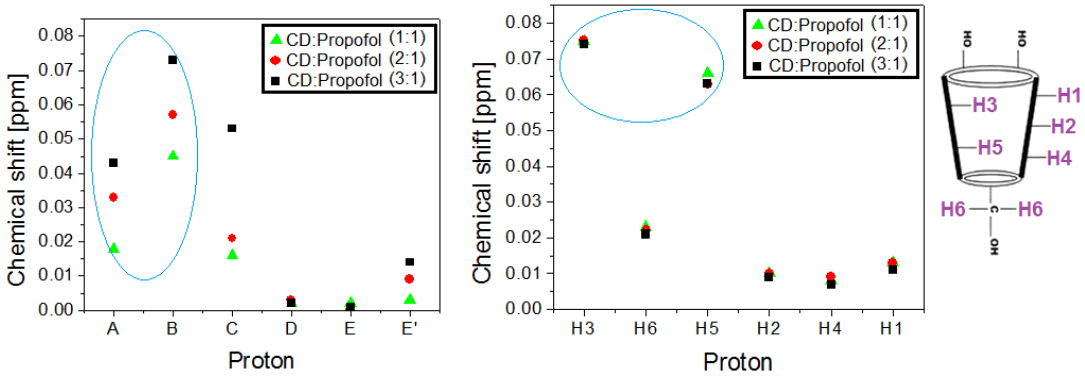
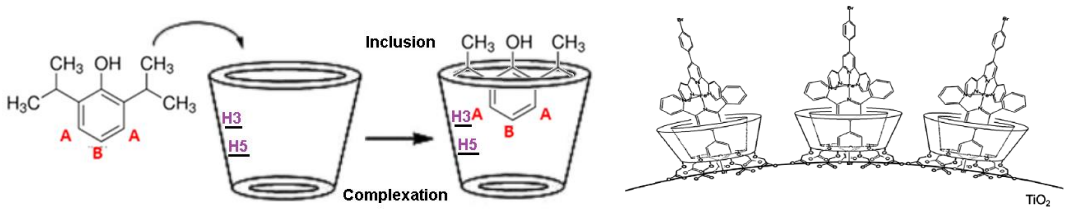


Figure 3.25: Summary of the changes in chemical shifts calculated from Fig. 3.23 and Fig. 3.24 with respect to the blue spectra for both guest and host molecules. (a) Variations for the protons of propofol and (b) variations for the protons of β −CD.

Therefore, the significant changes for the protons A and B in propofol and H3 and H5 for the host molecule (β −CD) are indicative of the inclusion occurrence depicted in Fig. 3.26a, i.e., the aromatic side of propofol is mostly set inside the cavity of the host β −CD for any of the three concentrations tested in NMR spectroscopy, demonstrating the inclusion configuration between these host-guest molecules.

The results presented in this subsection have demonstrated the complexation between β −CD and propofol and the mechanism of this inclusion mechanism is mainly due to Van der Waals forces and hydrophobic interactions [204]. The next step is to explain how this supramolecular host-guest interaction can be transduced onto the surface of optical fibres as a

means of developing cargo platforms for anchoring host molecules (similar to the scheme in Fig. 3.26b) and detect propofol, for instance, in aqueous solutions. Finally, it should be clarified that β −CD is the most commonly used host agent because its cavity size fits more satisfactorily to hormones, vitamins and many other compounds found in tissue and cell culture applications [174], [196].



(a) (b)

Figure 3.26: (a) Host-guest inclusion demonstrated through results presented in Fig. 3.25. (b) Representation of cyclodextrin and another type of guest molecule inclusion, both anchored on a cargo platform made of TiO_2 (schematic adapted from [205])

3.4.1 TiO_2 film based on Liquid Phase Deposition (LPD) imprinted for host-guest interaction and detection of propofol

Molecular imprinting is a promising approach to accomplish precise molecular recognition and, in general, the imprinting methods can be divided into two wide branches based on the matrix material used for template (analyte) incorporation: organic molecular imprinting (organic matrices) or inorganic molecular imprinting [134]. This and section 3.4.2 describe two approaches for the deposition of inorganic matrices molecularly imprinted for the detection of propofol. In particular, this section describes the method of Liquid Phase Deposition (LPD) of TiO_2 imprinted for host-guest interaction sites (β −CD/Propofol) and its characterization through UV-Vis and FTIR spectroscopy. These characterization techniques will be used to demonstrate the spectroscopy differences between pure TiO_2 films and imprinted TiO_2 with the organic molecules proposed in this research. The performance and

application of this functionalization technique onto an OFS for propofol detection will be presented in Chapter 5.

The LPD process was first developed in 1988 to form pure TiO_2 films [206] and it is well known that the morphology of these films (anatase, rutile, brookite or amorphous) depends on the substrate for deposition [207], pH, temperature and concentration of the solutions during deposition preparation [206], [208]. In addition, surface microstructure of the TiO_2 films can be modified when they are calcinated at high temperatures [206].

In this research, LPD deposition of TiO_2 films on substrates (or optical fibres) was made from ammonium hexafluorotitanate $(NH_4)_2TiF_6$ ($M_w = 197.93\ g/mol$, Mitsuwa Chemical Co. Ltd) in aqueous solution upon addition of boric acid (H_3BO_3, $M_w = 61.83\ g/mol$, Wako Pure Chemical Industries, Ltd.) in aqueous solution. All experiments were performed using deionized water (18.2 $M\Omega cm^{-1}$) obtained by reverse osmosis and subsequently subjected to ion exchange and filtration in a Milli-Q apparatus.

It is already known that the process starts by a ligand exchange equilibrium reaction between a titanium-fluoro complex ion $[TiF_6]^{2-}$ and water (Eq. 3.2). The addition of H_3BO_3 (Eq. 3.3) as a scavenger shifts equilibrium reaction (3.2) to the right by consumption of fluoride ions (F^-) to form more stable $BF_4{}^-$ ions, which promotes the consumption of non-coordinated F^- ions [206], [209].

$$[NH_4]_2TiF_6 + 2H_2O \rightarrow TiO_2 + 2NH_4 + 4HF \quad (3.2)$$

$$H_3BO_3 + 4HF \rightarrow BF_4 + H_3O^+ + 2H_2O \quad (3.3)$$

Aqueous solutions of $[NH_4]_2TiF_6$ and H_3BO_3 are prepared, mixed, stirred and used as treatment solution for deposition on a substrate. A molar ratio of $[NH_4]_2TiF_6$ / $H_3BO_3 = 1:2-4$ is suggested as most suitable for the formation of thin films [206].

Feng *et al*. [210] have claimed, for the first time, the feasibility of molecularly imprinted TiO_2 through a LPD process and demonstrated the formation of

binding sites for L-glutamic acid in TiO_2 films; they evaluated the transduction of the imprinted film using QCM and, as comparison, the results presented in their work followed similar transduction behavior than the results presented in this research (chapter 5) for the detection of propofol in aqueous solutions.

For this investigation, Table 3.3 presents a schematic of the materials used for imprinting the complex β −CD:Propofol on TiO_2 films produced by LPD. Firstly, an aqueous solutions of (1:1) β −CD:Propofol complex was prepared as a stock solution concentration of 1.6 mM which was sonicated and then stirred for more than 3 hours at c.a. 30 ^{0}C. After this, aqueous solutions of $[NH_4]_2TiF_6$ and H_3BO_3 were prepared with fourfold the concentration shown in Table 3.3 (100 mM : 200 mM for set 1). For instance, these precursor solutions were mixed as follows: 1 ml of complex β −CD:Propofol, 0.5 ml of $[NH_4]_2TiF_6$ and 0.5 ml H_3BO_3 to obtain the final concentrations of set 1. The mixture was stirred until all the compounds were mixed uniformly and used as the solution for the deposition on substrates (or optical fibres). In parallel, non-imprinted TiO_2 films were also prepared under exactly the same environmental conditions and concentrations for the purpose of comparison in the characterization of these films and their performance for the detection of propofol. Deposition time for the LPD process with imprinted and non-imprinted TiO_2 films onto optical fibres and substrates were between 15 and 42 hours at room temperature.

<table>
<tr><td>β −CD:Propofol
Ratio (1:1)</td><td>$[NH_4]_2TiF_6$: H_3BO_3
Ratio (1:2)</td></tr>
<tr><td rowspan="2">Final concentration: 0.8 mM</td><td>Final concentrations set 1:
25 mM : 50 mM</td></tr>
<tr><td>Final concentrations set 2:
50 mM : 100 mM</td></tr>
</table>

Table 3.3: Materials and typical final mixed concentrations used for the imprinting β −CD:Propofol complex on TiO_2 films. This deposition process is used onto optical fibres for detection of propofol (chapter 5).

Regarding the imprinted TiO_2 film and as established in equations (3.2) and (3.3), the addition of H_3BO_3 to the $[NH_4]_2TiF_6$ solution accelerates the hydrolysis reaction (ligand-exchange) and, simultaneously, several functional groups of the complex (multiple hydroxy groups of β −CD) react with the $[Ti(OH)_6]^{2-}$ species generated by the hydrolysis reaction of $[TiF_6]^{2-}$. Hydroxy groups from cyclodextrins are known to mediate compatibility with an inorganic-oxide matrix through hydrogen bonding [208].

Although LPD deposition times of TiO_2 films are long, this method is a convenient, low-energy and low-cost technique which provides an alternative approach to imprinting biomolecules in inorganic-oxide matrices. It should be said that, for the case of sensing propofol using the approach explained in this section, the template (propofol) from the complex needs to be removed from the organic-inorganic film created; this is normally done with appropriate organic solvents, in this case ethanol was used to remove propofol (5 min at room temperature).

Fig. 3.27 shows the set-up used for the deposition of the imprinted TiO_2 (with chemicals presented in Table 3.3) onto U-shaped fibres and after hydroxylation of the fibre surface with 1 wt% ethanolic KOH solution for 20 min; the set-up uses an HR-2000 spectrometer (resolution of 0.06 nm) and a HL-2000 tungsten-halogen lamp both from Ocean Optics. Data from the spectrometer is recorded in PC using the OOIBase32 operating software also from Ocean Optics; this software allows to record the spectra and single wavelength intensity tracking as fast as every 100 milliseconds. The experimental set-up for the deposition of the same film onto LPGs was as described in Fig. 3.15b using HL-2000 lamp and HR4000 spectrometer also from Ocean Optics; the interrogation system in this case was SpectraSuite® with sampling spectra at high scanning rate (Hz or KHz).

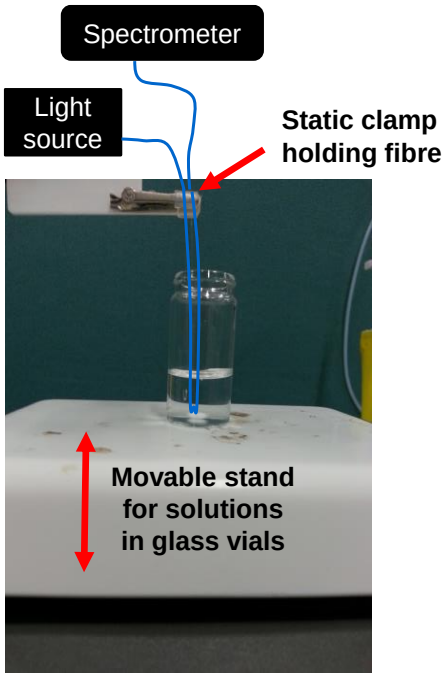
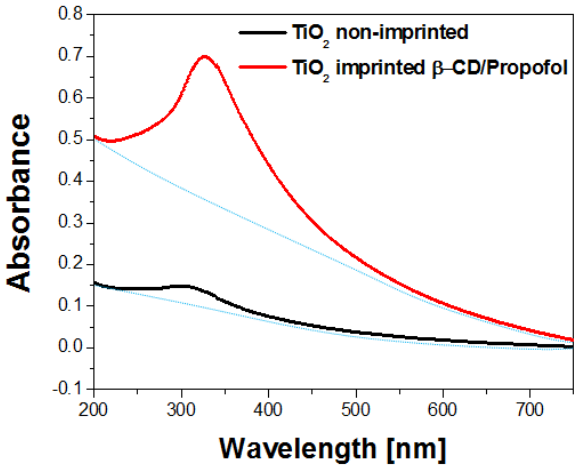
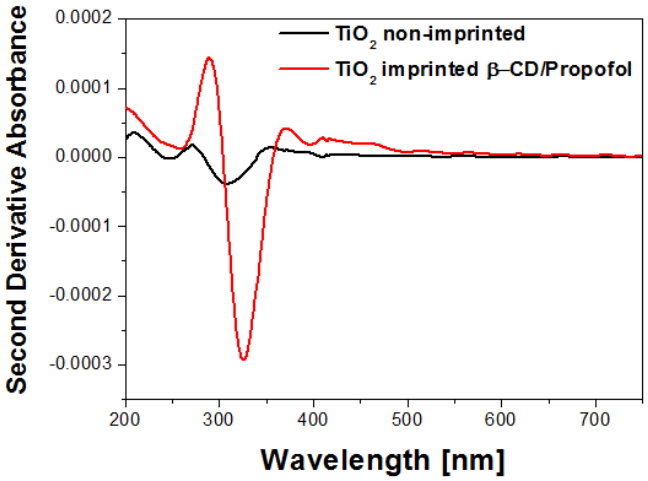


Figure 3.27: Set-up for the deposition of imprinted and non-imprinted TiO_2 films onto U-shaped fibres. The light source used was an HL2000 and the spectrometer was a HR2000 both from Ocean Optics.

Fig. 3.28a shows UV-Vis absorbance from the non-imprinted TiO_2 film and imprinted (β −CD:Propofol) TiO_2 film. Both films were deposited onto COC glass substrates previously cleaned (ethanol and deionized water), dried with N_2 gas, hydroxylated with 1 wt% ethanolic KOH for 20 min and using the LPD deposition concentrations of set 1 (Table 3.3, deposition time of 26.5 hr). Another cleaned and dried COC substrate was used as reference for blank measurements in the set-up previously shown in Fig. 3.3. Fig. 3.28b presents the second derivative method from the UV-Vis spectra shown in Fig. 3.28a for comparison between imprinted and non-imprinted TiO_2 films. Firstly, a baseline shown in blue in Fig. 3.28a demonstrates the absorbance due to the TiO_2 film deposited onto the substrate when it is nearly pure [211] and the increment in absorbance in the visible region is due to presence of the organic complex which can absorb light at different wavelengths (explained below).



(a)



(b)

Figure 3.28: (a) Comparison of the absorbance from imprinted and non-imprinted TiO_2 film deposited by LPD onto glass substrates. (b) Second derivative method from results shown in plot (a).

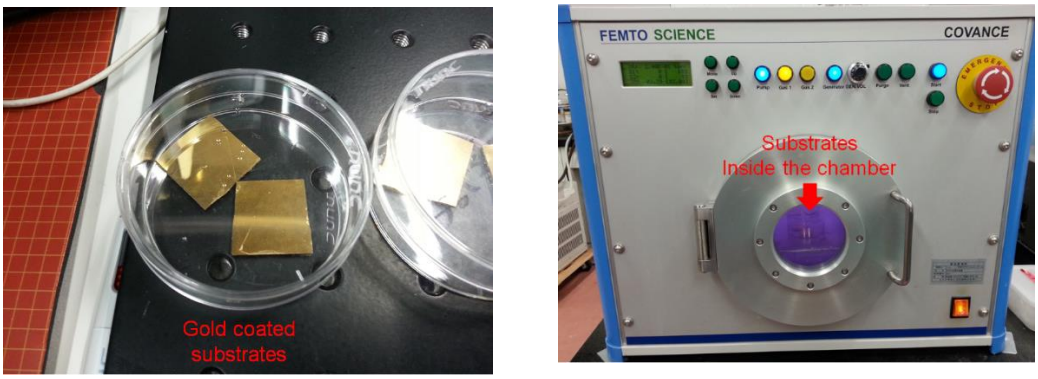
The second derivative UV-Vis spectroscopy method [212] is regularly used to quantitatively confirm maximum absorption measurements for compounds mixed in a multicomponent system [213]. In this case, the result presented in Fig. 3.28b was obtained following [214] and then performing the following processing steps in Matlab: (i) first derivative of spectra in Fig. 3.28a; (ii) application of smoothing filter Savitzky-Golay with 150 points and polynomial

order 5; (iii) second derivative and (iv) application of same Savitzky-Golay filter with same parameters of (ii).

The result presented in the original absorption spectra (Fig. 3.28a) confirms the range of absorption for cyclodextrins and propofol in the middle ultraviolet region between 200 and 300 nm [215]. The second derivative method (Fig. 3.28b) helps to identify critical points from the original absorption spectra. For instance, there is a turning point at ca. 286 nm in the original β −CD:Propofol/TiO_2 spectrum (Fig. 3.28a) which appears as a peak at the same wavelength in Fig. 3.28b. Similarly, the maximum absorbance at ca. 326 nm in the original β −CD:Propofol/TiO_2 spectrum (Fig. 3.28a) results as a negative peak in its second derivative plot (Fig. 3.28b). Additionally, in Fig. 3.28b, there are zero-crossing points at 258 nm, 304 nm (negative peak for the black curve) and 357.5 nm for the red curve; zero-crossing wavelengths are useful to discriminate between compounds in the overlapping bands [213], [216] and the results of Fig. 3.28b confirm that zero-crossing points are different between the black and red curves. Bailey *et al*. [212] have reported the wavelength 286 nm as attributable to the absorbance of propofol; Karim & Adnan [217], Kitamura & Imayoshi [218] and Özdemir & Biçer [215] have reported 260 nm as the maximum absorbance of β −CD. Nevertheless, the spectroscopic properties of the host-guest molecules tend to be modified as a result of the inclusion, usually to values higher than 300 nm for guest molecules already hosted by β −CD [213], [215], [217], [218] and this is clearly visible in the imprinted TiO_2 spectrum of Fig. 3.28a.

ATR - FTIR was used as a complementary technique for film characterization and thus corroborating spectroscopy differences between imprinted and non-imprinted TiO_2 films. Therefore, to test the differences between the imprinted and non-imprinted TiO_2 films using this technique, plain gold-coated silicon wafer substrates were cleaned (ethanol and deionized water), dried with N_2 gas and activated using a plasma surface treatment (Covance, FemtoScience Korea, Fig. 3.29b) for further thin film deposition, i.e.,

after plasma activation, the substrates were coated using the LPD process with the concentrations of set 1 (Table 3.3) and a deposition time of 21 hr for the imprinted case on the one hand, and same final concentrations of $(NH_4)_2TiF_6$: H_3BO_3 (25 mM : 50 mM) on the other for creating a pure TiO_2 film onto the gold coated substrate (non-imprinted case).



(a) (b)

Figure 3.29: (a) Plain gold coated silicon wafer substrates used for deposition of imprinted and non-imprinted TiO_2 films. (b) Plasma surface treatment chamber used at 0.24 torr of vacuum to functionalize the gold-coated substrates (allowing then deposition of titanium films afterwards).

After imprinting and non-imprinting TiO_2 LPD deposition onto the substrates shown in Fig. 3.29a, they were tested in the ATR-FTIR system explained in section 3.1.2. The FTIR spectrum from a gold coated substrate was taken as a reference baseline for the subsequent acquisition spectra of both imprinted-TiO_2 and non-imprinted-TiO_2 films. Tables 3.4 and 3.5 present the main vibrational modes and wavenumbers associated to TiO_2 and β −CD adsorbed to TiO_2 respectively when measured through FTIR; these wavenumbers are also highlighted in Fig. 3.30 for comparison. The National Institute of Standards and Technology (NIST) reports the wavenumbers from the strongest vibrational modes of propofol measured thorugh FTIR which are: 3610 cm^{-1}, 2930 – 2850 cm^{-1}, 1410 cm^{-1} and 1170 cm^{-1} [219]. For clarity, Fig. 3.30 is divided in four sections with vertical dashed lines in order to show the fourth main vibrational and stretching bands for pure TiO_2 films (non-imprinted)

and also for identifying more easily the vibrational and stretching bands for the imprinted TiO_2 case.

Non-imprinted TiO_2 - Modes and wavenumbers [cm^{-1}]
O – H vibration (H_2O); Ti – OH & N – H vibration for NH_4^+ ions: 2800 – 3800 cm^{-1} (1st section Fig. 3.30)
O – H and N – H bending vibrations: 1400 – 1750 cm^{-1} (2nd section Fig. 3.30)
Ti - F vibration: 700 – 900 cm^{-1} (3rd section Fig. 3.30)
Ti – O stretching and Ti – O - Ti bridging stretching: 400 – 700 cm^{-1} (4th section Fig. 3.30)

Table 3.4: FTIR spectral data for TiO_2 reported in reference [206].

β −CD adsorbed to TiO_2 - Main modes and wavenumbers [cm^{-1}]
ν(O – H): 3380 cm^{-1} (OH stretching groups, 1st section Fig. 3.30) ν(C – H): 2894 cm^{-1} (C-H stretching, 1st section Fig. 3.30) Adsorption from -CH_2- and –CH :2880 and 2930 cm^{-1} (1st section Fig. 3.30)
ν(C – O – C): 1034 cm^{-1} (2nd section Fig. 3.30) ν(C – O): 1145 cm^{-1} (2nd section Fig. 3.30) C – O conformation between TiO_2 and cyclodextrins: 1110 – 1160 cm^{-1} (2nd section Fig. 3.30)
C – H deformation vibration in carbohydrates and O – C – C – O relative ring vibration: 806 cm^{-1} (3rd section Fig. 3.30)

Table 3.5: FTIR modes for TiO_2/ β −CD reported in references [205], [215], [220], [221], [222], [223].

As can be confirmed in Fig. 3.30, adsorption of the complex β −CD:Propofol onto the TiO_2 surface is confirmed mainly from the appearance of the conformation stretching modes in the range between 1110 – 1160 cm^{-1}, i.e., ν(C – O – C): 1030 cm^{-1} and ν(C – O): 1158 cm^{-1} (*cf*. Table 3.5). Adsorption is also proved when O – H and N – H bending vibrations: 1400 – 1750 cm^{-1} are masked with mainly hydroxyl groups (ca.1650 cm^{-1}, Fig. 3.30) from the organic complex covering the TiO_2 surface. In addition, adsorption of the organic

complex β −CD:Propofol is evidenced through the shift obtained for vibrational modes ascribed to the O – H vibration of water adsorbed onto both films, non-imprinted and imprinted TiO_2 at 3410 cm^{-1} and 3360 cm^{-1} respectively.

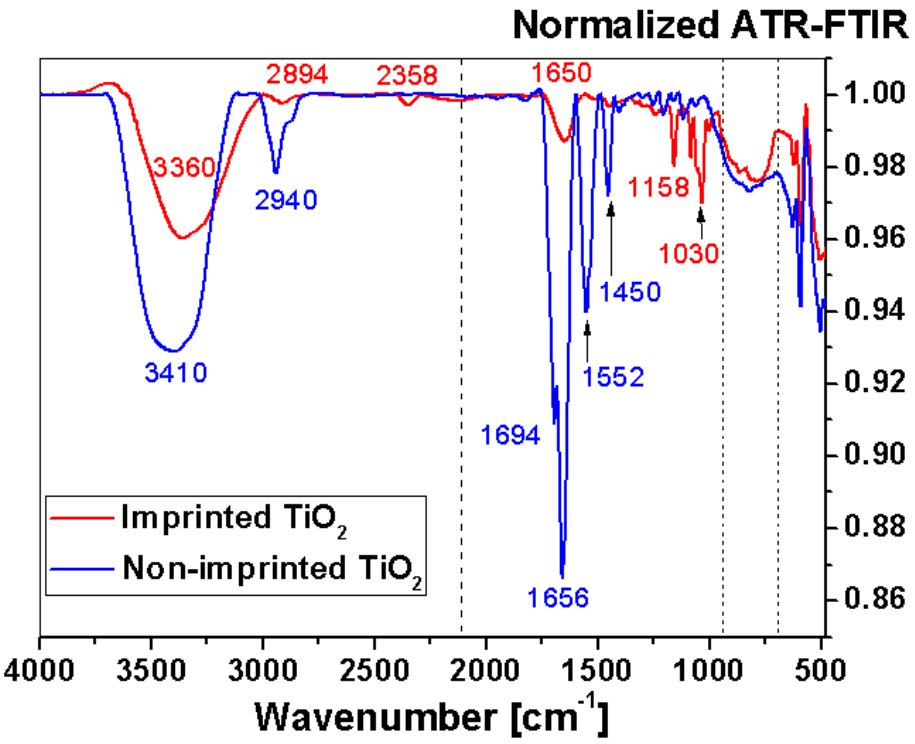


Figure 3.30: Comparison of ATR-FTIR spectra between pure TiO_2 and TiO_2 / (β −CD:Propofol).

3.4.2 Sol-gel preparation of mesoporous silica nanoparticles (MSNs) and TiO_2 imprinted for propofol detection

In analogy to the previous molecular imprinting method by LPD, this section describes another versatile and faster technique (sol-gel imprinting approach) for the deposition of films onto substrates or optical fibres to detect propofol. Any compound with functional groups from the smallest molecules to big structures such as proteins or cells can be the subject of imprinting in different porogens using water or dry organic solvents [21].

In organic molecular imprinting, the template molecule is linked to a functional monomer which in turn is cross-linked to an organic polymer, both polymerized together (for instance chemically) and then the template is removed to leave behind cavities specific for the analyte recognition. Inorganic molecular imprinting is based on a similar principle but using inorganic precursors such as metal alkoxides (Fig. 3.31) to form inorganic matrices via a sol-gel process that incorporates template molecules as shown in Fig. 3.31.

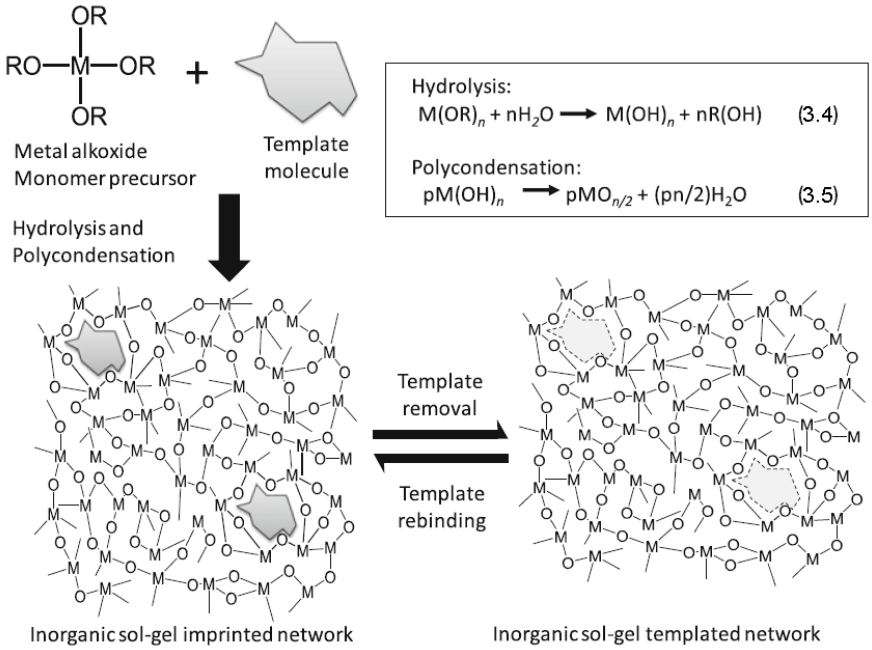


Figure 3.31: Schematic illustration of sol-gel approach; R=alkyl radical and M is a network-forming of metal alkoxides such as Ti or Si (adapted from [134]).

Most sol-gel techniques use water and low molecular weight alkoxides as precursors of the hydrolysis (Eq. 3.4, Fig. 3.31) and polycondensation (Eq. 3.5, Fig. 3.31). However, the hydrolysis reaction can also be promoted by acid catalysis and the polymerization process can be accelerated by basic catalysis [134]. In this section of the research, Titanium n-butoxide ($Ti(O\text{-}^{n}Bu)_4$, M_w=340.33, purchased from Kishida Chemical Co., Ltd) was used as a primary metal oxide precursor and it was dissolved with template propofol in aprotic solvent (Toluene:EtOH(99.5), (v/v) 1:1, $C_6H_5CH_3$=92.14, C_2H_5OH=46.07,

purchased from Wako Pure Chemical Industries, Ltd) to avoid hydrolysis at this stage and allow the template to bond to the adsorbing titanium alkoxide for more than 12 hr. For this case, 50 mM from the tension surface of Ti(O-^{n}Bu)$_4$ was mixed with 5 mM of propofol both dissolved in solvent Toluene:EtOH (1:1) and stirred overnight to allowed the complexation between Ti(O-^{n}Bu)$_4$ and template propofol.

Kunitake and Lee [224] are pioneer researchers in developing molecular imprinting achieved in ultrathin TiO_2 gel films via a surface sol-gel process. For instance, they have demonstrated the creation of imprints of carboxylic acids [224] and receptor sites by combination of β −CD/Bisphenol A [225]. This part of the research was designed in collaboration with Lee's laboratory at the University of Kitakyushu; as a first approach to target propofol and with the aim to enhance propofol detection sensitivity, the synthesis and use of MSNs was implemented as a first approach to increase surface area and, therefore, the number of imprints for the template analyte.

Synthesis of MSNs was as follows:

(i) 1.0 g of Cetyltrimethylammonium bromide (CTAB) was dissolved in 480 ml of deionized water (18.2 MΩcm^{-1}).

(ii) Addition of 3.5 ml of 2M NaOH (aq) as the sol-gel reaction catalyst was added.

(iii) The previous mixture was heated at 80 ^{0}C under vigorous mechanical stirring, then 5.0 ml of Tetraethylorthosilicate (TEOS) was introduced dropwise to the surfactant solution and it was left stirring for 2 h to give rise to white precipitates.

(iv) The solid product was filtered, washed with deionized water and MetOH, and dried in air.

(v) Removal of the surfactant template CTAB from the obtained product was dispersed ultrasonically and refluxed for 24 hr in a solution of 9.0 ml hydrochloric acid (HCl, 37.4%) and 160 ml of MetOH followed by washing with deionized water and methanol.

(vi) Finally the MSNs product was dried under high vacuum. Characterization from Lee's laboratory at the University of Kitakyushu provided MSNs with diameter of 180 nm with homogeneous pore distribution (ca. 3.4 nm) and surface area of ca. 900 m^2/g.

After stirring overnight the complexation between $Ti(O\text{-}^nBu)_4$ and propofol in toluene:ETOH (1:1), 1 ml of this solvent was used to prepare 0.5 wt% of MSNs and the mixture was stirred for 3 hr more. The last complete reaction generates a functionalization of MSNs by the complexed precursor $Ti(O\text{-}^nBu)_4$/Propofol. Thus, the network formed with metal alkoxides and the surface sol-gel process can be schematized as in Fig. 3.32.

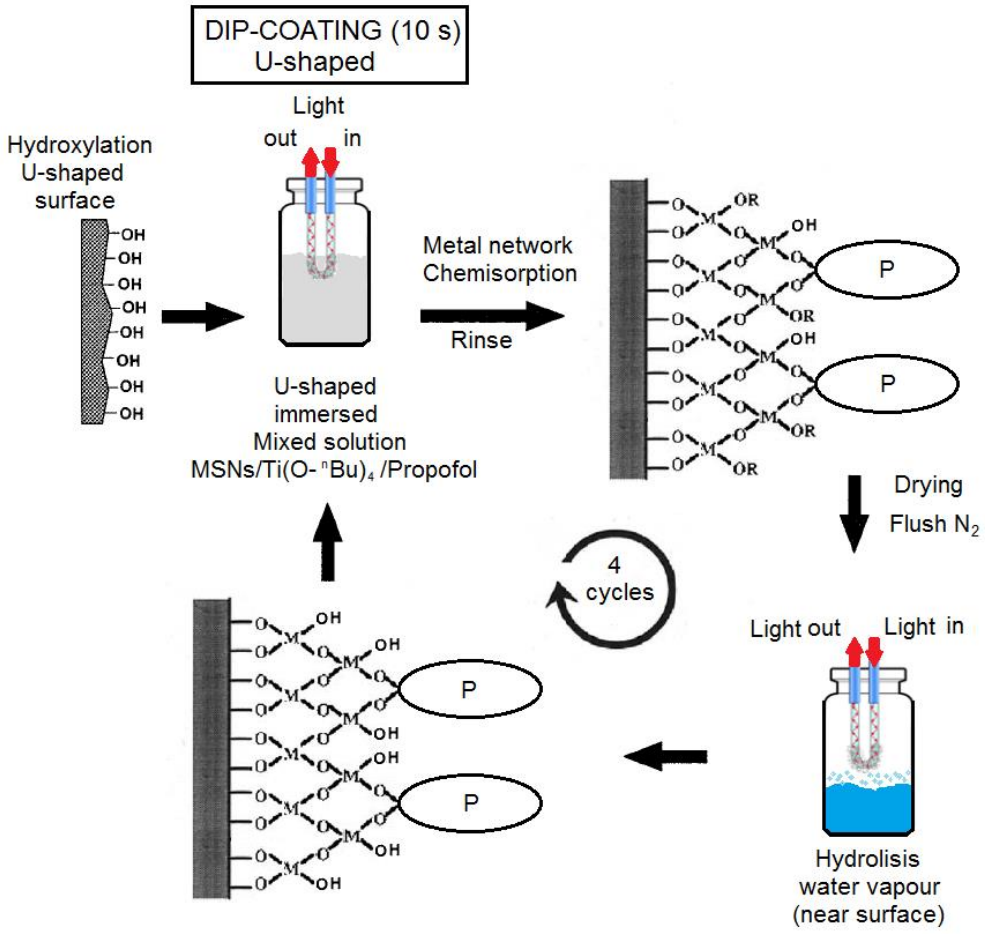


Figure 3.32: Schematic of the deposition process of the surface sol-gel method containing molecular imprints of an organic template molecule (propofol) (adapted from [226]).

The surface sol-gel method implemented (Fig. 3.32) was as follows:

(i) First step consisted in the hydroxylation of the U-shaped surface with 1 wt% ethanolic KOH (ethanol/water = 3:2, v/v) solution to terminate the surface with OH groups (20 min).

(ii) After drying, the U-shaped section was dip-coated in the as prepared complex solution (using set-up of Fig. 3.27), i.e., the U-shape fibre was maintained fixed with a static clamp and the dip coating was done manually (movable lift of Fig. 3.27) for 10 seconds; the metal alkoxide network in solution form layers covalently bound to the hydroxyl groups of the U-shaped surface.

(iii) The excessively adsorbed material is removed by flushing with N_2 and the chemisorbed amorphous metal oxide network is hydrolysed to provide new hydroxylated surface by locating the U-shaped section as near as possible of the tension surface of water.

(iv) This cycle process was repeated 4 times - from (i) to (iii) - to create a multilayer film.

During the experimental deposition, the first three hydrolysis periods lasted 5 min and fourth hydrolysis period was applied for 2.5 hr. In addition, transmission spectra could be recorded during all the experimental deposition of the sol-gel process as previously shown in Fig. 3.27, i.e., a HR-2000 spectrometer and a HL-2000 tungsten-halogen lamp were used to collect and provide a light spectrum through the fibre. Data from the spectrometer is recorded in PC using the OOIBase32 operating software (Ocean Optics); this software allows to record spectra and single wavelength intensity tracking as fast as every 100 milliseconds. Thus, transmission spectra could be recorded after each sol-gel process cycle (after hydrolysis).

Finally, as the final stage of this multilayer sol-gel process, the organic compound propofol incorporated in the multilayer metal oxide film needed to be removed by solvent washing as depicted in Fig. 3.31 and this was performed by dipping the U-shaped coated into solvent MetOH for 20 min

(small template molecules are easier to remove with solvent washing [224]). Under these conditions, imprints or cavities corresponding to the shape of propofol were produced within the metal oxide network and selectivity and adsorption to guest propofol was tested in aqueous solutions and gas phase as presented in chapter 5.

3.5 Summary comments

This chapter has firstly introduced the ancillary techniques SEM, TEM, FTIR spectroscopy, UV-Vis spectroscopy and NMR spectroscopy, all used for characterizing the nano-thin films deposited onto the sensors proposed in this research. Additionally, the methods and techniques used for fabricating optical fibre sensors have been explained in detail:

(1) LPGs were fabricated using the point-by-point approach and the amplitude mask technique to operate at or near the PMTP.

(2) FBGs were fabricated with the phase mask technique to create Bragg wavelength reflections between 1546 and 1552 nm.

(3) The facet end of optical fibres were prepared by cleaving the tip (SEM images were provided) in order to create Fabry-Pêrot sensors.

(4) U-shape probes were fabricated with an easy method by exposing the fibre to propane flame.

Last, two general functionalizing techniques were explained: the LbL method and two molecular imprinting methods, all characterized for being simple and non-expensive to perform with optical fibres. The LbL method is proposed for implementation on the tip of an optical fibre to create a Fabry-Pêrot type sensor for humidity sensing (chapter 4) and onto LPGs to create a biosensor for protein detection (chapter 5). Inorganic molecular imprinting is implemented onto LPGs and U-shape fibre sensors to create a biosensor for propofol detection (chapter 5).

Chapter 4: Optical fibre humidity sensor

The materials used for the development and functionalization of this OFS were presented in section 3.3.2 (using the LbL deposition method). A nano-thin film made of alternate layers of PAH and SiO_2 NPs was deposited onto the cleaved tip of an optical fibre coupler with the aim of developing a compact probe for humidity measurements in ventilator care equipment. The humidity OFS presented in this chapter behaves as a Fabry-Pêrot cavity (Fig. 1.15). The adsorption of water vapour by the thin film changes the optical thickness of the mesoporous film, which produces a change in the reflection signals and readout that can be used as a humidity-monitoring tool. In addition, an FBG written in the same fibre allows simultaneous temperature measurements and therefore the capability to show the sensor readouts as absolute humidity (AH).

This chapter presents the sensor calibration in a bench model against a commercially available temperature/humidity data logger (capacitive sensor for humidity, DS1923 individually calibrated in an NIST-traceable chamber). The sensitivity of the OFS is assessed in the humidity range from 5 %RH to 95 %RH for different bilayers of PAH and SiO_2 NPs. The response of the humidity OFS (1.13 s ± 0.30 s when the sensor response transitions from 92% RH to 42% RH) is faster than the electronic data logger used (datasheet response time 30 s, measured as 158 s). The calibration for the sensor response time is not performed using standard salt solutions as documented, for instance, in reference [38]. The humidity response time constant of sensor calibration follows the method implemented by the manufacturer of the capacitive sensor used as comparison for the OFS. The method is based on the average 1/e point as the sensor response transitions from 90% RH to 40% RH at equilibrium conditions and constant temperature (section 4.5).

After calibration, the optical fibre humidity sensor is tested in ventilator equipment, facemasks and nasal cannulas. The fast response time of the sensor proposed in this chapter enables humidity changes in individual human

breaths to be resolved and provides a potential use of the sensor to measure breathing rate and AH, as it is demonstrated in the bench top study using a mechanical ventilator, with preliminary tests in facemasks and nasal cannulas, and also demonstration in an animal study.

4.1 Introduction

There are a number of practical ways for building up optical fibre sensors to detect humidity ranging from evanescent wave type, in-fibre gratings (FBGs and LPGs) techniques, interferometric approaches, hybrid sensors (grating + interferometric) and absorption measurements [39], [38]. In addition, the humidity sensitive coatings deposited onto the optical fibres are key factors for the performance of the sensors. Alwis *et al.* [38] have published an excellent review of the current state of the art of optical fibre-based sensors for humidity and moisture containing a wide range of different types of sensitive materials (organic and inorganic) used for humidity sensing. Table 4.1 summarizes and presents some of these approaches.

Reference	Approach	Sensitive coating	Range (%RH)	Sensitivity Response time
2012 Zhang *et al.* [227]	FBG	No coating. PMMA cladding.	30 – 90	33.6 pm/%RH 7 min
2008 Venugopalan *et al.* [228]	LPG	Poly(vinyl alcohol)	75 - 97	5.68 nm/%RH < 1min
2010 Fuke *et al.* [229]	Evanescent Wave	Ag-Polyaniline	5 – 95	28.78 mV/%RH 30 s
2012 Liang *et al.* [230]	Interferometric	Poly(vinyl alcohol)	20 – 80	0.98 nm/%RH <6 s
2013 Mathew *et al.* [231]	Bragg grating + Interferometric	Agarose	60 – 90	0.163 dB/%RH <1 s
2009 Hernáez *et al.* [232]	Absorption	Indium tin oxide/PAH/ Poly(acrylic acid)	20 – 80	1.08 nm/%RH --
2008 Corres *et al.* [233]		SiO_2 NPs	75–100	0.3 dB/%RH <1 s

Table 4.1: Optical fibre-based humidity sensors with high sensitivities reviewed in [38].

Particularly, Corres *et al.* [233] first demonstrated a humidity sensor at the tip of an optical fibre based on a multilayer hydrophilic film comprised of layers of SiO_2 NPs with alternating pH. Through tests conducted using a humidity chamber, the sensor was demonstrated to have low hysteresis and fast response time. A simple experiment of monitoring 3 breaths on the sensor indicated potential for breathing rate monitoring. In this work, a sensor probe film has been developed by depositing alternate layers of PAH and SiO_2 NPs (section 3.3.2, chapter 3) on the cleaved tip of an optical fibre coupler (forming a Fabry-Pêrot cavity, Fig. 4.1). In contrast to Corres *et al*. [233], this work uses PAH, a highly hydrophilic polycation layer, to assemble a SiO_2 thin film. The PAH layer increases the sensitivity of the sensor due to high hydrophilicity and also reduces the number of deposited layers, thus increasing the efficiency of the fabrication procedure. In comparison to other sensing techniques, the approach proposed in this work has the advantage of simple configuration, small size probe (fibre tip), easy fabrication and low cost manufacture using the PAH/SiO_2 sensing film explained in section 3.3.2. This sensitive inorganic coating is a key factor that determines the hygroscopic properties and performance of the optical fibre humidity sensor presented in this chapter. Despite the fact that there have been several publications dedicated to measuring relative humidity and temperature simultaneously using different optical fibre structures [39], this work has been reviewed as the first work of its kind investigating the application of optical fibre temperature and humidity sensors to improve the performance of ventilator care equipment [19].

The next sections of this chapter will explain first the physical principle of how water vapour can be absorbed in the sensing film proposed for humidity sensing in this work; the results of the deposition of the thin film onto the tip of the fibre; the temperature sensitivity and humidity calibration based on the thickness or number of bilayers deposited, and the humidity sensor response time constant. The final sections will present the results obtained when the optical fibre humidity sensor was tested in a mechanical ventilator, in an animal

study and with preliminary trials of a recently approved (August 2017) ethical protocol to test the sensor in a human volunteer study.

4.2 Adsorption of water vapour molecules in the Fabry-Perot sensing film

Water can exist in two forms when carried in gas: “moisture” is water in liquid form that is suspended in a gas in the form of small droplets, and “humidity” is water vapour (i.e. in gas phase) [39]. Humidity can be described as “Absolute Humidity”(AH) or “Relative Humidity” (RH): AH is the mass of water vapour in a given volume of gas (mg H_2O/L or g/m^3), while RH is the amount of water vapour present in a gas as a percentage of the saturated vapour pressure capacity at a particular temperature [38], [107], [234]. Generally speaking, on exposure of the hydrophilic film to a humid environment (Fig. 4.1), the water vapour enters inside the film and forms new space, changing the effective refractive index (n_{eff}) and optical thickness of the film ($n_f \cdot L$), thus inducing a change in the overall reflection at the tip [27], [235]. Mathematically, the total reflection from the Fabry-Pêrot sensing film is calculated from Eqs. (1.15) presented in chapter 1.

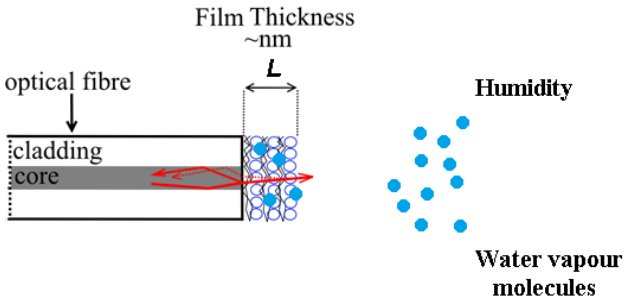


Figure 4.1: The OFS works as a Fabry-Pêrot cavity when a multilayer film of PAH/SiO_2 is deposited onto the tip (the optical thickness of the film changes when exposed to a humidified environment).

The mechanism of the adsorption of water vapour molecules on SiO_2 takes place firstly as chemisorption, followed by physisorption (Fig. 4.2) [32]. As shown in Fig. 4.2, firstly, the silica facilitates the dissociation of water vapour

in the vicinity of the surface into a hydroxyl group which binds to a metalloid cation site, and a proton binding to an oxygen anion site. Second, once hydroxylation of the surface is fulfilled, water vapour is physisorbed through double hydrogen bonds shared between hydroxyl groups. Upon finalization of the first physisorbed layer, subsequent layers are adsorbed via single hydrogen bonds. Lastly, after multiple physisorbed layers, water starts to be condensed into the capillary pores formed inside the film [32].

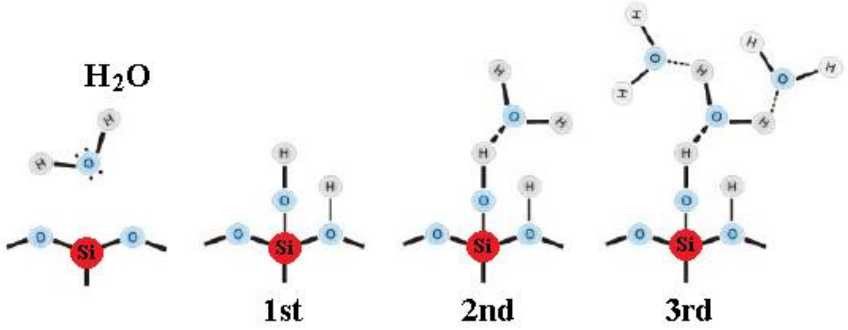


Figure 4.2: H_2O vapour adsorption on the metal oxide surface (modified from [32]).

If the humidity (H) and temperature (T) are chosen as the two variables to represent each thermodynamic state for the situation depicted in Fig. 4.1 and Fig. 4.2, then the infinitesimal change from the response (R) of the sensor is given by equation (4.1) [236],

$$dR = \left(\frac{\partial R}{\partial H}\right)_T dH + \left(\frac{\partial R}{\partial T}\right)_H dT \tag{4.1}$$

where $(\partial R/\partial H)_T$ is the sensitivity to humidity defined as the ratio of the change in the sensor output to the change in ambient humidity when temperature is constant; $(\partial R/\partial T)_H$ is the sensitivity of the sensor to temperature when humidity is kept constant.

Therefore, the sensitivity (S) and response (R) of optical fibre humidity sensors with non-temperature cross-talk and having a dependence on the

refractive index (n_f) change produced by the adsorptions of water vapour molecules is:

$$S = \frac{\partial R(n_f)}{\partial H} = \frac{\partial R}{\partial n_f} \cdot \frac{\partial n_f}{\partial H} \tag{4.2}$$

Equation (4.2) has applied the chain rule [237] and it is written as a partial differential equation due to the fact that some coatings might swell and present thickness changes. The term $\partial R/\partial n_f$ is the specific sensitivity given by the optical fibre structure used and the term $\partial n_f/\partial H$ is the hygroscopic property of the nano-film itself.

The parameter H in equations (4.1) and (4.2) can be either AH or RH, but in the field of mechanical ventilation RH is often used, and the relation between them is,

$$RH = \frac{P_w(T)}{P_{ws}(T)} \cdot 100\% \tag{4.3}$$

where P_w/P_{ws} is the ratio of the water vapour pressure to the saturation water vapour pressure at a specific temperature [145], [238]. The saturation vapour pressure $P_{ws}(T)$ dependency on temperature is not linear and it has been modelled by the National Bureau of Standards since 1934 [239]. Finally, the water vapour pressure can also be calculated from,

$$AH = C\frac{P_w}{T} \ [\mathrm{g/m^3}] \tag{4.4}$$

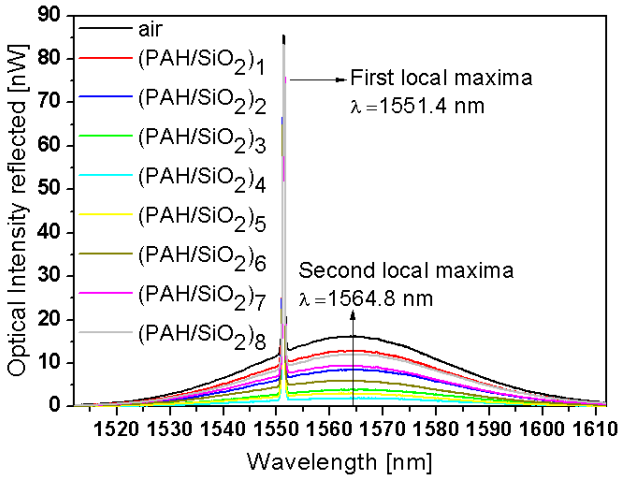
where $C = 2.16679\ \mathrm{gK/J}$ is a constant value and the water vapour is assumed to be an ideal gas [238].

4.3 Results of PAH/SiO_2 film deposition onto the optical fibre tip

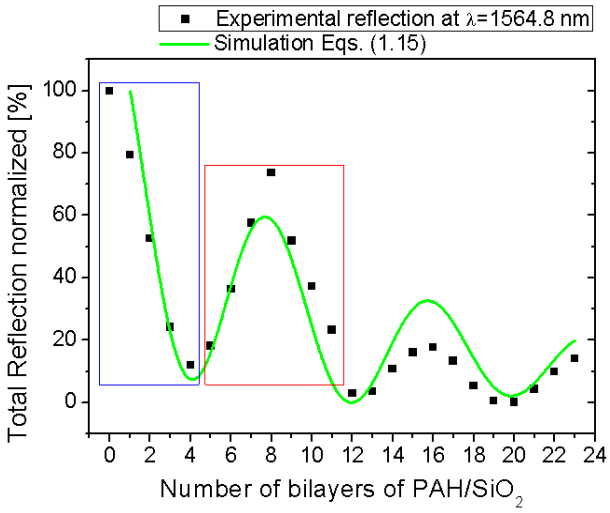
The experimental set-up for the deposition of the sensing film was presented in Fig. 3.18 (section 3.3.2, chapter 3) using a SMF coupler containing an FBG with Bragg wavelength at 1551.4 nm, an SLD light source and an I-MON spectrometer (sub-picometer resolution, Ibsen Photonics A/S) for acquiring the total reflection spectra. Fig. 4.3a shows the detected spectra during deposition of the first eight alternating bilayers of PAH and SiO_2, denoted as $(PAH/SiO_2)_1$, $(PAH/SiO_2)_2$ ... $(PAH/SiO_2)_N$ where N is the layer number. The first local maximum (λ =1551.4 nm) in Fig. 4.3a is due to the Bragg wavelength reflection from the FBG written in the core of the fibre; during film deposition temperature does not change and therefore the peak at 1551.4 nm does not shift. The second local maximum changes its amplitude over the number of bilayers deposited and it is used for tracking the reflections due to the Fabry-Pêrot cavity formed by the film onto the tip of the fibre. Fig. 4.3b plots the change in reflection intensity of the second local maximum (λ =1564.8 nm) after depositing each of 23 bilayers of PAH/SiO_2 (in this research the last layer is always made of SiO_2 NPs to favour water vapour adsorption as explained in section 4.2).

The experimental results shown in Fig. 4.3b demonstrate the reflection intensity decay expected from the simulation of Eqs. (1.15), using λ =1564.8 nm, 75 nm as the effective physical length of every bilayer, transmission loss factors of 0.05% and refractive indexes as follows: n_{eff} =1.28 (effective refractive index of sensing film), n_{fibre} =1.46 and $n_{air} = 1$. Therefore, it is anticipated from Fig. 4.3b that humidity sensing would be favored in the region of thicknesses between 7 and 11 bilayers of PAH/ SiO_2 where the total reflection is higher and the slope of the reflection change is also higher (red rectangle in Fig. 4.3b). The first pronounced reduction in reflection intensity (blue rectangle in Fig. 4.3b) should not be considered as a suitable option because the growth of the initial layers is not uniform due to lack of surface coverage. In this case, some parts will not be fully charged after deposition of

the first layers of PAH. This was confirmed in the results presented in section 3.3.2 of chapter 3 where Fig. 3.19a and Fig. 3.19b showed SEM images of the hydrophilic film created during the LbL assembly process. Comparison of Figs. 3.19a and 3.19b confirms that a highly uniform film is deposited onto the optical fibre only after 4 bilayers (this was also confirmed in reference [240]).



(a)



(b)

Figure 4.3: (a) Total reflection spectra measured using the set-up shown in Fig. 3.18 after deposition of bilayers of PAH/SiO_2 onto the tip of the fibre; (b) Tracking of the optical reflection intensity at the second local maxima (λ =1564.8 nm) after depositing each of 23 bilayers of PAH/SiO_2 on the tip of the fibre and simulation result using Eqs. (1.15), λ =1564.8 nm and $n_{eff} = 1.28$.

4.4 Humidity sensor tip calibration

Fig. 4.4 presents the experimental set up for humidity calibration measurements. The sensor probe (coated tip, Fig. 4.4) and a commercial capacitive data logger (Maxim Integrated, DS1923, RH range of 0% to 100%; accuracy ± 5% in the range of -20 ℃ to +85 ℃, resolution 0.04%RH in 16-bit mode, humidity response time constant of 30 s and optional temperature compensation) are placed 1 cm apart in a measuring cell (200 ml). The cell receives either humidified (via flowmeter F1, Cole-Parmer, OU-32460-42, range 0 L/min to 1 L/min) or dried (via flowmeter F2) gas through the circuit. The rate of flow via the gas inlet (L) is constant (1 L/min) and the flow meters enable different levels of humidification. Fibre tips with different numbers of bilayers were tested in order to ascertain the most sensitive response to humidity.

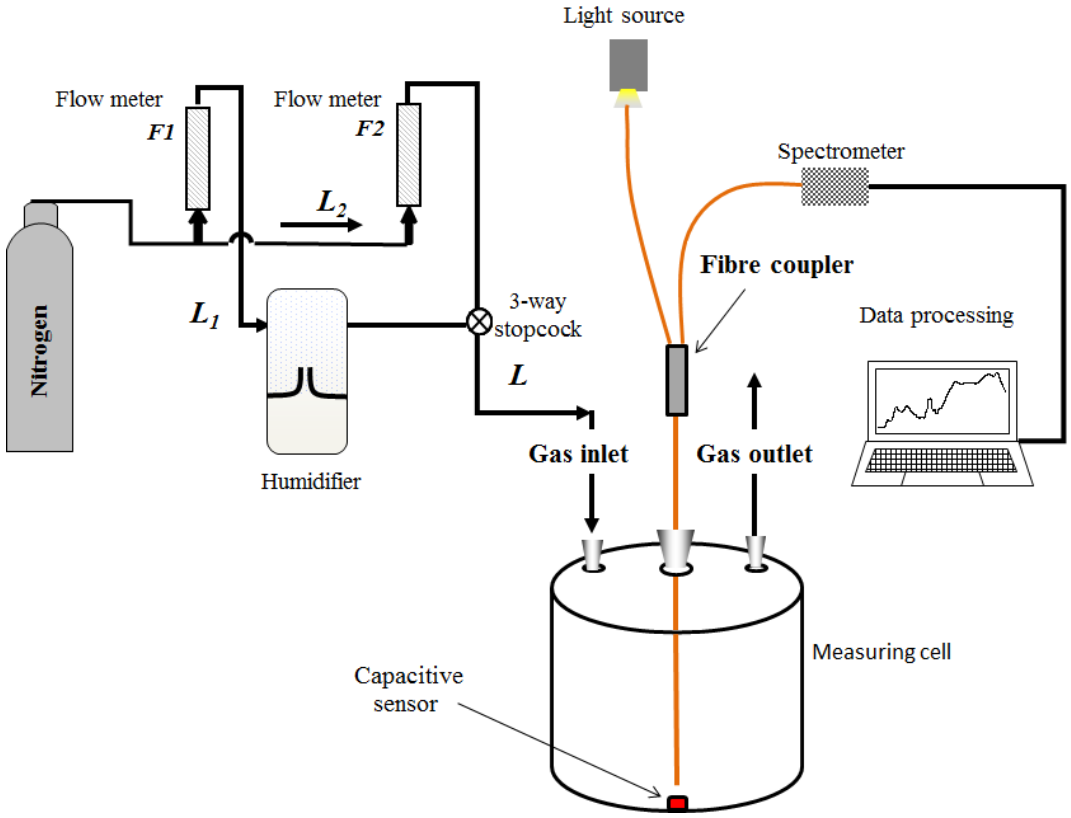


Figure 4.4: Humidification system to calibrate the optical fibre humidity sensor against a capacitive sensor; temperature inside the measuring cell was constant at 25.4 ℃ ± 0.4 ℃.

Deposition of PAH/SiO_2 films can be performed onto tips of MMF or SMF with analogous results. In this case, Fig. 4.5 shows a typical sensor response for a 4 bilayer film on exposure to different levels of humidity, using MMF coupler coated tips, broadband light source (HL-2000, Ocean Optics) and CCD spectrometer (HR4000, Ocean Optics). The reflection spectra acquired were in the visible range and only the wavelength λ = 618.13 nm is plotted in all figures of this subsection and subsections 4.5, 4.7 and 4.8 in order to measure the sensor response. It can be seen that the response of the optical fibre humidity sensor is inversely correlated with the response of the capacitive sensor (Figs. 4.5 and 4.6). It should be noted that in this calibration experiment the temporal transitions of the capacitive sensor and optical fibre sensor between every step in Fig. 4.5, are similar and are only limited by the rate of change of air in the flowmeters, i.e. the transition times are not related to the response time of the two sensors. The red line in Fig. 4.5 is the RH change measured by the capacitive sensor. The average temperature is 25.4 ± 0.4 ℃ during all measurements over the 30 min period.

The humidity levels (Fig. 4.5) produced with the air flowmeters depicted in Fig. 4.4 are:

(a) L_2=1.0 L/min, L_1=0.0 L/min.
(b) L_2=0.8 L/min, L_1=0.2 L/min.
(c) L_2=0.6 L/min, L_1=0.4 L/min.
(d) L_2=0.4 L/min, L_1=0.6 L/min.
(e) L_2=0.2 L/min, L_1=0.8 L/min.
(f) L_2=0.0 L/min, L_1=1.0 L/min.

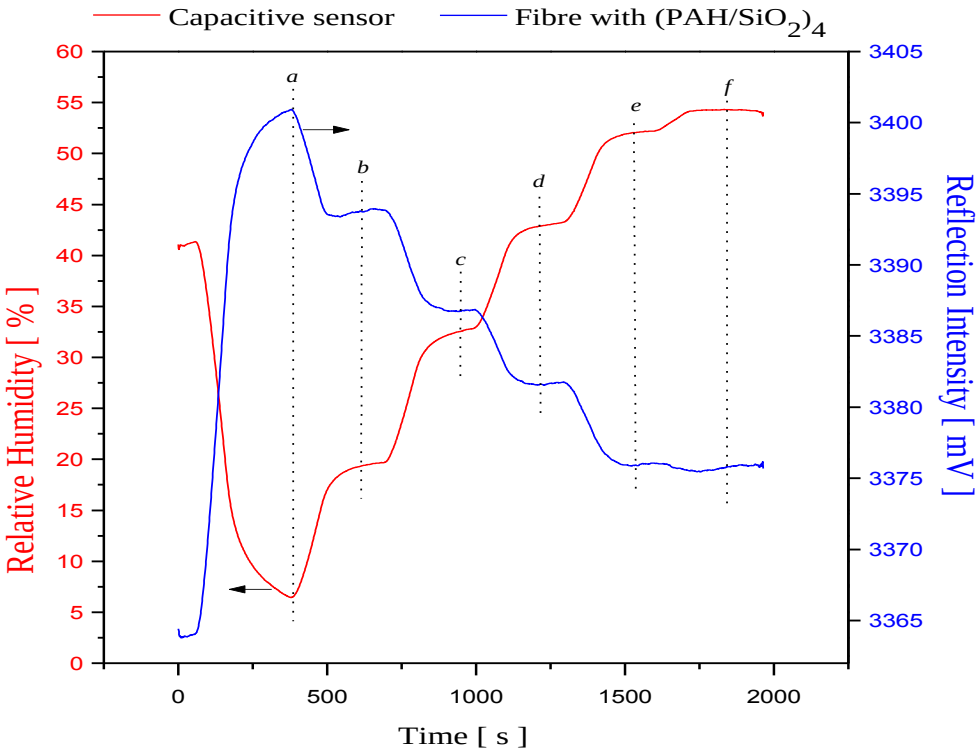


Figure 4.5: Dynamic change of the optical fibre humidity sensor (response at λ = 618.13 nm, applying a 5-point average filter every 20 s in time domain) modified with 4 bilayers thin film (blue line, $(PAH/SiO2)_4$) upon exposure to the different levels of humidity (red trace). The values correspond to flowmeter settings of (a) L_2=1 L/min, L_1=0 L/min; (b) L_2=0.8 L/min, L_1=0.2 L/min; (c) L_2=0.6 L/min, L_1=0.4 L/min; (d) L_2=0.4 L/min, L_1=0.6 L/min; (e) L_2=0.2 L/min, L_1=0.8 L/min; (f) L_2=0 L/min, L_1=1 L/min.

Fig. 4.6 shows the effect of the film thickness on the sensitivity. The thicker PAH/SiO_2 film leads to an increase in the sensitivity of the optical fibre humidity sensor. The increase of the geometrical thickness leads to a sinusoidal-type change in the reflection (tracked at specific wavelengths) whose intensity depends on the number of layers (Fig. 4.3b) [192], [241]. For three bilayers, the sensitivity was 0.26 mV/%RH, for four bilayers sensitivity increased to 0.53 mV/%RH and for nine bilayers, the sensitivity increased to 2.28 mV/%RH (Fig. 4.6). Briefly, the increase in the thickness between 7 and 11 bilayers produces higher sensitivity and sharper or more sensitive response to effective refractive

index change (typically from 1.22 to 1.33) and optical thickness when the mesoporous film is exposed to water vapour molecules [235], [233].

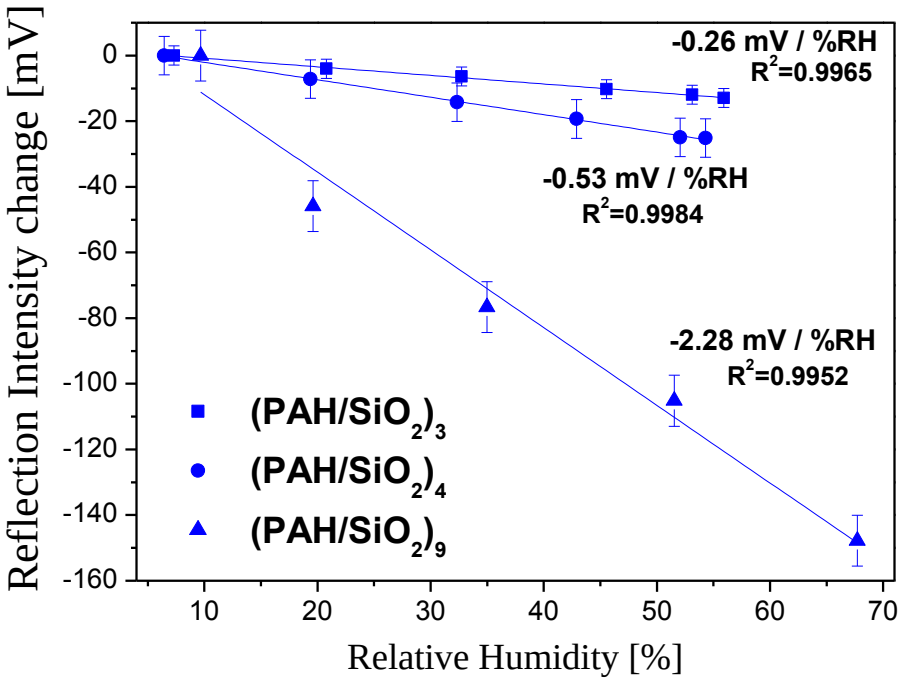


Figure 4.6: Calibration curves for three, four and nine alternate bilayers of PAH/SiO_2 film showing the sensitivity for each case. For the purpose of clarity, the calibration curves are placed in the same plot showing differences in reflection intensity with respect to the first experimental value in each calibration curve.

In order to investigate the repeatability and hysteresis of the sensor, the optical fibre humidity probe with 9 bilayers was tested further using the set-up shown in Fig. 4.4. Through repeating three times in both forward from ~5% RH to ~76% RH (red line, Fig. 4.7) and backward (blue line, Fig. 4.7) directions, the hysteresis of the optical fibre humidity sensor with $(PAH/SiO2)_9$ was obtained (Fig. 4.7). Finally, a least squares linear fit was performed on each calibration curve to obtain a sensitivity of 2.17mV/%RH (increasing humidity) and 2.28mV/%RH (decreasing humidity).

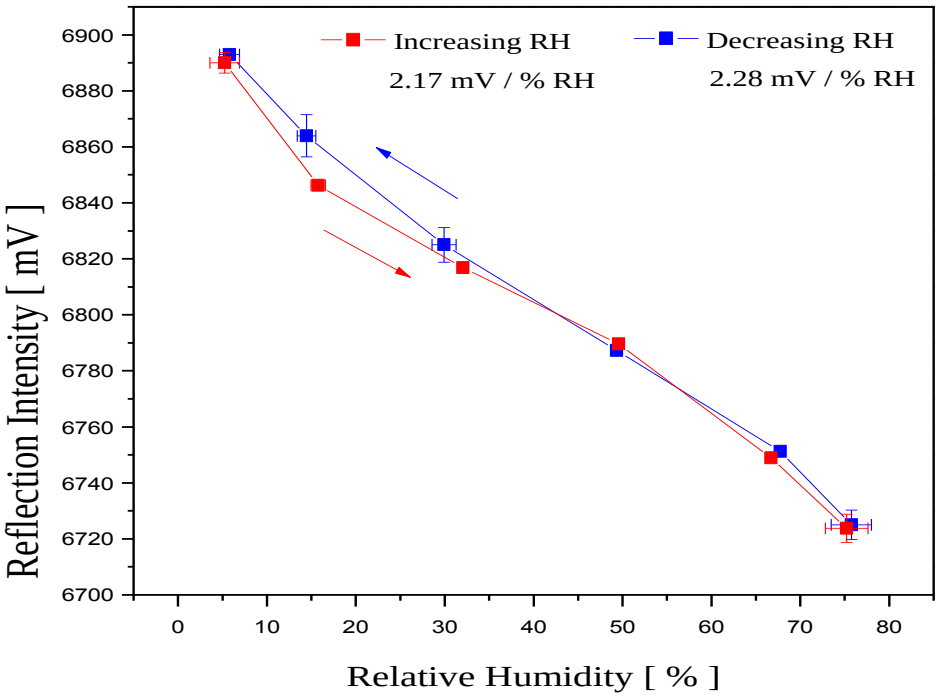


Figure 4.7: Hysteresis of the optical fibre humidity sensor with 9 bilayers. The red trace is obtained by increasing the RH from 5% RH to 76% RH, and plotting reflection intensity measured in the fibre against RH measured in the capacitive sensor. The blue trace shows the decrease in RH from 76% RH to 5% RH.

The result shown in Fig. 4.7 demonstrates that the OFS with 9 bilayers has higher hysteresis in the low %RH range (< 40 %RH). The hysteresis of the sensor in the range of interest is feasible for applying in medical devices used in the ICU (from section 4.7 to section 4.9) where higher levels of humidification are more likely to be found. Nonetheless, the result of Fig. 4.7 also shows that the standard deviations at higher levels of humidification (near 80 %RH) are larger most probably due to formation of condensation inside the film. This can be avoided by protecting the optical fibre tip with a wool-foam normally used in Heat and Moisture Exchangers (HMEs) as will be demonstrated in section 4.7.

4.5 Humidity sensor response time constant

Fig. 4.8 depicts the experimental set-up used to measure humidity response time constant. The optical fibre humidity probe was inserted into and extracted from the headspace of a Petri dish (65 ml) containing 10 ml of water. The fibre was contained inside a 23-gauge medical hypodermic needle in order to provide mechanical protection for the thin film deposited onto the tip of the fibre. The petri dish was closed until the humidity (measured using the capacitive sensor inside the petri dish) stabilized (92%RH). The external capacitive data logger monitored room humidity (42 %RH).

The experimental procedure for determining the humidity response time constant used by the manufacturer of the capacitive data logger was followed in order to make comparison with the optical fibre device. The average 1/e point as the sensor response transitions from 90% RH to 40% RH (in this case from 92% RH to 42% RH) at equilibrium conditions and constant temperature (in this case T=21.4 ± 0.2 ℃) was obtained by inserting and extracting the optical fibre humidity probe five times from the Petri dish.

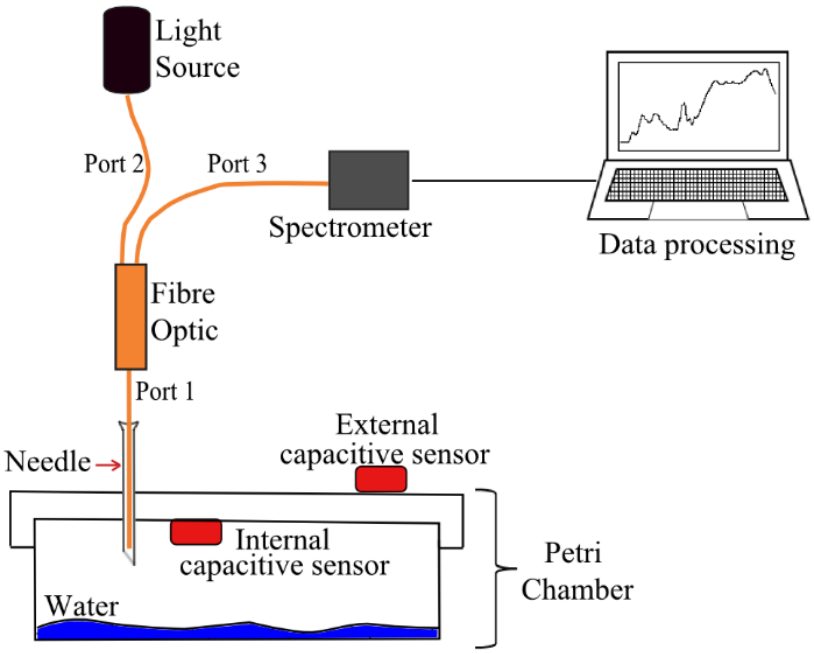


Figure 4.8: Set-up to measure the humidity response time constant.

Fig. 4.9 shows an example of a step response of the fibre humidity sensor upon insertion into the humid environment (Fig. 4.8). The red trace in Fig. 4.9 shows that the maximum humidity (92% RH) at saturation vapour pressure inside the Petri dish was reached after 20 min (measured by the internal capacitive sensor). The blue trace plots the response of the fibre sensor at saturation vapour pressure (from 1550 s to 1800 s).

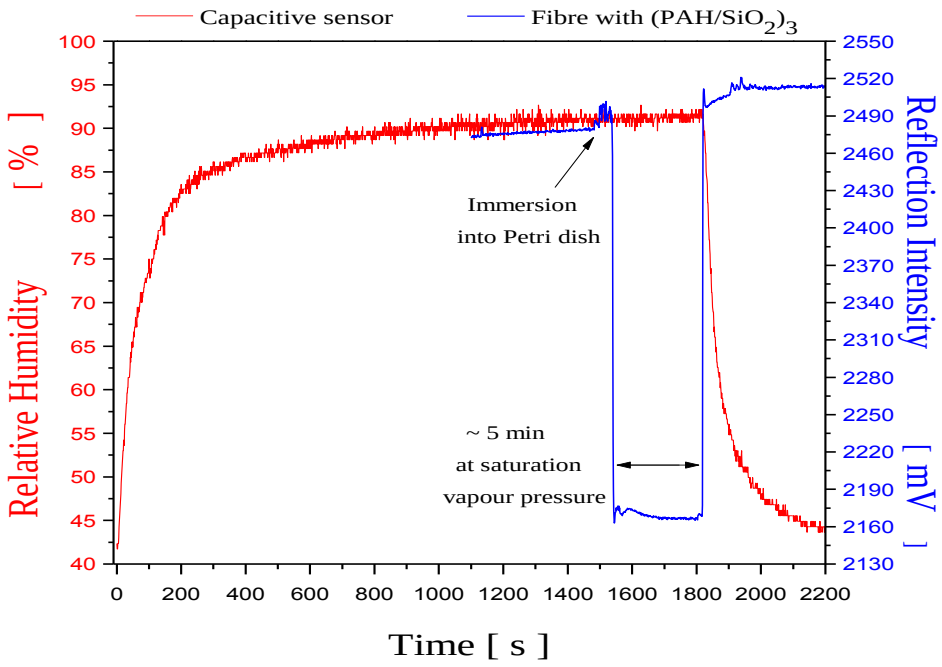


Figure 4.9: Comparison of the response of the optical fibre humidity sensor with $(PAH/SiO2)_3$ and the internal capacitive sensor depicted in Fig. 4.8.

After 1800 s in Fig. 4.9, both sensors, fibre and internal capacitive sensor, were simultaneously exposed to environmental room humidity through removing the Petri dish cover. The mean response time of the optical fibre humidity sensor (based on the 1/e point) was 1.13 s with a standard deviation error of ± 0.30 s based on five repeated measurements. The response time of the capacitive sensor was 158 seconds (five times longer than the time constant reported in the datasheet, 30 s).

4.6 Temperature and absolute humidity simultaneous calibration

The previous section aimed to characterize and determine the sensitivity to humidity. It also demonstrated a better response time than the commercially available capacitive sensor. The primary goal in this subsection is to present an extension of the optical fibre sensor through calibrating an FBG (with a peak reflection of λ =1550.6 nm at 22 ^{0}C) to measure temperature simultaneously and allow the calculation of absolute humidity levels through equations (4.3) and (4.4). Fig. 4.10 presents the experimental set-up for temperature and humidity simultaneous measurements in a drying and heating chamber (FD23, BINDER, Interior volume 20 L). After depositing 9 bilayers on the tip of the fibre as explained in section 4.3, the coated tip and the FBG were placed inside the climatic chamber along with two type-k thermocouples (USB TC-08 Data Logger, Pico Technology) and the capacitive humidity data logger. Once all the sensors were inside the chamber, the temperature was increased until after 300 s the temperature increased up to 60 ^{0}C and RH decreased to 9% (Fig. 4.11).

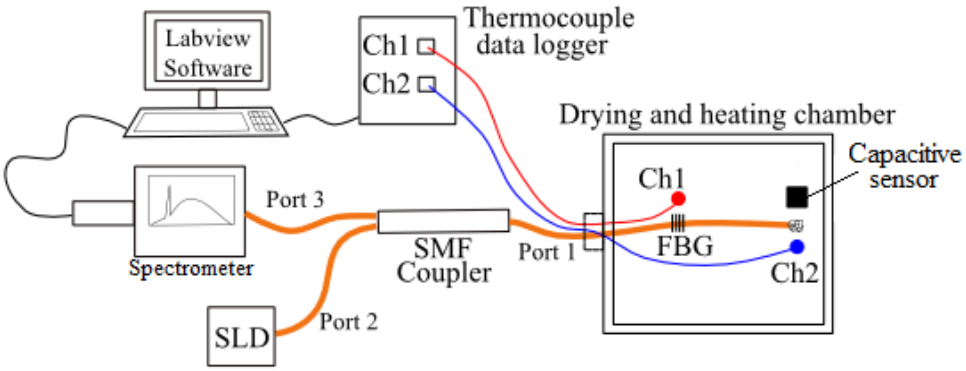
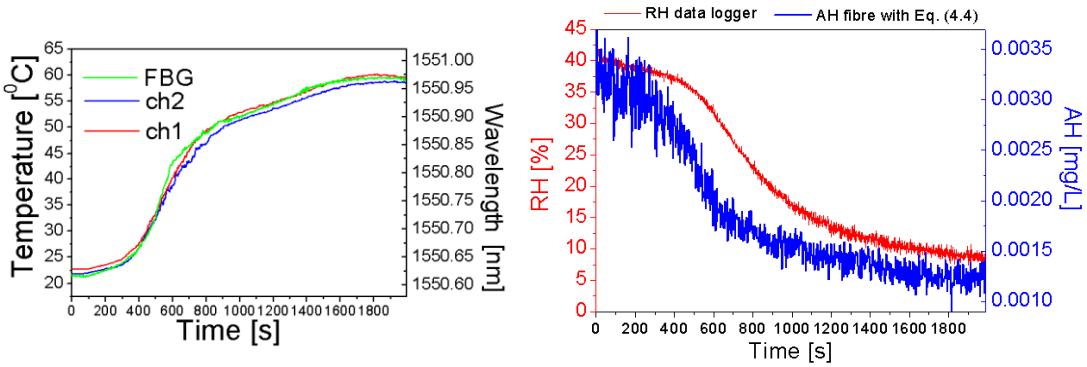


Figure 4.10: Set-up to test the optical fibre temperature-humidity sensor in a drying and heating chamber.

Fig. 4.11a compares the wavelength shift of the FBG and the readings from two thermocouples placed in the drying and heating chamber used for calibration; the Bragg wavelength shift sensitivity was linear 9.9 pm/^{0}C

(R^2=0.9993) when increasing temperature from 22 ^{0}C to 60 ^{0}C. The spectrometer used (I-MON512, Ibsen Photonics A/S) allows spectra acquisition at high scanning rate frequencies (Hz or KHz) and its interrogation software (based on Labview software provided by Ibsen Photonics A/S) allows a Gaussian fitting to track the Bragg wavelength shift when the surrounding temperature changes (cf. Fig. 1.9b).

Fig. 4.11b contrasts the AH measured with the OFS and the RH measured with the capacitive sensor, both placed in the climatic chamber for calibration (Fig. 4.10). To obtain the plot for Fig. 4.11b, the optical reflection intensity from the SMF coupler containing $(PAH/SiO_2)_9$ was firstly calibrated against RH measured with the capacitive sensor (sensitivity 2.5 mV/%RH). Then, the saturation vapour pressure (P_{ws}) in Eq. (4.3) is calculated from standard formulas [238], [239], [242] and taking the increase in temperature (22 to 60 ^{0}C) from Fig. 4.11a; in Eq. (4.3) instead of using the parameter RH from the capacitive sensor (red curve, Fig. 4.11a) the values used were those from the response of the OFS divided by the sensitivity 2.5 mV/%RH. Once the parameter P_w is known as explained before, Eq. (4.4) is applied to calculate AH from the response of the OFS (blue curve, Fig. 4.11b).



(a) (b)

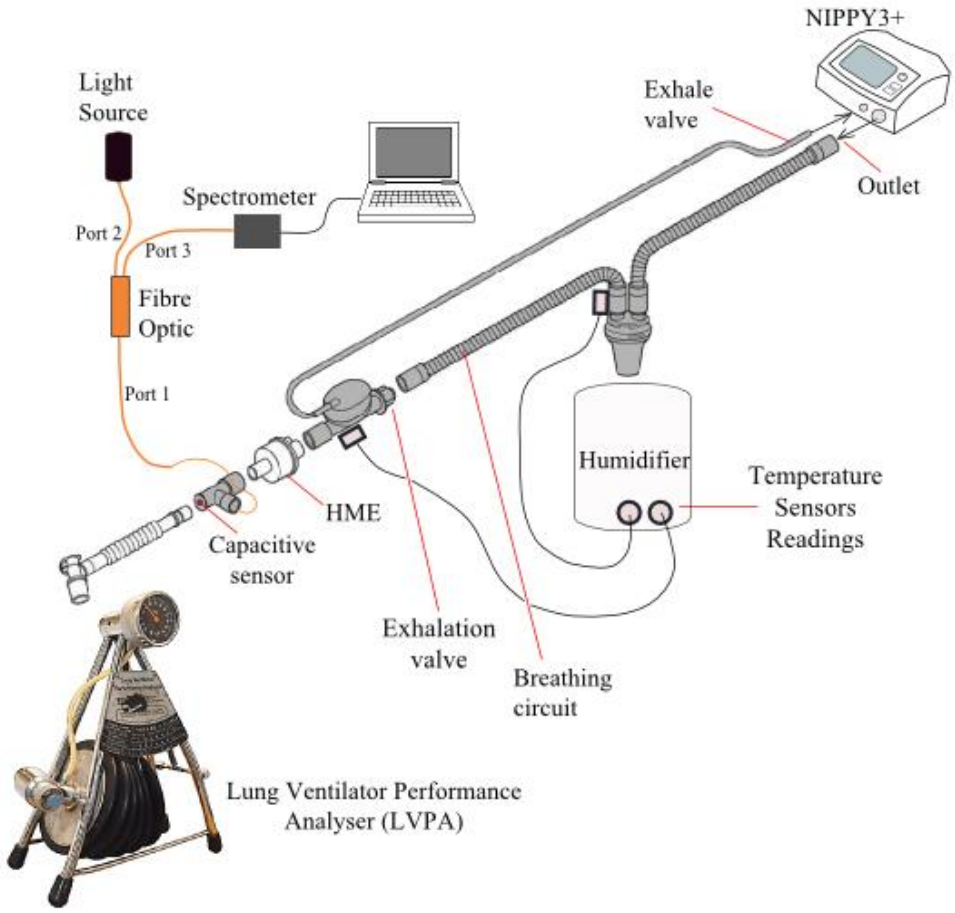
Figure 4.11: (a) Bragg wavelength from the spectra measured when port 1 of the fibre coupler was placed with two thermocouples inside a drying and heating chamber (Fig. 4.10); (b) AH measured with the OFS when the temperature increased from 22 ^{0}C to 60 ^{0}C.

4.7 Sensor testing in a breathing circuit connected to a positive pressure ventilator

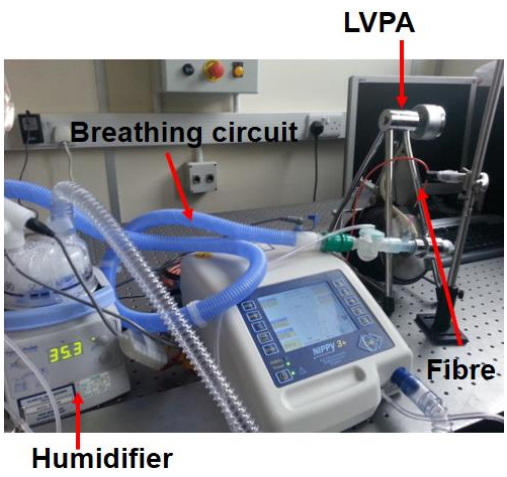
Two modes of ventilation were tested using a Non-Invasive Positive Pressure Ventilator (model NIPPY3+, B&D Electromedical Ltd, Figs. 4.12a and 4.12b): *pressure support ventilation* and *intermittent positive pressure ventilation (IPPV)*. The former may be used to achieve improved tidal volumes in spontaneously breathing patients who need assistance. The latter has been used to avoid intubation in patients with respiratory failure, to provide near-continuous ventilator support, improving oxygenation and decreasing hospital stay [243].

The set-up of the experiment using the ventilator was implemented with a heat and moisture exchanger (HME, anti-bacterial low resistance filter, B&D Electromedical Ltd) in the breathing circuit (Figs. 4.12a and 4.12b). The air outlet of the ventilator was connected to the humidification arm of the breathing circuit, providing active humidification by heating a water container (MR-850AEK, Fisher & Paykel Healthcare Ltd). The humidification arm was coupled with an exhalation valve which could be optionally connected to the HME. A T-valve linked the breathing circuit via a tube to a Lung Ventilator Performance Analyser (LVPA, previously marketed by BOC Medishield Ltd, Essex, UK) which is a mechanical analogue of the respiratory system, conventionally used for teaching and research [244], and thus allowing the OFS investigation of its potential use in critical care conditions.

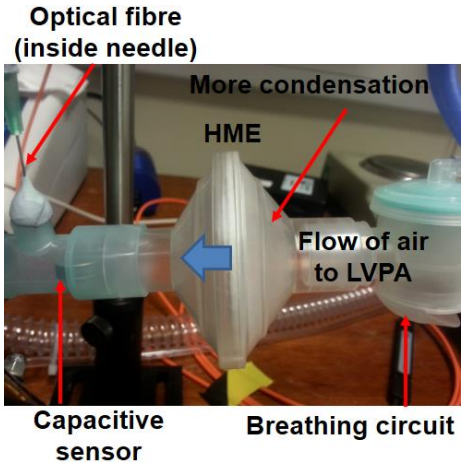
The OFS contained within a 23-gauge medical hypodermic needle and capacitive sensor were both placed in the T-piece valve (Figs. 4.12a and 4.12c). There were also two removable temperature probes integrated in the breathing circuit, one included in the humidifier itself and another placed at the end of the humidification arm, just before the connection with the exhalation valve (see Fig. 4.12a).



(a)



(b)



(c)

Figure 4.12: (a) Experimental set-up to measure the humidity level inside a breathing circuit connected to the ventilator. (b) Photograph of the experiment to measure humidity inside the breathing circuit without HME connected and the humidifier is based on heating the water container. (c) HME connected to the T-piece and exhalation valve of the breathing circuit.

Independent of the mode of ventilation used, the change of humidity throughout the breathing circuit was controlled by switching on/off the humidifier. There are several classifications of HMEs: hydrophobic, hygroscopic, and filtered HMEs [111], [109]. In this case, a filtered HME was used to reduce condensation in the T-piece (see left side of Fig. 4.12c) and the overall change of temperature inside the breathing circuit. The wool-foam material of this HME contains an anti-bacterial filter and hygroscopic properties that reduce water condensation and the presence of moisture (small droplets) on the side of the LVPA (Fig. 4.12c), improving the response of the optical fibre humidity sensor.

Fig. 4.13a shows the result of using the HME in the breathing circuit of the set-up presented in Fig. 4.12, demonstrating the pressure support mode of ventilation which is controlled by the breath of a patient except at the pressure limit (in this case 20 cm H_2O). The step change in humidity is created by switching ON the humidifier (at ca. 180 s in Fig. 4.13a) and later disconnecting the T-valve (at 1500 s in Fig. 4.13a). Using the HME in the breathing circuit, the readings of the optical fibre humidity sensor (*cf.* Figs. 4.13) are without noise produced mainly by formation of water condensation near the sensor and due to the presence of moisture (small droplets) that affect the fibre sensor performance (noise or artefacts in Fig. 4.13b). In Fig. 4.13b the increase in humidity was also caused by switching ON the humidifier at ca. 180 s. The overall change of temperature inside the T-piece was higher in this case (from 21.5 ^{0}C to 28.5 ^{0}C) and there were artefacts in the response of the fibre. The photograph of Fig. 4.12c confirms that an HME acts as a filter protecting the sensor against condensation that can produce noise (artefacts) and is useful as it restricts temperature variations (temperature change was higher in the result of Fig. 4.13b). Specifically, the right-hand side of Fig. 4.12c has more water condensation in this experimental test, as humidified gas from the ventilator side is warmer than the LVPA side.

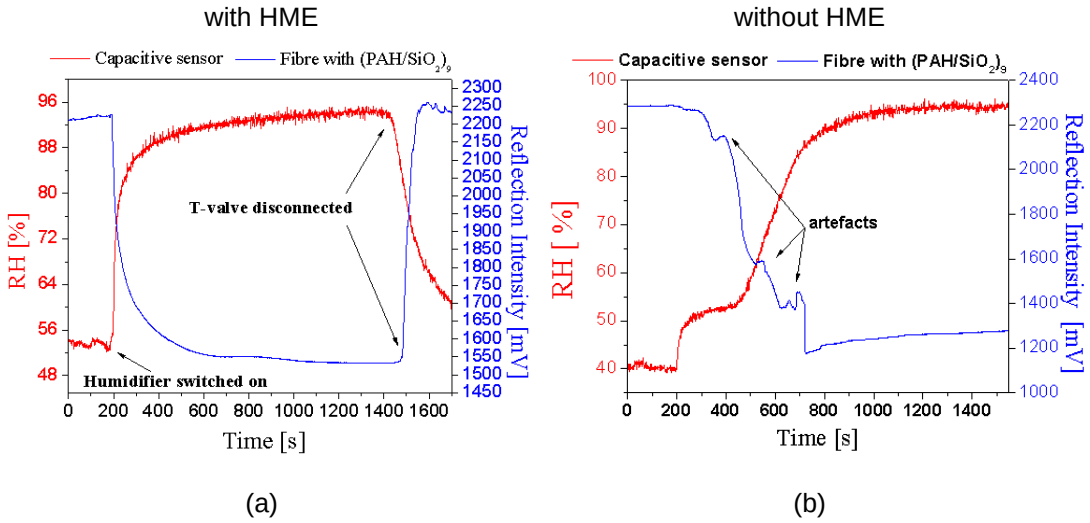


Figure 4.13: Comparison of readings for 20 cm H_2O of pressure support mode and 101 L/min in the ventilator settings; the red trace corresponds to the response of the capacitive sensor and the blue trace outputs the reflection intensity change of the optical fibre humidity sensor with nine bilayers. (a) Using HME in the breathing circuit and (b) without using HME in the breathing circuit.

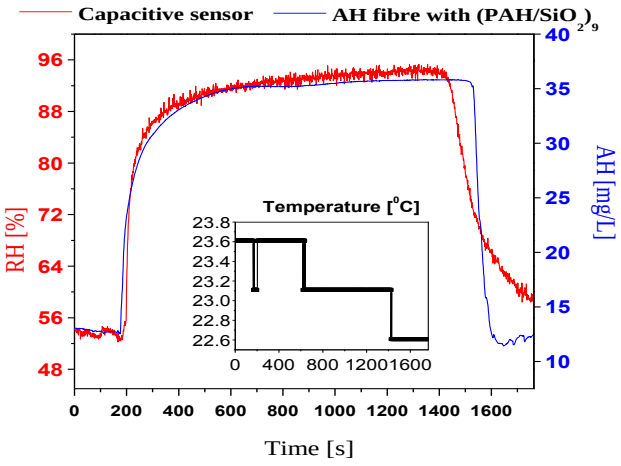


Figure 4.14: Calculation of AH from the result obtained in Fig. 4.13a using the response of the fibre (blue trace). The use of the HME in the breathing circuit keeps a stable variation of temperature (23.1 ^{0}C $\pm$ 0.5 ^{0}C).

The result of Fig. 4.13a is re-plotted in Fig. 4.14 in terms of the AH measured with the OFS, using Eqs. (4.3 - 4.4) and the Vaisala Humidity Calculator 5.0® [245] with an initial consideration that 55 %RH is equivalent to 11.4 mg H_2O/L at 1 atm and 23.1 ^{0}C . As can be seen in Fig. 4.14, the overall change of

temperature (during full measurement of ca. 1600 s) was 1.0 ℃ inside the T-piece in this case (23.1 ^{0}C $\pm$ 0.5 ^{0}C). Thus, the blue curve in Fig. 4.14 was obtained using Eqs. (4.3 - 4.4) and a sensitivity of 2.3 mV/%RH as calibrated in section 4.4. First, the saturation vapour pressure (P_{ws}) in Eq. (4.3) is calculated from standard formulas [238], [239] and taking the temperature shown in the inset of Fig. 4.14; in Eq. (4.3) instead of using the parameter RH from the capacitive sensor (red curve, Fig. 4.14) the values used were those from the response of the OFS (in mV) divided by the sensitivity 2.3 mV/%RH. Once the parameter P_w is known as explained before, Eq. (4.4) is applied to calculate AH from the response of the OFS (blue curve, Fig. 4.14). The values obtained from the OFS response in Fig. 4.14 were also confirmed with the Vaisala Humidity Calculator 5.0® [245].

Fig. 4.15 shows measurements taken with the optical fibre humidity sensor with nine bilayers and the capacitive sensor inside the T-piece of the breathing circuit (Figs. 4.12a and 4.12c) and using a different mode of ventilation, i.e., IPPV. This mode was first tested with a fixed pressure of 15 cm H_2O and 12 breaths per minute (breaths/min) with the humidifier switched ON. The output of a moving average filter (with 100 points) has been applied to the responses of the capacitive sensor and the optical fibre humidity sensor and the average baseline (black lines in Fig. 4.15) increased from 2968 mV to 3568 mV for the fibre sensor and decreased from 93%RH to 89%RH for the capacitive sensor during the measurement period (600s). The inset in Fig. 4.15 is a close up view between 200 and 260 seconds that corroborates that only the optical fibre humidity sensor can detect individual breaths due to its faster response. In addition, during the measurement period, the temperature only increased from 28.2 to 30.7 °C inside the T-piece.

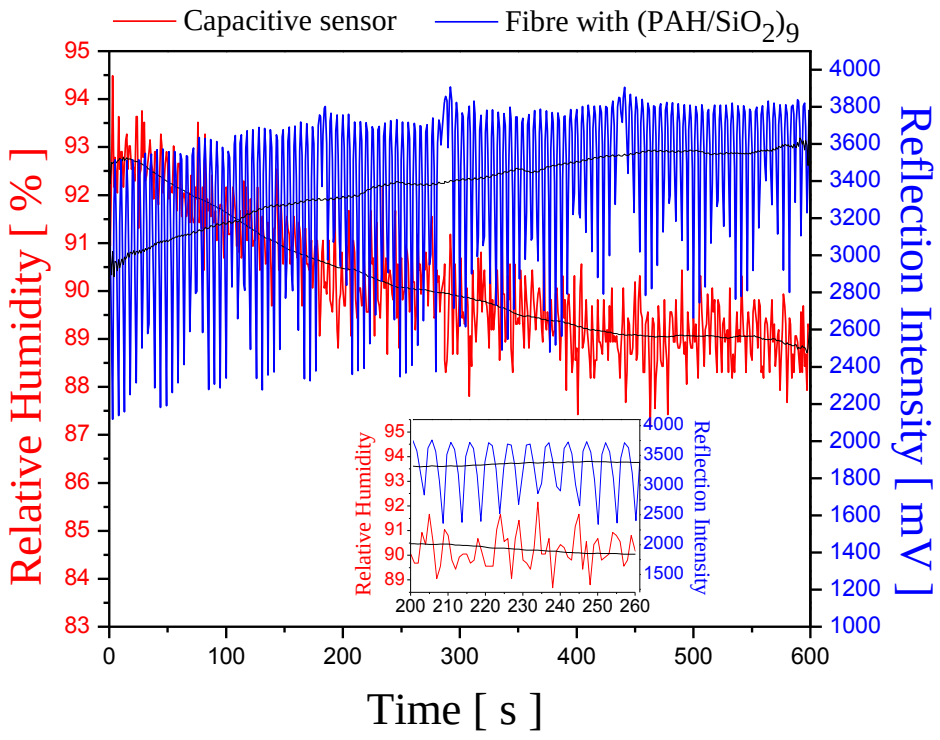
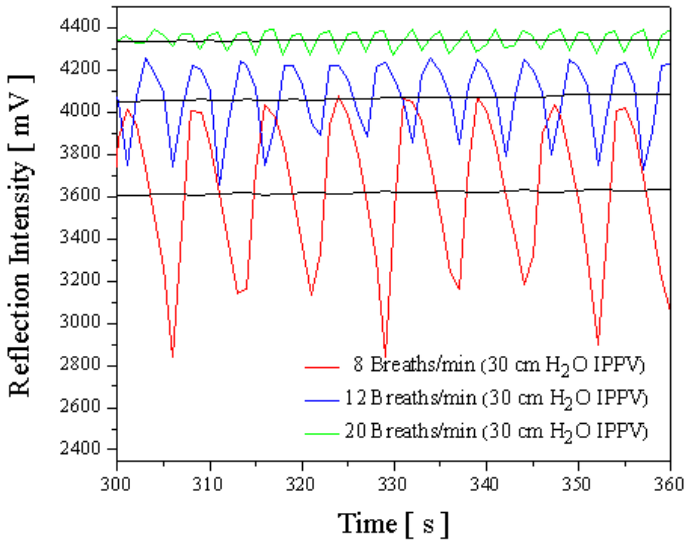


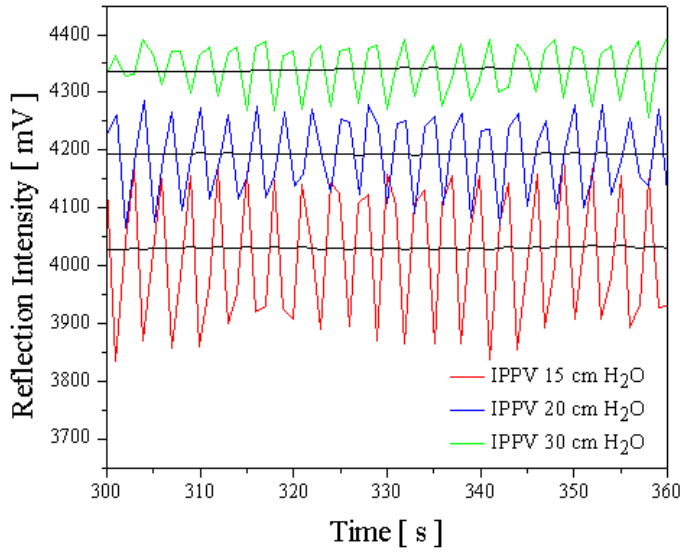
Figure 4.15: Comparisons of nine bilayer fibre response (blue trace) and capacitive sensor response (red trace) at 15 cm H_2O in IPPV mode and 12 breaths/min; the black traces correspond to the output of a moving average filter for each device response. The inset shows a zoomed time axis where the breath to breath variations in humidity can be observed using the optical fibre sensor.

Fig. 4.16a and Fig. 4.16b show a new subset of measurements for t = 300–360 s (600 s total experiment duration) with the optical fibre humidity sensor using nine bilayers deposited on the tip of the fibre. These measurements compare different breathing frequencies for the same pressure in IPPV mode and also compare different pressures of IPPV for the same frequency. The fast response of the sensor is again demonstrated through breath to breath humidity measurements. Fig. 4.16a confirms that the slower breath frequency will produce a smaller baseline reflection intensity and higher RH for a fixed ventilation pressure of 30 cm H_2O, i.e., independent of the level of humidity provided by the humidifier, a frequency of 8 breaths/min always produced a higher RH than for 12 breaths/min and 20 breaths/min. Fig. 4.16b shows that

at lower pressures, IPPV will produce a smaller baseline reflection intensity and higher RH for a fixed breath frequency of 20 breaths/min.



(a)



(b)

Figure 4.16: (a) Comparison of different breaths/min for same pressure of IPPV. (b) Comparison of different pressures of IPPV for the same frequency of breaths/min. The behavior shown in both figures is consistent for the whole experiment (600 s duration).

To support the sensitivity to humidity given by the film based on PAH/SiO_2 NPs, a final test was carried out by introducing a bare fibre tip inside the T-valve as shown in Fig. 4.12a along with the capacitive data logger and without the HME. Fig. 4.17 shows the results of this test when the ventilator was set for 5 min with a rate of 12 breaths/min and a pressure of 20 cm H_2O in IPPV mode. Ventilator and humidifier were switched ON at the same time, the RH increased from 85% to 91 %, temperature increased from 24.5 ^{0}C to 28 ^{0}C (inset of Fig. 4.17) and the bare fibre still could roughly detect breaths from the ventilator but its baseline did not follow the change of humidity as detected from the capacitive sensor in Fig. 4.17 (temperature compensation activated) and also as observed in previous results, for instance, when compared to Fig. 4.15. The bare fibre tip capability to still detect breaths from the ventilator is due to the change in the refractive index due to water vapour or moisture adsorption onto the fibre facet as explained by Fresnel coefficient reflections (section 1.4.3).

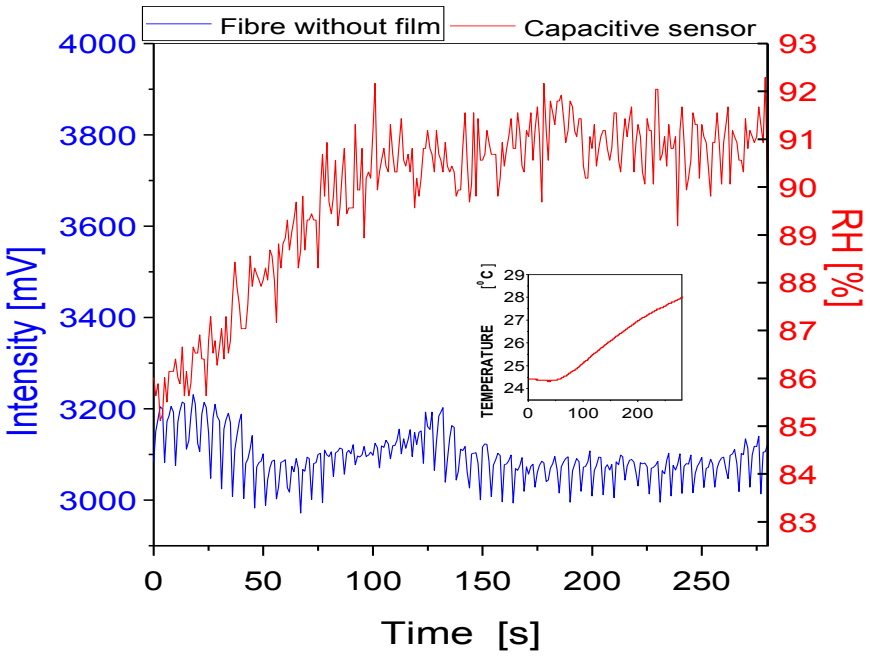
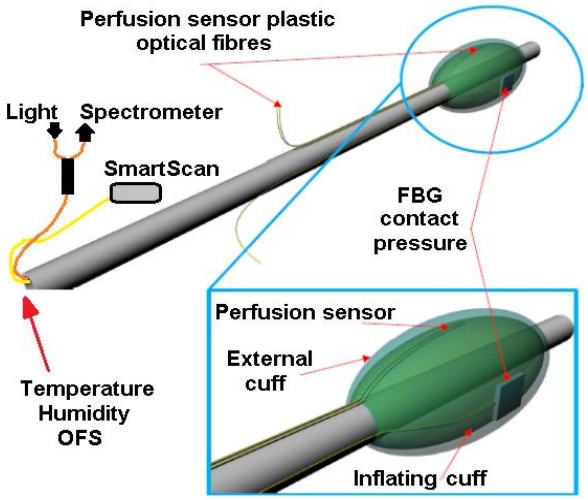


Figure 4.17: Comparisons of the bare fibre response (blue trace) and capacitive sensor response (red trace) at 20 cm H_2O in IPPV mode and 12 breaths/min; the inset corresponds to the change in temperature during full measurement.

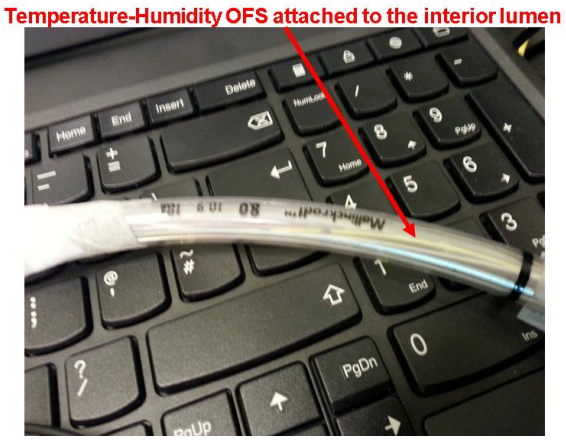
4.8 Sensor testing in an animal study

After calibration and investigation over a humidity range of 5%RH and 96 %RH using controlled bench-top setups (previous sections), the performance of the optical fibre humidity sensor was also evaluated as part of an animal study involving multi-parameter sensing using optical fibre technology [246]. Ethical approval was obtained and the process was carried out under the provisions of a Home Office license allowing for research work with animals. All procedures were performed in accordance with the UK Animals (Scientific Procedures) Act. 1986 under a project license held by Prof. D. Gardner (PPL 40-3410) and the study was performed in the primary licensed establishment located at the Sutton Bonington campus of the University of Nottingham. Additionally, all procedures were approved by the local animal welfare and ethical review board (AWERB), University of Nottingham.

The endotracheal tubes (ETTs) used were a modified size 8.0 Mallinckrodt (Covidien UK) and protocol design was carried out by the collaborators from the anaesthesia department of the Nottingham University Hospitals NHS Trust [246]. As part of the protocol, optical fibres with FBGs embedded in polymer patches (Fig. 4.18a) were integrated between two cuffs of the sensorized ETT containing also tissue perfusion sensors based on two plastic optical fibres (DB-500 Asahi Kasei, Tokyo Japan, Fig. 4.18a) and the optical fibre humidity sensor proposed in this research, attached to the interior lumen of same ETT (Photograph, Fig. 4.18b). Only the results for humidity and temperature sensing are presented in this subsection and the remaining results from the other optical fibre monitoring systems were published in reference [246]. Briefly, a patched FBG was used to monitor the cuff contact pressure onto the trachea of the studied animals and a combination of transmitter/receiver plastic optical fibres were used to monitor tissue perfusion via reflectance photoplethysmography in the animals.



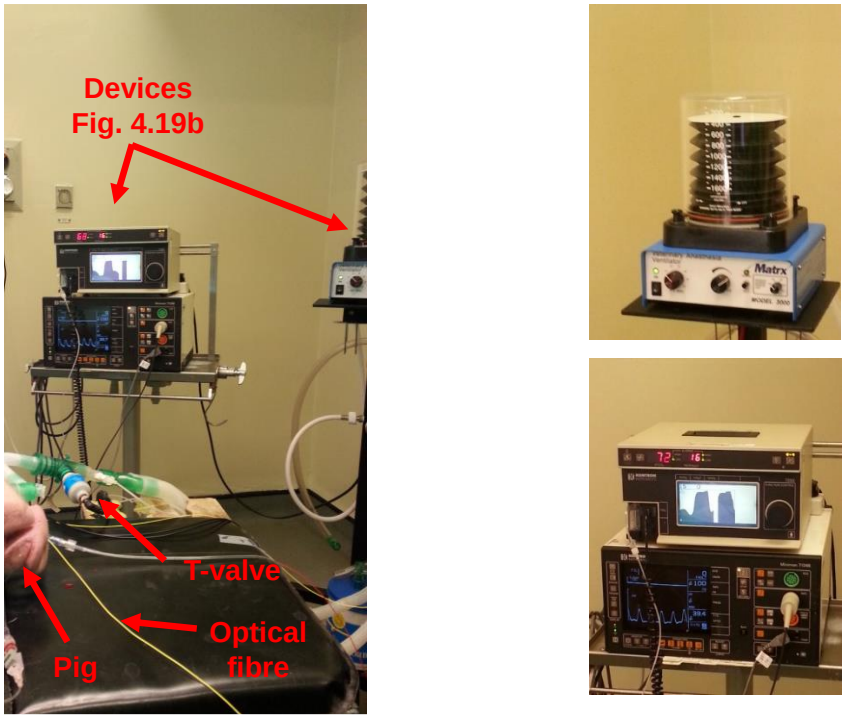
(a)



(b)

Figure 4.18: (a) Fibre optic pressure and perfusion sensors bonded to the ETT cuff and then enclosed within an external cuff; the optical fibre humidity-temperature sensors were attached to the interior lumen of the ETT. (b) Photograph of the OFS attached to the interior lumen of one ETT used during the study.

Six Canberra pigs in total were identified as a suitable animal model to check the function of optical fibre devices. Seven tubes were manufactured in total but only one of them was tested with the optical fibre humidity sensor attached to the interior lumen of the ETT and used only for one pig (Figs. 4.18 and 4.19).



(a) (b)

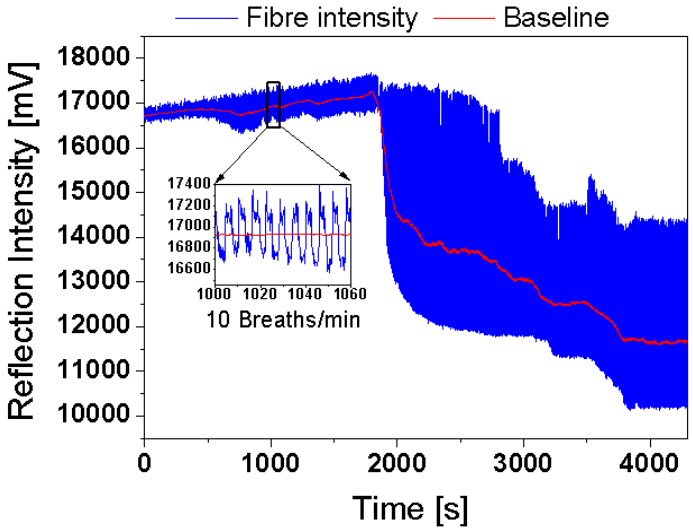
Figure 4.19: (a) Photograph of the intubated pig with the setup within the operating theatre. (b) (*Up*) Veterinary anaesthesia ventilator (Matrix® Model 3000, Midmark Animal Health Inc) and (*down*) Kontron Instruments monitors for end-tidal carbon dioxide ($ETCO_2$), nitrous oxide (N_2O), fraction of inspired oxygen (FiO_2), Electrocardiogram (ECG), temperature from rectal probe and the co-oximetry value (SaO_2) from arterial blood monitor.

Concurrent testing on an acute kidney injury model was being carried out by collaborators in veterinary sciences and nephrology in order to maximize the benefit from the loss of an animal. The Kontron instruments shown in Fig. 4.19b were mainly used for that simultaneous kidney injury study. The pigs were operated on at about 10 – 12 weeks of age and were fasted overnight with free access to water. They were managed using a standard anaesthetic protocol and were transferred to the operating theatre where procedures were carried out with them in the supine position with a slight right lateral tilt. The lungs were ventilated with a tidal volume of 10 – 12 ml/kg and the ventilator rate adjusted to maintain an end-tidal carbon dioxide concentration ($ETCO_2$) of 45 – 73 mmHg.

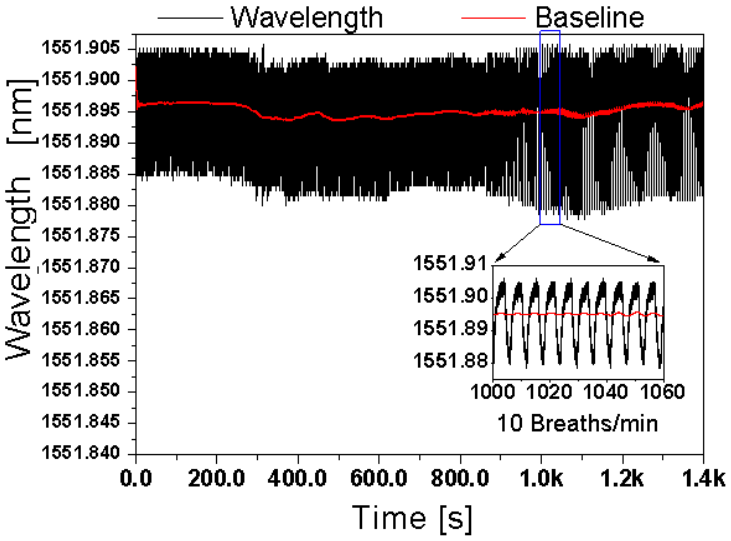
Optical fibre contact pressure and mucosal blood flow were collected at different positions to collect data from the contact pressure with the anterior, posterior and left walls of the trachea. The cuff was inflated with 5 mL of air as per the guidance of the veterinary anesthetists in every position of the trachea. A time of five minutes was allowed for the cuff pressure to equilibrate inflated and relevant data from optical fibres to measure pressure and blood flow were collected. Once done, the cuff was deflated, the ventilator was switched OFF, the ETT was rotated to the next position and then re-inflated again to contact with the tracheal surface. Only in one pig, simultaneous reflection intensity (related to humidity without temperature compensation) and wavelength shift (correlated to temperature) were measured with both a MMF coupler containing $(PAH/SiO_2)_9$ and a SMF containing an FBG (1551.7 nm) during all the procedure (a comparative data logger sensor was not used during this study). A time for equilibration of the ETT cuff pressure was allowed whilst continuously recording reflection intensity with the OFS using broadband light source (HL-2000), spectrometer (HR4000) and wavelength shift with an FBG interrogator (SmartScan, Smart Fibres Ltd., Fig. 4.18). The pigs underwent mechanical ventilation for a total duration of between two to three hours. Following completion of the studies, the pigs were humanely killed using a lethal injection of Sodium Pentobarbitone (200 mg/kg).

Fig. 4.20a shows the first hour response from the optical fibre humidity sensor recorded at λ =618.13 nm. The overall reflection intensity (blue trace) and its baseline (red trace) decreased only after 30 min meaning the abrupt increase in AH or moisture inside the trachea of the pig. The wavelength shift due to the ventilation air temperature was monitored with the FBG-based sensor and it kept relatively stable around 1551.895 nm (red baseline in Fig. 4.20b). The response from both fibres, intensity and wavelength shift, were started once the pig was already intubated such that the zero from both plots in Fig. 4.20 correspond to the measurements immediately after intubation of the pig. After 30 min of intubation the increase in the amount of moisture inside

the trachea could have affected the sensor performance but the sensor response was still able to detect breath-by-breath intensity change and wavelength changes during the full measurement period of 2.5 hr.



(a)



(b)

Figure 4.20: (a) Optical reflection intensity measured with the optical fibre humidity sensor placed inside the lumen of the ETT (the inset shows a close up of the breaths per min. measured between 1000 and 1060 s). (b) Wavelength shift from the FBG-based fibre placed inside the lumen of the ETT for the first 1400 s (the inset shows a close up of the breaths per min. measured between 1000 and 1060 s).

After the sharp change in reflection intensity observed in Fig. 4.20a, the baseline from this reflection (red trace in Figs. 4.21 and 4.22 calculated through applying a Savitzky-Golay filter with 1001 points and order 2) slightly decreased from around 11800 mV to 11000 mV until the end of the recording in the animal study as can be confirmed in Fig. 4.21; this figure shows the main maneuvers when the ventilator was OFF in order to rotate the ETT and measure contact pressure and blood flow [246] at different surface points of the animal trachea. Additionally, during the start of the measurement the ventilation rate was fixed at 10 breaths/min (Fig. 4.20) and it was changed to 16 breaths/min during the rotation maneuvers until the end of the recording (Fig. 4.21).

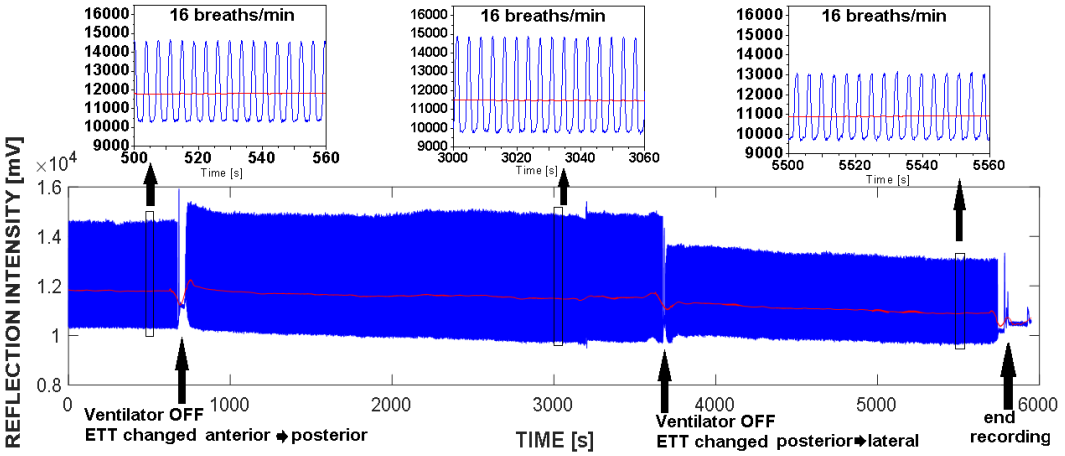
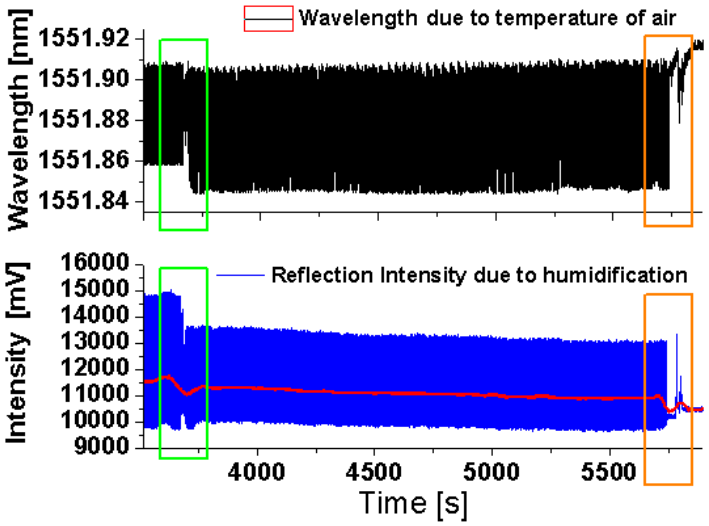


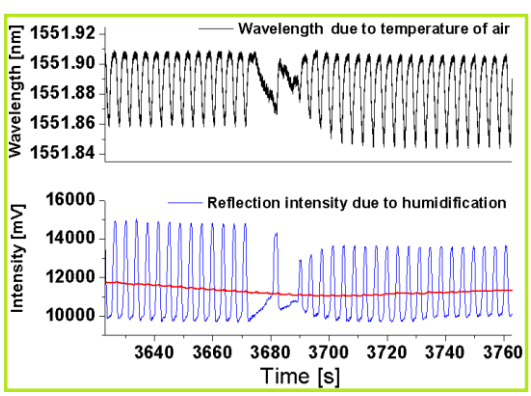
Figure 4.21: Optical reflection intensity measured at 618.13 nm with the optical fibre humidity sensor during the rotation maneuvers of the ETT; the insets show 1 min of the recording at different times during the animal study.

Fig. 4.22 presents a simultaneous comparison of the wavelength shift due to the temperature of ventilation air and reflection intensity measured by the humidity sensing probe with $(PAH/SiO_2)_9$, both compared in the last stage of the recording during the animal study, i.e., before and after the last rotation of the ETT (posterior to lateral). Fig. 4.22a shows the last 2385 seconds of measurement containing two sets of insets, the green indicates the last

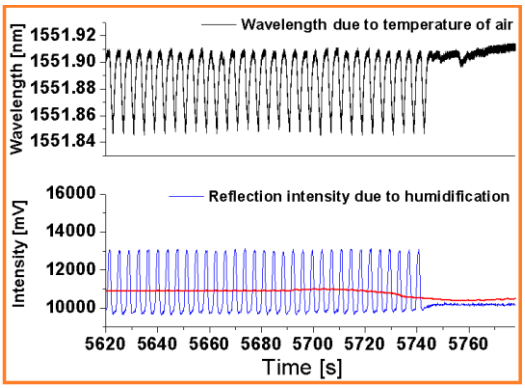
rotation of the ETT (shown separately in Fig. 4.22b) and the orange corresponds to the end of the recording (presented separately in Fig. 4.22c).



(a)



(b)



(c)

Figure 4.22: (a) Comparison of the wavelength shift and optical reflection intensity measured at 618.13 nm during the last 2385 s of the animal study; (b) shows a close up of the green area shown in (a) and (c) shows a close up of the last part of the measurement shown in orange in (a).

A comparative humidity/temperature data logger sensor was not used during the measurement showed from Fig. 4.20 to Fig. 4.22 and both fibre sensors were not calibrated before their implementation in this animal study. The results from these figures are qualitative and the humidity response from

the OFS with 9 bilayers is not compensated with the temperature. However, these results together with those presented in section 4.7, demonstrate the ability of the fibre sensors to detect breath-by-breath response related to the change of humidity and temperature during the mechanical ventilation of the animal.

4.9 Preliminary tests and protocol design for a clinical study in volunteers: Application to facemask and nasal cannulas

The results presented in section 4.7 demonstrated that an HME acts as a hygroscopic filter protecting the sensor against condensation that can produce artefacts and is useful as it restricts temperature variations. In this direction, it is also beneficial to monitor temperature as is needed in case the response of the fibre is reported as absolute humidity after the optical fibre sensor calibration. The calibration results obtained in section 4.4 were performed at a constant room temperature (23.0 ℃ ± 0.5 ℃). In practical use in non-invasive mechanical ventilation, large temperature variations can be avoided (up to ± 1 ℃) by using an HME in the breathing circuit (Fig. 4.13). In future, it would also be favourable to coat the tip of the hypodermic needle containing the fibre-optic sensor with the wool-foam material used in the HME (as shown in Fig. 4.23) to avoid condensation artefacts in the response of the sensor. Further improvements will involve writing an FBG into the fibre so that temperature can be simultaneously monitored in facemasks (Figs. 4.23 and 4.27) and nasal cannulas (Fig. 4.24) in human studies in the near future. It should be clarified from now that the results presented in this section compare qualitatively the response from the optical fibre sensors proposed and the response from the electronic data logger (DS1923). However, the final quantification of AH levels in facemasks can be performed as calculated in section 4.6 once the fibre sensors have been previously calibrated (with the inclusion of temperature compensation).

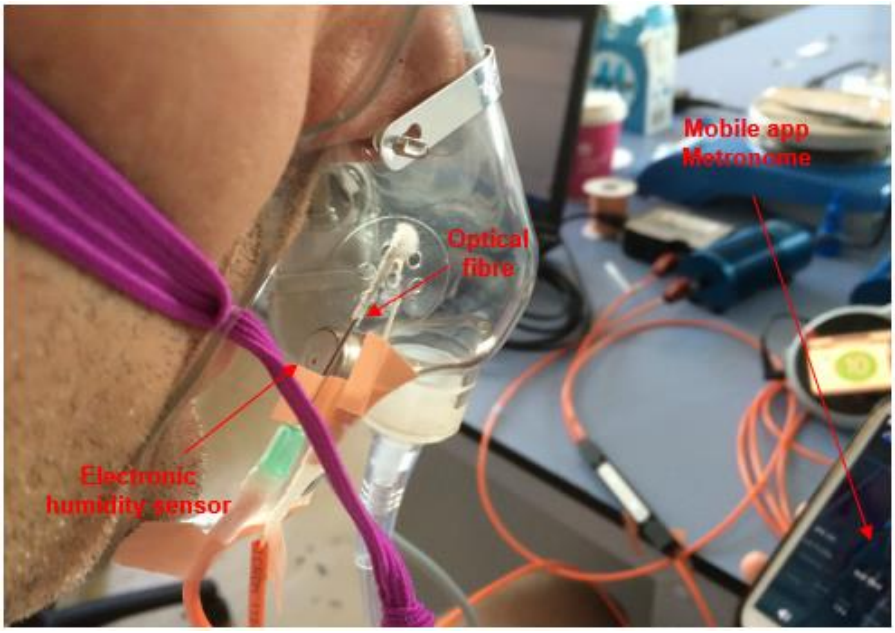


Figure 4.23: OFS bound to a facemask and protected with hypodermic needle containing the wool/foam material used in the HME; the capacitive data logger can also be placed inside the facemask for comparison and the volunteer will be expected to follow up the breaths indicated from a mobile application.

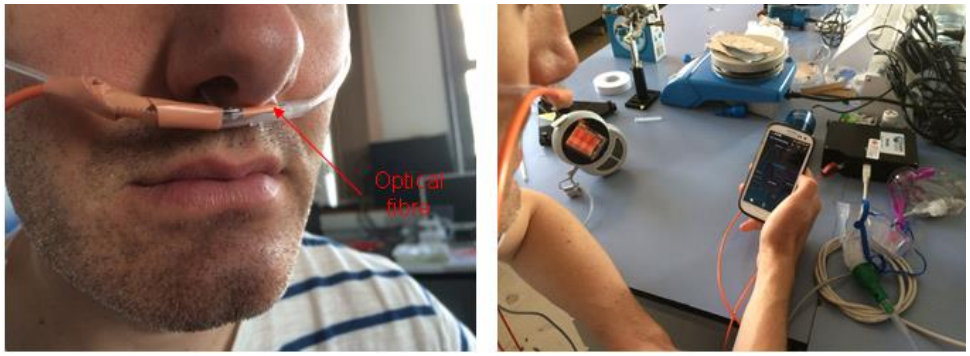


Figure 4.24: (a) Optical fibre humidity sensor bound outside the nasal cannula and protected with the hypodermic needle. (b) Study with volunteers will be planned to use a mobile app metronome for delivering different breath frequencies.

As part of a preliminary preparation of the clinical protocol design, exploratory tests were performed with a Venturi mask and trying different levels of Fraction of Inspired Oxygen (FiO_2). Fig. 4.25 plots the overall exploratory measurement using the optical fibre humidity sensor and the capacitive humidity sensor (Fig. 4.23) used before in section 4.7. Fig. 4.25b shows a close up from Fig. 4.25a when a 24% FiO_2 was supplied at 2 L/min and the human

breath changed from 10 breaths per minute (bpm) to 40 bpm. Fig. 4.25c presents a close up from Fig. 4.25a when the FiO_2 was changed to 50% FiO_2.

Figs. 4.25 to 4.27 demonstrate the effectiveness of the optical fibre humidity sensor for measuring breath frequencies from 10 bpm to 40 bpm. The ineffectiveness of the electronic humidity sensor for measuring high breath frequencies is due to its low response time; this fact was also demonstrated in section 4.7 of this chapter.

The averaged baseline of the blue waveform measured by the optical fibre humidity sensor corresponds qualitatively to the level of humidity when compared to the levels measured by the capactive sensor (Figs. 4.25 to 4.27). Oscillations allows the optical fibre sensor to calculate breathing rate (see also results obtained from nasal cannula in Fig. 4.26).

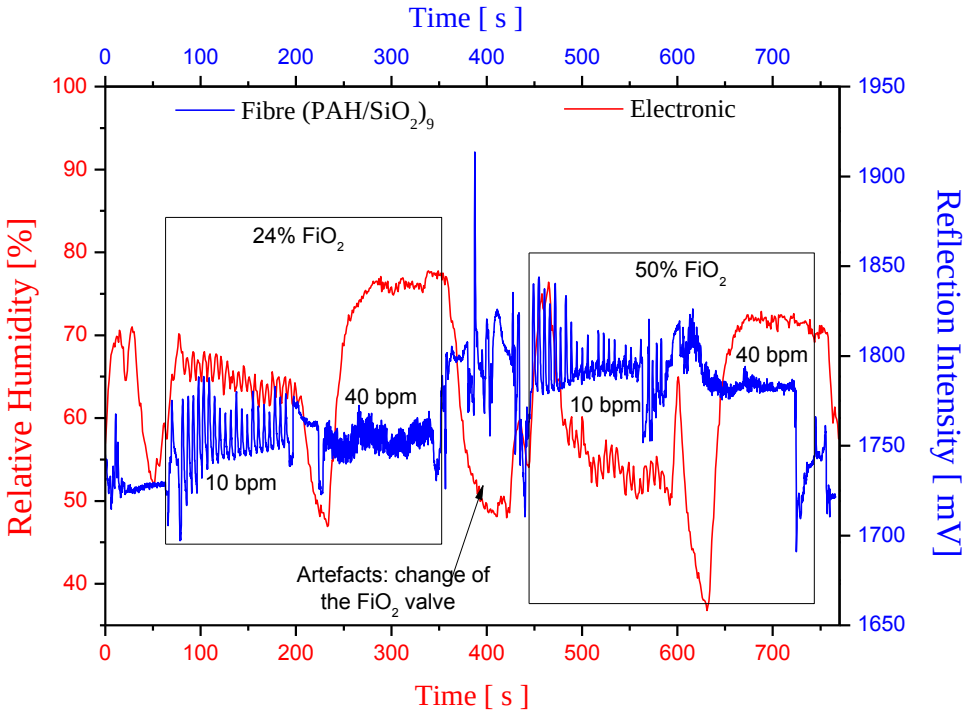


Figure 4.25 (a): Comparison of the response of the optical fibre humidity sensor (in blue and containing 9 bilayers of PAH/SiO_2) and the electronic humidity sensor (in red) when both are tested inside a Venturi mask (Fig. 4.23) and using two different percentages of FiO_2 (in each case the breath was changed from 10 to 40 bpm).

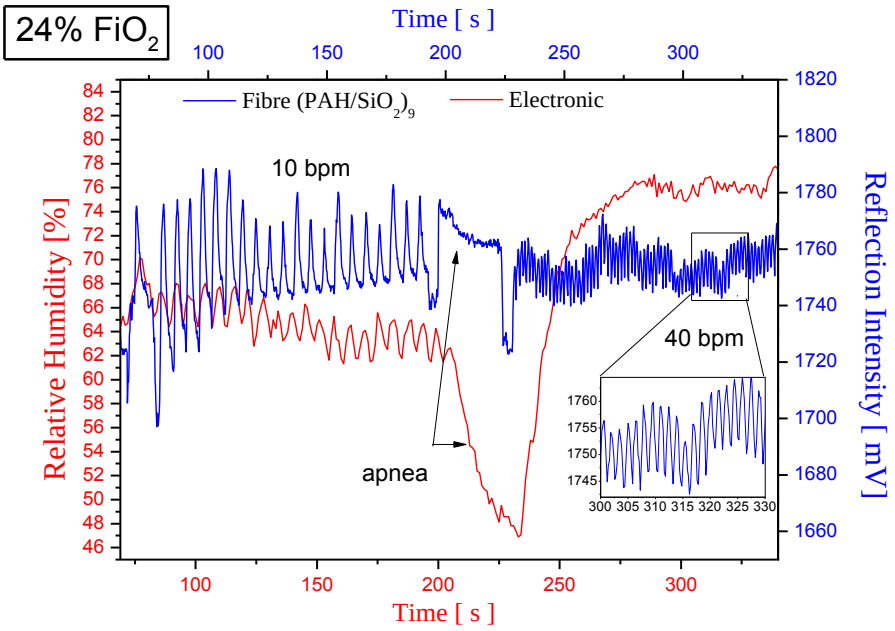


Figure 4.25 (b): Close up from 1st section shown in Fig. 4.25a (corresponding to delivering 24% FiO_2 into the Venturi mask). The electronic sensor can measure a baseline for the change in relative humidity, but the optical fibre humidity sensor is the only one capable of measuring both frequencies 10 and 40 bpm.

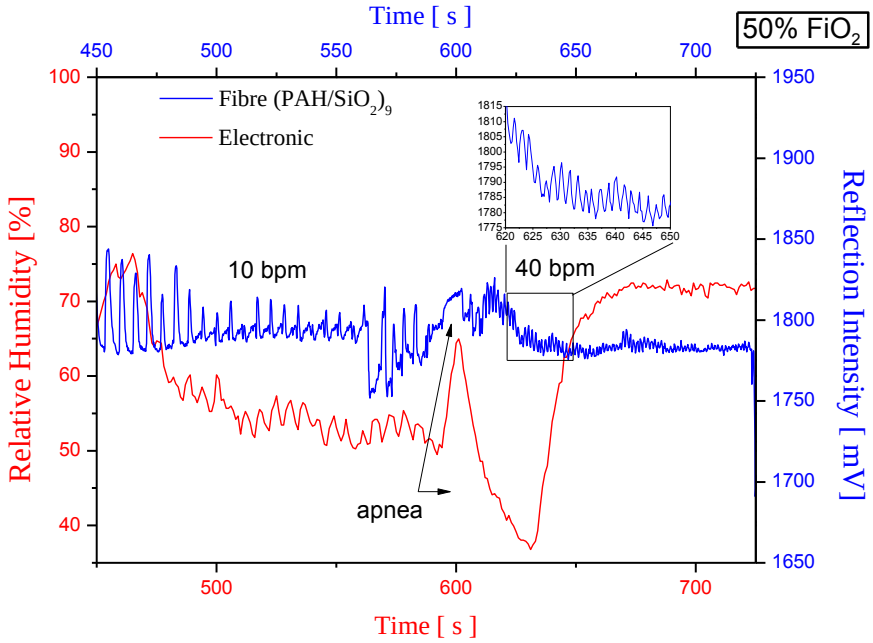


Figure 4.25 (c): Close up from 2nd section shown in Fig. 4.25a (corresponding to delivering 50% FiO_2 into the Venturi mask). The electronic sensor can measure a baseline for the change in relative humidity, but the optical fibre humidity sensor is the only one capable of measuring both frequencies 10 and 40 bpm.

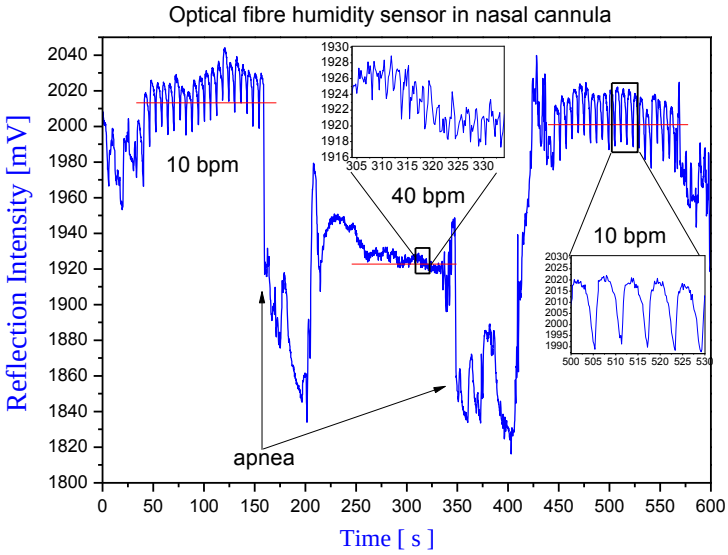


Figure 4.26: The optical fibre humidity sensor bound outside the nasal cannula (Fig. 4.24) is able to measure breath frequencies from 10 bpm to 40 bpm and apnea lapses between them.

Fig. 4.26 exhibits 1 cycle of repetition between 10 bpm and 40 bpm and performing apnea lapses between them; it confirms that 10 bpm produces a different level of baseline in humidity (shown in red) than 40 bpm and when the breath goes back to 10 bpm the red baseline also goes approximately back to the same intensity level. Therefore, the results of the previous and also this section demonstrate that the development of a portable optical fibre humidity sensor is feasible and can be easily embedded in ventilation masks or in elements of the breathing circuits used for ventilation.

Finally, results of Fig. 4.27a and Fig. 4.27b were obtained by breathing inside a respiR8® facemask when the coated (7 bilayers PAH/SiO_2) sensing tip was inside it (Fig. 4.27c). Tests in Fig. 4.27 were performed using a SMF coupler containing an FBG (λ_{Bragg}1546.3 nm); one port of the coupler is connected to a SLD light source (SUPERLUM) and the other port interrogated with the spectrometer (I-MON512, Ibsen Photonics A/S) at a frequency of 30 Hz. The plot of Fig. 4.27a was generated by tracking the intensity change of the maximum peak (at 1546 nm) of the reflection spectrum measured by the I-

MON spectrometer, and the plot of Fig. 4.27b was obtained by tracking the wavelength shift of the same peak (ca. 1546 nm) through fitting a Gaussian model (pre-defined function in Matlab calculated for every spectra recorded). The black curves in Figs. 4.27a and 4.27b have been obtained after applying a moving average filter (500 points in time domain) to the intensity change in the reflection spectrum and the Bragg wavelength shift respectively; the trends of these black traces followed the readings of the available commercial capacitive sensor (electronic logger, DS1923) as comparison. These results demonstrate the ability of the OFS to measure breath to breath changes (respiratory rate) in temperature and humidity simultaneously when 7 bilayers of PAH and SiO_2 were deposited onto the tip of the fibre.

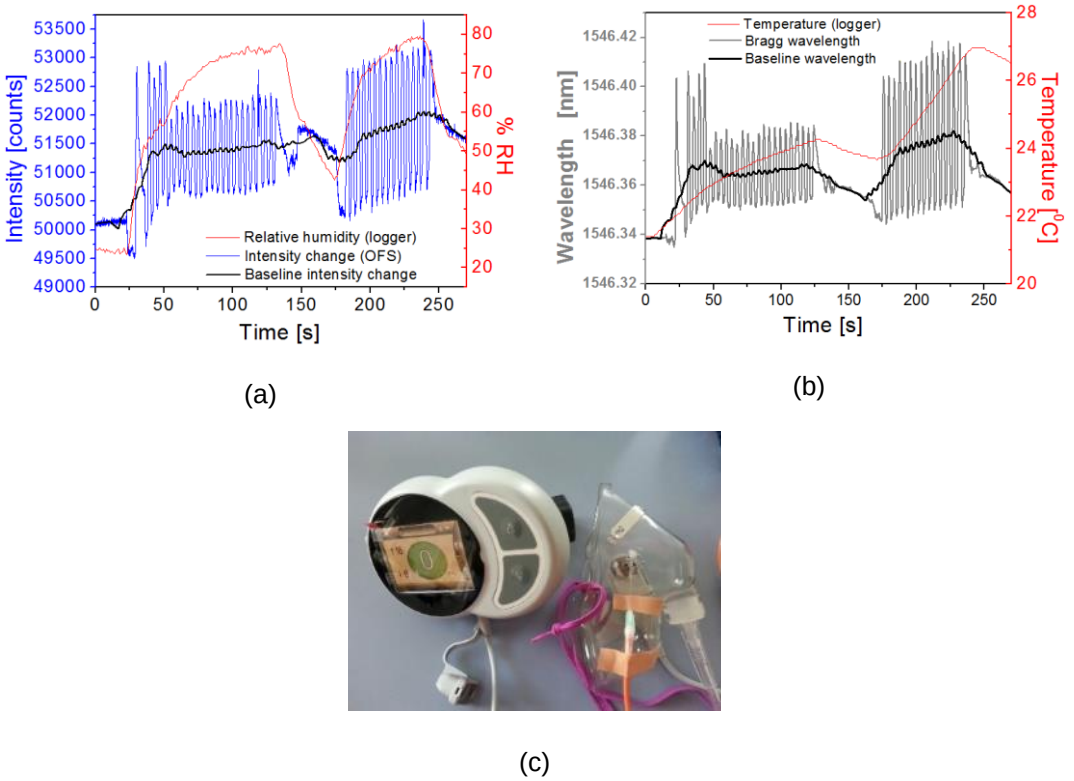


Figure 4.27: (a) Comparison between the change in intensity (measured from total reflection spectrum) and relative humidity (measured with a commercial electronic logger). (b) Comparison between the Bragg wavelength shift and temperature (measured with electronic logger). (c) Future application of the OFS as respiratory rate and humidity-temperature monitor in facemasks (photograph shows a commercial respiratory counter with facemask - respiR8®- together with the OFS proposed adhered to the facemask).

In this section, it should be also clarified that the FBG wavelength shift response was not calibrated before its implementation in the test of 4.27, but these results compare qualitatively the response from the OFS proposed and the response from the electronic data logger (DS1923). The final quantification of AH levels in facemasks can be performed as calculated in section 4.6 once the fibre sensors have been previously calibrated (with the inclusion of temperature compensation).

4.10 Chapter conclusions

Monitoring of temperature and humidity is essential in intensive care units and the development of new sensors helps to address an unmet clinical need. This chapter has shown its potential to measure breath to breath changes for both humidity and temperature through bench-top tests, one off animal study and a preliminary test for a protocol with volunteers recently approved as "*Validation of a novel fibre-optic sensor integrated in oxygen delivery devices as a respiratory rate monitor*".

Testing results in the bench-top using a mechanical ventilator demonstrated that in the optimum sensor design it will be necessarily to apply a protective wool/foam (similar material used in the HME, as shown in Fig. 4.23) when using the sensor in high condensation environments to avoid moisture artefacts in the response of the OFS.

Fabrication of the sensor is straightforward to obtain using the LbL method and optimum response sensitivity was demonstrated to be between seven and ten deposition bilayers of PAH and SiO_2 NPs with a satisfactory response time of 1.13 s ± 0.30 s.

Validation of the sensor in a one off animal study was encouraging reinforcing the requirements for further tests in a protocol with human volunteers. Despite the sensor not being protected with a needle and wool/foam against high moisture condensation, the response of the sensor

could measure breath to breath humidity during all of the 2.5 hr measurement in the animal study. Additionally, successful preliminary testing work in ventilation masks opens the real opportunity for application in a protocol with volunteers, thereby allowing further developmental stages such as a real time display processor for detecting RR and the creation of an alarm system based on breathing monitoring (including AH and temperature of air).

The next chapter will present the optical fibre sensors developed for the detection of the biochemical parameters of interest: propofol and a demonstration of a biosensing platform for protein.

Chapter 5: Optical fibre sensors for detection of biochemical parameters

This chapter presents two types of biosensors based on two main optical fibre structures: LPGs and U-shaped fibres. The first main section of this chapter (5.1) explains the development of a functionalized OFS for detection of the protein streptavidin. An LPG modified with a coating of silica core gold shell (SiO_2:Au) nanoparticles (NPs) deposited using the layer-by-layer (LbL) method is employed for the development of a biosensor. The SiO_2:Au NPs were electrostatically assembled onto the LPG with the aid of a poly(allylamine hydrochloride) (PAH) polycation layer (section 3.3.1). The LPG sensor operates at the phase matching turning point to provide the highest sensitivity. The SiO_2:Au NPs were modified with biotin, which was used as a ligand for streptavidin (SV) detection, i.e., the biotin-streptavidin interaction is used as a model system to characterise the performance of the biosensor. However, the selectivity of this biosensor towards a particular protein of interest in the ICU can be tailored simply by changing the nature of the ligand, making LPGs modified with SiO_2:Au NPs a generic sensing platform for biosensor development.

The second main section of this chapter (5.2) is dedicated to the proof of concept for the detection of propofol in-vitro conditions using LPGs and U-shaped fibres. The materials used for the functionalization of these sensors were presented in sections 3.4.1 and 3.4.2, both sensor configurations are based on the molecular imprinting of propofol onto TiO_2 and MSN-TiO_2 respectively. The first detection method is based on the host-guest interaction between cyclodextrin and propofol which allowed 0.65 µM as the lowest detection concentration of propofol in aqueous solution; the second method allowed improvement in the lowest concentration detected within the clinically relevant range.

5.1 Optical fibre sensor for protein detection

Fast, reliable and highly sensitive detection of proteins and antigen-antibody reaction kinetics is desired in biology and medicine because it can facilitate prompt disease diagnosis. The presence of various proteins, or changes in their concentration, can be linked with alterations in physiology and act as an indicator of problems in the organism [247]. The quantitative detection of such proteins is conducted mainly using SPR, planar waveguides [248] and various immunoassays, providing sensitivity typically down to pg/mL [249]. In the case of the ICU, recent reviews [250], [251] suggest that further research should develop better point-of-care tools to enable bedside practitioners to monitor optimal protein intake for individual patients; the biosensor based on OFS technology presented here might contribute to that purpose.

In spite of its high sensitivity, the main disadvantage of the SPR sensor is its price and real life applicability. A recent fabrication breakthrough in planar waveguides allows the use of grating coupled interferometry to achieve extremely high sensitivities to refractive index (RI) changes of the order of 10^{-7} and a protein surface coverage sensitivity of 0.1 pg/mm^2 [252]. In spite of this high sensitivity, their practicability for *in vivo* measurements remains limited. In this regard, optical fibre sensors modified with thin functional coatings offer a promising alternative to facilitate highly sensitive, selective and fast measurement in real time with a reported resolution of RI change of 10^{-6} [253]. Among various OFS designs and measurements schemes, refractometers and chemical sensors based on optical fibre gratings have been employed extensively, in part because they offer wavelength-encoded information [254], [255], which overcomes issues associated with intensity based approaches such as bias from movement artefacts or intensity drifting from the light source.

Similar to SPR and planar waveguide devices, LPG sensors can provide highly precise analytical information about adsorption and desorption processes associated with the RI and thickness of the sensing layer. For instance, the sensitivity of LPG sensors (ca. 1 nM for antigen–antibody

reactions) has been demonstrated to be of the same order of magnitude as SPR sensors [249], [256]. The high sensitivity of the LPG based optical fibre sensors operating at the phase matching turning point (PMTP) to RI change provides a high potential for detection of clinical analytes [257]. One of the earliest applications of an LPG to label free immunoglobulin (IgG) detection was demonstrated by DeLisa *et al*. [256]. The LPG was modified with goat anti-human IgG (antibody) and the detection of specific antibody/antigen binding was investigated in the range of the concentrations of 2-100 μg/ml. Pilla *et al*. [258] recently demonstrated an LPG immunosensor operating at the PMTP that provided a sensor with high sensitivity of 5 pg/mm^2 to anti-IgG analyte. Wang *et al*. [259] used ionic self-assembled multilayers onto the surface of the LPG with the aim of developing a biosensor using biotin–streptavidin as a demonstration bioconjugate pair. The lowest detected concentration of streptavidin was 12.5 μg/mL. Bandara *et al*. [260] recently reported detection of methicillin-resistant staphylococci using a biosensor assay consisting of nanoscale films onto an LPG.

The characteristics of optical fibre sensors, such as sensitivity, response/recovery times and especially selectivity, depend strongly on the performance capabilities and the properties of the functional layer. Research in the field of optical fibre sensors has focused on the development of new materials that can be used as sensitive elements. In this section, a novel biosensor based on an LPG coated with SiO_2:Au core/shell NPs is demonstrated with sensitivity to streptavidin of an order of magnitude greater than previously reported with LPG sensors [259]. The biosensor proposed in this chapter section provides a detailed study on the effect of the SiO_2 NPs' diameter and on the presence of Au NPs. Two sets of SiO_2:Au NPs of diameters 80 and 300 nm are used to generate coatings of different layer thickness and surface areas on the LPG sensing platform.

The biotin-streptavidin interaction was used as a model system to characterise the performance of the sensor. The biotin is attached directly to the Au shell of the SiO_2 NPs, providing a sensor with high selectivity for protein

detection. The selectivity of the sensor towards a particular protein of interest can be tailored simply by changing the nature of the ligand, making LPGs modified with SiO_2:Au NPs a generic sensing platform for biosensor development and therefore able to detect different type of proteins.

5.1.1 LPG biosensor parameters

Typically, protein (and propofol) binding to the functionalized LPG surface follows the Langmuir isotherm theory that can be described by [261]:

$$a = \frac{MkC}{1 + kC} \tag{5.1}$$

where a is the amount of analyte adsorbed, C is the solution concentration, M is the adsorption maximum and k is the equilibrium binding constant.

It can be assumed that the wavelength shift response of the LPG biosensor is proportional to the adsorption [262], [50] such that,

$$\Delta\lambda = \Delta\lambda_{max}\left(\frac{kC}{1 + kC}\right) \tag{5.2}$$

where $\Delta\lambda$ is the wavelength shift in the sensor due to the binding of the protein onto the self-assembled surface and $\Delta\lambda_{max}$ is the maximum wavelength shift due to complete formation of the protein layer.

In this section of the research work the Langmuir isotherm is linearized using the *reciprocal (Langmuir)* in order to estimate the parameters k and $\Delta\lambda_{max}$ [263], [264],

$$\frac{C}{\Delta\lambda} = \frac{1}{\Delta\lambda_{max}k} + \left(\frac{1}{\Delta\lambda_{max}}\right)C \tag{5.3}$$

The sensitivity (S) of the sensor for bio-molecule detection is given by [265],

$$S = \frac{\Delta\lambda_{max}}{\sigma_{max}} \tag{5.4}$$

where σ_{max} is the surface density of the protein under detection (streptavidin) when all binding sites of the other immobilized molecule are occupied (biotin).

The theoretical detection limit of the sensor can also be estimated [265]:

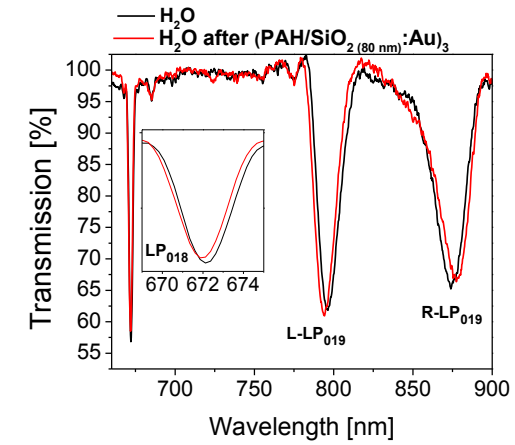
$$D_{LS} = \frac{R}{S} \tag{5.5}$$

where the estimation is only based on the spectrometer device resolution (R), the environmental and inherent thermal noise of the spectrometer are neglected [262] and S is the sensitivity calculated with Eq. (5.4).

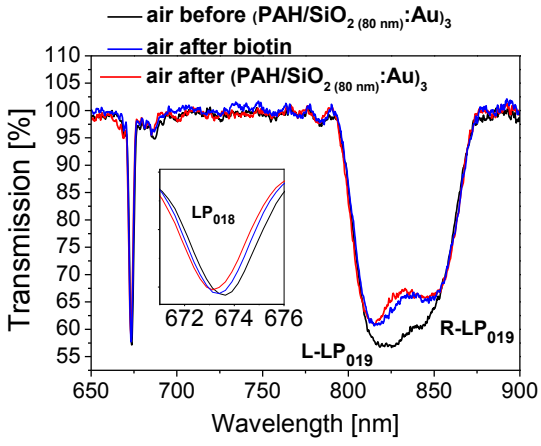
5.1.2 Results of PAH/SiO2:Au film deposition onto the LPG surface

LPGs of length 4 cm and with a grating period of 110.7 μm were fabricated in a point-by-point fashion (section 3.2.1). The experimental set-up for the deposition of the film onto the LPG surface was presented in Fig. 3.15b in section 3.3.1. The LPG gauge was placed inside a Teflon deposition cell for the coating assembly and later for the Streptavidin binding tests; a transmission spectrum with a broadband light source (HL-2000, Ocean Optics) and a spectrometer (HR4000, Ocean Optics) was used during all experiments. The grating period was selected such that the LPG operated at or near the PMTP, which, for coupling to a particular cladding mode (in this case LP_{019}), ensured optimised sensitivity for the sensor performance. Fig. 5.1a and Fig. 5.1b show the transmission spectra of the LPG measured in water and air before and after the deposition of three layers of $(PAH/SiO_{2(80\ nm)}:Au)_3$ film containing SiO_2 NPs with diameter of 80 nm. Fig. 5.1b also includes the

transmission spectrum after the binding of biotin. As explained in section 1.4.2 and published in [26], the first attenuation band (@ ca. λ=673 nm), corresponding to coupling to the LP_{018} cladding mode, exhibited blue wavelength shifts of ca. 0.5 nm and ca. 0.25 nm for $(PAH/SiO_{2(80\ nm)}:Au)_3$ film and biotin deposition, respectively. The second attenuation band (@ ca. λ=825 nm), corresponding to coupling to the LP_{019} cladding mode at the PMTP, exhibited wavelength shifts of 9.5 nm and 3.5 nm for L-LP_{019} (Left band LP_{019}) and R-LP_{019} (Right band LP_{019}), after three layers of $PAH/SiO_{2(80\ nm)}$:Au NPs film deposition as shown in Fig. 5.1b.



(a)



(b)

Figure 5.1: (a) The transmission spectrum of an LPG of period 110.7 µm measured with the LPG in water before and after film deposition. (b) In air: black line before and red line after $(PAH/SiO_{2(80\ nm)}:Au)_3$ film deposition; blue line presents the transmission spectrum after binding of biotin.

The results of Fig. 5.1 indicate successful deposition of the PAH/SiO_2:Au NPs film onto the LPG, confirming the SEM results (Figs. 3.16 and 3.17). The small wavelength shift observed after biotin adsorption, visible in the inset of Fig. 5.1b, most likely relates to the small RI change induced by the biotin molecule. After deposition of the (PAH/SiO_2:Au)$_3$ film and functionalization with biotin, two coated LPG sensors, one with 80 nm diameter SiO_2 NPs and another with 300 nm diameter SiO_2 NPs, were exposed to Streptavidin (SV) solutions of different concentrations.

5.1.3 Protein binding detection

Fig. 5.2a and Fig. 5.2b show the changes in the transmission spectrum of the LPG sensor modified with the (PAH/$SiO_{2(80\ nm)}$:Au)$_3$ film upon exposure to aqueous solutions of SV of different concentrations, obtained by removing, washing and drying the LPG after each exposure, measured in air and in solution, respectively. Similarly, Fig. 5.2c and Fig. 5.2d show the changes in the transmission spectrum of the LPG sensor modified with the (PAH/$SiO_{2(300\ nm)}$:Au)$_3$ film upon exposure to aqueous solutions of SV of different concentrations in air and in solution, respectively.

Similar to the binding of the SiO_2 NPs and biotin (Fig. 5.1), the adsorption of the SV leads to a blue wavelength shift of the first attenuation band LP_{018} (@ ca. λ=673 nm) and higher wavelength shifts for L-LP_{019} and R-LP_{019}, i.e., the magnitude of the change at the adsorption of the SV was significantly different in the LP_{019} as presented in Fig. 5.3a to Fig. 5.3d for the two coated LPGs tested: (PAH/$SiO_{2(80\ nm)}$:Au)$_3$ and (PAH/$SiO_{2(300\ nm)}$:Au)$_3$. The highest sensor sensitivity is obtained when working with differences between R-LP_{019} and L-LP_{019} for both LPG coated cases (all the blue curves in Fig. 5.3).

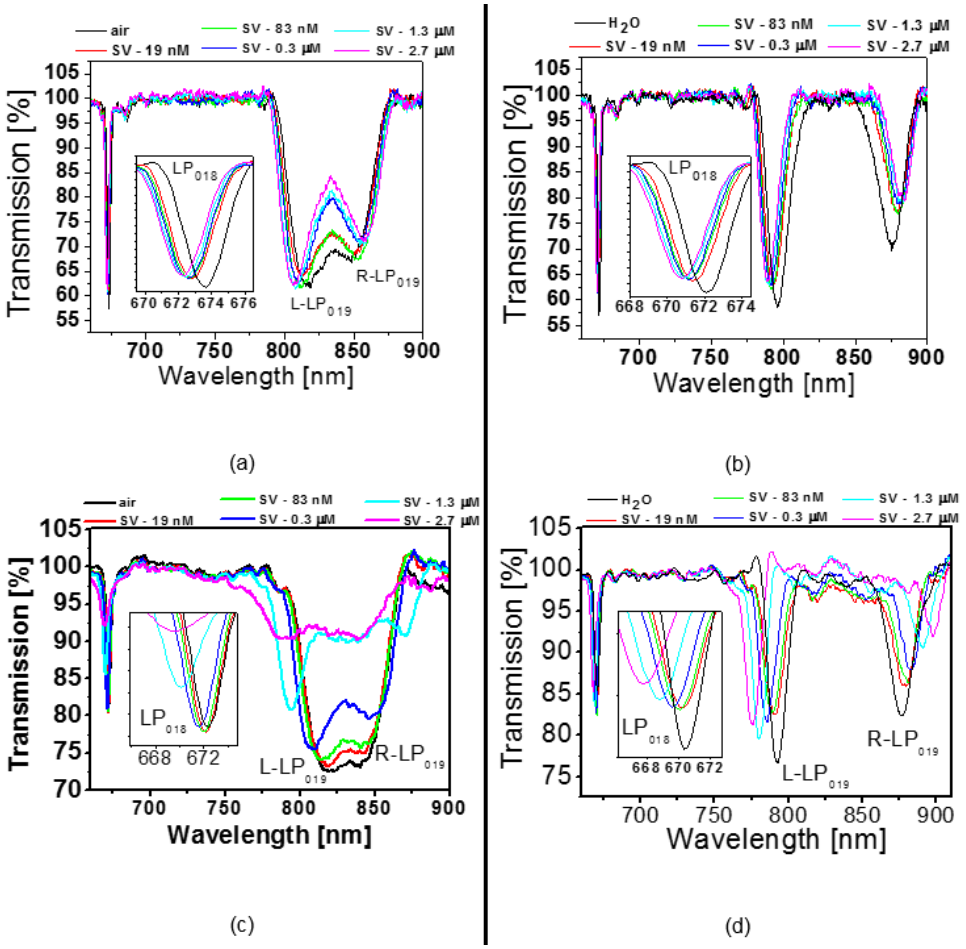


Figure 5.2: Transmission spectrum of the (PAH/$SiO_{2(80\ nm)}$:Au)$_3$ coated LPG modified on exposure to SV of different concentrations in: (a) air and (b) aqueous solution. Similarly, the transmission spectrum of the (PAH/$SiO_{2(300\ nm)}$:Au)$_3$ coated LPG modified on exposure to same SV concentrations in: (c) air and (d) aqueous solution.

In particular, the LP_{018} band shifted by ca. 1 nm for measurements both in air and in solution using the (PAH/$SiO_{2(80\ nm)}$:Au)$_3$ coated LPG and the LP_{018} band shifted by ca. 3 nm for measurements both in air and in solution using the (PAH/$SiO_{2(300\ nm)}$:Au)$_3$ coated LPG. Much greater changes of ca. 7 and 13 nm for L-LP_{019} and 7 and 9 nm for R-LP_{019} were measured in solution and in air, respectively when using the (PAH/$SiO_{2(80\ nm)}$:Au)$_3$ coated LPG (Figs. 5.3a and 5.3b). On the other hand, wavelength shifts of ca. 17 and 32 nm for L-LP_{019} and 21 and 47 nm for R-LP_{019} were measured in solution and in air, respectively when using the (PAH/$SiO_{2(300\ nm)}$:Au)$_3$ coated LPG (Figs. 5.3c and 5.3d). The wavelength shift at the SV binding is 30 times greater as compared

to the change caused by the biotin adsorption. This most plausibly is owing to the RI difference between the two compounds; the SV is much larger (52.8 kDa) as compared to the biotin (244.31 $gmol^{-1}$) and hence causes the higher RI change when adsorbed onto the surface of the LPG sensor. It should be noted that the difference between values obtained when measured in the solution and in the air is related to the bulk RI values of 1.33 and 1.00, respectively; the LPG with the current grating period operates closer to the PMTP at the bulk RI=1 and hence has higher sensitivity in air than in solution.

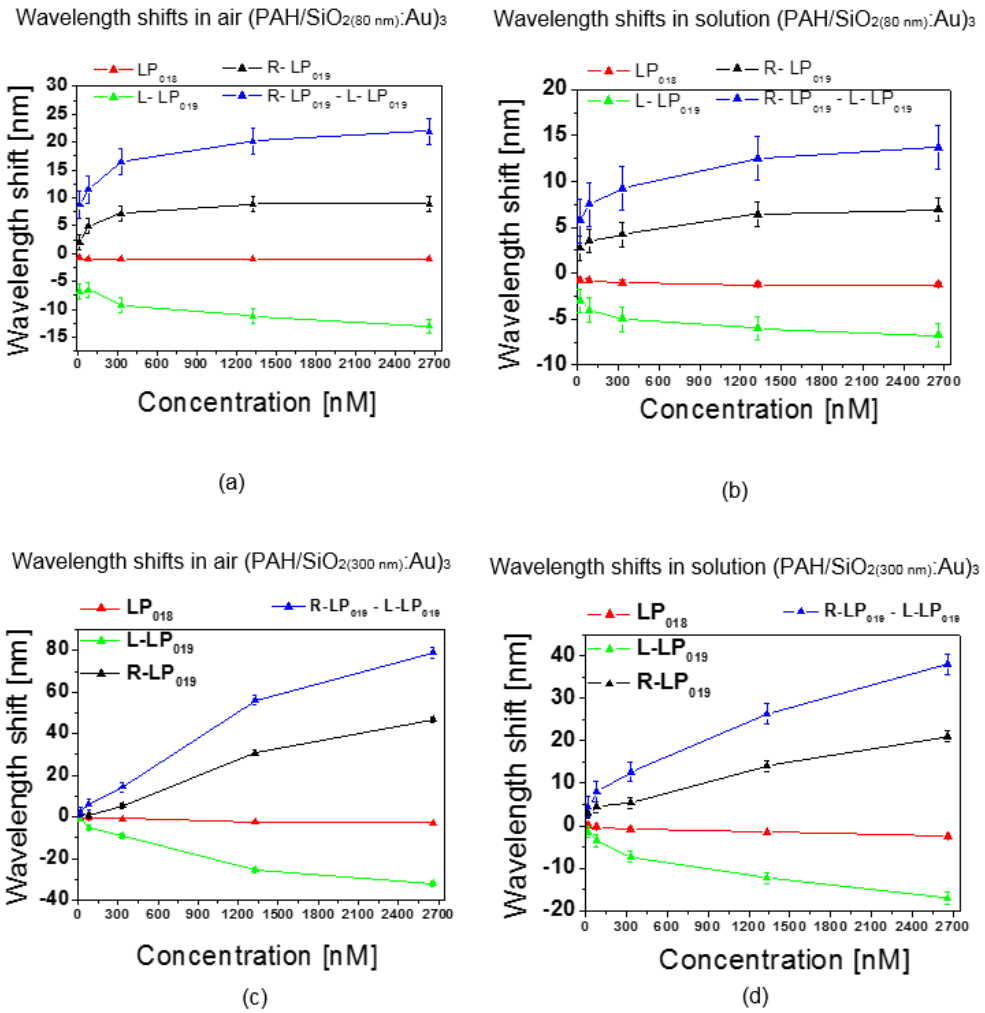


Figure 5.3: Wavelength shifts of LP_{018} and LP_{019} calculated from the transmission spectra plotted in Fig. 5.2 after the adsorption of same 5 concentrations of SV (standard deviations are calculated from five blank measurements of the LPG used). (a) and (b) Response of $(PAH/SiO_{2(80\ nm)}:Au)_3$ coated LPG in air and solution, respectively. (c) and (d) Response of $(PAH/SiO_{2(300\ nm)}:Au)_3$ coated LPG in air and solution, respectively.

5.1.4 Biosensor parameters in aqueous solutions and the effect of SiO2 NPs diameter

Data from Figs. 5.4a to 5.4d present the graphical method for calculating the equilibrium binding constant using the difference from R-LP_{019} - L-LP_{019} in wavelength shift (blue curves from Figs. 5.3b and 5.3d) after exposure to different concentrations of SV. Fig. 5.4a shows the fit of the Langmuir isotherm (Eq. 5.2) for the adsorption of SV to the biotin using the (PAH/$SiO_{2(80\ nm)}$:Au)$_3$ coated LPG. Fig. 5.4b shows the linearized form (Eq. 5.3) of the fit presented in Fig. 5.4a.

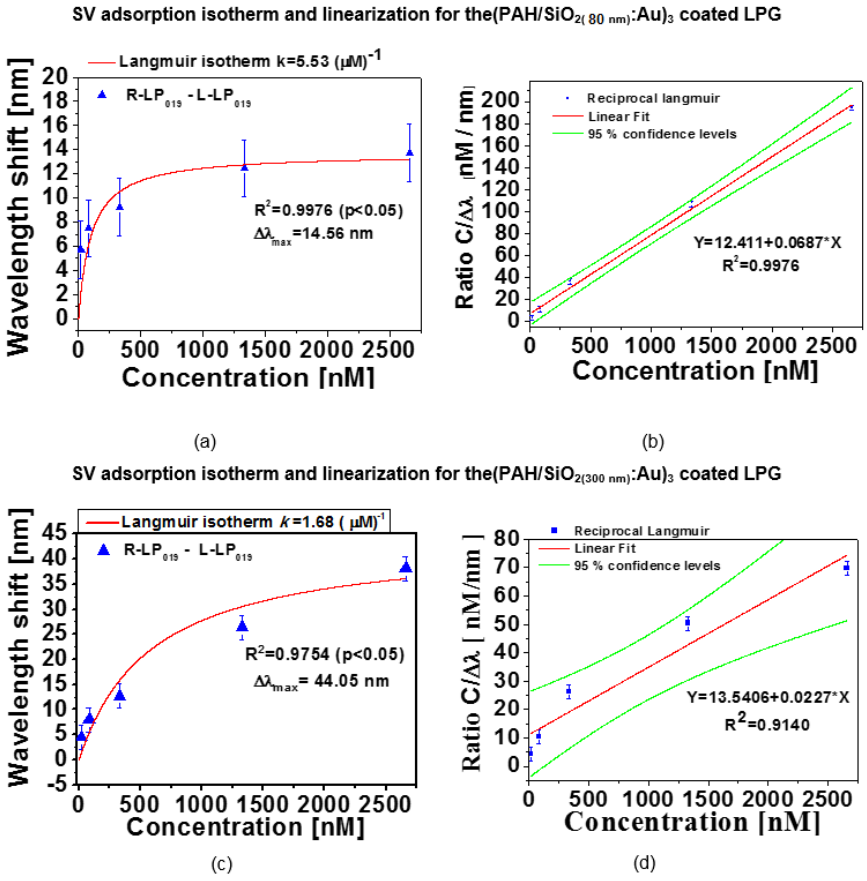


Figure 5.4: SV adsorption isotherms and their linearization for the coated LPGs. (a) & (c) Langmuir isotherm fits of (R-LP_{019} – L- LP_{019}) data from Fig. 5.3b and 5.3d respectively and (b) & (d) linearizations of Langmuir isotherm (Figs. 5.4a and 5.4c) using Eq. (5.3). The error bars represent the standard deviation of 5 blank measurements and the green lines provide the 95% confidence level [266], [267].

Similarly, Fig. 5.4c shows the fit of the Langmuir isotherm for the adsorption of SV to the biotin using the (PAH/$SiO_{2(300\ nm)}$:Au)$_3$ coated LPG. Fig. 5.4d shows the linearized form of the fit presented in Fig. 5.4c.

The estimation of the equilibrium binding constant (k) and the maximum wavelength shift ($\Delta\lambda_{max}$) is made from the linear fit presented in Fig. 5.4b and Fig. 5.4d, and comparing the adjusted linear equations (shown as insets in the graphs) with Eq. (5.3). Thus, using the linear fit form from the response of the (PAH/$SiO_{2(80\ nm)}$:Au)$_3$ coated LPG,

$$\frac{1}{\Delta\lambda_{max}} = 0.0687 \quad \rightarrow \quad \Delta\lambda_{max} = 14.56\ \text{nm} \tag{5.6}$$

$$\frac{1}{\Delta\lambda_{max}k} = 12.411 \quad \rightarrow \quad \frac{1}{(14.56)k} = 12.411 \quad \rightarrow \quad k = 5.53\ (\mu\text{M})^{-1} \tag{5.7}$$

and using these previous parameters in Eq. (5.2) the correlation coefficient was $R^2 = 0.9976$ between experimental data and the Langmuir isotherm plotted in Fig. 5.4a when the difference between the centre wavelengths of the R-LP_{019} and L-LP_{019} bands was considered.

Similarly, using the linear fit form from the response of the (PAH/$SiO_{2(300\ nm)}$:Au)$_3$ coated LPG shown in Fig. 5.4d,

$$\frac{1}{\Delta\lambda_{max}} = 0.0227 \quad \rightarrow \quad \Delta\lambda_{max} = 44.05\ \text{nm} \tag{5.8}$$

$$\frac{1}{\Delta\lambda_{max}k} = 13.5406 \quad \rightarrow \quad \frac{1}{(44.05)k} = 13.5406 \quad \rightarrow \quad k = 1.68\ (\mu\text{M})^{-1} \tag{5.9}$$

and the correlation coefficient was $R^2 = 0.9754$ between experimental data and the Langmuir isotherm plotted in Fig. 5.4c when the difference between the centre wavelengths of the R-LP_{019} and L-LP_{019} bands was considered.

Considering the average length of a streptavidin molecule as P_{SV} =4 nm [268], the theoretical surface density of streptavidin monolayer is,

$$\sigma_{max} = M_{SV}/N_A \cdot {P_{SV}}^2 = 62000\ /(6.0221 \times 10^{23})(4 \times 10^{-9})^2 = \\ = \quad 6.43\ \mathrm{ng/mm^2} \tag{5.10}$$

as calculated from the average length of a streptavidin molecule (P_{SV}) and taking $M_{\mathrm{SV}} = 62{,}000\ \mathrm{g/mol}$ as the estimated molecular weight of SV and $\mathrm{N_A} = 6.0221 \times 10^{23}\mathrm{mol}^{-1}$ as the Avogadro's number [268], [262].

Therefore, in addition to the difference in the equilibrium binding constants, $5.53\ (\mu\mathrm{M})^{-1}$ vs $1.68\ (\mu\mathrm{M})^{-1}$ for 80 nm and 300 nm diameter SiO_2 NPs respectively, the effect of these diameters on the LPG sensor is also reflected in the sensitivity and the theoretical limit of SV detection, i.e., using Eq. (5.4) the sensitivity of the proposed sensors are: $S = 14.56\ /6.43\ = 2.26\ \mathrm{nm}/(\mathrm{ng/mm^2})$ for the (PAH/$SiO_{2(80\ nm)}$:Au)$_3$ coated LPG and $S = 44.05\ /6.43\ = 6.85\ \mathrm{nm}/(\mathrm{ng/mm^2})$ for the (PAH/$SiO_{2(300\ nm)}$:Au)$_3$ coated LPG, where the maximum wavelength shifts were determined by the reciprocal Langmuir transformations of Fig. 5.4b and Fig. 5.4d. Applying Eq. (5.5), the theoretical limits of SV detection for both diameter cases are: $D_{LS} = 0.13/2.26 = 57.5\ \mathrm{pg/mm^2}$ for the (PAH/$SiO_{2(80\ nm)}$:Au)$_3$ coated LPG and $D_{LS} = 0.13/6.85 = 18.9\ \mathrm{pg/mm^2}$ for the (PAH/$SiO_{2(300\ nm)}$:Au)$_3$ coated LPG.

5.1.5 Sensor specificity, dynamic measurements and analytical estimation of the limit of detection (LoD)

The lowest tested and detected concentration with the coated LPGs proposed in previous sections was 19 nM. This section presents further optimization of an (PAH/$SiO_{2(80\ nm)}$:Au)$_3$ coated LPG (period of 110.8 μm) through testing lower concentrations and quantifying the limit of detection (LoD) [266], [267]. In addition, sensor specificity for the biotin-streptavidin interaction presented in

the previous section is highlighted through demonstration of the performance of a $(PAH/SiO_{2(80\ nm)})_3$ coated LPG with a period of 110.8 μm and without the addition of Au NPs. Fig. 5.5a and Fig. 5.5b show the performance for SV detection to biotin using the $(PAH/SiO_2)_3$ coated LPG without Au NPs in air and solution, respectively. The results shown in these figures were firstly obtained by depositing three bilayers of $PAH/SiO_{2(80\ nm)}$ without Au NPs and then exposing the coated LPG to biotin and eight different concentrations of SV afterwards, all as described in section 3.3.1. Figs 5.6a presents the change of the transmission spectrum (in air) for the $(PAH/SiO_{2(80\ nm)}:Au)_3$ coated LPG after the exposure to the same eight SV concentrations. Taking the wavelength shifts from the difference ($R\text{-}LP_{019}$ – $L\text{-}LP_{019}$) as demonstrated in previous section, Fig. 5.6b shows a comparison of the SV detection between the gold coated $(PAH/SiO_{2(80\ nm)}:Au)_3$ and the response of the non-gold coated LPG in aqueous solutions.

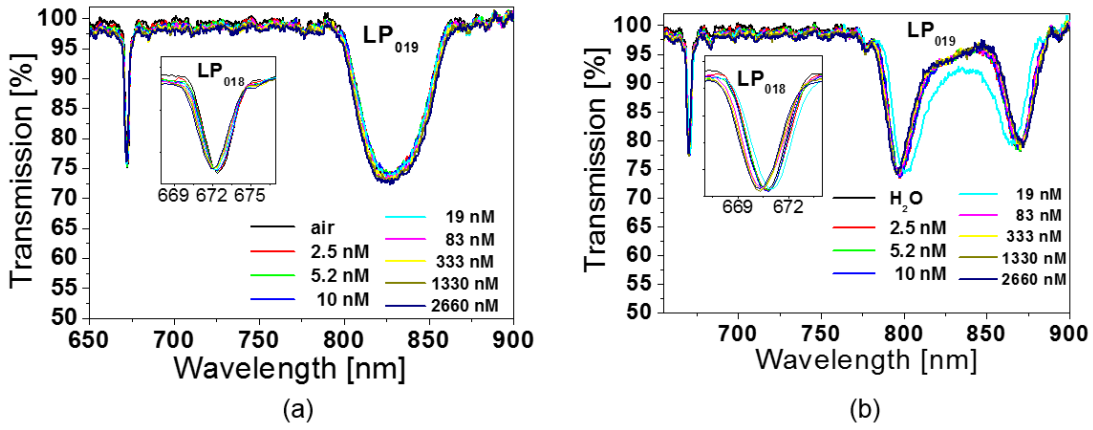


Figure 5.5: Transmission spectrum of the $(PAH/SiO_{2(80\ nm)})_3$ + biotin coated LPG without Au NPs on exposure to SV of eight different concentrations in: (a) air and (b) solution.

Fig. 5.6b demonstrates that the adsorption of SV is clearly enhanced by the presence of Au NPs; the equilibrium binding constant was $k = 6.2\ (\mu M)^{-1}$ for the $(PAH/SiO_{2(80\ nm)}:Au)_3$ coated LPG vs $k = 34.7\ (\mu M)^{-1}$ for the $(PAH/SiO_2)_3$ coated LPG. The maximum wavelength shift with Au NPs and SiO_2 NPs of 80 nm (red curve, Fig. 5.6b) was ca. 2 times greater than the maximum

wavelength shift without Au NPs (green curve, Fig. 5.6b). In addition, the wavelength shift due to the lowest detected concentration (2.5 nM) in the former case was also 2 times greater than the case without Au NPs, 2 nm vs 4 nm respectively.

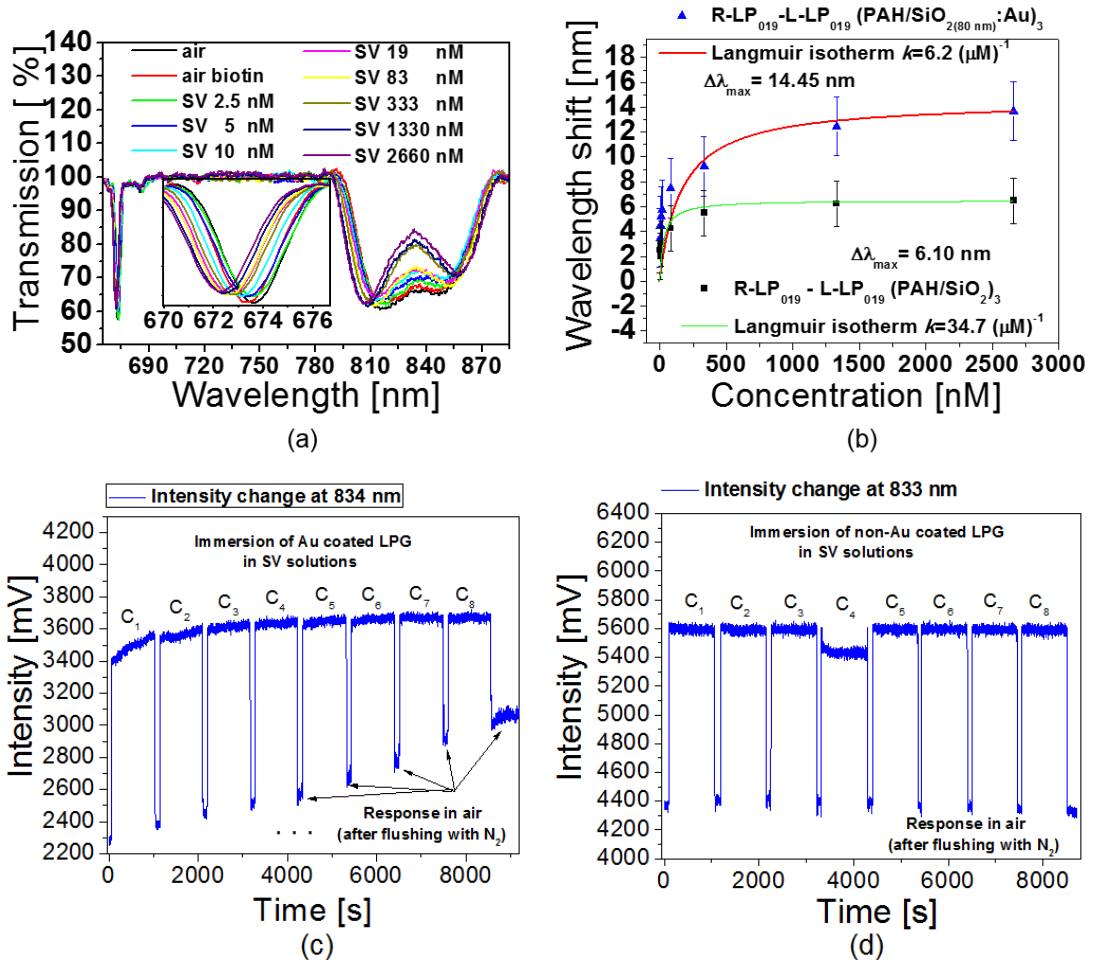


Figure 5.6: (a) Transmission spectrum of the $(PAH/SiO_{2(80\ nm)}:Au)_3$ coated LPG on exposure to SV of eight different concentrations in air. (b) Comparison of the response to SV adsorption between the $(PAH/SiO_{2(80\ nm)}:Au)_3$ and $(PAH/SiO_2)_3$ coated LPGs in solution. (c) The change in transmission of the $(PAH/SiO_{2(80\ nm)}:Au)_3$ coated LPG measured at fixed wavelength of 834 nm on immersion into solutions of different SV concentration. (d) The change in transmission of the non-gold coated LPG $(PAH/SiO_2)_3$ measured at 833 nm on immersion into the same set of SV solutions.

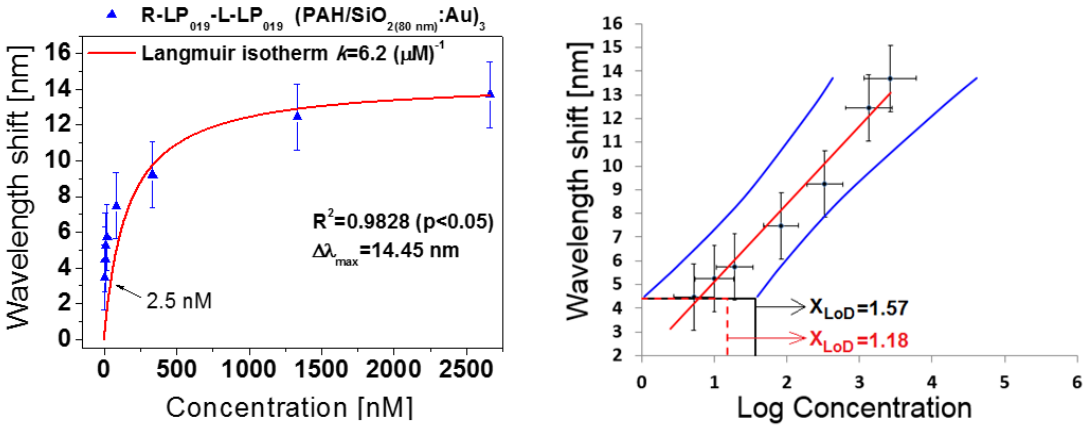
Figs. 5.6c and 5.6d show the dynamic response from the LPGs previously compared in Fig. 5.6b, i.e., the intensity change at fixed wavelength (in the LP_{019} band) against time as the sensors were inserted into the different SV

concentrations. Discontinuities are observed when the sensor was removed from SV due to the bulk RI change between water (n=1.33) and air (n=1), i.e., the large discontinuities in Figs. 5.6c and 5.6d are not related to the protein binding, but Fig. 5.6c confirms the dynamic adsorption of SV over time in each solution deposition with increased concentration (C_1=2.5 nM, C_2=5 nM, C_3=10 nM, C_4=19 nM, C_5=83 nM, C_6=333 nM, C_7=1330 nM, C_8=2660 nM). The exposure time to every SV concentration was 15 min and completion of SV binding to biotin was faster for higher concentrations in Fig. 5.6c. On the other side, immersion of the non-gold coated LPG (Fig. 5.6d) to the different SV concentrations remained relatively constant for both cases in air and solution; only the significant change in C_4 was due to movement artefacts on the system deposition (Fig. 3.15) during the measurement.

Finally, the LoD presented in section 5.1.4 assumes that the analytical sensor resolution is identical to the discretization limit of the spectrometer implemented and it was only used as a theoretical LoD estimation for comparison between two gold-coated LPGs containing two different SiO_2 NPs differing in diameter size. An improved statistical estimation of the LoD from data re-plotted in Fig. 5.7a is mainly based on the supplementary analytical tool of reference [267] . This tool determines the LoD using a calibration curve of n data pairs {x,y} and the average standard deviation of the sensor is estimated from the standard error of the fit. Additionally, the following assumptions are made: (1) the errors are normally (Gaussian) distributed and systematic errors have been corrected (or they are null); (2) the concentrations, x, of the {x,y} data pairs from the calibration curve (Fig. 5.7b) are known exactly and their errors are propagated statistically; (3) the calibration curve is linear and sensitivity near the LoD is identical to that of the entire calibration curve (slope), and (4) the standard deviations of the signal are the same for all concentration measurements (also error distributions of the blanks and concentration measurement have identical width).

The calibration curve presented in Fig. 5.7b was obtained by feeding the experimental data of Fig. 5.7a into an Excel sheet provided in supplementary

data of reference [267]. The statistical parameters were selected as follows: (i) blank measurements $b = 5$ and number of sample concentrations = 8; (ii) the confidence level (blue curves in Fig. 5.7b) is $(1 - \alpha) = 0.95$ where α is the α-quantile of the Student's t-function with $b - 1$ degrees of freedom and, therefore, the t-Student parameter value is $t_{0.05,4} = 2.776$.



(a) (b)

Figure 5.7: (a) Langmuir adsorption isotherm for the (PAH/$SiO_{2(80\ nm)}$:Au)$_3$ coated LPG on exposure to SV concentrations in solution (Fig. 5.6b). (b) Statistical estimation of the LoD based on references [266] and [267].

The LoD calculated from the method explained in reference [267] is 1.57 in logarithmic scale which is equivalent to 37.15 nM. The LoD calculated from the Excel sheet provided in reference [267] is larger than the value calculated from the signal response (the calibration curve) and standard deviation of the blank ($\sigma = 1.89$), i.e., the $X_{LOD} = 1.18$ in logarithmic scale pairs to the y-value equivalent to $3 * \sigma = 5.67$ in the same calibration curve [266]. Therefore the LoD estimation (anti-logarithm) for the latter case is 15.13 nM.

5.2 Optical fibre sensor for propofol detection in aqueous solutions and gas phase

This second section of the chapter is dedicated to the proof of concept for the detection of propofol under in-vitro conditions using both U-shaped fibres and LPGs. The materials used for the functionalization of these sensors were presented in sections 3.4.1 and 3.4.2. Section 3.4.1 explained the preparation and characterization of an imprinted TiO_2 based on LPD process and section 3.4.2 explained the preparation of another imprinted TiO_2 based on sol-gel preparation and including MSNs with the purpose of increasing sensitivity for propofol detection. For sections 5.2.1 to 5.2.3 the method explained in 3.4.1 was used and for sections 5.2.4 and 5.2.5 the method explained in 3.4.2 was used.

As discussed in section 2.1.4, monitoring of the delivery of propofol needs better engineering control to provide a safer induction and maintenance of anaesthesia. The most frequently used technologies to monitor levels of the concentration of propofol in blood or breath are HPLC and GC-MS, respectively. These devices are bulky, expensive and time-consuming to operate and obtain analytical results (ca. 2 hr). The technological trends in this area of research is towards the development of fabricating an on-line method that is less expensive and faster to obtain the concentration of propofol in the blood or from the breath of patients. Table 5.1 summarizes the general characteristics and range of concentrations measured from the current developments found in the literature.

Medical device and reference	***Main characteristics and concentrations measured***
Lab-on-chip spectrophotometric device using optical fibres [160].	* Propofol in plasma: 3 – 18 μg/ml. * Rapid detection in-vitro. * Needs azo-coupling reagent. * Lowest detection = 0.65 μg/ml.
Lab-on-chip using fluorescence optical fibre detection (FOFD) [90]. Validated with HPLC.	* Fluorescence measurements after reaction of propofol with Gibb's reagent. * Propofol concentrations in simulated whole blood samples: 0.10 – 15 μg/ml. * Rapid detection in vitro (5 min).
Lab-on-chip using micro-optics components and disposable microfluidic chip [158].	* Propofol concentrations in aqueous solutions: 0.25 – 10 ppm. * In-vitro tests. * Traditional molecular imprinting of propofol [269] on disposable microfluidic films. Lowest detection = 1.4 μM
Proton transfer reaction mass spectrometry (PTR-MS) [120]. Validated with HPLC.	* New device that measures Volatile Organic Compounds (VOCs) at low concentrations and real time (On-line continuous monitoring in-vivo). * Propofol range tested in plasma: 0.1 – 10 μg/ml. * Propofol measured in breath: 2 – 6 ppb.
Electrochemical gas sensor [159]. Validated with HPLC and GC-MS	* On-line monitoring in-vivo test in animals. * Propofol measured in plasma: 0.1 – 11 μg/ml. * Propofol range measured in breath: 0 – 32 ppb.
GC-MS and HPLC [119], [164]	* Gas sampling made with Tenax tubes and tested in GC-MS after thermodesorption. * Off-line monitoring discontinuous in-vivo. * Propofol measured in plasma: 0.3 – 3.3 μg/ml and 3.2 - 6.8 mg/l * Propofol range measured in breath: 2.8 – 22.5 ppb and 4.3 – 33.5 ng/l. Lowest detection = 3.6 ng/l (breath) and 0.2 mg/l (plasma).

Table 5.1: Current technologies found in the literature for measuring propofol concentration either in blood or from breath.

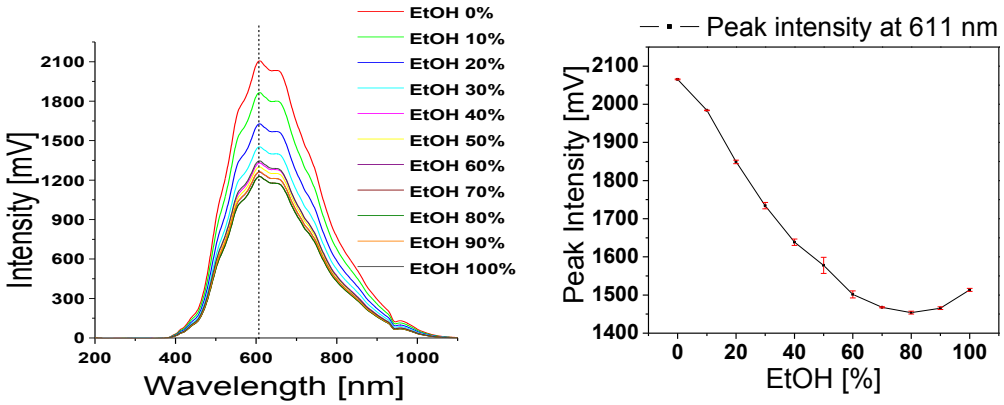
Medical device and reference	***Main characteristics and concentrations measured***
Ion-molecule reaction mass spectrometry (IMR-MS) [121]. Validated with HPLC.	* Measures organic and inorganic compounds in gases. *On-line and off-line monitoring in-vivo during mechanical ventilation. * Propofol range tested in plasma: 0.1 – 10 μg/ml. * Good correlation, range of Pearson r = 0.846 – 0.957 (P<0.01, n=6) from head space gas sampling and plasma.
Membrane inlet-ion mobility spectrometry (MI-IMS) [165]. Validated with HPLC and bispectral index (EEG).	* Gas samples. * On-line and off-line monitoring in-vivo. * Propofol range tested in plasma: 0.1 – 10 μg/ml.
GC-MS with headspace Solid-Phase Microextraction.	* Gas samples. * On-line and off-line monitoring in-vivo. * Propofol range tested in plasma: 0.1 – 10 μg/ml.
Photoacoustic spectroscopy in the UV region [166].	* On-line monitoring in-vitro. * Lowest detection in subparts of ppb.

Table 5.1 (Continuation): Current technologies found in the literature for measuring propofol concentration either in blood or from breath.

From the medical devices and techniques presented in Table 5.1, only the lab-on-chip or lab-on-fibre devices, an electrochemical gas sensor and photoacoustic method satisfy the need for more portable devices with faster analysis than HPLC and GC-MS. The rest of this section presents the results obtained with the OFS proposed for propofol detection as a proof of concept towards a portable, less expensive and easy to fabricate method for this purpose.

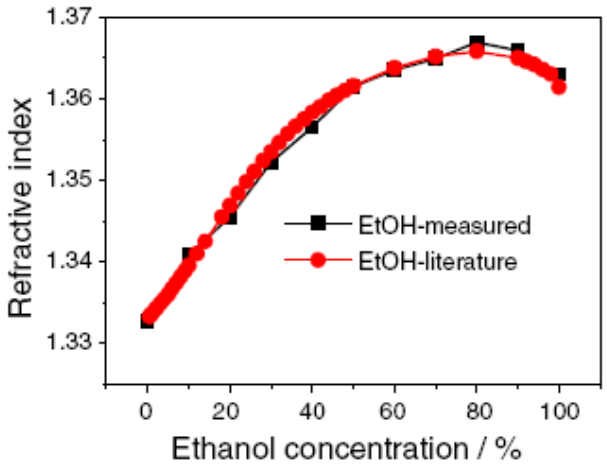
5.2.1 Results of imprinted TiO_2 deposition (based on LPD) onto U-shaped fibres

As mentioned in section 1.4.4, any U-shaped fibre probe can be firstly used as a refractometer. Fig. 5.8a and Fig. 5.8b present the response of a fabricated U-shaped fibre (diameter of 1.70 mm) on exposure to different wt.% concentrations of EtOH in deionised water and using the experimental set-up previously described in Fig. 3.27 (chapter 3). To create different refractive index units (RIU), different percentages of EtOH were mixed in deionised water, from 0 wt.% to 100 wt.% as described in reference [270]. Fig. 5.9a shows the equivalence (taken from [270]) between % of EtOH and RI which allows calculation of the sensitivity to RIU of the same U-shape fibre (Fig. 5.9b). Fig. 5.9b only presents the peak (at 611 nm) intensity change linearly related to RI from 0 wt.% to 70 wt.%, and the resulting sensitivity was 18377 mV/ RIU or 183.77 mV / 0.01 RIU. Similarly, 31 U-shaped fabricated fibres were calibrated in the same manner and the average sensitivity was (156.80 ± 28.47) mV / 0.01 RIU within a range of [103.82 mV / 0.01RIU, 226.53 mV / 0.01RIU].

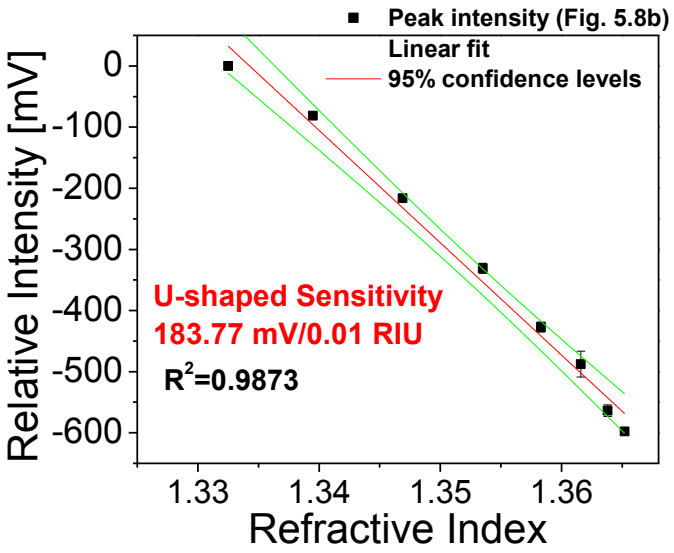


(a) (b)

Figure 5.8: (a) Transmission spectra of a U-shaped fibre (diameter 1.70 mm) on exposure to different wt.% of EtOH. (b) Maximum intensity peak tracking (at 611 nm) of the transmission spectra measured in (a) of this figure; the standard deviations are based on the measurement of five transmission spectra in every solution.



(a)

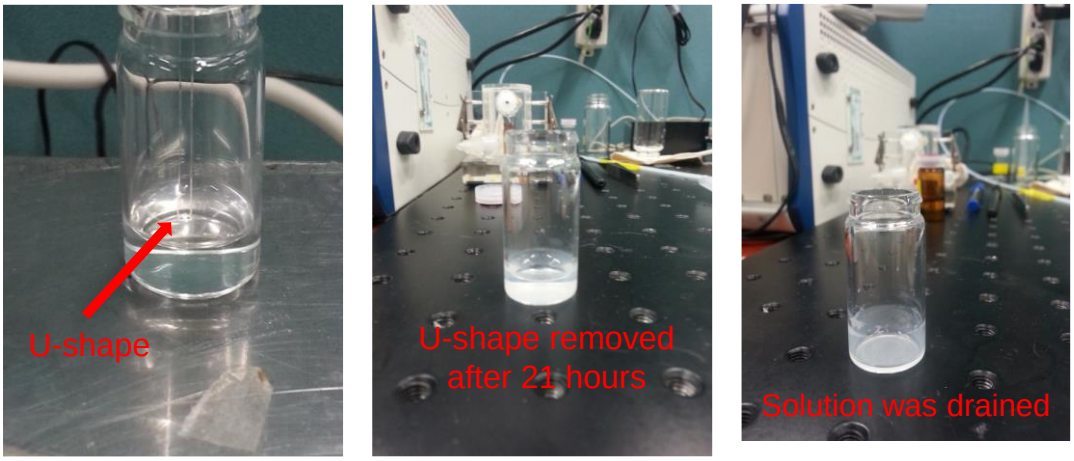


(b)

Figure 5.9: (a) Equivalence between EtOH % and RI as published in reference [270]. (b) Sensitivity to RIU (same U-shaped fibre) obtained from the peak response measured in Fig. 5.8b but calculated only from 0 wt. % to 70 wt. %.

After calculation of sensor sensitivity to RI using EtOH, the fabricated U-shape fibre was functionalized using the chemicals of Table 3.3 (chapter 3) for propofol sensing purposes. The set-up for experimental deposition was presented in Fig. 3.27, but the photograph of Fig. 5.10a shows how the fibre was immersed in the solution prepared as set 2 of Table 3.3, Fig. 5.10b

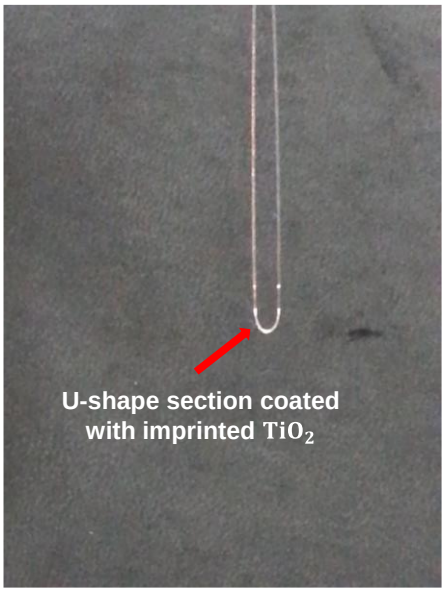
demonstrates how the imprinted TiO_2 thin film starts to develop on the inner walls of the glass vial used for deposition and finally, Fig. 5.10c shows how a thicker imprinted TiO_2 film was formed on the inner wall of the vial after 3 days (solution was drained in the photograph in (c)).



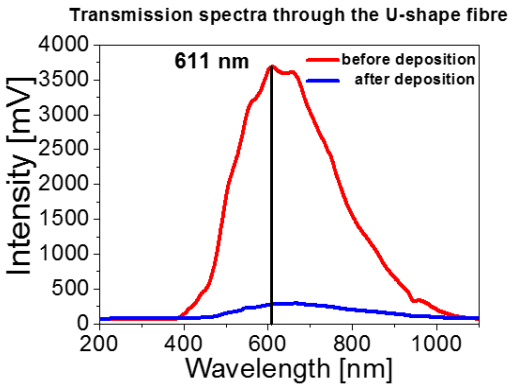
(a) (b) (c)

Figure 5.10: (a) U-shape fibre immersed in solution for imprinted TiO_2 deposition (kept inside for 21 h.) (b) Development of the imprinted TiO_2 film on the inner walls of the vial after 2 days. (c) Formation of a thicker imprinted TiO_2 film after 3 days.

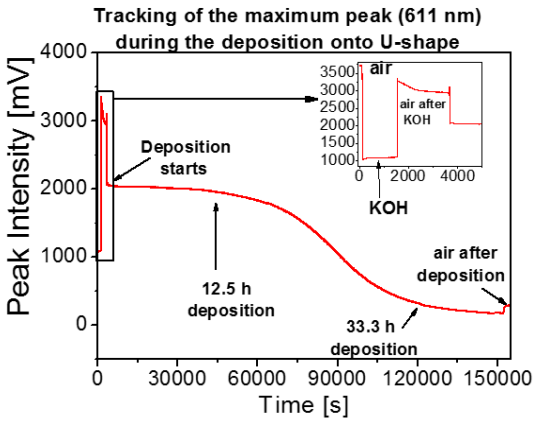
Similar to Fig. 5.10, the interface of the U-shape fibre immersed in the imprinted TiO_2 precursor solution was visible after 10 hours of deposition (Fig. 5.11a). In addition, using the experimental set-up of Fig. 3.27, the transmission spectrum through the U-shape fibre and its maximum intensity peak (Fig. 5.11b) could be tracked during film deposition (Fig. 5.11c). Fig. 5.11c presents the tracking of a single wavelength (611 nm) during the deposition of the imprinted TiO_2 film onto a U-shape fibre for 41 hours and using the set 1 of concentrations from Table 3.3 (chapter 3). The inset in Fig. 5.11c shows the preparation step for the deposition of the film, i.e., the hydroxylation of the fibre in KOH solution (20 min).



(a)



(b)



(c)

(b)

(c)

Figure 5.11: (a) Photograph of the U-shape probe coated with the imprinted TiO_2 film after immersion in the precursor solution (Fig. 5.10a) for more than 33 h. (b) Transmission spectra recorded in air before and after deposition of the film for 41 hr. and using the set-up of Fig. 3.27. (c) Tracking of the single wavelength 611 nm before, during and after the film deposition for 41 hr.

The visible spectrum of the light source shown in Fig. 5.11b decreased gradually by means of film growth onto the surface of the U-shape fibre and this change was dynamically tracked at 611 nm in the spectrometer (every second), i.e., the tracking at 611 nm (Fig. 5.11c) also demonstrated that the

intensity in the spectrometer decreased over time in relation to the increase of the film thickness onto the U-shape section. The overall intensity of the transmission spectrum (in air, Fig. 5.11b) decreased more than 90% after 41 hr. of film deposition which resulted in a thicker growth of the film (Fig. 5.11a). During all the experimental deposition process, ambient temperature and humidity were stable, 24 ^{0}C $\pm$ 2 ^{0}C and 38 %RH $\pm$ 3 %RH, respectively.

Fig. 5.12 demonstrates the change in peak intensity (*cf*. Fig. 5.11) due to deposition of the imprinted TiO_2 film based on different concentrations during the LPD process. Two U-shaped fibres (u1 and u2) were functionalized using the set 1 of concentrations of Table 3.3 [25 mM / 50 mM ($[NH_4]_2$ TiF_6 :H_3BO_3)] during deposition (Fig. 3.27); U-shaped fibres u3 to u5 were functionalized using the set 2 of concentrations of Table 3.3 and only u6 was functionalized with a concentration between the set 1 and set 2, i.e., 37.5 mM of $[NH_4]_2$ TiF_6 and 70 mM of H_3BO_3. Table 5.2 summarizes characteristics of the U-shaped fibres used, the set of concentrations prepared and the timing of deposition of each case.

U-shaped used	U-bent radii (mm)	Concentrations used (Table 3.3) $\beta - CD$:Propofol / ($[NH_4]_2$ TiF_6 :H_3BO_3)	Deposition time
U1	1.5	0.8 mM/25 mM :50 mM	ca. 21 hr
U2	1.7	0.8 mM/25 mM :50 mM	ca. 21 hr
U3	1.4	0.8 mM/ 50 mM : 100 mM	ca. 12.5 hr
U4	1.4	0.8 mM/ 50 mM : 100 mM	ca. 12.5 hr
U5	1.5	0.8 mM/ 50 mM : 100 mM	ca. 12.5 hr
U6	1.6	0.8 mM/ 37.5 mM : 70 mM	ca. 18 hr

Table 5.2: Summary of the U-shaped probes used in this part of the research.

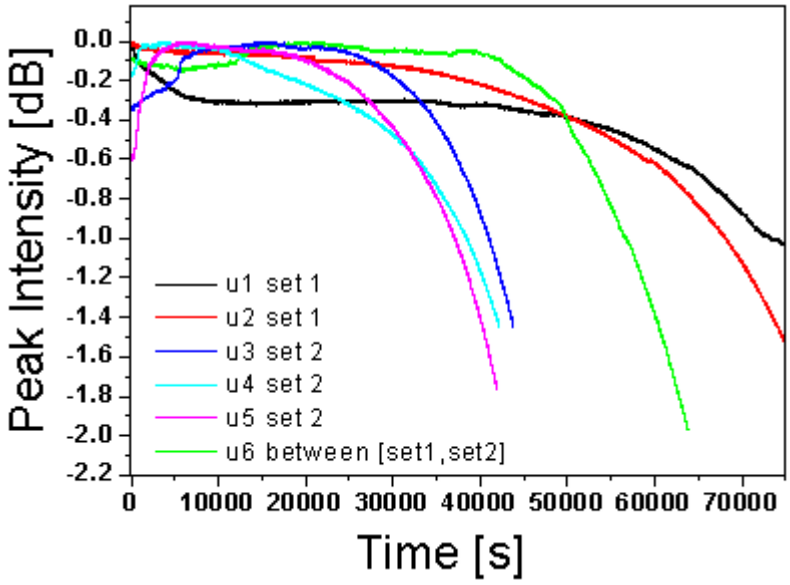


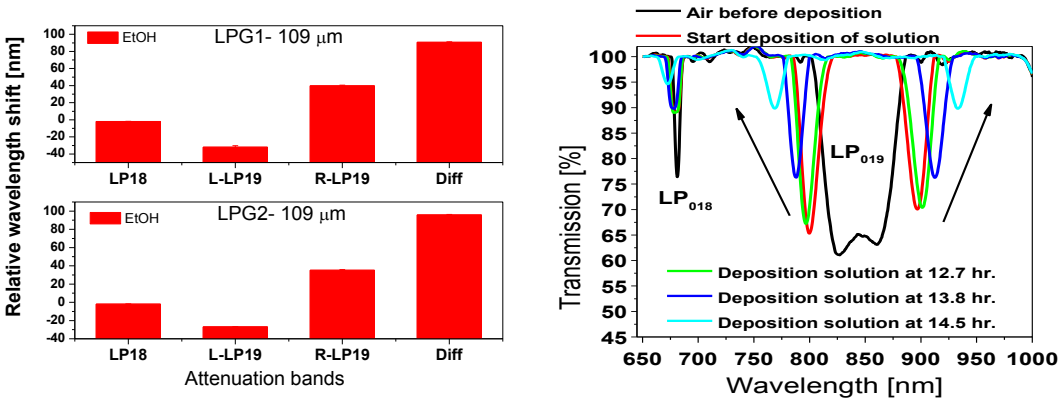
Figure 5.12: All film precursor depositions used 0.8 mM final concentration of β −CD/Propofol complex. Imprinted TiO_2 film deposition tracked from the maxima of transmission spectra for different concentrations (see Table 5.2).

All the curves in Fig. 5.12 are plotted from the moment when the U-shaped fibres were immersed in the precursor film solution until they were removed from the deposition vial (Fig. 3.27). It can be confirmed from Fig. 5.12 that the higher the final concentrations the faster rate of change in intensity over time which would mean a faster growth of film thickness during the LPD process. This result is in accordance to a previous publications of imprinting proteins in TiO_2 thin films by LPD and using a Quartz Crystal Microbalance (QCM) device [271].

5.2.2 Results of imprinted TiO_2 deposition (based on LPD) onto LPG fibres

Similar to U-shaped fibres, LPGs can be used as refractometers themselves and their sensitivity was tested before functionalization. The LPGs used in this subsection were fabricated via the amplitude mask technique (section 3.2.1) and all LPGs were working at or near the PMTP for the LP_{019} cladding mode.

For instance, using the experimental set-up previously explained in Fig. 3.15b, all the LPGs used were tested in 50 wt.% of EtOH to identify those LPGs with the highest sensitivity to RI change. Fig. 5.13a shows two examples of the wavelength shifts, relative to the location of the attenuation bands (LP_{018}, LP_{019}) in air, when two LPGs (both with period 109 μm) were exposed to 50 wt.% of EtOH.

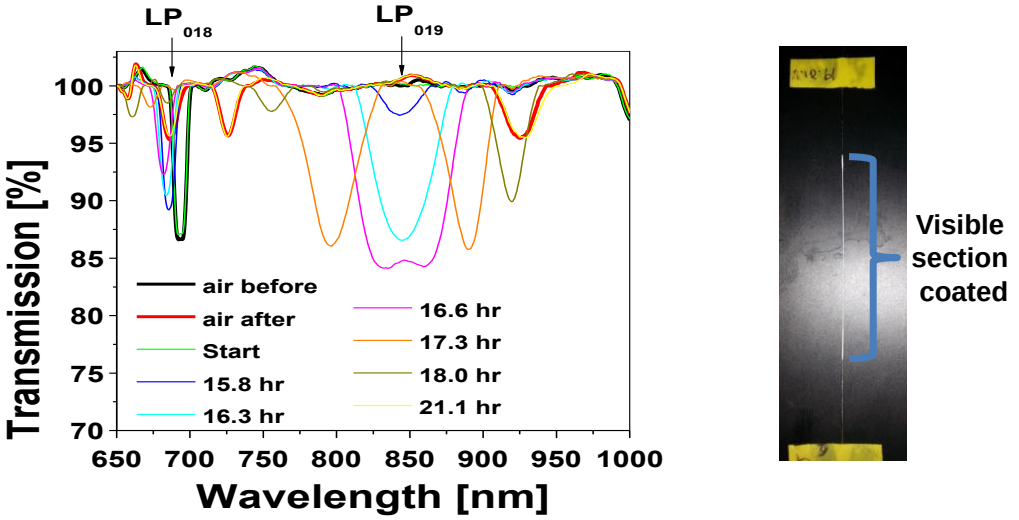


(a) (b)

Figure 5.13: (a) Relative wavelength shifts from the attenuation bands of two LPGs tested in 50 wt.% of EtOH ($\mathrm{Diff} = |\mathrm{R} - \mathrm{LP}_{019} - \mathrm{L} - \mathrm{LP}_{019}|$). (b) Evolution of the transmission spectra of LPG2 (Λ =109 μm) during deposition of the imprinted TiO_2 film (Environmental humidity and temperature were constant during all deposition, 41 % RH $\pm$ 3% and 25 ^{0}C $\pm$ 2 ^{0}C).

Fig. 5.13b presents the transmission spectra of LPG2 (Fig. 5.13a) before and during deposition of the imprinted TiO_2 film by LPD process and using the set 1 of concentrations of Table 3.3. A full video showing the evolution of the LP_{019} cladding mode for the case presented in Fig. 5.13b can be found in reference [272]; it can be confirmed that the two attenuation bands in LP_{019} (Fig. 5.13b) started to separate faster after 12 hr. and, after 14.5 hr., they vanished completely from the range between 700 and 1000 nm [272]. Similar results were found with a different LPG fabricated with another grating period (110.5 μm) and using the same set 1 of concentrations from Table 3.3. Fig. 5.14a shows the evolution of the transmission spectrum of this last LPG and

compares the spectra before, during and after a total deposition of 21 hr (also a full video can be found in reference [273]). Fig. 5.14b demonstrates how a thick and visible film develops onto the LPG after 21 hr of deposition.



(a) (b)

Figure 5.14: (a) Evolution of the transmission spectra of an LPG2 with period Λ =110.5 μm during deposition of the imprinted TiO_2 film. (b) Photograph of the LPG gauge when coated for more than 21 hr and using the experimental set-up of Fig. 3.15b (Environmental humidity and temperature were constant during all deposition, 66 % RH $\pm$ 2% and 24.8 ^{0}C $\pm$ 2 ^{0}C); the coated section length is ca. 4 cm in this case.

For the case of the LPG ($\Lambda = 110.5\,\mu m$) presented in Fig. 5.14a, the attenuation band associated with the cladding mode LP_{019} was null after fabrication (black spectrum). However, this band started to develop after 15 hr. of imprinted TiO_2 film deposition (blue spectrum) and after 16.6 hr. it began to split into the two bands R-LP_{019} (right) and L-LP_{019} (left) [273]. The results in Fig. 5.13b and Fig. 5.14a reflect the concepts explained in section 1.4.2 about the evolution of the attenuation band corresponding to the LP_{019} cladding mode in response to changes in the effective refractive index of the cladding (η^i_{clad}); in this case, the imprinted TiO_2 film starts to develop over time and this changes the optical thickness (product of the geometrical thickness and refractive index) of the coating which produces an increase in the effective refractive index of the cladding mode. This causes the phase matching curves

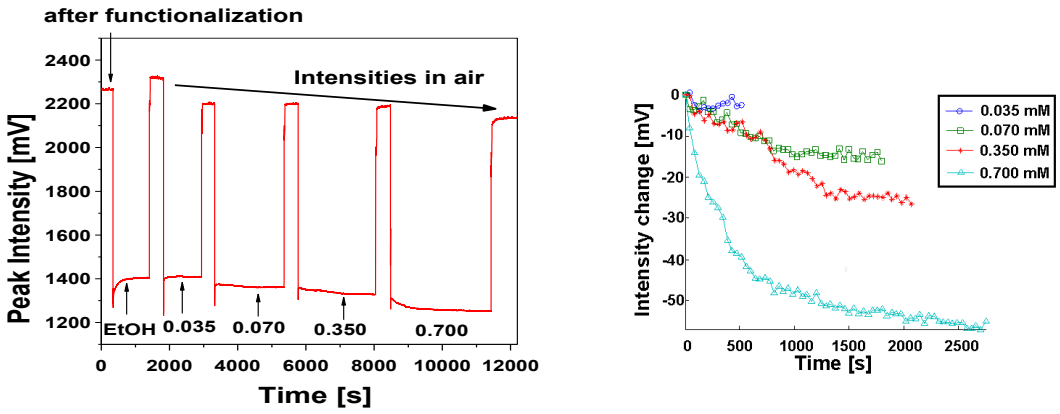
to change accordingly and results in the development and behavior of the LP_{019} band, as shown experimentally in Figs. 5.13b and 5.14a. Interestingly, both deposition cases of the imprinted TiO_2 film onto LPGs and U-shaped fibres show a turning point in the deposition time (between 14 and 16 hr.) where the formation of the film started to grow faster (using the set 1 of concentrations from Table 3.3). On the other hand, the set 2 of concentrations from Table 3.3 allowed faster coating growth onto the optical fibres, but had an impact on the sensitivity of the sensor as shown in the next section.

5.2.3 Propofol binding in aqueous solutions using U-shaped and LPG fibres

The first experiment to demonstrate the binding of propofol onto the functionalized U-shaped fibres was a discontinuous test. By tracking the maximum of the transmission spectrum, Fig. 5.15a explains this first result where, after functionalization (set 1, Table 3.3), the U-shaped fibre was immersed in EtOH for 10 min using the experimental set-up of Fig. 3.27. After removal of the analyte propofol with the organic solvent EtOH (Fig. 5.15a), the functionalized fibre was immersed discontinuously in four different stock aqueous solutions of propofol with concentrations 0.035 mM, 0.070 mM, 0.350 mM and 0.700 mM. Fig. 5.15b compares and demonstrates qualitatively that the rate of adsorption for each of these concentrations was different.

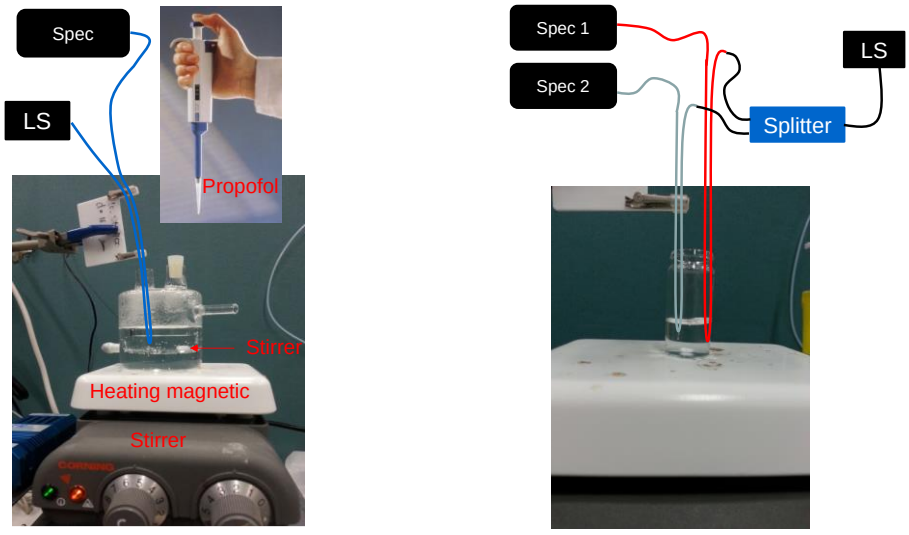
The second experiment for the binding of propofol was continuous and implemented as shown in Fig. 5.16a. The experimental set-up is similar to that previously presented in Fig. 3.27, yet in this case different amounts (using precision micro-pipettes) from a stock solution of propofol (0.5 mM for a bigger vial as in Fig. 5.16a and 20 μM with the smaller vial as in Fig. 5.16b) were dissolved in pure deionised water (initial volume $\leq$ 25 ml, typically 4 ml in Fig. 5.16b) producing increments in the concentration of propofol in the testing vial or beaker while producing a stable fluid dynamic state with a magnetic stirrer

as shown in Fig. 5.16. Fig. 5.16b shows the experimental set-up for simultaneously testing the binding of propofol in non-imprinted (or bare) and imprinted TiO_2 U-shaped fibres. Detailed results from these propofol binding experiments are presented from Fig. 5.17 to Fig. 5.19.



(a) (b)

Figure 5.15: (a) Change of the peak intensity (*cf*. Fig. 5.11b) after template removal in EtOH and after immersion of the U-shaped fibres in four stock aqueous solutions of propofol (in the milimolar range). (b) Normalized comparison of the response of the fibre during immersion of the four propofol aqueous solutions shown in (a).



(a) (b)

Figure 5.16: (a) Experimental set-up for a continuous test of the binding of propofol onto U-shaped fibres. (b) Simultaneous binding test in two U-shaped fibres. LS=Light source and Spec=Spectrometers (as in Fig. 3.27).

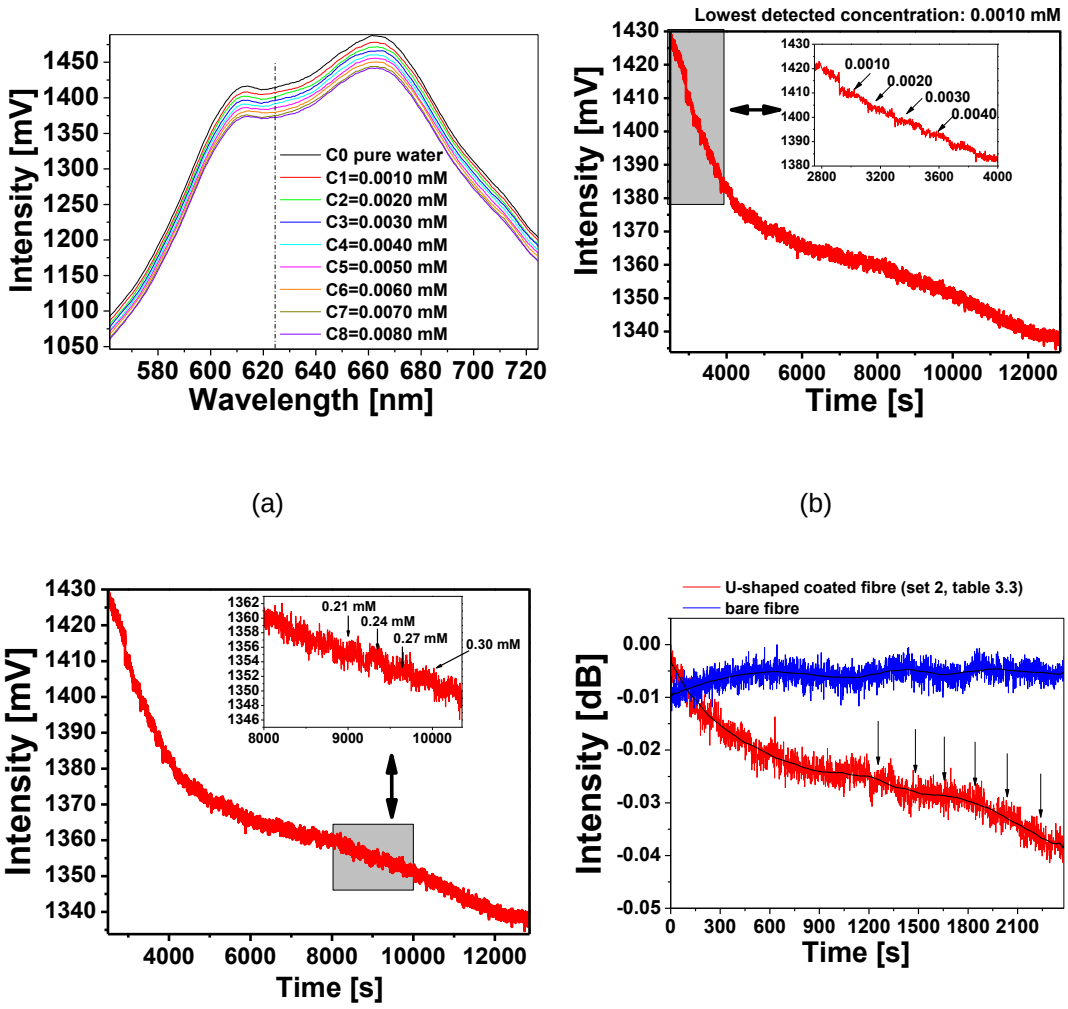


Figure 5.17: (a) Change of transmission spectra after pipetting the first eight concentrations of propofol (stock 0.5 mM). (b) Real time response at fixed wavelength while pipetting same stock solution with an inset to show the response to the first four concentrations. (c) Inset showing response to the middle of the range of concentrations tried and (d) shows a comparison between the response of a bare fibre and a U-coated fibre functionalized with the set 2 of concentrations from Table 3.3.

Fig. 5.17a shows how the transmission spectrum of a functionalized U-shaped fibre (set 1, Table 3.3) changed after pipetting the first eight concentrations of stock solution (0.5 mM) of propofol as depicted in Fig. 5.16a. Fig. 5.17b presents the specific change in intensity at a fixed wavelength (c.a. 625 nm from Fig. 5.17a) after pipetting several concentrations of propofol in the range of millimolar (mM); both results in Fig. 5.17a and Fig. 5.17b were

recorded every second and, after dipping the sensor into each propofol solution, a time of between 5 and 10 min was allowed for stabilization of each concentration. The inset in Fig. 5.17b shows a close up when pipetting the first four lowest concentrations and the inset in Fig. 5.17c presents another close up in the middle of the range of concentrations tried during same experiment (Figs. 5.17a and 5.17b). Finally, Fig. 5.17d shows an example of a real time and synchronized measurement from a U-coated fibre and a bare fibre; for this case the light source (LS) was connected to an optical fibre splitter (SPLIT200-UV-VIS, Ocean Optics, low attenuation from 300 to 1100 nm) and directed to two U-shaped fibres (Fig. 5.16b) which were interrogated using separate spectrometers (HR2000 and S1024DW, Ocean Optics) every second.

Fig. 5.18a demonstrates the effect of the deposition time on the response and sensitivity of two U-coated fibres with same radius of curvature and EtOH sensitivities (1.5 mm and 149.94 mV / 0.01 RI). Fig. 5.18b presents the re-usability test results of u1 from Fig. 5.18a. The data points plotted in Figs. 5.18a and 5.18b were obtained for a fixed wavelength (ca. 625 nm) where the absolute intensity changes were plotted and measured against the intensity value when the U-fibre was in pure water.

The re-use adsorption tests from Fig. 5.18b (red and blue curves) were performed and obtained after the first propofol binding test (black curve in Fig. 5.18b) and doing three preliminary steps before the re-binding test:

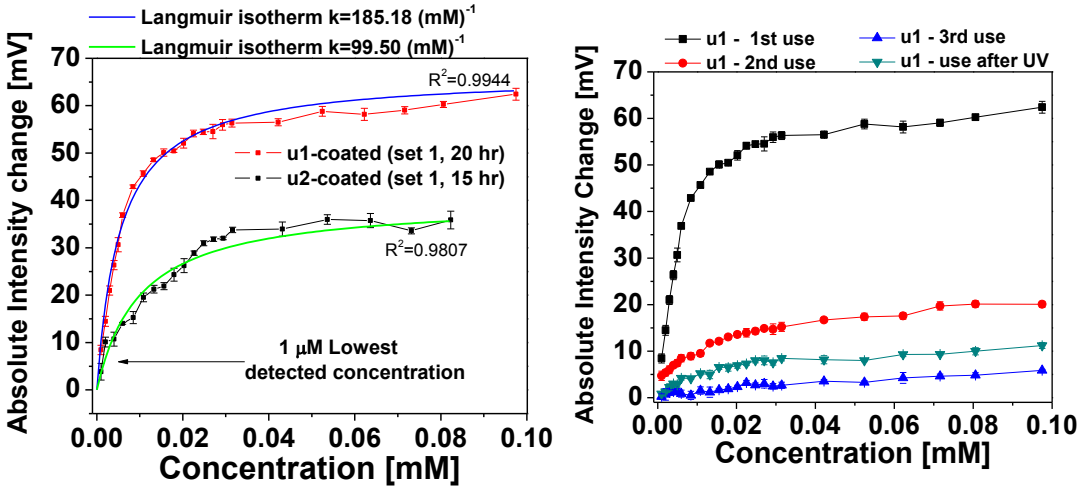
(1) Template analyte removal in EtOH for 3 min.

(2) Re-immersion of the U-shaped fibre in 1.6 mM stock aqueous solution of β −CD/Propofol for 1 hour.

(3) EtOH analyte removal for 3 min.

The sensitivity of u1 was improved after the third re-use trial and applying self-cleaning with a UV lamp (ca. 350 nm and 0.87 mW/cm^2) to the U-fibre for 1 hr. The second re-use of u1 reduced the propofol adsorption sensitivity by 67.9%; the third re-use diminished sensitivity by 90.6% and the use of extra

UV cleaning improved sensitivity by 27.3% (Fig. 5.18b). Therefore, re-usability of the U-coated sensors is not feasible unless the photocatalytic purification of organic compounds with UV light is used and the photoactive properties of TiO_2-Cyclodextrins [205],[220], open up an opportunity for re-usability as demonstrated in Fig. 5.18b.



(a) (b)

Figure 5.18: (a) Effect of functionalizing deposition time on sensitivity for the binding of propofol. (b) Re-usability of the same U-coated fibre and response after self-cleaning using UV light (all standard deviations are based on three measurements at the same concentration and using the same stock solution of propofol).

To demonstrate the effect of the sets of final concentrations used (Table 3.3) during sensor functionalization and the specificity given by the imprinted TiO_2 film for the detection of propofol, Fig. 5.19 compares the response of u1 (coated with set 1) from Fig. 5.18 and two U-shaped fibres (u2: 182.68 mV / 0.01 RI, u3: 172.83 mV / 0.01 RI) coated using the set 2 of concentrations from Table 3.3. In addition, the response from a non-imprinted TiO_2 coated U-shaped fibre was tested as qualitative comparison; all the curves plotted in Fig. 5.19 were obtained using the set-up of Fig. 5.16b and the sensitivities in Fig. 5.19 were obtained by linear regression for the lower range of concentrations shown.

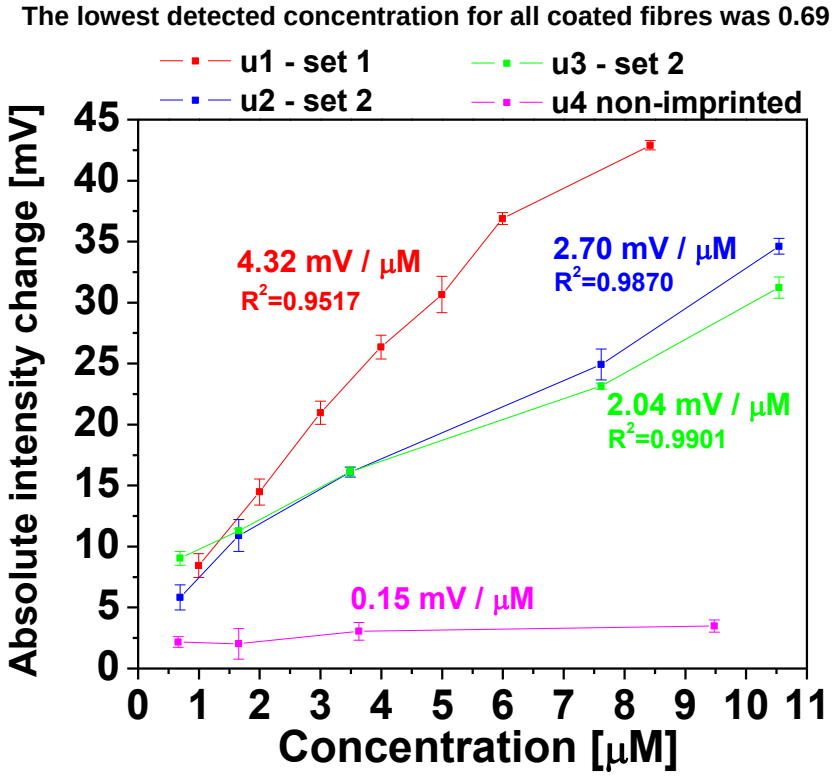
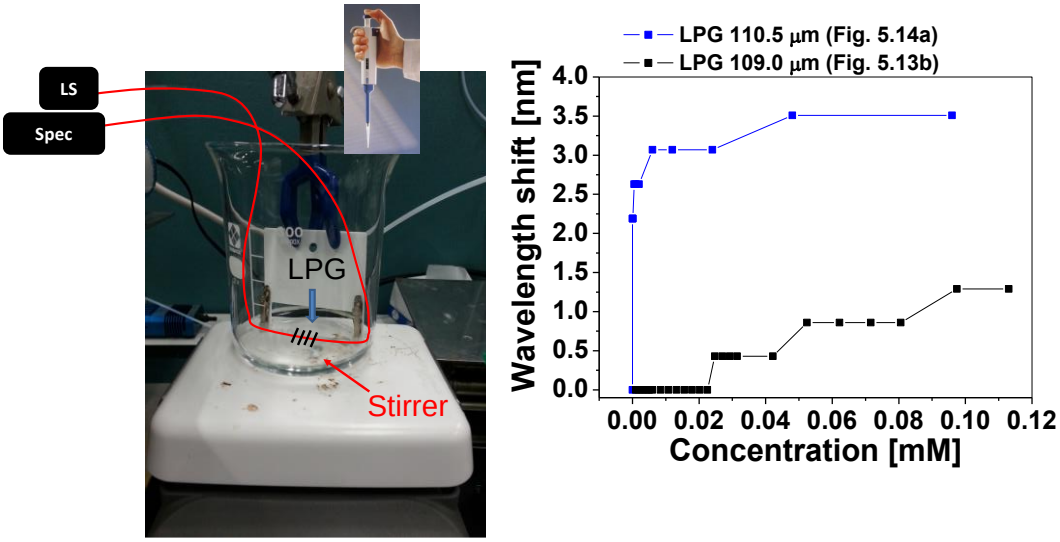


Figure 5.19: Comparison of sensitivities for the low concentration range between U-shaped fibres coated with two different sets of concentrations (Table 3.3) and a non-imprinted TiO_2 coated fibre.

Similarly to the U-shaped fibres, the LPG coated with the imprinted TiO_2 film of Fig. 5.14a was tested for the binding of propofol in aqueous solutions as shown in Fig. 5.20a. Fig. 5.20b shows the wavelength shifts of the attenuation band R-LP_{019} for the two LPGs coated with the imprinted TiO_2 film (Fig. 5.13b and Fig. 5.14a) and the shifts were obtained relative to the band position when the LPG was immersed in pure deionised water. The set of propofol concentrations was as in Fig. 5.18a and the response of the coated LPGs also exhibited Langmuir adsorption with the lowest detected concentration of 0.65 μM using the coated LPG of Fig. 5.14a.



(a) (b)

Figure 5.20: (a) Experimental set-up for a continuous test of the binding of propofol onto LPG coated fibres. (b) Results for the binding of propofol using the two coated LPGs of Figs. 5.14a and 5.13b and implementing the set-up shown in (a).

5.2.4 Results of imprinted MSN-TiO_2 deposition onto U-shaped fibres

This method was explained in section 3.4.2 which allows an improvement in the sensitivity of propofol detection through the use of MSNs in conjunction with TiO_2 as an inorganic matrix to imprint template (propofol) molecules. This method was applied to U-shaped fibres using 4 cycles of dip coating onto the U-probe, each followed by a hydrolysis period. Hydrolysis of the film is depicted in the inset of Fig. 5.21 where the U-coated probe was placed as near as possible to the tension surface of water. Fig. 5.21 presents the result of the deposition onto a U-probe with radius of 1.5 mm and sensitivity to EtOH of 168.97 mV / 0.01 RI, includes the hydroxylation of the fibre with KOH and, at the end, a step of template (analyte) removal was needed with MetOH (20 min) before testing this functionalized U-shaped fibre.

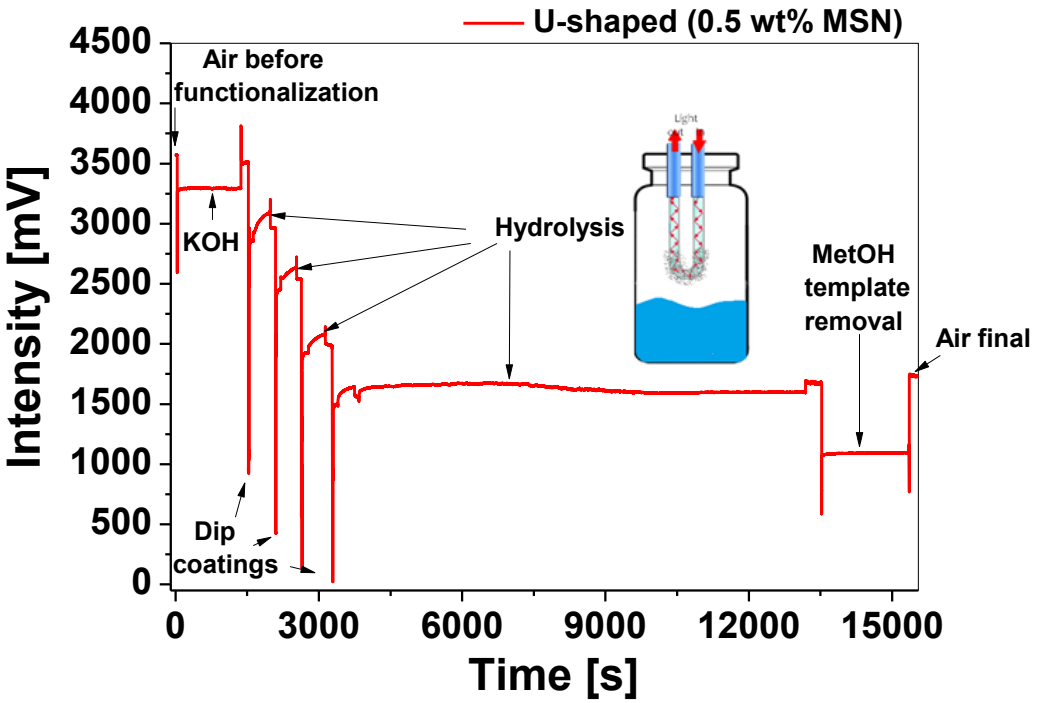


Figure 5.21: Intensity change at 625 nm for the deposition results onto a U-shaped fibre using dip coating method and the prepared film as described in section 3.4.2

The experimental set-up for this deposition process was as previously presented in Fig. 3.27. The U-shape fibre was maintained fixed with a static clamp and the dip coating was done manually (movable lift of Fig. 3.27) for 10 seconds. In Fig. 5.21, the first three hydrolysis periods lasted 5 min, the fourth hydrolysis was done for 2.5 hr and the MetOH removal period was performed for 20 min. Fig. 5.22 presents how the transmission spectra in air from the U-shaped fibre changed after each dip coated film deposition and hydrolysis period, and after template removal with MetOH. The result of Fig. 5.21 corresponds to a dynamic measurement at 625 nm (from spectra of Fig. 5.22) recorded at a scanning frequency of 1 Hz.

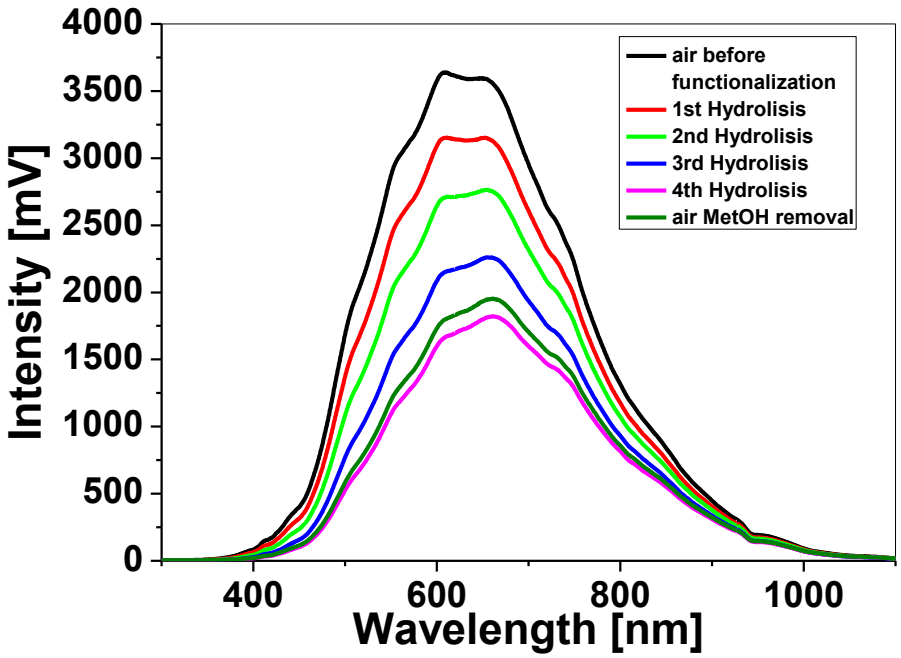


Figure 5.22: Transmission spectra changes over the deposition onto a U-shaped fibre using the dip coating method and deposition film explained in section 3.4.2.

5.2.5 Improvement of sensitivity in aqueous solutions

Using the method of section 3.4.2 and the U-shaped fibre functionalized as explained in the previous section, the limit of detection improved to successfully detect propofol in aqueous solutions within the clinical acceptable range and allowed the detection of propofol in a gas phase (next section). Firstly, Fig. 5.23 presents how the transmission spectrum from the U-coated fibre of Fig. 5.22 changed when exposed to lower concentrations in the nano-molar range. Fig. 5.24 then presents the results for the calculation of the absorbance onto the U-coated fibre when exposed to nano-molar concentrations of propofol and taking the transmission in pure water as a reference spectrum. The lowest detected concentration of propofol in aqueous solutions using the method explained in this subsection was 99 nM (Figs. 5.23 and 5.24).

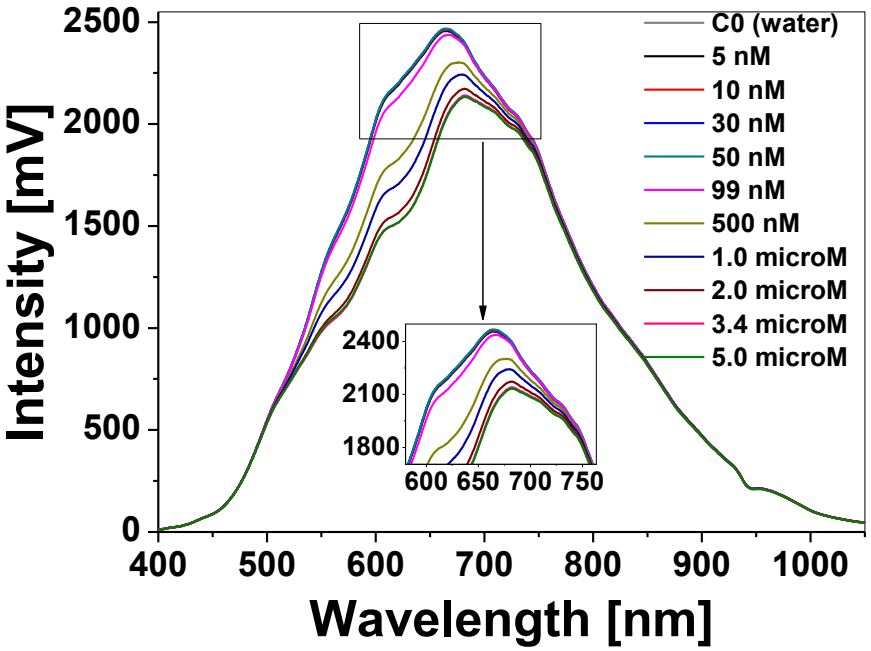


Figure 5.23: Transmission spectra changes over the binding of propofol in the nano-molar range.

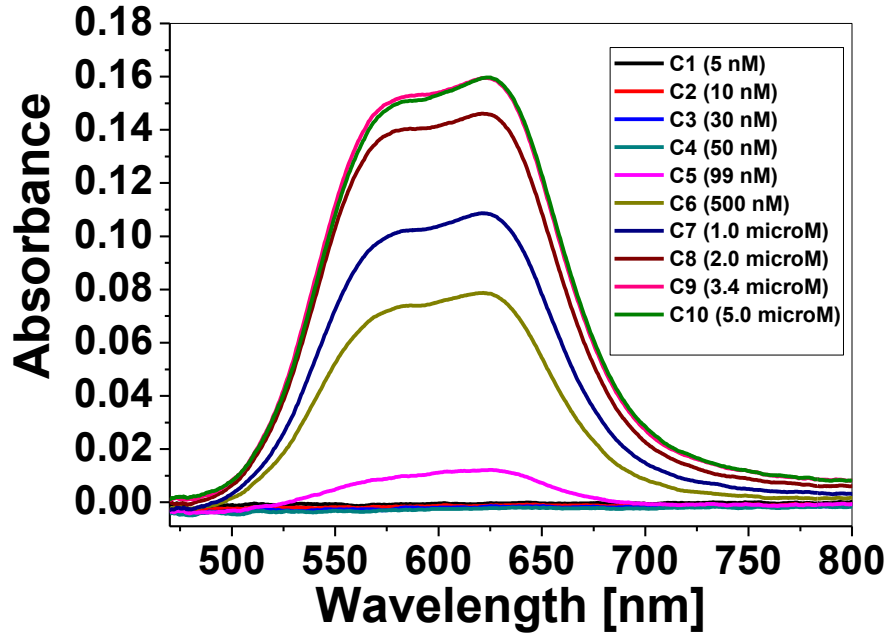


Figure 5.24: Absorbance spectra calculated from data of Fig. 5.23.

5.2.6 Propofol detection in gas phase

Once propofol detection was assured within the clinical range in aqueous solutions and using the same method of imprinted MSN-TiO_2 deposition as explained in Fig. 5.21, a U-shaped fibre with radius of 1.6 mm and sensitivity to EtOH of 177.76 mV / 0.01 RI was exposed to propofol in gas phase implementing the set-up presented in Fig. 5.25.

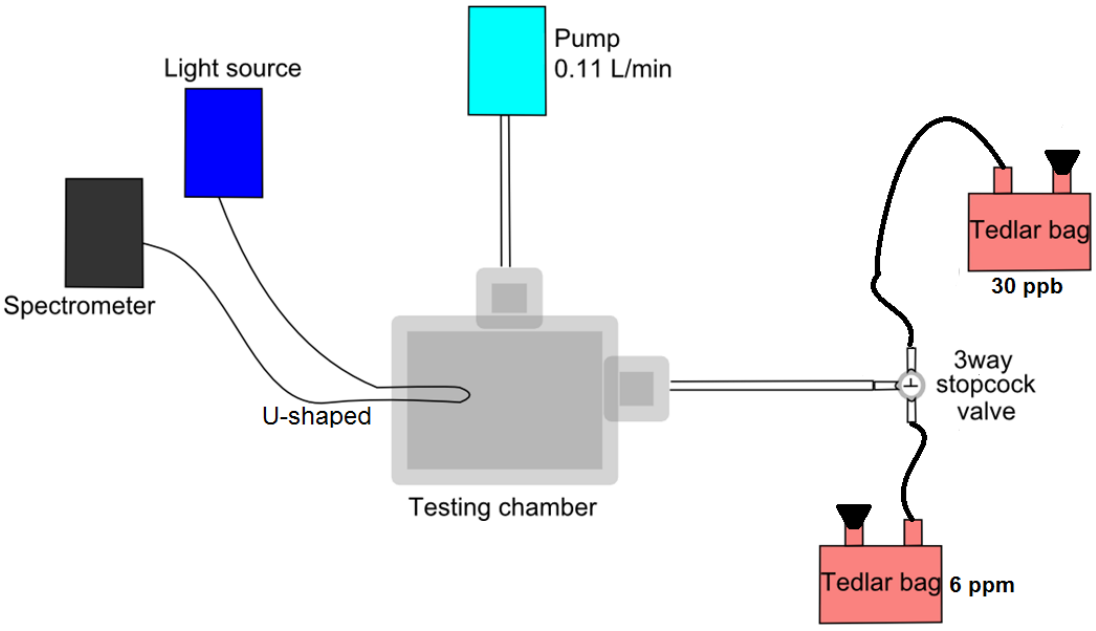
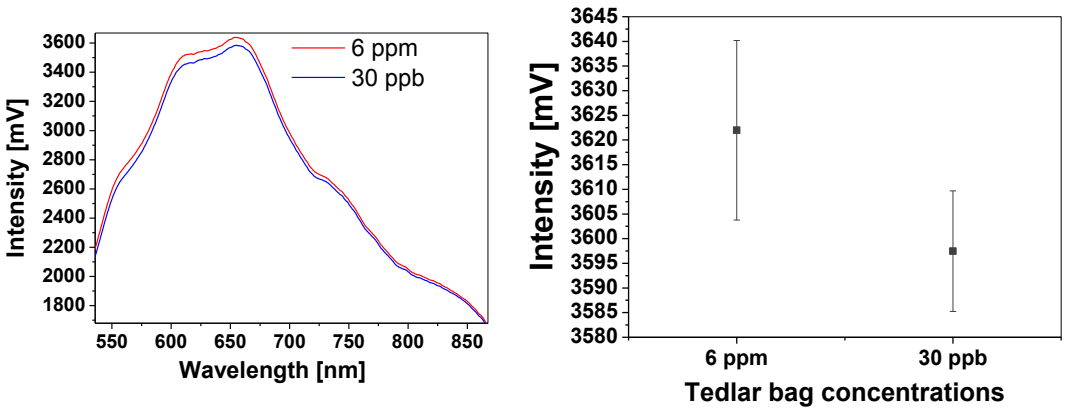


Figure 5.25: Experimental set-up for propofol detection in gas phase.

In Fig. 5.25, the spectrometer and light source used were HR2000 and HL-2000 from Ocean Optics as in experiments of previous sections. The U-coated probe was placed inside a testing chamber (1 cm^3 inner space) and this chamber had a sealed outlet connected to a suction pump (MP-Σ30, SIBATA) used at 0.11 L/min on one side, and a sealed inlet connected to PTFE hoses on the other; the latter inlet line was connected to a 3-way stopcock valve to interchange the propofol concentration between 6 ppm and 30 ppb (Fig. 5.25). To prepare these concentrations in tedlar bags, firstly 5 μl of liquid propofol

(without any treatment or further purification) was injected inside a 1 L tedlar bag and introduced in oven temperature at 50 ℃ for 1 hour in order to obtain a gas phase stock propofol concentration of 180 ppm at saturation vapour pressure [166]. After this, a 6 ppm tedlar bag of 3 L was created by mixing 100 ml of stock gas propofol and 2900 ml of pure air. Similarly, a 30 ppb tedlar bag of 3 L was obtained by mixing 15 ml of 6 ppm tedlar bag with 2985 ml of pure air.

Fig. 5.26a presents a comparison between transmission spectra measured when the U-coated probe was exposed to the two concentrations of 6 ppm and 30 ppb, both with fixed environmental humidity (64%RH) and temperature (23.5 ^{0}C). Fig. 5.26b demonstrates the difference between the maxima from the transmission spectra (655 nm) of Fig. 5.26a when the U-probe was alternately exposed three times to the concentrations contained in the tedlar bags (as depicted in Fig. 5.25).



(a) (b)

Figure 5.26: (a) Comparison of the transmission spectra when the U-shape fibre was exposed to 6 ppm and 30 ppb. (b) Mean and standard deviations of the maxima (655 nm) when exposed to same concentrations three times and using the set-up of Fig. 5.25

5.3 Chapter conclusions

The current clinical monitoring of propofol and proteins in the ICU demands technological improvements. Propofol levels in blood are only predicted based on algorithms using TIVA protocols and vital signs as surrogates of anaesthesia. Actual direct concentrations from arterial blood with HPLC or indirect samples from the breath of patients with GC-MS are time consuming to analyze. They are off line techniques and hence do not provide concentrations in real time. On the other hand, protein delivery in the ICU has been recently reviewed as an unmet clinical need where there is no direct technique for the measurement of nutritional biomarkers associated with this challenge. This part of the research proposes two biosensors as a proof of concept and engineering solution for these two clinical needs.

The effectiveness of two deposition techniques, the LbL method and inorganic molecular imprinting, were demonstrated to be effective for the biochemical parameters of interest. In addition, a biosensor for protein was demonstrated with a well-known biotin-streptavidin protein interaction; the results of this approach can be extended to other types of proteins or biomarkers of interest in the ICU by replacing the nature of the ligands and using the LbL method with SiO_2:Au core/shell NPs deposited as a sensing platform onto LPGs. Further biosensors, demonstrated with LPGs and U-shaped fibres, were proved to successfully detect propofol in aqueous solutions and gas phase within the clinical range of interest.

Sensitivity for protein detection was positively impacted with larger SiO_2 NPs (300 nm) having a theoretical limit of detection of $18.9\ \mathrm{pg/mm^2}$ with a coated-LPG $(PAH/SiO_{2(300\ nm)}:Au)_3$. The statistical LoD was found to be 15.13 nM but the lowest detected concentration was 2.5 nM using a coated LPG with $(PAH/SiO_{2(80\ nm)}:Au)_3$. As comparison, other studies have found sensitivities for antibody/antigen binding interactions between 2 and 100 µg/ml [256]. Pilla *et al*. [258] demonstrated an LPG immunosensor with sensitivity down to 5 pg/mm^2 and Wang *et al*. [259] obtained a LoD of 12.5 µg/ml for biotin-

streptavidin interaction. In this research the LoD was 15.13 nM = 0.83 µg/ml and the lowest detected concentration was 2.5 nM = 0.14 µg/ml for biotin-streptavidin in aqueous solutions.

The lowest detected concentration using host-guest imprinting on TiO_2 thin film (LPD process) was 0.65 µM=115.88 µg/ml with the aid of β −CD as host compound for propofol detection. Sensitivity was improved through direct imprinting of propofol molecules onto TiO_2 films but with the addition of MSNs to increase the imprinting surface area. The latter case allowed detection of lower concentrations in the nano-molar range (lowest concentration detected 99 nM=0.017 µg/ml) and obtained preliminary results for detection in gas phase, also with ppb values found in situ. As comparison, most of the approaches explained in section 2.2.3 were able to detect propofol either in aqueous solutions or blood within the clinical range between 0.1 µg/ml and 10 µg/ml. For instance, Li and Li [160] found a LoD of 0.65 µg/ml and Liu *et al*. [162] found a LoD of 0.75 µg/ml both in aqueous solutions. In gas phase, Grossherr *et al*. [119], Takita *et al.* [120], Hengstenberg *et al*. [159] and Gong *et al*. [164] measured propofol concentration from breath of patients between 2 ppb and 30 ppb. In contrast, only the functionalization method explained in section 3.4.2 of this research allowed detection in aqueous solutions (down to 99 nM) and gas phase within the clinical range of interest.

The next, and final chapter, will present a general discussion and the conclusions about the work developed and presented in this research.

Chapter 6: Discussion, conclusions and future work

This chapter presents separate sections for discussion and the conclusions of the two types of optical fibre sensors proposed in this research. These are:

(1) An OFS to be used during ventilation in the ICU as a respiration rate (RR), humidity and temperature monitor.
(2) An OFS for sensing biochemical parameters of interest in the ICU: propofol and a proof of the platform concept for protein detection.

Future work of this research will be explained towards the end of this chapter.

6.1 General discussion for the optical fibre humidity sensor

The current trends in new generation humidity sensors suggest that electronic-based technologies could be soon partly replaced by sensors that are based on photonic structures [39]. Kolpakov *et al*. [39] have reviewed that OFS technology has emerged as part of a 3rd generation type of humidity sensors demonstrating the best response time when compared to acoustic and electronic sensors. Cost-effectiveness is evident with some optical fibre structures that use a single LED and photodetector. Additionally, more compact FBG interrogators are emerging in the market allowing the option to create novel, portable and cost-effective medical devices based on OFS technology. The OFS presented in chapter 4 of this thesis is a good exemplar of this 3rd generation of humidity sensors; the results obtained during its calibration presented a linear and low hysteresis sensor with a response time within current fast trends reported in recent reviews [39], [38].

The novelty of the humidity sensor proposed in this research consisted of incorporating it in ventilator care equipment to monitor humidity and temperature and also demonstrating the potential application as a RR monitor through its embodiment in ventilators and other medical equipment such as ETTs, facemasks and nasal cannulas. In particular, the first intended application of the OFS is to control outputs (humidity and temperature) from

humidifiers usually used with mechanical ventilators. Heat wire humidifiers (as the one used in this research) are popular in the ICU for warming the gas delivered by the mechanical ventilator. The function of heat wire humidifiers is to use the warm wires inside the breathing circuit to avoid condensation inside the tubing. Additionally, they are equipped with two thermocouples, one at the outlet of the humidifier and the second at the distal part of the inspiratory limb, both with the simple strategy to keep an approximate temperature of 37 ^{0}C inside the inspiratory tubing (section 4.7). Massaroni *et al*. [16], Tanaka *et al*. [114], D'Amato *et al*. [145], Bodini *et al*. [113] and De Oliveira *et al*. [136] identified that default settings of humidifiers are not appropriate and able to provide optimal control and manipulate real AH delivered to the patient from the mechanical ventilator. Therefore, some authors such as Tanaka *et al*. [114], De Oliveira *et al*. [136] and Bodini *et al*. [113] have suggested to measure humidity and temperature in the Y-piece connection of the breathing circuit in order to pave way for new and more efficient strategies for the control of humidifiers. All these studies [114], [113], [136] were implemented with electronic-based sensors with long response time (see Table 2.2) as a tool for humidity and temperature monitoring, but without capability to detect breath to breath changes as in this research. Thus, the novelty of this research is evident and has been recently reviewed by Massaroni *et al*. [16] who mentioned that "Although several groups of research proposed fibre optic-based systems for simultaneous measurements of temperature and humidity using different principles of work, only Hernandez and coauthors [this PhD research] focused their attention on the measurements of these parameters in mechanical ventilation".

From the literature review summarised in Tables 2.2 and 2.3, it was confirmed that those approaches which aimed to measure RR through breathing monitoring do not measure breath by breath humidity change, and those techniques applied to measure humidity and temperature inside the Y-piece of the breathing ventilator circuit used electronic sensors with long response times, making them unable to measure RR. Only the ACE

assessment tool (custom-made electronic sensor) was fabricated and design to measure RR, humidity and temperature in laryngectomized patients where Zuur *et al*. [112], [137] also assessed the influence of the HME in laryngectomies obtaining a maximum AH measurement of 34.2 mg H_2O/L in the upper trachea. This value matches with the AH measured in Fig. 4.14 (maximum AH = 35 mg/L) using the heat wire humidifier and ventilator explained in section 4.7; the measurement was obtained with the calibrated response of the optical fibre humidity sensor proposed in this research. Similarly, this target level of AH matches with the mean measured value by Tanaka *et al*. [114] as 36.9 mg/L when using a thermo-hygrometer (electronic) inside the Y-piece of the circuit to control and optimize the ideal humidity target of 36.6 mg/L (hypothermic patients).

Additional remarks about this sensor are highlighted with the results obtained in the bench-top study (section 4.7), the one off trial in the animal study (section 4.8) and the preliminary tests for the protocol with human volunteers (section 4.9). These results demonstrate that the sensor could stand handling from the clinician/user when the sensor was placed inside the facemask (Fig. 4.23) or inside the lumen of the ETT (Fig. 4.18), bound to the nasal cannula (Fig. 4.24) or when the $\%FiO_2$ valve was changed (Fig. 4.25a). This is a necessity as medical practitioners will normally need to adjust any medical device especially in emergency situations. Therefore, locating the OFS inside a 23-gauge medical hypodermic needle provided additional mechanical protection to the film used for humidity sensing. Another optimization result was proven with the tests in the bench-top study, i.e., the results obtained in section 4.7 confirmed that a HME acts as a filter protecting the sensor against condensation and high moisture that can produce artefacts and is useful as it avoids large temperature variations (up to ± 1 ℃). In this direction, and in practical use during non-invasive mechanical ventilation, coating the tip of the hypodermic needle (containing the OFS) with the wool/foam material used in the HME helps to avoid artefacts produced by

condensation (Figs. 4.13 and 4.23). Overall, the results of sections 4.7 to 4.9 demonstrated the application-oriented customization of the sensor.

In general, all the electronic-based devices presented in the literature review for monitoring humidity, temperature and RR tend to be larger in size when compared to OFS technology. They also often contain metallic and conductive parts that are prone of electromagnetic interference in the theatre room or can cause burns on the patient's skin if used in the MRI field. In contrast, the OFS proposed in this research offers a significant control of humidity as an essential part of critical respiratory care with the advantages of providing optimal sensitivity, compactness and a considerably faster monitoring method.

6.2 Conclusions for the optical fibre humidity sensor

- The sensitivity, response time and hysteresis of a novel optical fibre humidity sensor, based on a Fabry-Perot cavity, has been investigated over a humidity range of 5% RH to 76% RH using a controlled bench-top set-up.
- Optimal sensor sensitivity was predicted to be between 7 and 11 bilayers, calibrated with low hysteresis and maximum sensitivity measured as 2.28 mV/%RH with 9 bilayers (~450 nm overall film thickness).
- The optical fibre humidity sensor proposed has a very simple and low cost porous structured sensing element obtained with PAH/SiO_2 using the LbL fabrication method.
- The response time constant of the optical fibre humidity sensor was 1.13 ± 0.3 s compared to the measured 158 s response for a commercial capacitive sensor under the same experiment conditions. This fast response time enabled changes in humidity in individual breaths to be resolved.

- After calibration, the performance of the sensor was evaluated in the breathing circuit of a mechanical ventilator where its faster response allowed monitoring of breath to breath humidity levels during different modes of ventilation and it has the capability to provide AH measurements when an FBG is included for simultaneous temperature measurements.
- The fast response of the sensor also means that it is possible to track humidity changes in an individual's respiratory rate (or apnea) during non-invasive ventilation (facemasks and nasal cannulas) even with unusually low (10 breaths/min) or high (40 breaths/min) respiratory rates, with different percentages of FiO_2.
- The results demonstrate that the development of a portable optical fibre humidity sensor is feasible and can be easily embedded in ventilation masks or in elements of the breathing circuits used for ventilation.
- All the components of the optical sensor require no electrical current and are made of nonmagnetic materials. Thus, the device could be used during MRI, oncological treatments and during anaesthesia.

6.3 General discussion for sensing biochemical parameters of interest in the ICU

There were two parameters of interest studied in this research: propofol and a proof of a platform concept for protein detection. The latter used the biotin-streptavidin interaction as a model system to characterise the performance of the coating proposed for LPGs, since the properties of the biotin-streptavidin interaction are well known. Experiments with the clinically relevant proteins in the ICU would use the characterisation information presented in this research from the streptavidin experiments. Thus, to extend the application to clinically relevant proteins, the biosensor presented in this research will have to further address:

(1) Enhancement of the LPG surface coating coverage (Fig. 3.17) with PAH/SiO_2:Au NPs by modifying adsorption efficiency of SiO_2 NPs via its surface modification, e.g., providing higher number of ligands that will intensify the negative charge of the NPs.
(2) Enhancement of the coverage of the SiO_2 NPs with Au NPs through improving the initial procedure used to synthesize the SiO_2:Au NPs.
(3) Optimization of reproducibility with the UV laser-based fabrication of LPGs to operate as close as possible to the PMTP and obtain the highest sensitivity for analyte detection.
(4) Before using this platform model for detection of the clinically relevant proteins and immobilize over the SiO_2:Au NPs sensors to enable the analysis of physiological biomarkers (section 2.1.4), a preliminary test stage is needed with a more complex matrix of analytes (mixed with SV) to establish the selectivity of the biosensor proposed to its bio-target.

The stage of the approach for protein detection is still a proof of concept, but tis application-orientated to clinically relevant proteins in the ICU (section 2.1.4) finds novelty as nowadays there is not a relevant monitor for protein administration in the ICU [118] that allows clinicians to know when enough is enough. Heyland *et al*. [118] have reviewed a series of prospective biomarkers for sufficient protein/amino acid administration in blood or via urinary catheters, but optimization of protein delivery in the ICU is an open area of current debate and research. In this research, the sensitivity of the proposed biosensor for protein detection is at least one order of magnitude greater than previously reported optical fibre streptavidin biosensors [26], [259]. Additionally, the statistical LoD=15.13 nM or the lowest detected concentration of 2.5 nM dictates the possibility of this sensor to be applied to a broader range of analytes such as drugs (vancomycin, [253]) in blood with a LoD requirement in the nM range or possibly some other proteins in blood such as interleukin-6 with concentrations down to ng/ml [274].

With regard to the detection of propofol, to the best of the author's

knowledge, detection of propofol with OFS technology has not been attempted through an ***analytics approach*** (Fig. 1.16), i.e., detection of the analyte directly onto the surface of an OFS. In section 2.2.3, only five ***lab-on-chip*** (Fig. 1.16) approaches and one electrochemical sensor were found in the literature review as attempts to provide an on-line and more compact device for measuring propofol concentrations in aqueous or blood samples. Most of these approaches managed to perform rapid detection of propofol (ca. 5 min) within the expected clinical range in blood samples: 0.1 μg/ml – 10 μg/ml. The niche application of propofol detection using OFS technology still needs engineering improvements as some approaches (e.g. [158], LoD=1.4 μM = 0.25 mg/ml) are expensive to fabricate. Others (e.g. [160], LoD=0.65 μg/ml) need to use additional reagents to apply a colorimetry approach based on absorbance or use expensive optical filters and collimators [90], or use non-specific method of extraction such as SPE (e.g. [162], LoD= 0.75 μg/ml). In contrast, the OFS for propofol detection proposed in this research detected down to a concentration of 0.65 μM = 115.88 μg/ml using the β −CD/propofol imprinted thin film of section 3.4.1 and down to a concentration of 99 nM = 0.017 μg/ml in aqueous solution by using the propofol imprinted film with higher surface area described in section 3.4.2. Therefore, the biosensor proposed in this research offers an alternative and less expensive option of detection since interrogation of U-shaped fibres only requires a single LED and a photodetector. However, the biosensor still needs to be tested in a whole blood samples or lysed blood samples to test its selectivity to target the analyte.

Similarly, some current techniques used to monitor anaesthetic and VOCs from breath allow on-line and real time monitoring of the analyte but the devices are bulky and expensive [121], [165]. GC-MS has been the most frequently used technique to determine concentration of propofol from breath of patients anaesthetized and clinical studies have reported a range between 2.8 to 22.5 ppb [119], 2 to 6 ppb [120] or 4.3 to 33.5 ng/l [164]. Propofol detection in gas phase was also demonstrated with a U-shaped fibre coated

with the method described in section 3.4.2 and using only two sets of concentrations, 6 ppm and 30 ppb (section 5.2.6), both with fixed environmental humidity (64%RH) and temperature (23.5 ^{0}C).

Therefore, the novelty of this sensor resides in the ability to create imprints of propofol directly onto the surface of the fibre structure, which is achieved using the fabrication methods explained in both sections 3.4.1 and 3.4.2. This application approach still needs investigation in vitro through bench-top studies, allowing continuous measurement of propofol mixed with other types of organic or interfering compounds.

6.4 Conclusions about sensing biochemical parameters of interest in the ICU

- An LPG coated with a (PAH/SiO_2:Au)$_3$ film and functionalized with biotin was used as a sensor for the detection of streptavidin protein. The sensor presented Langmuir adsorption to SV concentrations with a maximum wavelength shift of 44.05 nm, equilibrium binding constant of 1.68 $(\mu M)^{-1}$, sensitivity of 6.85 $\mathrm{nm}/(\mathrm{ng}/\mathrm{mm}^2)$ and theoretical LoD of 18.9 $\mathrm{pg}/\mathrm{mm}^2$.
- The diameter of SiO_2 NPs impacted sensitivity such that an LPG coated with (PAH/$SiO_{2(80\ nm)}$:Au)$_3$ film had 3 times lower sensitivity than an LPG coated with (PAH/$SiO_{2(300\ nm)}$:Au)$_3$. However, further experiments with (PAH/$SiO_{2(80\ nm)}$:Au)$_3$ tested with lower concentrations down to 2.5 nM successfully detected by the biosensor with specificity of 237% (ratio of maximum adsorption wavelength shifts, Fig. 5.6b) compared to a coating without Au NPs and the statistical LoD for the coated LPG with (PAH/$SiO_{2(80\ nm)}$:Au)$_3$ was 15.13 nM.
- The properties of the proposed platform sensor for clinically relevant proteins in the ICU could be tailored simply by changing the ligand

(instead of biotin), which allows targeting other type of protein compounds in the nano-molar range.

- As a first method, U-shaped fibres and LPGs functionalized with host-guest imprinted TiO_2 thin films were used to test propofol detection in aqueous solutions. Two sets of concentrations from the precursors of the thin film were tested to optimize deposition time and growth speed of the film onto the surface of optical fibres. A deposition time between 15 and 21 hr. with a set of concentrations of 0.8 mM /25 mM :50 mM for $\beta - CD$:Propofol / ($[NH_4]_2$ TiF_6 :H_3BO_3) was found to be optimum to obtain the highest sensitivity with Langmuir adsorption in the mili-molar range, a maximum intensity change of 61 mV and an equilibrium binding constant of 185.18 $(mM)^{-1}$. Under the same deposition thin film conditions, the maximum sensitivity (linear) in the micro-molar range was 4.32 mV / μM with a specificity of 2880% (ratio of sensitivities, Fig. 5.19) when compared to a non-imprinted TiO_2 thin film and tested under the same range of propofol concentrations.
- Langmuir adsorption of propofol in the mili-molar range was confirmed with the functionalisation of LPGs using the same host-guest imprinted TiO_2 thin film as with U-shaped fibres. The lowest detected concentration with a coated LPG (Λ =110.5 μm) was 0.65 μM and the lowest detected concentration with a coated U-shaped fibre was 0.69 μM.
- Detection limits were improved by adding MSNs and direct propofol imprinting onto inorganic TiO_2 films. The well-known and characterised surface area of the MSNs used allowed detection of propofol concentrations down to 0.99 nM in aqueous solutions. Once sensitivity to propofol is ascertained in aqueous solution, the deposition method can be extended to functionalise U-shaped fibres and detect propofol in gas phase (6 ppm and 30 ppb).

- The proposed biosensor for propofol detection has been implemented using two simple and low cost film sensing elements obtained with inorganic molecular imprinting.
- Propofol was successfully detected in aqueous solutions within the clinical range and gas phase detection was achieved when testing two fixed concentrations previously prepared in tedlar bags.

6.5 Future work

There is an immediate need for further fundamental research to investigate the two optical fibre sensors proposed for humidity and protein sensing. These include:

1) Surface coverage, sensitivity and response time are impacted by the size of the SiO_2 NPs and its surface modifications with higher number of ligands that will intensify their negative charge before they are coated with PAH.

2) In the case of the propofol biosensor, there is a need to perform in vitro measurements using bench-top studies with a ventilator or pure air flow to monitor propofol in gas phase continuously; both type of sensors (humidity and detection of volatile propofol) can be studied simultaneously to evaluate cross-talk effects between them.

3) Recent publications [145], [16], [114], [136], [137] have demonstrated that a heat wire humidifier in conjunction with a HME helps to target optimum levels of AH during ventilation. However, a list of influencing factors affect the performance of the ventilator and under-humidification or over-humidification still needs investigation. The environmental room humidity and temperature, settings of the humidifier (to target 37 ^{0}C at the distal part of the inspiratory limb) and ventilator settings (minute volume, tidal volume, pressure support, IPPV, $\%FiO_2$) all affect the real values of AH delivered to the anaesthetized patients.

As a visionary project, real time monitoring of anaesthetic propofol from the breath of patients and complemented with a humidity optical fibre sensor as a multi-sensing system in the same application is feasible. The LPG fabrication laboratory in the University of Nottingham has the facility to fabricate arrays of LPGs in the same fibre, then multiplexing and simultaneous measurement of humidity and propofol will be possible in the near future.

The optical fibre sensors proposed in this research could be considered as adding tiles to current known trend developments such as in the European project OFSETH (Optical Fibre Sensors Embedded into technical Textile for Healthcare) where investigations have focused on the monitoring of anaesthetized patients treated under MRI [70], e.g., patients under anaesthesia are usually transferred from the induction room to the MRI room and taken back still under anaesthesia. A continuous monitoring during this transfer is required but medical staff normally interchange between different devices as some of them are not transportable or MRI compatible. All of the components of the optical sensors suggested in this work require no electrical current and are made of non-magnetic materials and thus the devices could be used during MRI, oncological treatments or during anaesthesia. Future immediate work will investigate the applications of this sensor in volunteers, and a variety of patient groups. A first protocol with volunteers has recently been approved as "*Validation of a novel fibreoptic sensor integrated in oxygen delivery devices as a respiratory rate monitor*".

Overall this work has been wonderfully enjoyable and has opened up tremendous opportunities in the world of optical micro sensors that the author expects will provide a significant increase in the care of patients in the hospitals of the future.

Appendix: Control of contact pressure and bacteria monitoring during intubation

Most of the results presented in section A.1 were obtained during the first year of my PhD research as exploratory work to test the contact pressure between the cuff of an ETT and a trachea model using bare FBGs. These preliminary results of contact pressure obtained with FBGs were published as a conference paper [18] in collaboration of researchers from Cranfield University and the QMC university hospital of Nottingham. This work was a preparatory research stage for using optical fibre sensors in ETTs to measure contact pressure. However, the research was continued and improved by the collaborators through using patched FBGs and measure contact pressure with higher sensitivity [15], i.e., the FBGs were encased in an epoxy UV-cured polymer which improved the tensile strength of the gauge section for continuous measurements of pressure within the desirable clinical range.

Similarly, the results presented in section A.2 were also obtained during the first year of my PhD research as exploratory work to verify whether optical fibre sensors can be used to monitor biofilm formation (bacteria growth) onto the gauge section of an LPG. Preliminary results were positive towards the implementation of these types of sensors, however, this application was further undertaken and improved by another PhD student (not published yet) from the research group to which I belong to.

A.1 Contact pressure measurements with FBG sensors

ETTs have a pilot balloon which is inflated through a spring-loaded one way valve using a syringe. A manometer was connected to the system through a 3-way stopcock valve which is in turn connected to the syringe and the pilot balloon of the ETT through the use of well sealed medical hoses. FBG sensors were attached to the cuff of the ETT and introduced to the cylinder tube used

as a trachea model. The reflection from the FBGs were obtained using a SmartScan interrogator (Smart Fibres Ltd.).

Contact pressure measurements with patched FBGs (Figs. A1 and Fig. 1.9c, sensitivity: 2.1×10^{-2} nm/KPa) were demonstrated to be more suitable, reliable and reproducible than bare FBGs and flexiforce sensors (TEKSCAN A201, sensitivity: 71.3 mV/KPa). Table s1 summarizes the advantages and disadvantages between the three types of contact pressure-related sensors and Tables s2.1 and s2.2 present a comparison of results when all the sensors were tested in a trachea model (Figs. A1 and A3).

FBG patched sensors (Fig. A1, 1544 nm and 1549 nm, 60% reflection): • Robustness in sensor performance (flat and curved surfaces of phantom models). • Less prone to strain artefacts during inflation of the cuff (blue circle in Fig. A2). • Sensor indicates the exact moment in contact with the trachea wall. • Size of the patch can be reduced.
Flexiforce sensor (Fig. A3, A201 TEKSCAN): • Prone to artefacts when folded or measuring under uneven surfaces. • This sensor needs to receive a constant load on the full sensing area (diameter of 9.53 mm).
Bare FBG sensors (Fig. A5, 1544 nm and 1549 nm, 60% reflection): • Less robust than FBGs with patch. • Prone to strain artefacts during inflation of the cuff (blue rectangle in Fig. A6), producing a negative response of 3.0 KPa. • Less reliable response when measuring surfaces with curvature.

Table s1: Advantages and disadvantages of the contact pressure sensors tested.

FBGs in patches showed more robustness in performance (Fig. A2); polymer patches aided to neglect the wavelength shift response from the FBG while the inflation of the cuff started to increase between the first 10 and 20 seconds in Fig. A2 (blue circle) and provided a method to know the exact time when the cuff comes into contact with the trachea wall (indicator for sealing and avoiding over-inflation afterwards). On the other hand, flexiforce sensors and bare FBGs (glued to the cuff) were more prone to strain artefacts during the inflation of the cuff before sealing the wall of the trachea (Figs. A4 and A6). Flexiforce sensors response showed more drifting and instability in the signal over the full range of pressure (Fig. A4) and some bare FBGs had opposite wavelength shift during inflation of the cuff (Fig. A6).

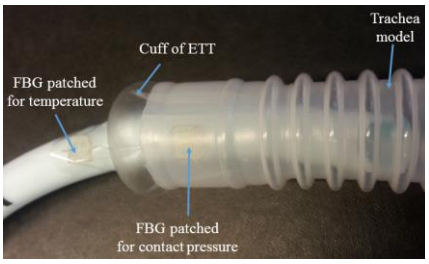
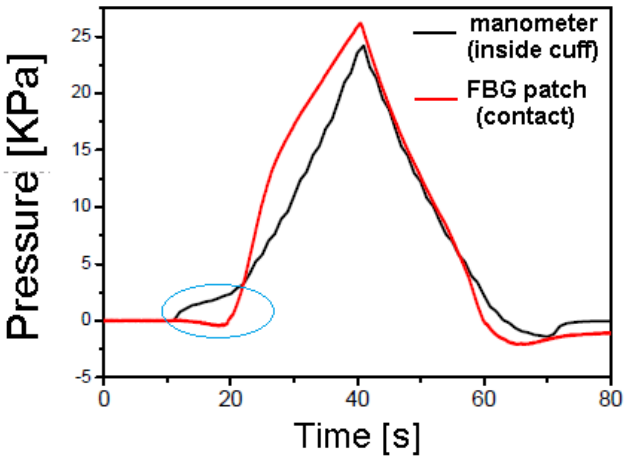
TYPE CONTACT-PRESSURE SENSOR	RESULTS COMPARED TO INTRACUFF PRESSURE WITH MANOMETER
 Figure A1. FBGs with patch	 Figure A2: Result of FBG in patch.

Table s2.1: Comparison of results between patched FBG sensor and manometer. The second patched FBG is used as reference temperature sensor for the application.

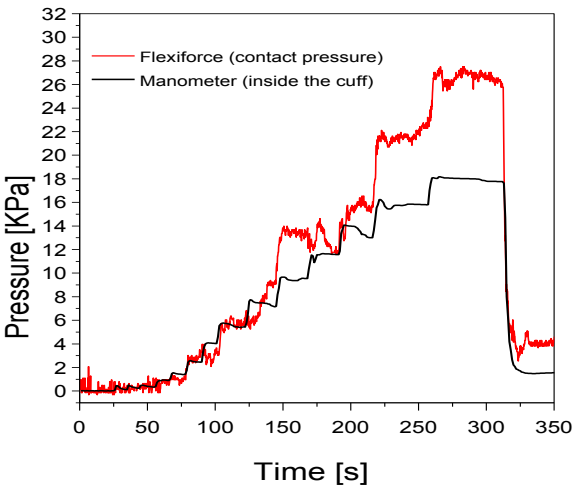
TYPE CONTACT-PRESSURE SENSOR	RESULTS COMPARED TO INTRACUFF PRESSURE WITH MANOMETER
 Figure A3: Flexiforce (A201)	 Figure A4: Result with flexiforce.

Table s2.2: Comparison of results between flexiforce, bare FBG sensors and manometer.

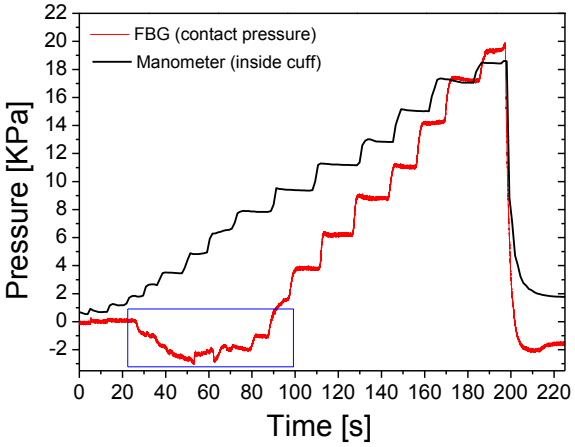
TYPE CONTACT-PRESSURE SENSOR	RESULTS COMPARED TO INTRACUFF PRESSURE WITH MANOMETER
 Figure A5. Bare FBGs glued.	 Figure A6. Result of bare FBGs (glued).

Table s2.2 (Continuation): Comparison of results between flexiforce, bare FBG sensors and manometer.

A.2 Bacteria growth biofilm measurements with LPG sensors

An LPG with period $\Lambda = 110.7$ μm working at the PMTP was used to test preliminary results of applying an LPG-based sensor as refractometer and track directly the growth of biofilm onto the LPG surface which is immersed in media with cultures of Pseudomona Aeruginosa (PA, Fig. A7). These results show how the transmission spectrum of the LPG-based sensor changed due to the variation in biofilm formation of PA over time.

The experimental set-up used was as shown in Fig. 3.15b and the measurements were performed in a temperature controlled room (at ca. 37^0C). The LPG was connected to a tungsten-halogen lamp on one side (HL-2000, Ocean Optics) and a spectrometer (HR4000, resolution 0.13 nm, Ocean Optics) on the other.

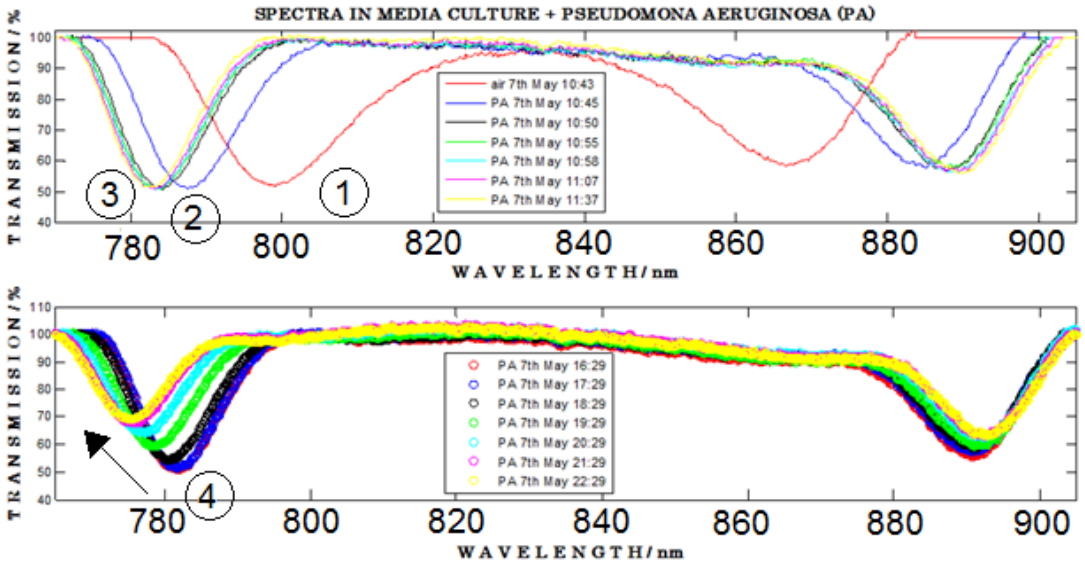


Figure A7: Transmission spectra of the LPG used to monitor change in growth of Pseudomona Aeruginosa (PA) onto the LPG surface. Steps 1 to 4 in circles indicate the progression of transmission spectra over time.

Fig. A.7 shows the performance of the LPG sensor to monitor bacteria biofilm growth onto its surface every 5 or 10 min (top Fig. A7) or every hour (bottom Fig. A7). In top part of Fig. A7, L-LP_{019} (left attenuation band of the LP_{019}) is located at ca. 799 nm in air and after immersion to media culture with PA (step 2, Fig. A7), the L-LP_{019} shifts to ca. 789 nm due to bulk aqueous refractive index change (~1.33). Immediately after 5 min of immersion in media culture, the refractive index jumps to ca. 782 nm (step 3, Fig. A7) and only after 6.5 hr. of the initial immersion of media culture, the L-LP_{019} starts to shift progressively every hour as shown in the bottom graph of Fig. A7. This phenomenon observed onto the LPG surface is attributed to the refractive index change caused by the growth of PA biofilm.

References

[1] M. Born, E. Wolf and A. B. Bhatia, Principles of optics: electromagnetic theory of propagation, interference and diffraction of light, 7th ed., Cambridge: Cambridge University Press, 2002.

[2] E. Hecht, Optics, 4th ed., London: Addison-Wesley, 2002.

[3] G. Keiser, "Optical Fiber for Biophoptonics Applications," in *Biophotonics. Concepts to Applications*, K. H. Becker, S. Hassani, B. Munro, R. Needs, J. Di Meglio, W. T. Rhodes, S. Scott, H. E. Stanley, M. Stutzmann and A. Wipf, Eds., Newton, Springer Science+Business Media Singapore, 2016, pp. 53-89.

[4] B. A. Saleh and M. C. Teich, "Fiber Optics," in *Fundamentals of Photonics*, 2nd ed., Boston, Massachussets: John Wiley & Sons, Inc., 2007, pp. 325-364.

[5] G. R. Fowles, Introduction to modern optics, 2nd ed., New York: Dover Publications, Inc., 1975.

[6] G. Keiser, F. Xiong, Y. Cui and P. Ping Shum, "Review of diverse optical fibers used in biomedical research and clinical practice," *Journal of Biomedical Optics,* vol. 19, no. 8, pp. 080902-1-080902-29, August 2014.

[7] B. Culshaw and A. Kersey, "Fiber-Optic Sensing: A Historical Perspective," *Journal of lightwave technology,* vol. 26, no. 9, pp. 1064-1078, 1 May 2008.

[8] J. Zheng and S. Albin, "Self-referenced reflective intensity modulated fiber optic displacement sensor," *Optical Engineering,* vol. 38, no. 2, pp. 227-232, February 1999.

[9] N.A, "MTI Instruments," Jenn Mathews Marketing Consulting, 2017. [Online]. Available: https://www.mtiinstruments.com/products/non-contact-measurement/fiber-optic-sensors/fiber-optic-mti-2100-fotonic-sensor/#brochure. [Accessed 8 September 2017].

[10] S. Korposh, *Class lecture, Topic: Principles of application of the optical fibres to chemical sensing.,* Kitakyushu: The Nanomaterials and Nanostructure Chemical Sensors. The University of Kitakyushu., 2009.

[11] K. Grattan and B. T. Meggitt, Chemical and environmental sensing, Boston: Kluwer Academic Publisher, 1999.

[12] L. Mescia and F. Prudenzano, "Advances on Optical Fiber Sensors," *Fibers,* vol. 2, pp. 1-23, 2014.

[13] S. Korposh, S.-W. Lee, S. James, R. Tatam and S. P. Morgan, "Biomedical application of optical fibre sensors," in *Quantum Sensing and Nano Electronics and Photonics XIV, Proc. of SPIE 10111, 101112Y-1*, San Francisco, California, U.S., 2017.

[14] R. Kashyap, Fiber Bragg Gratings, San Diego, California: Academic Press Elsevier, 2010.

[15] R. Correia, O. R. Blackman, F. U. Hernandez, S. Korposh, S. P. Morgan, B. R. Hayes-Gill, S. W. James, D. Evans and A. Norris, "Highly sensitive contact pressure measurements using FBG patch in endotracheal tube cuff," in *Proc. of SPIE: Sixth European Workshop on Optical Fibre Sensors.*, Limerick, Ireland, 2016.

[16] C. Massaroni, M. A. Caponero, R. D'Amato, D. Lo Presti and E. Schena, "Fiber Bragg Grating Measuring System for Simultaneous Monitoring of Temperature and Humidity in Mechanical Ventilaton," *Sensors,* vol. 17, no. 749, p. S17040749, 2017.

[17] R. Correia, E. Chehura, J. Li, S. W. James and R. P. Tatam, "Enhanced sensitivity fibre Bragg grating (FBG) load sensor," *Measurement Science and Technology,* vol. 21, no. 094006, p. 7pp, 2010.

[18] F. U. Hernandez, R. Correia, S. Korposh, S. P. Morgan, B. R. Hayes-Gill, S. W. James, D. Evans and A. Norris, "Measurements of endotracheal tube cuff contact pressure using fibre Bragg gratings," in *24th International Conference on Optical Fibre Sensors*, Santander,, 2015.

[19] J. Acorbe, J. M. Corres, F. J. Arregui and I. R. Matias, "Recent Developments in Fiber Optics Humidity Sensors," *Sensors,* vol. 17, no. 4, p. s17040893, April 2017.

[20] S. W. James and R. P. Tatam, "Optical fibre long-period grating sensors: characteristics and application," *Measurement Science and Technology,* vol. 14, pp. R49-R61, 2003.

[21] S. Korposh, S.-W. Lee and S. James, "Long Period Grating Based Fibre Optic Chemical Sensors," in *Fiber Optic Sensors: Current Status and Future Possibilities*, I. R. Matias, S. Ikezawa and J. Corres, Eds., Switzerland, Springer International Publishing, 2017, pp. 241-267.

[22] V. Bathia, "Applications of long-period gratings to single and multi-parameter sensing," *Optics Express,* vol. 4, no. 11, pp. 457-466, 1999.

[23] V. Bhatia, D. K. Campbell, D. Sherr, T. G. DAlberto, N. A. Zabaronick, G. A. TenEyck, K. A. Murphy and R. O. Claus, "Temperature-Insensitive and Strain-Insensitive Long-Period Grating Sensors for Smart Structures," *Optical Engineering,* vol. 36, no. 7, pp. 1872-1876, Jul 1997.

[24] S. Korposh, S. W. James, S.-W. Lee, S. Topliss, S. C. Cheung, W. J. Batty and R. P. Tatam, "Fiber optic long period grating sensors with a nanoassembled mesoporous film of SiO2 nanoparticles," *Optics Express,* vol. 18, no. 12, pp. 13227-13238, 2010.

[25] R. Y. Wong, E. Chehura, S. E. Staines, S. W. James and R. P. Tatam, "Fabrication of fiber optic long period gratings operating at the phase matching turning point using an ultraviolet laser," *Applied Optics,* vol. 53, no. 21, pp. 4669-4674, 20 July 2014.

[26] L. Marques, F. U. Hernandez, S. W. James, S. P. Morgan, M. Clark, R. P. Tatam and S. Korposh, "Highly sensitive optical fibre long period gratings biosensor anchored with silica

core gold shell nanoparticles," *Biosensors and Bioelectronics,* vol. 75, pp. 222-231, 15 January 2016.

[27] F. U. Hernandez, S. P. Morgan, B. R. Hayes-Gill, D. Harvey, W. Kinnear, A. Norris, D. Evans, J. G. Hardman and S. Korposh, "Characterization and Use of a Fiber Optic Sensor Based on PAH/SiO2 Film for Humidity Sensing in Ventilator Care Equipment," *IEEE Trans. Biomed. Eng.,* vol. 63, no. 9, pp. 1985-1992, September 2016.

[28] F. U. Hernandez, R. Correia, S. P. Morgan, B. Hayes-Gill, D. Evans, R. Sinha, A. Norris, D. Harvey, J. G. Hardman and S. Korposh, "Simultaneous temperature and humidity measurements in a mechanical ventilator using an optical fibre sensor," in *Proc. of SPIE: Sixth European Workshop on Optical Fibre Sensors.*, Limerick, Ireland., 2016.

[29] Z. L. Ran, Y. J. Rao, W. J. Liu, X. Liao and K. S. Chiang, "Laser-micromachined Fabry-Perot optical fiber tip sensor for high-resolution temperature independent measurement of refractive index," *Optics Express,* vol. 16, no. 3, pp. 2252-2263, February 2008.

[30] F. J. Arregui, I. R. Matías, K. L. Cooper and R. O. Claus, "Simultaneous Measurement of Humidity and Temperature by Combining a Reflective Intensity-Based Optical Fiber Sensor and a Fiber Bragg Grating," *IEEE Sensors,* vol. 2, no. 5, pp. 482-487, October 2002.

[31] C. E. Lee, W. N. Gibler, R. A. Atkins and H. F. Taylor, "In-Line Fiber Fabry -Perot Interferometer with High-Reflectance Internal Mirrors," *Journal of Lightwave Technology,* vol. 10, no. 10, pp. 1376-1379, 1992.

[32] C. Huang, W. Xie, D. Lee, C. Qi, M. Yang, M. Wang and J. Tan, "Optical Fiber Humidity Sensor With Porous TiO2/SiO2/TiO2 Coatings on Fiber Tip," *IEEE PHOTONICS TECHNOLOGY LETTERS,* vol. 27, no. 14, pp. 1495-1498, 15 July 2015.

[33] S. K. Khijwania, K. L. Srinivasan and J. P. Singh, "An evanescent-wave optical fiber relative humidity sensor with enhanced sensitivity," *Sensors and Actuators B,* vol. 104, pp. 217-22, 2005.

[34] N. Paliwal, N. Punjabi, J. John and S. Mukherji, "Design and Fabrication of Lossy Mode Resonance Based U-Shaped Fiber Optic Refractometer Utilizing Dual Sensing Phenomenon," *Journal of Lightwave Technology,* vol. 34, no. 17, pp. 4186-4193, September 2016.

[35] M. Yang, J. Peng, G. Wang and J. Dai, "Fiber Optic Sensors Based on Nano-Films," in *Fiber Optic Sensors. Current Status and Future Possibilities.*, vol. 21, I. R. Matias, S. Ikezawa and J. Corres, Eds., Switzerland, Smart Sensors, Measurement and Instrumentation. Springer International Publishing., 2017, pp. 1-30.

[36] P. Vaiano, B. Carotenuto, M. Pisco, A. Ricciardi, G. Quero, M. Consales, A. Crescitelli, E. Esposito and A. Cusano, "Lab on Fiber Technology for biological sensing applications," *Laser & Photonics Reviews,* vol. 10, no. 6, pp. 922-961, 2016.

[37] I. R. Matias, S. Ikezawa and J. Corres, Eds., Fiber Optic Sensors. Current status and future possibilities., Switzerland: Springer International Publishing, 2017.

[38] L. Alwis, T. Sun and K. Grattan, "Optical fibre-based sensor technology for humidity and moisture measurement: Review of recent progress," *Measurement,* vol. 46, pp. 4052-4074, 2013.

[39] S. A. Kolpakov, N. T. Gordon, C. Mou and K. Zhou, "Toward a New Generation of Photonic Humidity Sensors," *Sensors,* vol. 14, pp. 3986-4013, 26 February 2014.

[40] J. Buerck, S. Roth, K. Kraemer, M. Scholz and N. Klaas, "Application of a fiber-optic NIR-EFA sensor system for in situ monitoring of aromatic hydrocarbons in contaminated groundwater," *Journal of Hazardous Materials,* vol. 83, no. 1-2, pp. 11-28, 2001.

[41] R. Selyanchyn, S. Korposh, W. Yasukochi and S.-W. Lee, "A preliminary test for skin gas assessment using a porphyrin based evanescent wave optical fiber sensor," *Sensors & Transducers,* vol. 125, no. 2, pp. 54-67, 2011.

[42] P. Zubiate, C. R. Zamarreño, I. Del Villar, I. R. Matias and F. J. Arregui, "High sensitive refractometers based on lossy mode resonances (LMRs) supported by ITO coated D-shaped optical fibers.," *Optics Express,* vol. 23, no. 6, pp. 8045-8050, March 2015.

[43] T. H. Nguyen, T. Sun and K. T. Grattan, "Surface plasmon resonance based fibre-optic chemical sensor for the detection of cocaine," in *Sixth European Workshop on Optical Fibre Sensors. Proc. SPIE 9916, 991612.*, Limerick, Ireland., 2016.

[44] R. K. Verma and B. D. Gupta, "Surface plasmon resonance based U-shaped fiber optic sensor with enhanced sensitivity," in *ICOP 2009-International Conference on Optics and Photonics*, Chandigarh, India, 2009.

[45] F. U. Hernandez, T. Wang, S. Korposh, S. Correia, B. R. Hayes-Gill, J. Hromadka, N. N. Mohd Hazlan, A. Norris, D. Evans, L. S.-W. and S. P. Morgan, "Optical fibre sensing during critical care," in *Proc. of SPIE Vol. 10340. International Conference on Biophotonics V.*, Fremantle, Western Australia, 2017.

[46] M. Chavko, W. A. Koller, W. K. Prusaczyk and R. M. McCarron, "Measurement of blast wave by a miniature fiber optic pressure transducer in the rat brain," *Journal of Neuroscience Methods,* vol. 159, no. 2, pp. 277-281, 2007.

[47] E. Cibula and D. Donlagic, "Miniature fiber-optic pressure sensor with a polymer diaphragm," *Applied Optics,* vol. 44, no. 14, pp. 2736-2744, 2005.

[48] D. Lee, M. Yang, C. Huang and J. Dai, "Optical Fiber High-Temperature Sensor Based on Dielectric Films Extrinsic Fabry–Pérot Cavity," *IEEE Photonics Technology Letters,* vol. 26, no. 21, pp. 2107-2110, 2014.

[49] M. Jedrzejewska-Szczerska, P. Wierzba, A. A. Chaaya, M. Bechelany, P. Miele, R. Viter, A. Mazikowski, K. Karpienko and M. Wróbel, "ALD thin ZnO layer as an active medium in a fiber-optic Fabry–Perot interferometer," *Sensors and Actuators A: Physical,* vol. 221, pp. 88-94, 2015.

[50] L. H. Chen, C. C. Chan, R. Menon, P. Balamurali, W. C. Wong, X. M. Ang, P. B. Hu, M. Shaillender, B. Neu, P. Zu, Z. Q. Tou, C. L. Poh and K. C. Leong, "Fabry–Perot fiber-optic

immunosensor based on suspended layer-by-layer (chitosan/polystyrene sulfonate) membrane," *Sensors and Actuators B,* vol. 188, pp. 185-192, June 2013.

[51] F. J. Arregui, Y. Liu, I. R. Matias and R. O. Claus, "Optical fiber humidity sensor using a nano Fabry–Perot cavity formed by the ionic self-assembly method," *Sensors and Actuators B,* vol. 59, pp. 54-59, 1999.

[52] Y. Lin, Y. Gong, Y. Wu and H. Wu, "Polyimide-coated fiber Bragg grating for relative humidity sensing," *Photonic sensors,* vol. 5, no. 1, pp. 60-66, 2015.

[53] G. Berruti, M. Consales, M. Giordano, L. Sansone, P. Petagna, S. Buontempo, G. Breglio and A. Cusano, "Radiation hard humidity sensors for high energy physics applications using polyimide-coated fiber Bragg gratings sensors," *Sensors and Actuators B: Chemical,* vol. 177, pp. 94-102, 2013.

[54] S. F. Correia, P. Antunes, E. Pecoraro, P. P. Lima, H. Varum, L. D. Carlos, R. A. Ferreira and P. S. André, "Optical Fiber Relative Humidity Sensor Based on a FBG with a Di-Ureasil Coating," *Sensors,* vol. 12, no. 7, pp. 8847-8860, 2012.

[55] N. A. David, P. M. Wild and N. Djilali, "Parametric study of a polymer-coated fibre-optic humidity sensor," *Measurement Science and Technology,* vol. 23, p. 035103, 2012.

[56] A. J. Swanson, S. G. Raymond, S. Janssens, R. D. Breukers, M. D. Bhuiyan, J. W. Lovell-Smith and M. R. Waterland, "Development of novel polymer coating for FBG based relative humidity sensing," *Sensors and Actuators A: Physical,* vol. 249, pp. 217-224, 2016.

[57] J. Hromadka, R. Correia and S. Korposh, "Fabrication of fiber optic long period gratings operating at the phase matching turning point using an amplitude mask.," in *SPIE, Sixth European Workshop on Optical Fibre Sensors.*, Limerick, Ireland, 2016.

[58] J. Hromadka, S. Korposh, M. C. Partridge, S. W. James, F. Davis, D. Crump and R. P. Tatam, "Multi-parameter measurements using optical fibre long period gratings for indoor air quality monitoring," *Sensors and Actuators B: Chemical,* vol. 244, pp. 217-225, February 2017.

[59] T. Schuster, R. Herschel, N. Neumann and C. G. Schäfer, "Miniaturized Long-Period Fiber Grating Assisted Surface Plasmon Resonance Sensor," *Journal of Lightwave Technology,* vol. 30, no. 8, pp. 1003-1008, 2012.

[60] T. Wang, W. Yasukochi, S. Korposh, S. W. James, R. P. Tatam and S.-W. Lee, "A long period grating optical fiber sensor with nano-assembled porphyrin layers for detecting ammonia gas," *Sensors and Actuators B: Chemical,* vol. 228, pp. 573-580, 2016.

[61] S. James and R. P. Tatam, "Fibre optic sensors with nano-structured coatings," *Journal of Optics A: Pure and Applied Optics,* vol. 8, pp. S430-S444, 2006.

[62] J. Hromadka, S. Korposh, M. C. Partridge, S. James, F. Davis, D. Crump, S.-W. Lee and R. P. Tatam, "Multi-parameter measurements using optical fibre long period gratings for indoor air quality monitoring," in *25th International Conference on Optical Fiber Sensors*, Jeju, South Korea, 2017.

[63] J. Hromadka, B. Tokay, S. James, R. P. Tatam and S. Korposh, "Optical fibre long period grating gas sensor modified with metal organic framework thin films," *Sensors and Actuators B Chemical,* vol. 221, pp. 891-899, July 2015.

[64] S. Korposh, R. Selyanchyn, S. James, R. P. Tatam and S.-W. Lee, "Identification and quality assessment of beverages using a long period grating fibre-optic sensor modified with a mesoporous thin film," *Sensing and Bio-Sensing Research,* vol. 1, pp. 26-33, 2014.

[65] S. Korposh, I. Chianella, A. Guerreiro, S. Caygill, S. A. Piletsky, S. W. James and R. P. Tatam, "Selective vancomycin detection using optical fibre long period gratings functionalized with molecularly imprinted polymer nanoparticles," *Analyst,* vol. 139, pp. 2229-2236, 2014.

[66] B. Culshaw, "Optical Fiber Sensor Technologies: Opportunities and - Perhaps - Pitfalls," *Journal of Lightwave Technology,* vol. 22, no. 1, pp. 39-50, January 2004.

[67] O. Hirofumi, T. Wang and S.-W. Lee, "Selective Methanol Gas Detection Using a U-bent Optical Fiber Modified with a Silica Nanoparticle Multilayer," *Electronics and Communications in Japan,* vol. 100, no. 2, pp. 166-171, 2017.

[68] A. B. Socorro and S. Díaz, "Trends in Fibre-Optic Uses for Personal Healthcare and Clinical Diagnostics," in *Fiber Optic Sensors. Current Status and Future Possibilities*, Switzerland, Smart Sensors, Measurement and Instrumentation. Springer International Publishing, 2017, pp. 115-147.

[69] C. Massaroni, P. Saccomandi and E. Schena, "Medical Smart Textiles Based on Fiber Optic Technology: An Overview," *Journal of Functional Biomaterials,* vol. 6, pp. 204-221, 2015.

[70] K. Krebber, "Smart Technical Textiles Based on Fiber Optic Sensors," in *Current Developments in Optical Fiber Technology*, Rijeka, Croatia, InTech, 2013, pp. 319-344.

[71] T. Allsop, K. Carroll, G. Lloyd, D. J. Webb, M. Miller and I. Bennion, "Application of long-period-grating sensors to respiratory plethysmography," *Journal of Biomedical Optics,* vol. 12, no. 6, pp. 064003-1-13, 2007.

[72] D. Gomez, S. P. Morgan, B. R. Hayes-Gill and S. Korposh, "Polymeric fibre optic sensor based on SiO2 nanoparticle film for humidity sensing on wounds.," in *Sixth European Workshop on Optical Fibre Sensors (EWOFS'2016). Proc. SPIE 9916, 991623.*, Limerick, Ireland., 2016.

[73] K. Bremer and B. Roth, "Fibre optic surface plasmon resonance sensor system designed for smartphones," *Optics Express,* vol. 23, pp. 17179-17184, 2015.

[74] B. Berg, B. Cortazar , D. Tseng, H. Ozkan, S. Feng, Q. Wei, R. Yan-Lok Chan, J. Burbano, Q. Farooqui, M. Lewinski, D. Di Carlo, O. B. Garner and A. Ozcan, "Cellphone-Based Hand-Held Microplate Reader for Point-of-Care Testing of Enzyme-Linked Immunosorbent Assays," *American Chemical Society Nano,* vol. 9, no. 8, pp. 7857-7866, 2015.

[75] Y. Liu, Q. Liu, S. Chen, F. Cheng, H. Wang and W. Peng , "Surface plasmon resonance biosensor based on smartphone platforms," *Scientific Reports. Nature,* vol. 5, p. 12864, 2015.

[76] C. Shi, S. Giannarou, S.-L. Lee and G.-Z. Yang, "Simultaneous Catheter and Environment Modeling for Trans-catheter Aortic Valve Implantation," in *IEEE/RSJ International Conference on Intelligent Robots and Systems (IROS 2014).*, Chicago, IL, U.S., 2014.

[77] J. W. Arkwright, D. H.-C. Wang, S. A. Maunder, N. G. Blenman, I. Underhill, V. Patton and P. G. Dinning, "Exploring the dark continent with fibre Bragg gratings," in *23rd International Conference on Optical Fibre Sensors, Proc. SPIE 91573H*, Santander, Spain., 2014.

[78] A. Nilsson, Q. Zhang and J. Styf, "Evaluation of a fiber-optic technique for recording intramuscular pressure in the human leg," *Journal of Clinical Monitoring and Computing,* vol. 30, no. 5, pp. 699-705, 2015.

[79] S. Poeggel, D. Tosi, F. Fusco, J. Ippolito, L. Lupoli, V. Mirone, S. Sannino, G. Leen and E. Lewis, "Fiber-Optic EFPI Pressure Sensors for In Vivo Urodynamic Analysis," *IEEE Sensors Journal,* vol. 14, no. 7, pp. 2335-2340, 2014.

[80] K. Chatterjee, "The Swan-Ganz Catheters: Past, Present, and Future: A Viewpoint," *Circulation AHA journal,* vol. 119, pp. 147-152, 2009.

[81] A. Cusano, D. Paladino and A. Iadicicco, "Microstructured Fiber Bragg Gratings," *Journal of Lightwave technology,* vol. 27, no. 11, pp. 1663-1697, 2009.

[82] G. Quero, A. Crescitelli, D. Paladino, M. Consales, A. Buosciolo, M. Giordano, A. Cutolo and A. Cusano, "Evanescent wave long-period fiber grating within D-shaped optical fibers for high sensitivity refractive index detection," *Sensors and Actuators B: Chemical,* vol. 152, no. 2, pp. 196-205, 2011.

[83] A. Ricciardi, M. Consales , G. Quero, A. Crescitelli, E. Esposito and A. Cusano, "Lab-on-Fiber devices as an all around platform for sensing," *Optical Fiber Technology,* vol. 19, pp. 772-784, 2013.

[84] S. Deki, Y. Aoi, Y. Asaoka, A. Kajinami and M. Mizuhata, "Monitoring the growth of titanium oxide thin films by the liquid-phase deposition method with a quartz crystal microbalance," *Journal of Materials Chemistry,* vol. 7, no. 5, pp. 733-736, 1997.

[85] R. Selyanchyn, S. Wakamatsu, K. Hayashi and S.-W. Lee, "A Nano-Thin Film-Based Prototype QCM Sensor Array for Monitoring Human Breath and Respiratory Patterns," *Sensors,* vol. 15, pp. 18834-18850, 2015.

[86] H. H. Kim, H. J. Jeon, H. K. Cho, J. H. Cheong and J. S. Go, "HIGHLY SENSITIVE MEMS BIOSENSORS FOR THE DETECTION OF HUMAN PAPILLOMA VIRUS BY USING MAGNETIC FORCE," in *18th International Conference on Miniaturized Systems for Chemistry and Life Sciences*, San Antonio, Texas, U.S., 2014.

[87] S. Poeggel, D. Tosi, D. Duraibabu, G. Leen, D. McGrath and E. Lewis, "Optical Fibre Pressure Sensors in Medical Applications," *Sensors,* vol. 15, pp. 17115-17148, 2015.

[88] S. O'Keeffe, C. Fitzpatrick, A. Fernandez Fernandez, E. Lewis and A. Al-Shamma'a, "Optical fibre sensor for the online monitoring of gamma radiation doses," *Journal of Physics: Conference Series,* vol. 76, p. 012057, 2007.

[89] C. Fitzpatrick, C. O'Donoghue, J. Schöbel, B. Bastiaens, P. Van der Slot, E. Lewis and D. Pendrill, "A large core polymer optical fibre sensor for x-ray dosimetry based on luminescence occurring in the cladding," *Measurement Science and Technology,* vol. 15, p. 1586, 2004.

[90] L. Li, H. Ding, B. Di, W. Li and J. Chen, "Rapid detection of propofol in whole blood using an automated on-line molecularly imprinted pretreatment coupled with optical fibre detection," *Analyst,* vol. 137, pp. 5632-5638, 2012.

[91] S. M. Koenig and J. D. Truwit, "Ventilator-Associated Pneumonia: Diagnosis, Treatment, and Prevention," *Clinical Microbiology Reviews,* vol. 19, no. 4, pp. 637-657, October 2006.

[92] C. Mietto, R. Pinciroli, N. Patel and L. Berra, "Ventilator Associated Pneumonia: Evolving Definitions and Preventive Strategies.," *Respiratory Care,* vol. 58, no. 6, pp. 990-1007, June 2013.

[93] W. L. Rowe, "Economics and anaesthesia," *Anaesthesia,* vol. 53, pp. 782-788, 1998.

[94] J. R. Sneyd and K. A. Holmes, "Inhalational or total intravenous anaesthesia: is total intravenous anaesthesia useful and are there economic benefits?," *Current Opinion in Anesthesiology,* vol. 24, no. 2, pp. 182-187, April 2011.

[95] B. Musizza and S. Ribaric, "Monitoring the Depth of Anaesthesia," *Sensors,* vol. 10, pp. 10896-10935, 3 December 2010.

[96] J. Rinehart, N. Liu, B. Alexander and M. Cannesson, "Closed-Loop Systems in Anesthesia: Is There a Potential for Closed-Loop Fluid Management and Hemodynamic Optimization?," *Anesthesia & Analgesia,* vol. 114, no. 1, pp. 130-143, January 2012.

[97] K. Leslie, O. Clavisi and J. Hargrove, "Target-controlled infusion versus manually-controlled infusion of propofol for general anaesthesia or sedation in adults," *Anesthesia & Analgesia ,* vol. 107, no. 6, p. 2089, 2008.

[98] A. Bienert, P. Wiczling, E. Grzeskowiak, J. B. Cywinski and K. Kusza, "Potential pitfalls of propofol target controlled infusion delivery related to its pharmacokinetics and pharmacodynamics," *Pharmacological reports,* vol. 64, pp. 782-795, 2012.

[99] L. A. Tafur and E. Lema, "Total Intravenous Anaesthesia: from Pharmaceutics to Pharmacokinetics," in *Rev Colomb Anestesiol*, Bogotá, 2010.

[100] P. S. Glass and I. J. Rampil, "Automated Anesthesia. Fact or Fantasy?," *Anesthesiology,* vol. 95, no. 1, pp. 1-2, Jul 2001.

[101] R. D. Seegobin and G. L. Van Hasselt, "Endotracheal cuff pressure and tracheal mucosal blood flow: endoscopic study of effects of four large volume cuffs.," *British Medical Journal,* vol. 288, pp. 965-968, 31 March 1984.

[102] N. K. Chadha, A. Gordin, I. Luginbuehl, G. Patterson, P. Campisi, G. Taylor and V. Forte, "Automated Cuff Pressure Modulation," *Arch Otolaryngol Head Neck Surg,* vol. 137, no. 1, pp. 30-34, January 2011.

[103] L. Lorente, M. Lecuona, A. Jiménez , M. L. Mora and A. Sierra, "Ventilator-associated pneumonia using a heated humidifier or a heat and moisture exchanger: a randomized controlled trial," *Critical Care,* vol. 10, no. 4, pp. 1-7, 2006.

[104] G. De Pascale, M. A. Pennisi, M. S. Vallecoccia, G. Bello, R. Maviglia, L. Montini, V. Di Gravio, S. L. Cutuli, G. Conti and M. Antonelli, "CO2 driven endotracheal tube cuff control in critically ill patients: A randomized controlled study," *PLOS ONE,* vol. 12, no. 5, p. e0175476, 2017.

[105] J. Brimacombe, C. Keller and J. Margreiter, "A Pilot Study of Left Tracheal Pulse Oximetry," *Anesthesia & Analgesia,* vol. 91, pp. 1003-1006, 2000.

[106] S. L. Stewart, J. A. Secrest, B. R. Norwood and R. Zachary, "A comparison of endotracheal tube cuff pressures using estimation techniques and direct intracuff measurement," *American Association of Nurse Anesthetists,* vol. 71, no. 6, pp. 443-447, December 2003.

[107] T. Williams, "Humidification in intensive care," *The Southern African Journal of Critical Care,* vol. 21, no. 1, pp. 26-31, July 2005.

[108] A. M. Esquinas Rodriguez, R. Scala, A. Soroksky, A. BaHammam, A. de Klerk, A. Valipour, D. Chiumello, C. Martin and A. E. Holland, "Clinical review: Humidifiers during non-invasive ventilation - key points and practical implications," *Critical Care,* vol. 16, no. 203, pp. 1-7, 2012.

[109] R. D. Restrepo and B. K. Walsh, "Humidification During Invasive and Noninvasive Mechanical Ventilation: 2012," *Respiratory Care,* vol. 57, no. 5, pp. 782-788, May 2012.

[110] F. Lellouche, S. Qader, S. Taille, A. Lyazidi and L. Brochard, "Under-humidification and over-humidification during moderate induced hypothermia with usual devices," *Intensive Care Med,* vol. 32, pp. 1014-1021, 2006.

[111] J. Zuur, S. Muller, F. de Jongh, N. van Zandwijk and F. Hilgers, "The physiological rationale of heat and moisture exchangers in post-laryngectomy rehabilitation: a review," *Eur Arch Otorhinolaryngol,* vol. 263, pp. 1-8, 2006.

[112] J. K. Zuur, S. H. Muller, F. H. C. de Jongh, M. J. van der Horst, M. Shehata, J. van Leeuwen, M. Sinaasappel and F. J. M. Hilgers, "A newly developed tool for intra-tracheal temperature and humidity assessment in laryngectomized individuals: the Airway Climate Explorer (ACE)," *Medical & Biological Engineering & Computing,* vol. 45, pp. 737-745, 13 July 2007.

[113] A. Bodini, M. Serpelloni, E. Sardini, N. Latronico, M. R. Tommasi and M. Filippini, "Low-Power Wireless System for Temperature and Humidity Monitoring in Artificial Ventilation,"

in *IEEE International Symposium on Medical Measurements and Applications (MeMeA)*, Benevento, Italy., 2016.

[114] Y. Tanaka, S. Iwata, M. Kinoshita, K. Tsuda, S. Tanaka, N. Hara, R. Shindou, E. Harada, R. Kijima, O. Yamaga, H. Ohkuma, K. Ushijima, T. Sakamoto, Y. Yamashita and O. Iwata, "Insufficient Humidification of Respiratory Gases in Patients Who Are Undergoing Therapeutic Hypothermia at a Paediatric and Adult Intensive Care Unit," *Hindawi Canadian Respiratory Journal,* vol. Article ID 8349874, p. 6 pages, 2017.

[115] J. Chastre and J. Y. Fagon, "Ventilator-Asscociated Pneumonia," *American Journal of Respiratoryand Critical Care Medicine,* vol. 165, pp. 867-903, 2002.

[116] L. D. Bos, P. J. Sterk and M. J. Schultz, "Volatile Metabolites of Pathogens: A Systematic Review," *PLOS Pathogens,* vol. 9, no. 5, pp. 1-8, May 2013.

[117] K. Ng, "The Independent UK," 7 November 2015. [Online]. Available: http://www.independent.co.uk/news/science/this-is-what-happens-to-your-brain-when-you-go-under-anaesthesia-a6725386.html. [Accessed 23 September 2017].

[118] D. K. Heyland, P. J. Weijs, J. A. Coss-Bu, B. Taylor, A. S. Kristof, G. E. O'Keefe and R. G. Martindale, "Protein Delivery in the Intensive Care Unit: Optimal or Suboptimal?," *Nutrition in Clinical Practice,* vol. 32, no. 1, pp. 58S-71S, 2017.

[119] M. Grossherr, A. Hengstenberg, T. Meier, L. Dibbelt, B. W. Igl, A. Ziegler, P. Schmucker and H. Gehring, "Propofol concentration in exhaled air and arterial plasma in mechanically ventilated patients undergoing cardiac surgery," *British Journal of Anaesthesia,* vol. 102, no. 5, pp. 608-13, 2009.

[120] A. Takita, K. Masui and T. Kazama, "On-line monitoring of end-tidal propofol concentration in anesthetized patients.," *Anaesthesiology,* vol. 106, pp. 659-64, 2007.

[121] C. Hornuss, S. Praun, J. Villinger, A. Dornauer, P. Moehnle, M. Dolch, E. Weninger, A. Chouker, C. Feil, J. Briegel, M. Thiel and G. Schelling, "Real-time Monitoring of Propofol in Expired Air in Humans Undergoing Total Intravenous Anesthesia," *Anesthesiology,* vol. 106, pp. 665-74, 2007.

[122] P. J. Weijs, R. N. Dickerson, D. K. Heyland, F. A. Moore, S. J. Rugeles and S. A. McClave, "Experimental and Outcome-Based Approaches to Protein Requirements in the Intensive Care Unit," *Nutrition in Clinical Practice,* vol. 32, no. 1, pp. 77S-85S, 2017.

[123] A. F. Pacela, "Impedance Pneumography - A Survey of instrumentation techniques," *Medical and biological engineering,* vol. 4, no. 1, pp. 1-15, 1966.

[124] J. M. Van De Water, B. E. Mount, J. R. Barela, R. Schuster and F. S. Leacock, "Monitoring the Chest with Impedance," *Chest,* vol. 64, no. 5, pp. 597-603, 1973.

[125] J. A. Anderson and W. F. Vann, "Respiratory monitoring during pediatric sedation: pulse oximetry and capnography," *Pediatric Dentistry,* vol. 10, no. 2, pp. 94-101, 1988.

[126] R. Soto, E. Fu, H. Vila and R. V. Miguel, "Capnography Accurately Detects Apnea During Monitored Anesthesia Care," *Anesthesia & Analgesia,* vol. 99, no. 2, pp. 379-382, 2004.

[127] L. Wiklund, B. Hok, K. Stahl and A. Jordeby-Jonsson, "Postanesthesia Monitoring Revisited: Frequency of True and False Alarms from Different Monitoring Devices," *Survey of Anesthesiology,* vol. 39, no. 1, p. 16, 1995.

[128] I. Smith, J. Mackay and N. Fahrid, "Respiratory rate measurement: a comparison of methods," *British Journal of Healthcare Assistants,* vol. 05, no. 01, pp. 18-23, 2011.

[129] A. D. Wilson and M. Baietto, "Applications and Advances in Electronic-Nose Technologies," *Sensors,* vol. 9, pp. 5099-5148, 2009.

[130] S.-I. Ohira, J. Li, W. A. Lonneman, P. K. Dasgupta and K. Toda, "Can Breath Isoprene Be Measured by Ozone Chemiluminescence?," *Analytical Chemistry,* vol. 79, pp. 2641-2649, 2007.

[131] M. Righettoni, A. Tricoli and S. E. Pratsinis, "Si:WO3 Sensors for Highly Selective Detection of Acetone for Easy Diagnosis of Diabetes by Breath Analysis," *Analytical Chemistry,* vol. 82, pp. 3581-3587, 2010.

[132] K. Toda, J. Li and P. K. Dasgupta, "Measurement of Ammonia in Human Breath with a Liquid-Film Conductivity Sensor," *Analytical Chemistry,* vol. 78, pp. 7284-7291, 2006.

[133] J. H. Leopold, A. Abu-Hanna, C. Colombo, P. J. Sterk, M. J. Schultz and L. D. Bos, "Factors Influencing Continuous Breath Signal in Intubated and Mechanically-Ventilated Intensive Care Unit Patients Measured by an Electronic Nose," *Sensors,* vol. 16, no. 1337, p. s16081337, 2016.

[134] S.-W. Lee, S. Korposh, R. Selyanchyn and T. Kunitake, "Fundamentals and Perspectives in Sensor Applications," in *Handbook of molecular imprinting. Advanced sensor applications.*, S. Lee and T. Kunitake, Eds., Boca Raton, Florida U.S., Taylor & Francis Group, LLC., 2012, pp. 3-45.

[135] N. Yagi, S. Nagami, M.-k. Lin, T. Yabe, M. Itoda, T. Imai and Y. Oku, "A noninvasive swallowing measurement system using a combination of respiratory flow, swallowing sound, and laryngeal motion," *Medical & Biological Engineering & Computing,* vol. 55, pp. 1001-1017, 2017.

[136] S. A. De Oliveira, L. M. Lucio, N. S. Modolo, Y. Hayashi, M. G. Braz, L. R. de Carvalho, L. G. Braz and J. R. C. Braz, "The Humidity in a Low-Flow Drager Fabius Anesthesia Workstation with or without Thermal Insulation or a Heat and Moisture Exchanger: A Prospective Randomized Clinical Trial," *PLOS ONE,* vol. 12, no. 1, p. e0170723, 2017.

[137] J. K. Zuur, S. H. Muller, A. Vincent, M. Sinaasappel, F. H. de Jongh and F. J. Hilgers, "Assessment of tracheal temperature and humidity in laryngectomized individuals and the influence of a heat and moisture exchanger on tracheal climate," *Head & Neck,* vol. 30, pp. 1072-1082, 2008.

[138] S. Ingelstedt, "Studies on the conditioning of air in the respiratory tract," *Acta Otolaryngolica,* vol. 56, pp. 1-80, 1956.

[139] T. Keck, J. Durr, R. Leiacker, G. Rettinger and A. Rozsasi, "Tracheal climate in laryngectomees after use of a heat and moisture exchanger," *Laryngoscope,* vol. 115, no. 3, pp. 534-537, 2005.

[140] R. D. McRae, A. S. Jones, P. Young and J. Hamilton, "Resistance, humidity and temperature of the tracheal airway," *Clinical Otolaryngology,* vol. 20, no. 4, pp. 355-356, 1995.

[141] Y. Kang, H. Ruan, Y. Wang, F. J. Arregui, I. R. Matías and R. O. Claus, "Nanostructured optical fibre sensors for breathing airflow monitoring," *Measurement Science and Technology,* vol. 17, pp. 1207-1210, 2006.

[142] F. C. Favero, J. Villatoro and V. Pruneri, "Microstructured optical fiber interferometric breathing sensor," *Journal of Biomedical Optics,* vol. 17, no. 3, pp. 037006-1, 2012.

[143] M. Morisawa, Y. Natori, T. Taki and S. Muto, "Recognition of Devoiced Vowels Using Optical Microphone Made of Multiple POF Moisture Sensors," *Electronics and Communications in Japan,* vol. 93, no. 9, pp. 306-311, 2010.

[144] S. Akita, A. Seki and K. Watanabe, "A monitoring of breathing using a hetero-core optical fiber sensor," in *Proc. of SPIE Vol. 7981, Sensors and Smart Structures Technologies for Civil, Mechanical, and Aerospace Systems*, San Diego, California. U.S., 2011.

[145] R. D'amato, M. A. Caponero, E. Schena, P. Saccomandi and C. Massaroni, "Fabrication and preliminary assessment of a fiber optic-based relative humidity sensor for application in mechanical ventilation," *IEEE Instrumentation and Measurement Society,* 2017 in Press..

[146] C. Hamel and E. Pinet, "Temperature and pressure fiber-optic sensors applied to minimally invasive diagnostics and therapies," *Progress in Biomedical Optics and Imaging,* vol. 7, no. 6, pp. 1605-7422, 2006.

[147] S. Silvestri and E. Schena, "Optical-Fiber Measurement Systems for Medical Applications," in *Optoelectronics- Devices and Applications*, P. P. Predeep, Ed., Rijeka, Croatia, Intech, 2011, pp. 205-224.

[148] S. Sondergaard, S. Karason, A. Hanson, K. Nilsson, S. Hojer, S. Lundin and O. Stenqvist, "Direct Measurement of Intratracheal Pressure in Pediatric Respiratory Monitoring," *Pediatric Research - Nature,* vol. 51, no. 3, pp. 339-345, 2002.

[149] M. D. Ivanovic and J. Petrovic, "A long-period fibre grating monitor of respiratory volumes for the use in non-invasive mechanical ventilation," *Optical and Quantum Electronics,* vol. 48, p. 346, 2016.

[150] I. Martin-Loeches, L. D. Bos and E. C. Goligher, "Will all ARDS patients be receiving mechanical ventilation in 2035? Yes," *Intensive Care Medicine,* vol. 43, no. 4, pp. 568-569, 2016.

[151] M. A. Zawawi, S. O'Keffe and E. Lewis, "Intensity-modulated fiber optic sensor for health monitoring applications: a comparative review," *Sensor Review,* vol. 33, no. 1, pp. 57-67, 2013.

[152] A. F. Silva, J. P. Carmo, P. M. Mendes and J. H. Correia, "Simultaneous cardiac and respiratory frequency measurement based on a single fiber Bragg grating sensor," *Measurement Science and Technology,* vol. 22, p. 075801 (5pp), 2011.

[153] J. P. Carmo, A. M. F. da Silva, R. P. Rocha and J. H. Correia, "Application of Fiber Bragg Gratings to Wearable Garments," *IEEE Sensors,* vol. 12, no. 1, pp. 261-266, 2012.

[154] A. Grillet, D. Kinet , J. Witt, M. Schukar, K. Krebber, F. Pirotte and A. Depre, "Optical Fiber Sensors Embedded Into Medical Textiles for Healthcare Monitoring," *IEEE Sensors,* vol. 8, no. 7, pp. 1215-1222, 2008.

[155] D. Lau, Z. Chen, J. T. Teo, S. H. Ng, H. Rumpel, Y. Lian, H. Yang and P. L. Kei, "Intensity-Modulated Microbend Fiber Optic Sensor for Respiratory Monitoring and Gating During MRI," *IEEE Transactions on Biomedical Engineering,* vol. 60, no. 9, pp. 2655-2662, 2013.

[156] W. J. Yoo, K. W. Jang, J. K. Seo, J. Y. Heo, J. S. Moon, J. Y. Park and B. Lee, "Development of Respiration Sensors Using Plastic Optical Fiber for Respiratory Monitoring Inside MRI System," *Journal of the Optical Society of Korea,* vol. 14, no. 3, pp. 235-239, 2010.

[157] M. M. Struys, T. De Smet, L. F. Versichelen, S. Van de Velde, R. Van den Broecke and E. P. Mortier, "Comparison of Closed-loop Controlled Administration of Propofol Using Bispectral Index as the Controlled Variable versus "Standard Practice" Controlled Administration," *Anesthesiology,* vol. 95, pp. 6-17, 2001.

[158] C.-C. Hong, P.-H. Chang, C.-C. Lin and C.-L. Hong, "A disposable microfluidic biochip with on-chip molecularly imprinted biosensors for optical detection of anesthetic propofol," *Biosensors and Bioelectronics,* vol. 25, pp. 2058-2064, 2010.

[159] A. Hengstenberg, M. Grossherr, T. Meier, L. Dibbelt and H. Gehring, "Continuous Real-Time Monitoring of Propofol in Breathing Gas during Anesthesia," in *American Society of Anesthesiologists. The Anesthesiology annual meeting. A577*, 2006.

[160] L. Li and Y. Li, "Study of az-coupling derivatization by sequential injection coupled with spectrophotometric optical fibre detection for propofol analysis," *Analytical Methods,* vol. 8, pp. 6176-6184, July 2016.

[161] L. McGaughran, L. J. Voss, R. Oliver, M. Petcu, P. Schaare, J. P. Barnard and J. W. Sleigh, "Rapid measurement of blood propofol levels: A proof of concept study," *Journal of Clinical Monitoring and Computing,* vol. 20, pp. 109-115, 2006.

[162] B. Liu, D. M. Pettigrew, S. Bates, P. G. Laitenberger and G. Troughton, "Performance evaluation of a whole blood propofol analyser," *Journal of Clinical Monitoring and Computing,* vol. 26, pp. 29-36, 2012.

[163] F. Kivlehan, E. Chaum and E. Lindner, "Propofol detection and quantification in human blood: the promise of feedback controlled, closed-loop anesthesia," *Analyst,* vol. 140, pp. 98-106, 2015.

[164] Y. Gong, E. Li, G. Xu, H. Wang, C. Wang, P. Li and Y. He, "Investigation of Propofol Concentrations in Human Breath by Solid-Phase Microextraction Gas Chromatography-Mass Spectrometry," *The journal of International Medical Research,* vol. 37, pp. 1465-1471, 2009.

[165] Y. Liu, Y. Gong, C. Wang, X. Wang, Q. Zhou, D. Wang, L. Guo, X. Pi, X. Zhang, S. Luo, H. Li and E. Li, "Online breath analysis of propofol during anesthesia: clinical application of membrane inlet-ion mobility spectrometry," *Acta Anaesthesiologica Scandinavica,* vol. 59, pp. 319-328, 2015.

[166] T. Laurila, T. Sorvajärvi, J. Saarela, J. Toivonen, D. W. Wheeler, L. Ciaffoni, G. A. Ritchie and C. F. Kaminski, "Optical detection of the anesthetic agent propofol in the gas phase," *Analytical Chemistry,* vol. 83, pp. 3963-3967, 2011.

[167] N.A., "Quantum made simple. Scanning electron microscopy," Physics Reimagined, 2017. [Online]. Available: http://toutestquantique.fr/en/scanning-electron/. [Accessed 11 June 2017].

[168] N.A., "NMRC Nanoscale and Microscale Research Centre," NMRC hub. The University of Nottingham, 20 April 2016. [Online]. Available: http://www.nottingham.ac.uk/nmrc/facilities/emsuite/sem.aspx. [Accessed 10 June 2017].

[169] T. Nobuo, Ed., Scanning Transmission Electron Microscopy of Nanomaterials. Basics of Imaging and Analysis., Nagoya: Imperial College Press, 2014.

[170] N.A., "ATR accesories. An overview," Technical report. PerkinElmer Life and Analytical Sciences., Shelton, C.T. USA, 2004.

[171] P. R. Griffiths and J. A. de Haseth, "Attenuated Total Reflection," in *Fourier Transform Infrared Spectrometry*, New Jersey, John Wiley & Sons, Inc., 2007, pp. 321-348.

[172] R. Stanley, "Plasmonics in the mid-infrared," *Nature Photonics,* vol. 6, pp. 409-411, July 2012.

[173] S. Beck, "Across the Spectrum: Instrumentation for UV-Vis spectrophotometry.," 2 February 1998. [Online]. Available: http://www.the-scientist.com/?articles.view/articleNo/18797/title/Across-the-Spectrum--Instrumentation-for-UV-Vis-Spectrophotometry/. [Accessed 19 June 2017].

[174] A. Ejchart and W. Kozminski, "NMR of Cyclodextrins and Their Complexes," in *Cyclodextrins and Their Complexes. Chemistry, Analytical Methods, Applications.*, H. Dodziuk, Ed., Weinheim, Wiley-VCH Verlag GmbH & Co. KGaA., 2006, pp. 231-254.

[175] S. A. Richards and J. C. Hollerton, Essential Practical NMR for Organic Chemistry, Singapore: John Wiley & Sons, Ltd, 2011.

[176] H. Günter, NMR spectroscopy. Basic principles, Concepts, and Applications in Chemistry, Third ed., Darmstadt: Wiley-VCH Verlag GmbH & Co. KGaA, 2013.

[177] N.A., "Safety Office from the University of Nottingham," 1 August 2013. [Online]. Available: http://www.nottingham.ac.uk/safety/. [Accessed 24 May 2017].

[178] T. Moseley and G. Zabierek, "Guidance on the safe use of laser in education and research.," Association of University Radiation Protection Officers (AuRPO), 2012.

[179] R. Y. Wong, "Advanced fibre optic long period grating sensors; design, fabrication and sensing," Ph.D. dissertation, Engineering Photonics, Schoolf of Engineering, Cranfield Univ., Cranfield, UK., 2014.

[180] M. L. Dockney, S. W. James and R. P. Tatam, "Fibre Bragg gratings fabricated using a wavelength tuneable laser source and a phase mask based interferometer," *Measurement Science and Technology,* vol. 7, pp. 445-448, 1996.

[181] G. R. Fowles, Introduction to modern optics, 2nd ed., New York: Dover publications, Inc., 1975.

[182] J. C. Huie, "Guided molecular self-assembly: a review of recent efforts.," *Smart Materials and Structures,* vol. 12, pp. 264-271, March 2003.

[183] Y. Liu, A. Rosidian, K. Lenahan, Y.-X. Wang, T. Zeng and R. O. Claus, "Characterization of electrostatically self-assembled nanocomposite thin films.," *Smart Materiasl and Structures,* vol. 8, pp. 100-105, 1999.

[184] K. L. Cooper, "Electrostatic Self-Assembly of Linear and Nonlinear Optical Thin Films," PhD dissertation. Faculty of the Virginia Polytechnic Institute and State University., Blacksburg, Virginia., 1999.

[185] E. Guzmán, A. Mateos-Maroto, M. Ruano, F. Ortega and R. G. Rubio, "(in press). Layer-by-layer polyelecrolyte assemblies for encapsulation and release of active compounds.," *Advances in Colloid and Interface Science. ,* 2017.

[186] X. Zhao, "Study of Multimode Extrinsic Fabry-Perot Interferometric Fiber Optic Sensor on Biosensing," MSc dissertation. Electrical and Computer Engineering. Faculty of the Virginia Polytechnic Institute and State University., Blacksburg. Virginia., 2006.

[187] K. Van der Maaden, J. Tomar, W. Jiskoot and J. Bouwstra, "Chemical Modifications of Silicon Surfaces for the Generation of a Tunable Surface Isoelectric point," *Langmuir,* vol. 30, pp. 1812-1819, January 2014.

[188] W. Stöber and A. Fink, "Controlled Growth of Monodisperse Silica Spheres in the Micron Size Range," *Journal of Colloid and Interface Science,* vol. 26, pp. 62-69, 1968.

[189] C. Bonnard, D. S. Papermaster and J. -P. Kraehenbuhl, "The streptavidin-biotin bridge technique: Application in light electron microscope immunocytochemistry.," in *Immunolabelling for Electron Microscopy.*, New York, Elsevier, 1984, pp. 95-111.

[190] L. Zhu, D. Xue and Z. Wang, "Metallic Cation Induced One-Dimensional Assembly of Poly(acrylic acid)-1-Dodecanethiol-Stabilized Gold Nanoparticles.," *Langmuir,* vol. 24, pp. 11385-11389, 2008.

[191] M. Yang, J. Peng, G. Wang and J. Dai, "Fiber Optic Sensors Based on Nano-Films," in *Fiber Optic Sensors. Current Status and Future posibilities.*, I. R. Matias, J. Corres and S. Ikezawa, Eds., Switzerland, Springer , 2017, pp. 1-30.

[192] I. Del Villar, I. R. Matías, F. J. Arregui and R. O. Claus, "Fiber-Optic Hydrogen Peroxide Nanosensor," *IEEE Sensors Journal,* vol. 5, no. 3, pp. 365-371, June 2005.

[193] V. Mohanta and S. Patil, "Enhancing surface coverage and growth in layer-by-layer assembly of protein nanoparticles," *Langmuir,* vol. 29, no. 43, pp. 13123-13128, August 2013.

[194] J. Bravo, L. Zhai, Z. Wu, R. E. Cohen and M. F. Rubner, "Transparent Superhydrophobic Films Based on Silica Nanoparticles," *Langmuir,* vol. 23, no. 13, pp. 7293-7298, January 2007.

[195] B. Voncina and V. Vivod, "Cyclodextrins in Textile Finishing," in *Eco-Friendly Textile Dyeing and Finishing*, D. M. Gunay, Ed., InTech online, 2013, pp. 53-75.

[196] V. Caligur, "Cyclodextrins," *BioFiles,* vol. 3, no. 3, pp. 32-33, 2008.

[197] T. Irie and K. Uekama, "Cyclodextrins in peptide and protein delivery," *Advanced Drug Delivery Reviews,* vol. 36, no. 1, pp. 101-123, 1 March 1999.

[198] F. Maestrelli, M. Bragagni and P. Mura, "Advanced formulations for improving therapies with anti-inflammatory or anaesthetic drugs: A review.," *Journal of Drug Delivery Science and Technology,* vol. 32, no. Part B, pp. 192-205, April 2016.

[199] N.A., "Drugbank 5.0," Alberta Innovates - Health Solutions, The Metabolomics Innovation Centre (TMIC), 13 June 2005. [Online]. Available: https://www.drugbank.ca/drugs/DB00818. [Accessed 16 June 2017].

[200] N. "Spectral Database for Organic Compounds SDBS," National Institute of Advanced Industrial Science and Technology (AIST)., [Online]. Available: http://sdbs.db.aist.go.jp/sdbs/cgi-bin/direct_frame_disp.cgi?sdbsno=862 . [Accessed 20 June 2017].

[201] N. Takahara, T. Wang and S.-W. Lee, "Selective Adsorption of Molecules by Imprinted Titania Nanohybrid Thin Films with Anchored Cyclodextrin Host Molecules," *Kobunshi Ronbunshu,* vol. 70, no. 5, pp. 214-220, May 2013.

[202] G. N. Reiner, L. Fernandes Fraceto, E. de Paul, M. A. Perillo and D. A. García, "Effects of Gabaergic Phenols on Phospholipid Bilayers as Evaluated by 1H-NMR," *Journal of Biomaterials and Nanobiotechnology,* vol. 4, pp. 28-34, June 2013.

[203] E. Locci, S. Lai, A. Piras, B. Marongiu and A. Lai, "13C-CPMAS and 1H-NMR Study of the Inclusion Complexes of ß-Cyclodextrin with Carvacrol, Thymol, and Eugenol Prepared in Supercritical Carbon Dioxide.," *Chemistry and Biodiversity,* vol. 1, pp. 1354-1366, 2004.

[204] S. Saha, A. Roy, K. Roy and M. N. Roy, "Study to explore the mechanism to form inclusion complexes of ß-cyclodextrin with vitamin molecules," *Nature, Scientific Reports.,* vol. 6, p. 35764, October 2016.

[205] S. H. Toma, J. A. Bonacin, K. Araki and H. E. Toma, "Selective host-guest interactions on mesoporous TiO2 films modified with carboxymethyl-ß-cyclodextrin," *Surface Science,* vol. 600, pp. 4591-4597, August 2006.

[206] Y. Jia-Guo, Y. Huo-Gen, C. Bei, Z. Xiu-Jian, Y. Jimmy C. and H. Wing-Kei, "The Effect of Calcination Temperature on the Surface Microstructure and Photocatalytic Activity of TiO2 Thin Films Prepared by Liquid Phase Deposition," *The Journal of Physical Chemistry B,* vol. 107, pp. 13871-13879, October 2003.

[207] Y. Paz, "Self-assembled monolayers and titanium dioxide: From surface patterning to potential applications," *Beilstein Journal of nanotechnology,* vol. 2, pp. 845-861, 2011.

[208] L. Li, X. Sun, Y. Yang, N. Guan and F. Zhang, "Syntehsis of Anatase TiO2 Nanoparticles with ß-Cyclodextrin as a Supramolecular Shell," *Chemistry - An Asian Journal,* vol. 1, pp. 664-668, 2006.

[209] H.-K. Lee, D. Sakemi, R. Selyanchin, C.-G. Lee and S.-W. Lee, "Titania Nanocoating on MnCO3 Microspheres via Liquid-Phase Deposition for Fabrication of Template-Assisted Core−Shell- and Hollow-Structured Composites," *Applied Materials & Interfaces,* vol. 6, pp. 57-64, 2014.

[210] L. Feng, Y. Liu and J. Hu, "Molecularly Imprinted TiO2 Thin Film by Liquid Phase Deposition for the Determination of L-Glutamic acid," *Langmuir,* vol. 20, pp. 1786-1790, 2004.

[211] F. B. Li and X. Z. Li, "The enhancement of photodegradation efficiency using Pt-TiO2 catalyst," *Chemosphere,* vol. 48, pp. 1103-1111, May 2002.

[212] L. C. Bailey, K. T. Tang and B. A. Rogozinski, "The determination of 2,6-diisopropylphenol (propofol) in an oil in water emulsion dosage form by high-performance liquid chromatography and by second derivative UV spectroscopy," *Journal of Pharmaceutical & Biomedical Analysis,* vol. 9, no. 6, pp. 501-506, 1991.

[213] G. Granero, C. Garnero and M. Longhi, "Second derivative spectrophotometric determination of trimethoprime and sulfamethoxazole in the presence of hydroxypropyl-ß-cyclodextrin (HP-ß-CD)," *Journal of Pharmaceutical and Biomedical Analysis,* vol. 29, pp. 51-59, 2002.

[214] S. Kus, Z. Marczenko and N. Obarski, "Derivative UV-VIS Spectrophotometry in Analytical Chemistry," *Chemia Analityczna (Warsaw),* vol. 41, pp. 899-927, 1996.

[215] N. Özdemir and E. Biçer, "Voltammetric, Spectroscopic and Thermal Studies on the Binding of Some Heterocyclic Azo Compounds with α- and β-Cyclodextrins: pH Effect and Association Affinity," *Russian Journal of Electrochemistry,* vol. 53, no. 5, pp. 486-499, 2017.

[216] C. Balestrieri, G. Colonna, A. Giovane, G. Irace and L. Servillo, "Second-Derivative Spectroscopy of Proteins," *European Journal of Biochemistry,* vol. 90, pp. 433-440, 1978.

[217] Z. Karim and R. Adnan, "The β-cyclodextrin-chitosan inclusion complex: Characterization and application in the removal of pesticides in wastewater," *Archives of Environmental Science,* vol. 6, pp. 1-12, 2012.

[218] K. Kitamura and N. Imayoshi, "Second-Derivative Spectrophotometric Determination of the Binding Constant between Chlorpromazine and β-Cyclodextrin in Aqueous Solutions," *Analytical Sciences,* vol. 8, pp. 497-501, 1992.

[219] N.A., "2,6-Diisopropylphenol," National Institute of Standards and Technology. U.S. Department of Commerce., 2017. [Online]. Available: http://webbook.nist.gov/cgi/cbook.cgi?ID=C2078548&Mask=80. [Accessed 5 July 2017].

[220] J. Feng, A. Miedaner, P. Ahrenkiel, M. E. Himmel, C. Curtis and D. Ginley, "Self-Assembly of Photoactive TiO2-Cyclodextrin Wires," *Journal of the American Chemical Society. Communications,* vol. 127, pp. 14968-14969, 2005.

[221] J. C. Yu, Z.-T. Jiang, H.-Y. Liu, J. Yu and L. Zhang, "β-Cyclodextrin epichlorohydrin copolymer as a solid-phase extraction adsorbent for aromatic compounds in water samples," *Analytica Chimica Acta,* vol. 477, pp. 93-101, 2003.

[222] Z. Zheng, L. Zhang, Y. Liu and H. Wang, "A facile and novel modification method of β-cyclodextrin and its application in intumescent flame-retarding polypropylene with melamine phosphate and expandable graphite," *Journal of Polumer Research,* vol. 4, pp. 74-91, 2016.

[223] D. Zhao, L. Zhao and C.-S. Zhu, "Water-insoluble β-cyclodextrin polymer crosslinked by citric acid: synthesis and adsorption properties toward phenol and methylene blue," *Journal of Inclusion Phenomena and Macrocyclic Chemistry,* vol. 63, pp. 195-201, 2009.

[224] T. Kunitake and S.-W. Lee, "Molecular imprinting in ultrathin titania gel films via surface sol–gel process," *Analytica Chimica Acta,* vol. 504, pp. 1-6, 2004.

[225] D.-H. Yang, M.-J. Ju, A. Maeda, K. Hayashi, K. Toko, S.-W. Lee and T. Kunitake, "Design of highly efficient receptor sites by combination of cyclodextrin units and molecular cavity in TiO2 ultrathin layer," *Biosensors and Bioelectronics,* vol. 22, pp. 388-392, 2006.

[226] S.-W. Lee, I. Ichinose and T. Kunitake, "Molecular Imprinting of Azobenzene Carboxylic Acid on a TiO2 Ultrathin Film by the Surface Sol-Gel Process," *Langmuir,* vol. 14, pp. 2857-2863, 1998.

[227] W. Zhang, D. J. Webb and G.-D. Peng, "Investigation Into Time Response of Polymer Fiber Bragg Grating Based Humidity Sensors," *IEEE Journal of Lightwave Technology,* vol. 30, no. 8, pp. 1090-1096, 2012.

[228] T. Venugopalan, T. Sun and K. Grattan, "Long period grating-based humidity sensor for potential structural health monitoring," *Sensor and Actuators A,* vol. 148, pp. 57-62, 2008.

[229] M. V. Fuke, P. Kanitkar, M. Kulkarni, B. B. Kale and R. C. Aiyer, "Effect of particle size variation of Ag nanoparticles in polyaniline composite on humidity sensing," *Talanta,* vol. 81, pp. 320-326, 2010.

[230] H. Liang, Y. Jin, J. Wang and X. Dong, "Relative Humidity sensor based on polarization maintaining fiber loop mirror with polymer coating," *Microwave and Optical Technology Letters,* vol. 54, pp. 2364-2366, 2012.

[231] J. Mathew, Y. Semenova and G. Farrell, "Fiber optic hybrid device for simultaneous measurement of humidity and temperature," *IEEE Sensors Journal,* vol. 13, no. 5, pp. 1632-1636, 2013.

[232] M. Hernáez, C. R. Zamarreño, I. R. Matías and F. J. Arregui, "Optical fiber humidity sensor based on surface plasmon resonance in the infrared region," *Journal of Physics: Conference Series,* vol. 178, no. 1, p. 012019, 2009.

[233] J. M. Corres, I. R. Matias, M. Hernaez, J. Bravo and F. J. Arregui, "Optical Fiber Humidity Sensors Using Nanostructured Coatings of SiO2 Nanoparticles," *IEEE Sensors,* vol. 8, no. 3, pp. 281-285, 2008.

[234] S. Bell, "A beginner's guide to humidity measurement," October 2011. [Online]. Available: http://www.npl.co.uk/upload/pdf/Beginner%27s%20guide%20to%20humidity%20measurement%20(draft%20for%20comment).pdf. [Accessed 19 July 2017].

[235] J. S. Santos, I. M. Raimundo Jr, C. M. Cordeiro, C. R. Biazoli, C. A. Gouveia and P. A. Jorge, "Characterisation of a Nafion film by optical fibre Fabry-Perot interferometry for humidity sensing," *Sensors and Actuators B: Chemical,* vol. 196, pp. 99-105, 2014.

[236] E. Fermi, Thermodynamics, New York: Dover Publications, Inc., 1936.

[237] J. Stewart, Calculus, 7th ed., Belmont, CA: Brooks/Cole Cengage Learning, 2012.

[238] Y. Alanoly, "Vaisala Humidity 101 - Humidity, Theory, Terms & Definitions.," Vaisala, 11 October 2008. [Online]. Available: http://www.vaisala.com/Vaisala%20Documents/Common%20Files/Humidity101_HumidityTheoryTermsDefinitions.pdf?_ga=1.214434967.1482519469.1446505017. [Accessed 20 July 2017].

[239] N. S. Osborne and C. H. Meyers, "A formula and tables for the pressure of saturated water vapour in the range 0 to 374 C.," *Journal of Research of the National Bureau of Standards. US department of Commerce,* vol. 13, pp. 1-20, 1934.

[240] I. Del Villar, I. R. Matías , F. J. Arregui and R. O. Claus, "Fiber-Optic Hydrogen Peroxide Nanosensor," *IEEE Sensors Journal,* vol. 5, no. 3, pp. 365-371, 2005.

[241] F. J. Arregui and I. R. Matias, "Optical fiber nanometer-scale Fabry–Perot interferometer formed by the ionic self-assembly monolayer process," *Optics Letters,* vol. 24, no. 9, pp. 596-598, 1999.

[242] N.A., "VAISALA HUMIDITY CONVERSION FORMULAS Ref B210973EN-F," 2013. [Online]. Available: http://www.vaisala.com/Vaisala%20Documents/Application%20notes/Humidity_Conversion_Formulas_B210973EN-F.pdf. [Accessed 25 July 2017].

[243] P. Leger, J. M. Bedicam, A. Cornette, O. Reybet-Degat, B. Langevin, J. M. Polu, L. Jeanin and R. Dominique, "Nasal Intermittent Positive Pressure Ventilation. Long-term Follow-up in patients with severe Chronic Respiratory Insufficiency," *CHEST,* vol. 105, no. 1, pp. 100-105, January 1994.

[244] M. K. Chakrabarti and M. K. Sykes, "Evaluation of the lung ventilator performance analyser," *Anaesthesia,* vol. 31, pp. 521-528, 1976.

[245] N.A., "Vaisala Humidity Calculator 5.0," 2014. [Online]. Available: http://go.vaisala.com/humiditycalculator/5.0/. [Accessed 26 July 2017].

[246] R. Correia, R. Sinha, A. M. Norris, S. Korposh, S. Talbot, F. U. Hernandez, B. R. Hayes-Gill and S. P. Morgan, "Optical fibre sensing at the interface between tissue and medical device," in *Proc. SPIE: International Conference on Biophotonics V, Vol 10340*, Perth, Australia., 2017.

[247] J. D. Wulfkuhle, L. A. Liotta and E. F. Petricoin, "Proteomic applications for the early detection of cancer.," *Nature Reviews Cancer,* vol. 3, no. 4, pp. 267-275, 2003.

[248] N. Orgovan, B. Peter, S. Bosze, J. J. Ramsden, B. Szabo and R. Horvath, "Dependence of cancer cell adhesion kinetics on integrin ligand surface density measured by a high-throughput label-free resonant waveguide grating biosensor," *Scientific Reports,* vol. 4, no. 4034, p. 8p, 2014.

[249] J. Homola, "Surface Plasmon Resonance Sensors for Detection of Chemical and Biological Species," *Chemical Reviews,* vol. 108, no. 2, pp. 462-493, 2008.

[250] D. K. Heyland, P. J. Weijs, J. A. Coss-Bu, B. Taylor, A. S. Kristof, G. E. O'Keefe and R. G. Martindale, "Protein Delivery in the Intensive Care Unit: Optimal or Suboptimal?," *Nutrition in Clinical Practice,* vol. 32, no. 1, pp. 58S-71S, 2017.

[251] P. J. Weijs, R. N. Dickerson, D. K. Heyland, F. A. Moore, S. J. Rugeles and S. A. McClave, "Experimental and Outcome-Based Approaches to Protein Requirements in the Intensive Care Unit," *Nutrition in Clinical Practice,* vol. 32, no. 1, pp. 77S-85S, 2017.

[252] D. Patko, K. Cottier, A. Hamori and R. Horvath, "Single beam grating coupled interferometry: high resolution miniaturized label-free sensor for plate based parallel screening," *Optics Express,* vol. 20, no. 21, pp. 23162-23173, 2012.

[253] S. Korposh, S. James, R. P. Tatam and S.-W. Lee, "Optical fibre long-period gratings functionalized with nano-assembled thin films: Approaches to chemical sensing.," in

Current trends in short- and long-period gratings., Cuadrado-Laborde, Ed., Croatia, InTech, 2012, pp. 63-86.

[254] S. James and R. Tatam, "Fibre optic sensors with nano-structured coatings," *Journal of Optics A: Pure and Applied Optics,* vol. 8, pp. S430-S444, 2006.

[255] S. James and R. P. Tatam, "Optical fibre long-period grating sensors: characteristics and application," *Measurement Science and Technology,* vol. 14, no. 5, pp. R49-R61, 2003.

[256] M. P. DeLisa, Z. Zhang, M. Shiloach, S. Pilevar, C. C. Davis, J. S. Sirkis and W. E. Bentley, "Evanescent wave long-period fiber bragg grating as an immobilized antibody biosensor," *Analytical Chemistry,* vol. 72, no. 13, pp. 2895-2900, 2000.

[257] V. Mishra, N. Singh, U. Tiwari and P. Kapur, "Fiber grating sensors in medicine: Current and emerging applications," *Sensors and Actuators A: Physical,* vol. 167, no. 2, pp. 279-290, 2011.

[258] P. Pilla, A. Sandomenico, V. Malachovska, A. Borriello, M. Giordano, A. Cutolo, M. Ruvo and A. Cusano, "A protein-based biointerfacing route toward label-free immunoassays with long period gratings in transition mode," *Biosensors and Bioelectronics,* vol. 31, no. 1, pp. 486-491, 2012.

[259] Z. Wang, J. R. Heflin, K. Van Cott, R. H. Stolen, S. Ramachandran and S. Ghalmi, "Biosensors employing ionic self-assembled multilayers adsorbed on long-period fiber gratings," *Sensors and Actuators B: Chemical,* vol. 139, no. 2, pp. 618-623, 2009.

[260] A. B. Bandara, Z. Zuo, S. Ramachandran, A. Ritter, J. R. Heflin and T. J. Inzana, "Detection of methicillin-resistant staphylococci by biosensor assay consisting of nanoscale films on optical fiber long-period gratings," *Biosensors and Bioelectronics,* vol. 70, pp. 433-440, 2015.

[261] D. G. Kinniburgh, "General Purpose Adsorption Isotherms," *Environ. Sci. Technol.,* vol. 20, pp. 895-904, 1986.

[262] L. H. Chen, C. C. Chan, K. Ni, P. B. Hu, T. Li, W. C. Wong, P. Balamurali, R. Menon, M. Shaillender, B. Neu, C. L. Poh, X. Y. Dong, X. M. Ang, P. Zu, Z. Q. Tou and K. C. Leong, "Label-free fiber-optic interferometric immunosensors based on waist-enlarged fusion taper," *Sensors and Actuators B: Chemical,* vol. 178, pp. 176-184, 2013.

[263] J. Tellinghuisen, "The Least-Squares Analysis of Data from Binding and Enzyme Kinetics Studies: Weights, Bias, and Confidence Intervals in Usual and Unusual Situations," in *Methods in Enzymology*, Nashville Tennessee, U.S., Department of Chemistry, Vanderbilt University., 2009, pp. 499-529.

[264] S. Maguis, G. Laffont, P. Ferdinand, B. Carbonnier, K. Kham, T. Mekhalif and M.-C. Millot, "Biofunctionalized tilted Fiber Bragg Gratings for label-free immunosensing," *Optics Express,* vol. 16, no. 23, pp. 19049-19062, 2008.

[265] C. A. Barrios, M. J. Bañuls, V. González-Pedro, K. B. Gylfason, B. Sánchez, A. Griol, A. Maquieira, H. Sohlstrom, M. Holgado and R. Casquel, "Label-free optical biosensing with slot-waveguides," *Optics Letters,* vol. 33, no. 7, pp. 708-710, 2008.

[266] M. Belter, A. Sajnóg and D. Baralkiewicz, "Over a century of detection and quantification capabilities in analytical chemistry – Historical overview and trends," *Talanta,* vol. 129, pp. 606-616, 2014.

[267] H.-P. Loock and P. D. Wentzell, "Detection limits of chemical sensors: Applications and misapplications," *Sensors and Actuators B: Chemical,* vol. 173, pp. 157-163, 2012.

[268] H. Li, S. Ha Park, J. H. Reif, T. H. LaBean and H. Yan, "DNA-Templated Self-Assembly of Protein and Nanoparticle Linear Arrays," *J. AM. CHEM. SOC.,* vol. 126, pp. 418-419, 2004.

[269] M. Petcu, P. N. Schaare and C. J. Cook, "Propofol-imprinted membranes with potential applications in biosensors," *Analytica Chimica Acta,* vol. 504, pp. 73-79, 2004.

[270] S. Korposh, S.-W. Lee, S. W. James and R. P. Tatam, "Refractive index sensitivity of fibre-optic long period gratings coated with SiO2 nanoparticle mesoporous thin films," *Measurement Science and Technology,* vol. 22, no. 7, p. 10 p, 2011.

[271] L. Feng, Y. Liu and J. Hu, "Molecularly Imprinted TiO2 Thin Film by Liquid Phase Deposition for the Determination of L-Glutamic Acid.," *Langmuir,* vol. 20, pp. 1786-1790, 2004.

[272] F. U. Hernandez Ledezma, "Imprinted TiO2 deposition onto LPG (period 109 microm). YouTube: OFS, 2017," August 2017. [Online]. Available: https://www.youtube.com/watch?v=aodhpAxx7fU. [Accessed 12 August 2017].

[273] F. U. Hernandez Ledezma, "Imprinted TiO2 deposition onto LPG (period 110.5 microm). YouTube: OFS, 2017," August 2017. [Online]. Available: https://www.youtube.com/watch?v=C4j-41uyr7s. [Accessed 12 August 2017].

[274] R. Kapoor and C.-W. Wang, "Highly specific detection of interleukin-6 (IL-6) protein using combination tapered fiber-optic biosensor dip-probe," *Biosensors and Bioelectronics,* vol. 24, no. 8, pp. 2696-2701, 2009.